EXCLUSIVE QCD FACTORIZATION AND SPIN PHENOMENA AT HIGH ENERGY COLLIDERS

By

Zhite Yu

A DISSERTATION

Submitted to
Michigan State University
in partial fulfillment of the requirements
for the degree of

Physics — Ph.D.

2023

ABSTRACT

EXCLUSIVE QCD FACTORIZATION AND SPIN PHENOMENA AT HIGH ENERGY COLLIDERS

By

Zhite Yu

This PhD thesis is divided into two distinct parts. The first part focuses on hard exclusive scattering processes in Quantum Chromodynamics (QCD) at high energies, while the second part delves into spin phenomena at the Large Hadron Collider (LHC).

Hard exclusive scattering processes play a crucial role in QCD at high energies, providing unique insights into the confined partonic dynamics within hadrons, complementing inclusive processes. Studying these processes within the QCD factorization approach yields the generalized parton distribution (GPD), a nonperturbative parton correlation function that offers a three-dimensional tomographic parton image within a hadron. However, the experimental measurement of these processes poses significant challenges. This thesis will review the factorization formalism for related processes, examine the limitations of some widely used processes, and introduce two novel processes that enhance the sensitivity to GPD, particularly its dependence on the parton momentum fraction x.

The second part of the thesis centers on spin phenomena, specifically single spin production, at the LHC. Noting that a single transverse polarization can be generated even in an unpolarized collision, this research proposes two new jet substructure observables: one for boosted top quark jets and another for high-energy gluon jets. The observation of these phenomena paves the way for innovative tools in LHC phenomenology, enabling both precision measurements and the search for new physics.

TABLE OF CONTENTS

Part I

QCD Factorization for Exclusive Processes

Chapter 1

Introduction

Within the Standard Model of particle physics, Quantum Chromodynamics (QCD), the quantum theory describing the strong interaction, is the most special part. The Lagrangian governing the dynamics of the theory has colored fields, quarks and gluons, as the fundamental degrees of freedom, while the physical spectrum consists of color-neutral particles, hadrons, that are composite states of the former. The colored particles are never observed in isolation, a property called color confinement, which is the defining feature of QCD but which is still established as an experimental fact instead of having been derived from the first principles of QCD. Although it is believed that QCD has all the components for confinement to emerge, it has not been explicitly shown.

As a result of confinement, the study of the strong interactions among quarks and gluons is always directly involved with hadrons. The color interactions are so strong that the quarks and gluons are strongly bound inside the hadrons. On the other hand, however, the color interactions get weaker as the interacting scales become higher. This phenomenon is called asymptotic freedom [Gross and Wilczek(1973), Politzer(1973)], which was historically sought first as a necessary condition for describing the strong interaction. In a hard collision involving hadrons in the initial or final states, interaction happens at a short time and distance scale so that the strength of the QCD interaction is very weak, and it is the quark and gluon degrees of freedom that are directly involved. The latter now behave almost as

free particles, so they are collectively called partons.[1] As partons move away from the hard interaction, the distance between them becomes larger and larger, and the color interaction becomes stronger and stronger, which eventually turns the partons into hadrons, a process called hadronization.

Therefore, hard scattering processes of hadrons typically involve QCD in a full range of scales, from the hard scale characterized by the hard probe, where the color interactions are weak and perturbative, down to the low scale characterizing the hadronization, where the color interactions become strong enough to confine the colored degrees of freedom into hadrons. It is perhaps an ultimate goal to be able to describe such a full process at all scales within QCD, especially the low scales dominated by the nonperturbative regime of the color interaction. This task, however, is unprecedentedly difficult. Even a semi-complete solution has not been achieved, yet. The only nonperturbative method so far is given by Lattice QCD [Workman et al.(2022)]; it, however, still suffers from limitations from computational resources and timing and from the intrinsic Euclidean nature instead of the real Minkowski nature. Furthermore, Lattice QCD is more of simulating the physical results with the QCD Lagrangian rather than describing the physical mechanisms. A fully analytic solution is still desirable. With that said, though, the results from Lattice QCD are still valuable inputs to our endeavor to understand the nonperturbative QCD interaction.

Another approach, given such a situation, to understanding how colors are confined in hadrons is by probing the hadronic structures in a phenomenological way. This is done

[1] In many contexts, the term "parton" loosely refers collectively to a quark or gluon, with no regard to the interaction scale. Here I restrict its meaning to hard scattering regime because in the bound state of a hadron, the interaction among the colored degrees of freedom is so strong that the latter do not have clear particle properties. So when referring to them as partons, I mean that we are working in the kinematic regime where the hadron is probed at a short distance scale, so that the color interaction becomes weak and the *particle* nature of quarks and gluons emerges. In this sense, the concept of "particles" is by itself a concept for perturbative interactions, but not for a theory with strong interactions.

through hard scattering experimental processes in which the hadrons are hit by high-energy beams of elementary or hadronic particles or large-momentum hadrons are produced in the collision of elementary particles. First of all, such processes are probing the partonic degrees of freedom, so are indeed sensitive to the color interactions. Second, the hard scale implies that there is one stage in the process where the QCD interaction becomes weak and one can utilize perturbative calculation method, by virtue of the asymptotic freedom.

The QCD factorization theorem [Collins et al.(1989)Collins, Soper, and Sterman, Collins(2013)] has been developed to make full use of the asymptotic freedom by factorizing the dynamics at the hard perturbative momentum scale and that at the low nonperturbative scale. Effectively, it gets around the nonperturbative region by identifying good cross sections (or good physical observables) whose *leading* nonperturbative dynamics can be organized into some distribution functions characterizing the full nonperturbative partonic dynamics within hadrons, while whose other non-leading nonperturbative contributions are shown to be suppressed by inverse powers of the large momentum scale of the collision. By neglecting the non-leading contributions, the remaining part involves purely the hard momentum scales so as one can reliably use perturbation theory on the weakly coupled on-shell partons. It comes as a result of the factorization theorem that the nonperturbative dynamics associated with each explicitly observed hadron is independent of each other and the resultant distribution function only depends on each hadron itself, but not on the specific processes. Such property is termed universality of the distribution functions, which, albeit not perturbatively calculable, can be fitted from experimental data. In reality, these distribution functions can be represented as correlation functions of quark or gluon fields between hadronic states. Such field-theoretic definitions also allow them to be calculated using nonperturbative approaches like Lattice QCD [Constantinou et al.(2021)]. Once obtained, they can be used as inputs to

make predictions for different hard scattering processes at different energies. In this way, although universality does not come as a prerequisite of establishing factorization in the first place, it is the universality that equips factorization with a predictive power.

On the other hand, the universality of the parton correlation functions, especially with the field-theoretic operator definitions, enables them to be studied on their own, and thereby uncover certain aspects of the confined partonic dynamics. This is how factorization serves as a phenomenological way to probe the hadron structures. Since the colors are fully entangled inside hadrons, the hadron structures in terms of partons are far more complicated than the atomic structures in terms of electrons. The best one can do phenomenologically to probe hadron structures is to study various parton correlation functions. Those correlation functions are in turn embedded by factorization formalism into physical observables in hard scattering processes. Different processes give probe to different correlation functions.

The simplest process is the deeply inelastic scattering (DIS), in which a high-energy electron beam is scattered off the hadronic target, be it a single hadron like a proton or neutron or a nucleus, with a large momentum transfer $q = l - l'$, where l and l' are the momenta of the electron before and after the scattering, respectively, and $Q \equiv \sqrt{-q^2}$ is much greater than the hadronic scale, $\Lambda_{\rm QCD} \simeq 200$ GeV. In the final state, only the scattered electron is identified and measured, and everything else is *inclusively* summed over. At leading power of $\Lambda_{\rm QCD}/Q$, the cross section is dominated by the scattering configuration where the target enters the hard interaction via one single energetic parton (which can also be accompanied by arbitrarily many gluons of scalar polarization in a gauge theory with a covariant gauge). The inclusiveness of the hadronic final states causes the soft gluon exchanges between the scattered parton and the beam remnants to be suppressed by $1/Q$, and thus makes the dynamics of the target evolution independent of the rest of the scattering. In

this way, the DIS cross section is factorized into a set of parton distribution functions (PDFs) $f_{i/h}(x)$, which, loosely speaking, count the parton number densities at a given longitudinal momentum fraction x of a fast moving hadron h, for each parton flavor i being a quark q, antiquark ($\bar{q}$), or gluon (g).

The factorization formula of the DIS cross section and the concept of PDF date back to 1969 before the invent of QCD when Feynman first proposed the parton model [Feynman(1969)]. Nevertheless, a carefully formulated factorization formalism based on the first principles of QCD leads to many fruitful results. Below are a few relevant ones to this paper.

(1) It identifies the factorization formalism as being separating hard and low energy scales, and makes a consistent use of asymptotic freedom.

(2) It provides a clear operator definition for the PDF, allowing it to be studied by itself within field theory, and an unambiguous procedure for perturbatively calculating the hard parton scattering cross sections $\hat{\sigma}(x)$, whose convolution with the PDFs gives the full cross section at leading power of $1/Q$, allowing one to go to any perturbative orders in principle, which in turn allows the fitting of PDFs to data at any perturbative order.

(3) By carefully separating hard and low scales with renormalization effects taken into account, the factorization formalism introduces a factorization scale μ to the PDF and hard scattering coefficients, so that they are now dependent on one more variable and shall be written as $f_{i/h}(x,\mu)$ and $\hat{\sigma}(x,\mu)$. Then the full hadronic cross section σ of the DIS is expressed as,

$$\sigma_h(x_B,Q) = \sum_{i=q,\bar{q},g} \int_{x_B}^{1} dx\, f_{i/h}(x,\mu)\, \hat{\sigma}(x_B/x, Q/\mu) + \mathcal{O}\left(\frac{\Lambda_{\rm QCD}}{Q}\right), \qquad (1.1)$$

where $x_B = Q^2/2P \cdot q$ is the Bjorken variable with P being the hadron momentum.

(4) The physical requirement that the whole cross section σ_h not depend on μ leads to a set of evolution equations, called DGLAP equations [Dokshitzer(1977), Gribov and Lipatov(1972), Lipatov(1974), Altarelli and Parisi(1977)], for the PDFs and hard coefficients, controling their dependence on μ, whose solution gives an efficient way to resum all logarithms of Q/Λ, improving the precision of Eq. (1.1).

(5) The factorization procedure can be generalized to other processes besides DIS, including semi-inclusive DIS (SIDIS) in lepton-hadron collisions, and Drell-Yan processes in hadron-hadron collisions. With the clear operator definitions of the PDFs, one can show their exact universality, so as to maximize the predictive power of factorization.

(6) The full spin dependence of both the hadrons and partons can be consistently included, together with their evolution equations.

(7) The systematic formulation brings the power suppressed terms in Eq. (1.1) under control, such that one can also include higher-power terms, with new parton distribution functions, if desired.

(8) It can be easily generalized (although with practical complications) to different kinds of inclusive processes involving more than one scales, especially when they are widely separated. This leads (consistently) to, among others, a new kind of factorization, called transverse-momentum-dependent (TMD) factorization, giving rise to a new plethora of distribution functions for probing the hadron structure.

(9) The same factorization formalism can be applied to exclusive processes where one observes all final state particles. Such processes complement the inclusive ones by

probing hadron structures in further different aspects, which will form the focus of this paper.

QCD factorization formalism has been extremely successful in interpreting high energy experimental data from all facilities around the world, covering many orders in kinematic reach in both x and Q and as large as 15 orders of magnitude in difference in the size of observed scattering cross sections, which is a great success story of QCD and the Standard Model at high energy and has given us the confidence and the tools to discover the Higgs particle in proton-proton collisions [Chatrchyan et al.(2012a), Aad et al.(2012)], and to search for new physics [Cid Vidal et al.(2019)].

However, the probe with a large momentum transfer Q is so localized in space, $1/Q \ll R$ with $R \sim 1/\Lambda_{\rm QCD}$ being the typical hadron size, that it is not very sensitive to the details of confined *three-dimensional* (3D) structure of the probed hadron, in which a confined parton should have a characteristic transverse momentum scale $\langle k_T \rangle \sim 1/R \ll Q$ and an uncertainty in transverse position $\delta b_T \sim R \gg 1/Q$. This calls for the need to go beyond the longitudinal hadron structures described by PDFs, probed by the DIS. Recently, new and more precise data are becoming available for the so-called *two-scale* observables, which have a hard scale Q to localize the collision so as to probe the partonic nature of quarks and gluons, but at the same time entail a *controllable* soft scale to give a handle for the dynamics taking place at $\mathcal{O}(1/R)$. Such two-scale observables can be well described by generalizing the factorization formalism for the fully inclusive DIS. Distinguished by their inclusive or exclusive nature, the generalized factorization theorems enable quantitative matching between the measurements of such two-scale observables and the 3D internal partonic structure of a colliding hadron.

For inclusive two-scale observables, one well-studied example is the production of a massive boson that decays into a pair of measured leptons in hadron-hadron collisions, known as

the Drell-Yan process, as a function of the pair's invariant mass Q and transverse momentum q_T in the lab frame [Collins et al.(1985)Collins, Soper, and Sterman]. When $Q \gg 1/R$, the production is dominated by the annihilation of one active parton from one colliding hadron with another active parton from the other colliding hadron, including quark-antiquark annihilation to a vector boson (γ, W/Z) or gluon-gluon fusion to a Higgs particle. When $Q \gg q_T \gtrsim 1/R$, the measured transverse momentum q_T of the pair is sensitive to the transverse momenta of the two colliding partons before they annihilate into the massive boson, providing the opportunity to extract the information on the active parton's transverse motion inside the colliding hadron, which is encoded in the TMD PDFs (or simply, TMDs), $f_{i/h}(x, k_T, \mu^2)$ [Collins(2013)], whose dependence on the factorization scale μ has been included. Like PDFs, TMDs are universal distribution functions to find a parton i with a longitudinal momentum fraction x *and* transverse momentum k_T from a colliding hadron of momentum p with $xp \sim \mu \sim Q \gg k_T$, and describe the 3D motion of this active parton, its flavor dependence and its correlation with the property of the colliding hadron, such as its spin [Bacchetta et al.(2007)Bacchetta, Diehl, Goeke, Metz, Mulders, and Schlegel, Diehl(2016)]. For a spin-1/2 target, there are 8 different types of TMDs, for both quark and gluon partons, categorized by the dependence on the parton and target spins, which greatly generalizes the 3 types of quark PDFs and 2 types of gluons PDFs. Although this poses new challenges for a full extraction of TMDs from experimental data, it undoubtedly provides more opportunities to probe multifaceted aspects of the hadronic structures.

However, due to the inclusive nature, the probed transverse momentum k_T of the active parton in the hard collision is *not* the same as the intrinsic or confined transverse momentum of the same parton inside a bound hadron [Qiu et al.(2020)Qiu, Rogers, and Wang]. As the colliding hadron is broken by the large momentum transfer Q, the fast-moving partons

travel with bare colors, whose strong interactions among each other trigger a complex series of parton emissions and evolutions. Such collision-induced partonic radiation, called parton shower, generates an additional transverse momentum to the probed active parton, which is encoded in the evolution equation of the TMDs and could be non-perturbative, depending on the hard scale Q and the phase space available for the shower. With more data from current and future experiments, including both lepton-hadron and hadron-hadron collisions, better understanding of the scale dependence of TMDs could provide us with valuable information on the confined motion of quarks and gluons inside a bound hadron [Accardi et al.(2016), Abdul Khalek et al.(2021), Liu et al.(2021a)Liu, Melnitchouk, Qiu, and Sato, Liu et al.(2021b)Liu, Melnit

In contrast, in exclusive hadronic scattering processes, the colliding hadron(s) are not broken, so the corresponding observables could be directly related to intrinsic properties of hadrons, without being interfered by parton showers. In order to employ asymptotic freedom for perturbative calculation, it is necessary to have a hard scale $Q \gg 1/R$ for good exclusive observables. Then, as will be discussed in detail in this paper, the amplitudes of such exclusive processes can also be factorized into nonperturbative parton correlation functions, with coefficients capturing the hard scattering of the partons that can be calculated perturbatively. The resultant correlation functions also have field-theoretic definitions, which can be studied on their own and encode information on the confined parton dynamics complementary to inclusive processes.

The simplest hard exclusive process is large-angle meson scattering [Lepage and Brodsky(1980), Brodsky and Lepage(1989)], with the simplest example being the scattering of electron e and neutral pion π^0,

$$e + \pi^0 \to e + \gamma, \tag{1.2}$$

which in the center-of-mass (c.m.) frame produces an electron and photon pair with a large scattering angle. At a high collision energy, this process contains a hard scale Q that is characterized by the large transverse momentum of the final-state e or γ. Then at the leading power of $1/Q$, the annihilation of the π^0 happens through *two* collinear parton lines, which are constrained to be a quark-antiquark pair by isospin symmetry. By slightly generalizing the factorization of DIS, one can express the amplitude of Eq. (1.2) in terms of the convolution of the *distribution amplitude* (DA), $D(z)$, of the pion and a hard coefficient $C(z)$. In contrast to inclusive processes, whose factorization is at cross section level, the factorization of exclusive processes works at amplitude level, and the resultant correlation functions correspond to amplitudes. In this way, $D(z)$ is the probability amplitude of turning the pion into a pair of quark and antiquark, carrying longitudinal momentum fractions z and $1-z$, respectively, of the pion, in a way analogous to a hadron wavefunction. The parton distribution function, on the other hand, is analogous to square of the hadron wavefunction, (with certain degrees of freedom traced over). The process in Eq. (1.2) can also be reversed, with the pion being produced in the final state. The factorization equally applies and results in a DA $\bar{D}(z)$ that gives the transition amplitude from a pair of collinear quark-antiquark pair into a pion. The operator definitions of $D(z)$ and $\bar{D}(z)$ simply related them by a complex conjugate.

The single-meson process in Eq. (1.2) can be generalized to involve more mesons and also to large-angle scattering involving baryons. The factorization formalism can be similarly applied, with a DA associated with each hadron in the initial or final state. A detailed knowledge of the z dependence of DAs entails how the hadron momentum is distributed among the valence partons.

Slightly more complicated exclusive processes involve diffracted hadrons. The simplest example is given by replacing the pion in Eq. (1.2) by a h of any flavor and also adding

another hadron h in the final state with a slightly diffracted momentum,

$$e(l) + h(p) \to e(l') + h(p') + \gamma(k), \tag{1.3}$$

where the same label p is used for both the protons and initial-state proton momentum. In the c.m. frame of the scattering, we require the transverse momenta of the final-state electron and photon to be much greater than that of the diffracted proton,

$$l'_T \sim k_T \sim q_T \gg p'_T \sim \sqrt{-t}, \tag{1.4}$$

with $t = (p - p')^2$. Consider the scattering channel when the photon $\gamma(k)$ is not radiated by the electron, the diffracted hadron is then connected by *two* collinear parton lines to the hard scattering, which is characterized by a hard scale $Q \sim q_T$. By generalizing the factorization for Eq. (1.2), we can factorize the amplitude of Eq. (1.3) into a new type of parton correlation functions, generalized parton distributions (GPDs) $F_h^i(x, \xi, t)$, convoluted with hard coefficients $C_i(x, xi; Q)$ that can be perturbatively calculated. The GPD combines the PDF and DA into a coherent picture, with x playing the role of the longitudinal parton momentum fraction, which is like the x variable of the PDF, and ξ characterizing the longitudinal momentum transfer from the hadron h to the hard interaction, which plays the role of the pion momentum in the DA.

More importantly, the GPD contains one more soft scale $\boldsymbol{\Delta}_T \equiv \boldsymbol{p}_T - \boldsymbol{p}'_T$ that is controllable, similar to the k_T dependence in TMDs. Thus the diffractive hard exclusive processes provide another type of good two-scale observables. Here, by Fourier transforming the GPD with respect to $\boldsymbol{\Delta}_T$ to the position space $\boldsymbol{b}_T$ in the forward limit ($\xi \to 0$),

the transformed GPD $f_{i/h}(x, \boldsymbol{b}_T)$ as a function of b_T provides a transverse spatial distribution of the parton i inside the hadron h at a given value of the parton momentum fraction x [Burkardt(2000), Burkardt(2003)]. That is, measuring GPDs could provide an opportunity to study QCD tomography to obtain 3D parton images in the x and $\boldsymbol{b}_T$ space, which complements the 3D images encoded in TMDs in the x and $\boldsymbol{k}_T$ space. The spatial b_T dependence could allow us to define an effective hadron radius in terms of its quark (or gluon) spatial distributions, $r_q(x)$ (or $r_g(x)$), as a function of x, in contrast to its electric charge radius [Hofstadter and McAllister(1955), Hofstadter(1956), Simon et al.(1980)Simon, Schmitt, Borkowski, and Walther, Bernauer et al.(2010), Bernauer et al.(2014), Zhan et al.(2011), Mihovilovič et al.(2017), Mihovilovič et al.(2021), Xiong et al.(2019)], allowing us to ask some interesting questions, such as should $r_q(x) > r_g(x)$ or vice versa, and could $r_g(x)$ saturate if $x \to 0$, which could reveal valuable information on how quarks and gluons are bounded inside a hadron. By virtue of the exclusiveness, $\boldsymbol{\Delta}_T$ is measured in experiments and directly correspond to the GPD variable, without contamination from any parton showers. The 3D pictures entailed in GPDs can thus be unambiguously extracted.

However, there are obstacles in the way to use exclusive processes to probe hadron structures. First, the exclusiveness dictates each hard scattered hadron or each diffracted hadron to be connected to the hard scattering by two collinear parton lines. Compared to inclusive processes, this causes a penalty of one power suppression of $1/Q$. As a result, the cross sections become lower as one goes to higher energies. The accessible data are therefore limited to a finite range of Q. Second, the intriguing parton pictures encoded in DAs and GPDs require a precision knowledge of them as functions of z or x. This is, however, hard to extract, for two following reasons. (1) The exclusive factorization happens at the amplitude level, and the convolution variable z or x is the parton loop momentum, flowing through the active

parton pair defining the DAs or GPDs, whose integration is always from 0 to 1 or -1 to 1, and is never pinned down to a particular value. This is in sharp contrast to the factorization of inclusive processes like the DIS, which happens at the cross section level. As shown in Eq. (1.1), the probed x is constrained within the range $[x_B, 1]$. At the leading perturbative order, x is also equal to the x_B, which is a direct experimental observable. (2) For most of the known DA or GPD-related processes, the convolutions of the hard coefficients with DA or GPDs only give "moment-type" information, like the integral $\int_0^1 dz\, D(z)/z$ for the DA or $\int_{-1}^1 dx\, F(x,\xi,t)/(x-\xi+i\varepsilon)$ for the GPD. Extracting full details of DAs or GPDs from such moments does not yield a unique solution. Third, for diffractive processes, there is one extra channel where the diffracted hadron is connected to the hard scattering by one virtual photon if its quantum state is allowed. As we will show, the single photon exchange channel has one power enhancement compared to the GPD channel, so could dominate the contribution to the total amplitude and also interfere with the GPD-sensitive channels. This causes a large background for extracting the GPDs. It will be the main focus of this paper to try to improve the extraction of GPDs, especially their x dependence.

The structure of this paper is organized as the following. In Ch. 2, I will review the factorization formalism, in the context of simple processes like the representative Sudakov form factor, and inclusive processes like the DIS. The key elements of factorization, including the Libby-Sterman analysis, power counting, subtraction formalism, Ward identity, and unitarity. In Ch. 3, we will extend the factorization formalism to exclusive processes. First I will show the factorization for $2 \to 2$ large-angle meson scattering, starting with one-meson process in Eq. (1.2) gradually increasing the meson number, and ending at meson-meson scattering into two mesons. The extension to baryonic or $2 \to n$ ($n > 2$) case should be straightforward and will not be discussed. Then I will generalize the large-angle

factorization to the single-diffractive case. This will introduce a complication due to a pinch in the Glauber region. However, thanks to the single-diffractive constraint, this pinch will be avoided by deforming the contour of soft gluon momentum. This will lead to a unified factorization for a general type of hard exclusive processes that only involves one single diffraction. Our argument will also indicate that as one goes beyond single-diffractive cases, the contour deformation will not be allowed to get away with the Glauber pinch, and thus they will not be factorizable. After setting up the factorization formalism for the single-diffractive processes, Ch. 4 will be devoted to the phenomenological study of GPDs, especially to their x dependence. I will review the definitions of GPDs and the parton pictures encoded therein, and then briefly discuss the many popular processes for probing GPDs, especially their drawbacks in the x dependence. Then after a systematic discussion on the sensitivity to x dependence, I will introduce two new processes that provide enhanced sensitivity to the x dependence. I will first give a detailed discussion on the calculation of their hard coefficients, and then organize them into observables, including both unpolarized differential cross sections and various polarization asymmetries. Finally, I will demonstrate how enhanced x sensitivity can help us determine the GPDs. In Ch. 5, we conclude this paper and present the outlook for the future.

Chapter 2

QCD Factorization: principles and applications to inclusive processes

QCD is a special theory with drastically distinct physics phenomena at the two opposite ends of the energy spectrum. From the expression of running QCD coupling we can infer that at high-energy or short-distance scale, the coupling α_s decreases asymptotically to zero such that the quarks and gluons are asymptotically free particles with their interactions as perturbations on their free motion, whereas at the low-energy or long-distance side, the coupling strength becomes increasingly larger and blows up at the Landau pole $\Lambda_{\rm QCD}$, and hence the quarks and gluons strongly interact with each other and the perturbative picture breaks down. Although this picture is obtained within perturbation theory, the RGE solution has resummed a certain logarithmic order to all perturbative orders in α_s and reflects some aspects of the nonperturbative domain, which is also confirmed by the fact that $\Lambda_{\rm QCD}$ is of the same order of the hadron size $R \sim 1$ fm $\simeq 200$ MeV. So while it is not likely to be the case that the coupling α_s indeed becomes infinite at $\Lambda_{\rm QCD}$, it certainly implies that the perturbation description cannot be extrapolated beyond that scale. Some nonperturbative mechanism must kick in at $\mu \gtrsim \Lambda_{\rm QCD}$ to resolve the perturbative singularity, and confine the quarks and gluons within bound hadrons. In this way, elementary fields in the QCD Lagrangian do not appear individually in nature, but it is their bounds states, hadrons, that

are directly observed in reality.

This is the basic intuitive picture of QCD. Its speciality in this aspect is that one cannot separate the strong interaction from the particle constituents, like what one may consider for the electroweak sector of the SM. The QCD by itself is a nonperturbatively strongly interacting theory, as well as self-contained and self-explained. Therefore, any experiments one may possibly do to probe the QCD dynamics are directly involved with hadrons, and the associated nonperturbativity. QCD factorization is a method or formalism that applies to certain kinds of processes involving one (or more) hard scale Q by separating the short-distance dynamics, which can be perturbatively treated with the quark and gluon degrees of freedom, from the long-distance dynamics, which is proved to correspond to certain nonperturbative universal process-independent parton correlation functions in the hadrons. Those functions can be obtained by fitting various different processes to the experiments and facilitate the predictive power of QCD. On the other hand, a precise knowledge of those functions also uncovers valuable aspects of the hadron structures.

In this section, I will review important concepts and technicalities of QCD factorization, using some familiar inclusive processes as examples. This will serve as a useful background and comparison for the exclusive processes to be treated in the next section.

2.1 Factorization as a power expansion

2.1.1 Feynman's intuition and parton model

Factorization is the rigorous mathematical formulation of the Feynman's parton model [Feynman(1969)] from the first principles of QCD. To motivate the starting point of factorization, I briefly review the Feynman's intuition leading to the parton model.

In the deep inelastic scattering (DIS) of electron e and proton p,

$$e(k) + p(P) \to e(k') + X, \tag{2.1}$$

the electron exchanges a virtual photon γ^* of momentum $q = k - k'$ that has a high virtuality $Q = \sqrt{-q^2}$ to localize the interaction within the size $\delta r \sim 1/Q$. When working in the center-of-mass (CM) frame, the fast-moving proton undergoes Lorentz contraction and dilation, such that

(1) from the perspective of the hard interaction, the proton appears as a flat plate of transverse width $R \sim 1/\Lambda_{\rm QCD}$,

(2) the parton constituents, called partons by Feynman and later identified as quarks and gluons, are more or less evenly distributed in this "flat plate", and

(3) the interaction among the partons happens in a time scale $\tau \sim 1/\Lambda_{\rm QCD}$ in the proton rest frame, and now becomes dilated to be $\tau' \sim (Q/m)\tau \sim Q/\Lambda^2_{\rm QCD}$, where we used the fact that the proton mass m is of the same order as $\Lambda_{\rm QCD}$.

Now (2) implies that when the electron (or the virtual photon) hits one parton in the proton, which happens in the distance scale $\delta R \sim 1/Q$ with a duration $\delta t \sim 1/Q$, the probability for a second parton to participate in the hard interaction is of the order $\delta r/R \sim 1/(QR) \sim \Lambda_{\rm QCD}/Q$, which is suppressed as $Q \gg \Lambda_{\rm QCD}$. The partons confined in the hadrons are never freely on shell, but engage in strong interactions with other partons and have virtualities of order $\Lambda^2_{\rm QCD}$. During the hard interaction, the interaction between partons is suppressed by $\delta t/\tau' \sim \Lambda^2_{\rm QCD}/Q^2$, by (3), so the role played by the parton virtualities in the hard interaction is also suppressed.

As a result, the hard interaction between the electron and proton is actually between the electron and a single free on-shell parton. The whole DIS cross section can be approximated by the product of the probability of finding one parton out of the proton and the cross section of the electron scattering off a free parton. The factorization formula written down following this intuition constitutes the Feynman's parton model [Feynman(1972)]. The Feynman's parton model predates the establishment of QCD and will receive further corrections and developments from QCD. But it makes clear the important principle of factorization that we are approximating the full hadron cross section by expanding in terms of the power of Λ_{QCD}/Q. Factorization is valid up to a power correction.

2.1.2 Assumptions of factorization

In order to derive factorization from the first principles of QCD, we need to systematize the power expansion of the full hadronic cross sections. Without being able to solve QCD non-perturbatively, this cannot be constructed from zero, but has to rely on certain assumptions on the nonperturbative nature of QCD. These assumptions need not be made very precise, and should be moderate enough so as not to contradict our first intuitions and experiments. For our purpose, we take the following assumptions:

(1) A hadron entering the interaction is connected to a group of parton lines that make up a correct quantum number. The connection vertex can be thought of as some wave function which does not need to be made clear. All possible parton configurations should be included, with different probability amplitudes. This assumption makes concrete the discussion of the hadron scattering in terms of its parton constituents.

(2) Inclusive processes involve a sum over final states, which in reality are all kinds

of hadronic states. In perturbative picture, those hadronic states emerge from the hadronization of partonic states. We take the assumption that the sum over hadronic states is equivalent to the sum over partonic states,

$$\sum_X |X_h; \text{out}\rangle\langle X_h; \text{out}| \Longleftrightarrow \sum_X |X_{q,g}; \text{out}\rangle\langle X_{q,g}; \text{out}|. \tag{2.2}$$

Note that this is not an equal sign, because the partons can easily make up a color non-singlet state. Since initial states are usually color singlets, those non-singlet states necessarily give zero results. This assumption avoids dealing with the details of parton to hadron transitions in the final states, as the latter is not clearly understood.

(3) The sum over all perturbative Feynman diagrams in terms of partons, whether it converges or not, represents the true nature. This assumption also underlies the perturbation theory for the electroweak interaction, but has more significance for the nonperturbative theory, QCD. It is also the foundation of the previous two assumptions.

(4) The configuration in which all the partons connected to the hadrons are highly virtual is strongly suppressed. In the opposite limit, when the partons have low virtuality, we expect nonperturbative dynamics to kick in and slowly saturates the kinematic region with the parton virtuality $k^2 \lesssim \Lambda^2_{\text{QCD}}$. This will be made more precise in Sec. 2.2.2 that if the low-virtuality region is not associated with a pinch singularity, one can deform the contour of the parton momentum to stay away from a low virtuality. It is only at *pinched* low-virtuality regions that genuine nonperturbative dynamics dominates.

2.2 Libby-Sterman analysis

2.2.1 Two examples of pinch singularity

To understand the significance and get some feelings of pinch singularity, let us first study two simple toy examples.

The first example is given by the one-dimensional integral

$$I_1(m) = \lim_{\epsilon \to 0^+} \int_{-\infty}^{\infty} \frac{dx}{2\pi} \frac{1}{x^2 - m^2 + i\epsilon}, \tag{2.3}$$

where the limit $\epsilon \to 0^+$ is to remind that the same $i\epsilon$ prescription as in Feynman integrals applies here to shift the poles $\pm m$ on the integration contour to lower and upper half planes respectively. We will suppress the limit $\epsilon \to 0^+$ later if no confusion occurs. Because of the $i\epsilon$ prescription, the integration variable x should be considered as a complex variable whose integration contour is on the whole real axis. By the normal trick of Wick rotation $x \to ix$, this integral can be easily evaluated,

$$I_1(m) = -\frac{i}{2m}. \tag{2.4}$$

Why is the integral $I_1(m)$ singular at $m = 0$? As $m \to 0$, the two poles $\pm m \mp i\epsilon$ approach each other and coalesce at 0 as $m = 0$. These two coalescing poles lie on different sides of the integration contour and pinch it at the origin such that no matter how we deform the contour, it must pass through the poles as 0. Around the pole, we are dealing with an integral $\int_0 dx/x^2$, which diverges in a power form, and hence $I_1(m) \propto 1/m$ has a power singularity of m as $m \to 0$. Such singularity due to a pair of coalescing poles pinching the

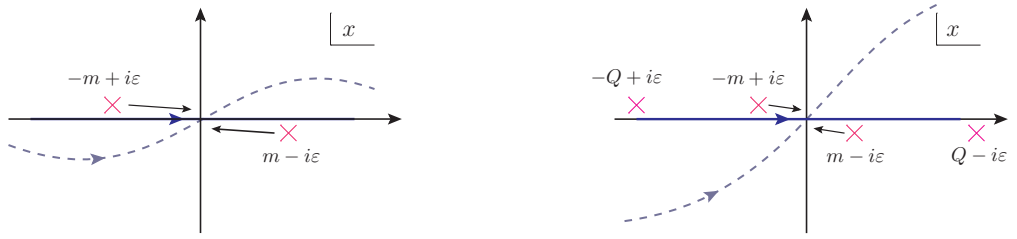

(a) (b)

Fig. 2.1: Integration contours of x in (a) Eq. (2.3) and (b) Eq. (2.9) on the complex plane, respectively. The poles $\pm m \mp i\epsilon$ approach the origin as $m = 0$ and pinch the the contour in both cases. When $m \neq 0$, we can deform the contours up to m, as indicated by the dashed blue lines.

integration contour is called pinch singularity.

When $m \neq 0$, the pinch becomes inexact. And then we can deform the contour to stay away from the two poles $\pm m \mp i\epsilon$, but only up to the extent of $\mathcal{O}(m)$, i.e., in the region near the poles, the distance between the contour and the poles is at most m, $|x - (\pm m)| \lesssim m$, as shown in Fig. 2.1(a) by the dashed blue line. In this region, the integral has a power counting

$$\int_{\sim m} \frac{dx}{x^2 - m^2 + i\epsilon} \sim m \cdot \frac{1}{m^2} \sim \frac{1}{m}, \tag{2.5}$$

where we count $|dx|$ as m and $|x^2 - m^2|$ as m^2. This agrees with the exact solution in Eq. (2.4). The region with $|x| \gg m$ does not suffer from any pinched poles, so we can deform the contour to make x arbitrarily large, which gives infinitesimal contribution to the integral,

$$\int_{\gg m} \frac{dx}{x^2 - m^2 + i\epsilon} \sim \int_{x \gg 1} \frac{dx}{x^2} \sim 0. \tag{2.6}$$

In this way, the main contribution to the integral $I_1(m)$ comes from the region near the two poles $\pm m$ that would become pinched as $m \to 0$.

We can understand this further by taking the two poles $\pm m$ to be on the same half plane,

which gives a modified integral

$$I_1'(m) = \int_{-\infty}^{\infty} \frac{dx}{(x - m + i\epsilon)(x + m + i\epsilon)} = \int_{-\infty}^{\infty} \frac{dx}{x^2 - m^2 + i\epsilon\,\mathrm{sgn}\,[x]}. \tag{2.7}$$

Since both poles $\pm m - i\epsilon$ lie on the lower half plane, we can uniformly deform the integration contour to the upper half plane all the way to infinity, which kills the whole integral,

$$I_1'(m) = \lim_{K\to\infty} \int_{-\infty}^{\infty} \frac{dx}{(x + iK - m + i\epsilon)(x + iK + m + i\epsilon)} = 0, \tag{2.8}$$

as can be easily verified from the direct evaluation of Eq. (2.7) by residue theorem.

Therefore, the pinch singularity at $m = 0$ becomes the region that gives important contribution to the integral when $m \neq 0$.

Now we consider the second toy example,

$$I_2(m, Q) = \int_{-\infty}^{\infty} \frac{d^2\boldsymbol{x}}{(\boldsymbol{x}^2 - m^2 + i\epsilon)(\boldsymbol{x}^2 - Q^2 + i\epsilon)}, \tag{2.9}$$

which is a two-dimensional integral with an extra hard scale $Q \gg m$. A direct evaluation gives

$$I_2(m, Q) = -\frac{1}{4\pi(Q^2 - m^2)} \ln \frac{Q^2}{m^2} \simeq -\frac{1}{4\pi Q^2} \ln \frac{Q^2}{m^2} \times \left[1 + \mathcal{O}\left(\frac{m^2}{Q^2}\right)\right], \tag{2.10}$$

where in the second step we also gave the approximation to the leading power of m^2/Q^2.

Similar to Eq. (2.4), I_2 is also singular as $m \to 0$, but logarithmically. This is also due to the pinched poles $\pm m \mp i\epsilon$ as $m \to 0$. Around the poles, the integral now counts as $I_2 \sim d^2\boldsymbol{x}/(\boldsymbol{x}^2 Q^2) \sim dx/(xQ^2)$, which diverges logarithmically due to the two-dimensional

integration measure. When $m \neq 0$, we can deform the contour to avoid the poles $\pm m$ but only up to m, so that the contribution of the region near those poles is of the order

$$\int_{\sim m} \frac{d^2\boldsymbol{x}}{(\boldsymbol{x}^2 - m^2 + i\epsilon)(\boldsymbol{x}^2 - Q^2 + i\epsilon)} \sim \frac{m^2}{m^2 \cdot Q^2} \sim \frac{1}{Q^2}, \tag{2.11}$$

where we counted $d^2\boldsymbol{x}$ as m^2, and neglected m^2 and x^2 with respect to Q^2.

Apart from the poles $\pm m$, I_2 has two additional poles $\pm Q \mp i\epsilon$. We take $Q \gg m$ to be large, so these two poles do not give pinch singularity, but they still keep the contour from being arbitrarily deformed. In the region with $|x| \sim Q$, the distance between the contour and the poles $\pm Q$ is at most of order Q, as shown in Fig. 2.1(b), so this region gives a power counting

$$\int_{\sim Q} \frac{d^2\boldsymbol{x}}{(\boldsymbol{x}^2 - m^2 + i\epsilon)(\boldsymbol{x}^2 - Q^2 + i\epsilon)} \sim \frac{Q^2}{Q^2 \cdot Q^2} \sim \frac{1}{Q^2}, \tag{2.12}$$

where we have counted both $d^2\boldsymbol{x}$ and $|\boldsymbol{x}^2 - Q^2|$ as Q^2.

In the scenario with $Q \gg m$, the region $|x| \sim m$ is usually called the soft region, and $|x| \sim Q$ the hard region. This is an example of two regions, and we notice from Eqs. (2.11) and (2.12) that both regions have the power counting $1/Q^2$. The intermediate region should also have the same power counting and give the result

$$\frac{1}{Q^2} \int_{\sim m}^{\sim Q} \frac{dx}{x} \sim \frac{1}{Q^2} \ln \frac{Q}{m}. \tag{2.13}$$

The region with $|x| \gg Q$ is referred to as the UV region in a Feynman integral context. Here because of the UV counting $d^2x/x^4 \sim 1/x^2$ as $|x| \to \infty$, it does not contribute to I_2.

In this way, we can understand the result in Eq. (2.10). The integration of $\boldsymbol{x}$ runs over the whole domain from $-\infty$ to ∞, and the scales m and Q appear in the final integral

result through pinch singularities. Here we are using the term "pinch singularity" in a more general sense, not necessarily related to a genuine singularity, but referring to the fact that the contour is constrained by two poles on different sides so that it is forced to go through the region set by those poles. The pinch singularity is a necessary condition for the associated region to make an important contribution to the integral, true for both soft and hard regions. As we have seen from Eq. (2.13), if two regions have the same power counting, their intermediate region leads to a logarithmic contribution interpolating the two regions.

2.2.2 Power expansion and pinch singularity

Physical amplitudes are represented by Feynman diagrams and are given by Feynman integrals of the the parton loop momenta, which can be written as

$$I(p,m) = \int d^d k \frac{X(k;p,m)}{\prod_{j=1}^{N} (D_j(k;p,m) + i\epsilon)^{n_j}}, \tag{2.14}$$

where k, p, and m denotes the array of all the loop momenta, external momenta, and masses, respectively, all being multidimensional. The denominator $D_j(k;p,m)$ is at most a quadratic form of its arguments, and the numerator $X(k;p,m)$ is a polynomial. Typically, $n_j = 1$ for all j.

The external momenta $p = \{p_1, p_2, \cdots, p_n\}$ define $n + C_n^2 = n(n+1)/2$ scales, given by their virtualities $Q_i^2 = p_i^2$ and scalar products $Q_{ij}^2 = p_i \cdot p_j$. We examine the simplest case when there is a single hard scale Q, provided by one or more of the $|Q_{ij}^2|$'s, which is much larger than all the other scales, i.e., mass, virtuality, and Q_{ij}^2 scales[1], which are taken to be of the same order, to be referred to as the soft scale and denoted as M. Such a two-scale

[1]The case of a highly virtual photon as in DIS should be considered as being embedded into the full diagram, with the electron and proton being the external particles.

integral can be examined through the power expansion, which can be schematically written as

$$I(Q,M) = Q^{\dim I} \cdot \sum_{n=-n_0}^{\infty} \left(\frac{M}{Q}\right)^n \left[\sum_{i=0}^{\infty} I_{n,i} \ln^i\left(\frac{Q}{M}\right)\right], \tag{2.15}$$

where n, n_0 and i are integers, $I_{n,i}$ are scaleless functions of M/Q, and the logarithmic dependences on Q/M have been explicitly separated out. In the kinematic regime $Q \gg M$, it would be a good approximation to only keep the leading term (or first few terms) in the power series [Eq. (2.15)]. The Feynman's parton model described in Sec. 2.1 motivates the conjecture that the leading-power approximation should give a factorization structure.

How do we systematically obtain such a power expansion? First, we rescale all the variables in Eq. (2.14) by Q,

$$k \to Q\,\tilde{k}, \quad p \to Q\,\tilde{p}, \quad m \to Q\,\tilde{m}. \tag{2.16}$$

This separates a factor $Q^{\dim I}$ and converts Eq. (2.14) into a scaleless integral,

$$\tilde{I}(p,m) = I(p,m)/Q^{\dim I} = \int d^d\tilde{k} \frac{X(\tilde{k};\tilde{p},\tilde{m})}{\prod_{j=1}^{N}(D_j(\tilde{k};\tilde{p},\tilde{m}) + i\epsilon)^{n_j}}. \tag{2.17}$$

The scenario $Q \gg M$ can be approached by taking the limit $Q \to \infty$, under which all the external particles become massless and on shell and all the mass scales vanish,

$$\tilde{p}_i^2 = p_i^2/Q^2 \to 0, \quad \tilde{m}_i^2 = m_i^2/Q^2 \to 0. \tag{2.18}$$

The scalar products $\tilde{p}_i \cdot \tilde{p}_j$ becomes a scaleless constant of order 1 if i and j are separated by a constant angle, or vanishing if they become collinear to each other. In this way, the the

high-Q limit is equivalent to taking all the mass scales to 0 and all the external particles to be massless and on shell. This massless limit implies singularities for the terms in Eq. (2.15) with $n \leq 0$. More leading terms correspond to more severe mass divergences. Hence, the problem of obtaining the power expansion in M/Q is converted to the problem of finding mass divergences in the corresponding massless theory.

Where does the mass divergence come from? The loop momentum $\tilde{k}$ in Eq. (2.17) is integrated from $-\infty$ and ∞, and the $i\epsilon$ prescription implies that we should consider the integral as a multidimensional integration of a complex variable $\tilde{k}$ on the real axis. There are poles along the integration contour, given by the zeros of one or more $D_j(\tilde{k};\tilde{p},\tilde{m})$'s. If the contour is not trapped around the poles, we can deform the contour to stay away from them such that on the deformed contour, $|D_j| = \mathcal{O}(1)$ instead of 0. This gives a contribution of order 1 to the integral. However, if the contour deformation is forbidden by a pair of or more pinched poles, the integration is forced to include the region where one or more D_j is vanishing. Such regions give singular contribution to the integral, which may or may not be remedied by the numerator X and integration measure.

This is the case for the massless theory with $\tilde{m}, \tilde{p}^2 \to 0$. For finite $\tilde{m}$ and $\tilde{p}^2$, the pinch is no longer exact, and we are allowed to deform the contour to stay away from the poles that would become pinched as $\tilde{m}, \tilde{p}^2 \to 0$, but only up to the extent of order M, such that in the region near those poles, the previously vanishing propagators $D_j(\tilde{k};\tilde{p},\tilde{m})$ are now of order M^2/Q^2 or M/Q, depending on their dimensions. Without considering the numerator and integration measure, this pinched region would give power enhanced contribution to the integral with respect to the hard region where all propagators are of order 1. Therefore, we conclude that *the pinch singularities in the corresponding massless theory specify the important integration regions in the massive theory.*

The above discussion only concerns the pure perturbative Feynman integrals and assumes all particles are massive to regulate the mass divergences. In the real case of QCD, there is indeed a massless gluon, which can cause exact pinch singularity to the Feynman integral. However, around the pinched poles, there are some parton propagators with vanishing virtualities. By the fourth assumption in Sec. 2.1.2, when partons have virtualities that are less than or of the same order of $\Lambda^2_{\rm QCD}$, we should expect nonperturbative dynamics to come in and rescue the perturbative singularities. In this way, the soft scale in the full theory is not given by the masses of partons, but by the intrinsic QCD scale $\Lambda_{\rm QCD}$, or the hadron mass scale. And we expect the nonperturbative effects not to change the power counting of the perturbative theory, but only to smoothly regulate the singular behavior, playing a role similar to a mass scale. Following this, *the perturbative pinch singularities do not lead to genuine divergences in the amplitudes or cross sections, but imply the regions in the parton momentum integrations that are sensitive to nonperturbative QCD dynamics.*

This idea is an underlying (usually implicit) foundation of the applications of perturbative QCD. Without the knowledge of the nonperturbative solution to QCD, it indicates two approaches for predicting high-energy scattering experiments, (1) to separate the part of a diagram containing the propagators that are pinched on shell from the propagators with high virtualities (with or without contour deformation), and (2) to design suitable observables for which the perturbative pinch singularities cancel, so that the infrared sensitivity is cancelled. The first approach leads to factorization, in which the subdiagrams containing the pinched propagators will be organized into universal parton correlation functions, and the subdiagrams with highly virtual propagators have little sensitivity to the infrared QCD dynamics and constitute a hard scattering coefficient. Following the second approach are defined the so-called infrared-safe observables, which can be reliably calculated using perturbative

method. We will see that to obtain the factorization for most processes, both approaches are needed; in particular, we need to show the cancellation of soft gluon connections.

2.2.3 Landau criterion for pinch singularity

The first step to derive factorization is to identify the pinch singularities in the corresponding massless theory, obtained by rescaling all the momentum and mass scales by the hard scale Q, as in Eq. (2.16). This task is easy for simple low-dimensional integrals like Eqs. (2.3) and (2.9), but not for multidimensional Feynman integrals; even the simple one-loop Sudakov form factor [Fig. 2.2(a)] becomes not trivial. A systematic criterion for pinch singularity is therefore needed, which is given by Landau equations [Landau(1959), Collins(2020)]. For the Feynman integral in Eq. (2.14) (or the corresponding massless one), a singular point k_S makes a subset of the denominators D_j's vanish. The sufficient and necessary condition for this singularity to be pinched is that the first derivatives of those D_j's at k_S are linearly dependent, with non-negative coefficients, i.e.,

$$D_j(k_S) = 0, \text{ for } j \in S_N \subset \{1, 2, \cdots, N\}, \quad \text{and} \tag{2.19a}$$

$$\sum_{j \in S_N} \lambda_j \frac{\partial D_j(k_S)}{\partial k_S^\mu} = 0, \text{ with } \lambda_j \geq 0, \text{and at least one } \lambda_j \text{ is strictly positive.} \tag{2.19b}$$

Note that in the notation k, we have assembled all the loop momenta $\{k_1, k_2, \cdots, k_L\}$ by a direct sum, so the index μ in Eq. (2.19) actually runs over $4L$ components. Hence Eq. (2.19b) is true for each loop momentum.

$$\sum_{j \in S_N,\, j \in \text{ loop } l} \lambda_j \frac{\partial D_j(k_{Sl})}{\partial k_{Sl}^{\mu_l}} = 0, \quad l = 1, 2, \cdots, L, \tag{2.20}$$

where k_l is the loop momentum for the loop l, and L denotes the total loop number.

Finding all solutions to the Landau equation is made simple by the Coleman-Norton theorem [Coleman and Norton(1965)]. A single diagram may be associated with different solutions in which different sets of propagators D_j go on shell. For those propagators that are not on shell, we contract the corresponding lines in the Feynman diagram to points and obtain a *reduced diagram*. In the reduced diagram, each loop gives an equation as Eq. (2.20). Suppose a certain loop momentum k flows through n lines, we assign to each vertex a spacetime coordinate, x_a^μ, $(a = 1, 2, \cdots, n)$, and define the spacetime distance between two adjacent vertices j_a and j_b that are connected by the line j,

$$\Delta x^\mu_{j_a j_b} = \Delta x^\mu_{j_a} - \Delta x^\mu_{j_b} = \lambda_j \frac{\partial D_j(k)}{\partial k_\mu}. \tag{2.21}$$

Recall that we are dealing with massless theory, and the condition $D_j(k) = 0$ implies that each propagating line is on shell. In most cases, $D_j(k)$ takes a quadratic form like $(k+p)^2$, such that $\partial D_j(k)/\partial k^\mu$ gives the momentum of the internal line, whose direction is oriented according to the direction of k. By interpreting λ_j as the ratio of the travel time $\Delta x^0_{j_a j_b}$ to the propagating energy $\partial D_j(k)/\partial k_0$,

$$\lambda_j = \Delta x^0_{j_a j_b} \Big/ \frac{\partial D_j(k)}{\partial k_0}, \tag{2.22}$$

we have

$$\Delta x^\mu_{j_a j_b} = \Delta x^0_{j_a j_b} \cdot v_j^\mu, \tag{2.23}$$

where $v_j^\mu = \partial^\mu D_j(k)/\partial^0 D_j(k) = (1, \boldsymbol{p}_j/E_j) = (1, \boldsymbol{v}_j)$ is the four-velocity of the particle on line j. In this way, $\Delta x^\mu_{j_a j_b}$ becomes the spacetime elapse of a physically propagating on-shell

(massless) particle, whose velocity is set by its momentum $\partial^\mu D_j(k) \equiv \partial D_j(k)/\partial k_\mu$. And then the condition in Eq. (2.20) is equivalent to

$$\sum_{j\in S_N, j\in \text{ loop } l} \Delta x^\mu_{j_a j_b} = 0, \tag{2.24}$$

where the direction $j_b \to j_a$ is the same as the loop momentum k. Eq. (2.24) gives a consistent condition for a physically realizable classical process of particle propagation: by orienting all lines as going forward with positive energy, each line represents a on-shell particle propagating with a certain velocity determined by its on-shell momentum, and they can scatter, split, and merge at each vertex, subject to momentum conservation.

The above conclusions apply to both massive and massless theories. But for the concern of determining leading-power contributions, we are interested in the massless limit of the massive theory. Then the task of determining the reduced diagrams is very easy. All the internal lines in the reduced diagrams carry on-shell lightlike momenta and propagate in certain directions at the speed of light, or they have zero momenta and can be attached anywhere.

2.2.4 Example: Sudakov form factor

As a simple example, in Fig. 2.2(a) is shown the one-loop diagram for Sudakov form factor, where a virtual photon with momentum $q = (Q, 0, 0, 0)$ decays into a quark-antiquark $(q\bar{q})$ pair, which go to opposite directions along the z axis, with momenta

$$p_1 = \frac{Q}{2}(1, 0, 0, 1), \quad p_2 = \frac{Q}{2}(1, 0, 0, -1). \tag{2.25}$$

To obtain the reduced diagram, we contract internal lines and identify the resultant diagram as a physically realizable process. For the simplest example, we contract all the three propagators into the reduced vertex, which is called the hard vertex, and obtain the reduced diagram in Fig. 2.2(b). Since it reduces to a tree-level diagram, the meaning of physical process is evident. Now since there is no internal line, this diagram does not contain a pinch. Strictly speaking, this is not an example of pinch singularity, nor a solution to Landau equation because it requires all $\lambda_j = 0$ in Eq. (2.19b). But we will see that this diagram still gives an important contribution to the integral.

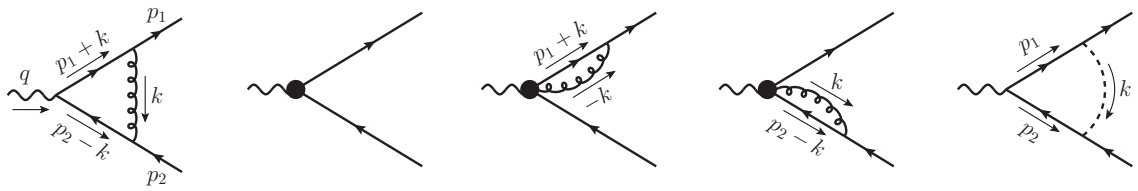

(a) (b) (c) (d) (e)

Fig. 2.2: The one-loop diagram of Sudakov form factor in QCD (a) and its reduced diagrams (b)-(e).

For a less trivial example, we only contract the propagator $p_2 - k$ and obtain the reduced diagram in Fig. 2.2(c). For it to correspond to a physical process, we need both $p_1 + k$ and $-k$ to be lightlike and propagating along the same direction,

$$\lambda_q(p_1 + k) = \lambda_g(-k), \tag{2.26}$$

with $\lambda_{q,g} > 0$, which is just Eq. (2.19b) with $\lambda_{\bar{q}} = 0$ for the coefficient of the antiquark propagator. In this case, the gluon is propagating in a direction collinear to the quark line. Similarly, contracting the propagator $p_1 + k$ gives the reduced diagram in Fig. 2.2(d), in which the gluon is propagating collinearly to the antiquark line.

If we do not contract any propagators, the diagram cannot correspond to a physical process unless the gluon has a zero (or *soft*) momentum, $k = 0$. A zero-momentum particle does not exist as a real particle, so has no meaning in the sense of "propagating with a certain velocity". To embed it into the picture depicted by Coleman and Norton, we interpret the soft particle as having an infinite wavelength, which is not a local particle and can instantaneously connect any two vertices in the reduced diagram. In terms of Landau condition, a soft propagator gives $\partial D_s(k)/\partial k^\mu = 0$ at the point $k = 0$, which automatically satisfies Eq. (2.19b) if $\lambda_s = 1$ and all the other λ_j's are zero. This pinch singularity is given by the reduced diagram in Fig. 2.2(e) in which the soft gluon is represented by the dashed line. The soft pinch singularity is the endpoint of the collinear pinch singularity by taking $\lambda_q = 0, \lambda_g = 1$ and $k = 0$ in Eq. (2.26).

Such procedure can be easily generalized to an arbitrary diagram. In any reduced diagram, the collinear lines coming out of the hard vertex move away from each other at the speed of light. They can only split and combine in their moving directions, and lines of different collinear directions never meet again. Therefore, the collinear sectors are defined by the external particles. Each external lightlike particle with a momentum of order Q defines a collinear direction, along which there can be arbitrarily many collinear lines, as shown in Fig. 2.3, where there are two collinear sectors C_q and $C_{\bar{q}}$, associated with the quark and antiquark, respectively. The hard vertex H contains arbitrarily many propagators whose virtualities are of order Q^2. On top of these, there can be arbitrarily many soft lines connecting onto C_q, $C_{\bar{q}}$, and H, as indicated by the blue dashed lines. They are collected by the soft subdiagram S (which is not necessarily connected).

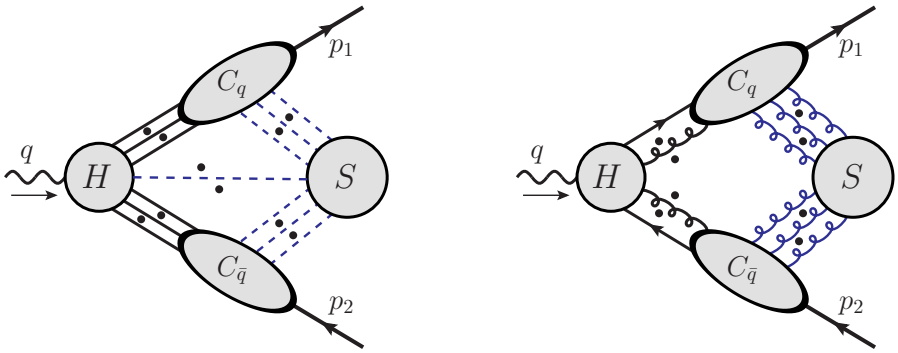

Fig. 2.3: (a) General reduced diagram for Sudakov form factor. H is the hard subgraph that contains arbitrarily many propagators which are not pinched and whose virtualities are of order Q^2 after proper contour deformations. C_q and $C_{\bar{q}}$ are collinear subgraphs, which are connected to H by arbitrarily many collinear propagators. S is the soft subgraph, which is connected to C_q, $C_{\bar{q}}$, and H by arbitrarily many soft propagators. S is not necessarily connected. The dots refer to any arbitrary collinear or soft lines. (b) The leading region for Sudakov form factor. The dots refer to any arbitrary collinear or soft longitudinally polarized gluon lines that can be added.

2.3 Power counting of pinch singularity

2.3.1 Pinch surface: intrinsic and normal coordinates

For the example of one-loop Sudakov form factor discussed at the end of Sec. 2.2.3, the soft pinch singularity is a point $k^\mu = 0$ in the 4-dimensional Minkowski space of the loop momentum k, while the collinear pinch singularities are two straight lines,

$$k = (\alpha\, p_1^+, 0^-, \mathbf{0}_T) \text{ with } \alpha \in (0,1) \tag{2.27}$$

for the quark-collinear region and

$$k = (0^+, \beta\, p_2^-, \mathbf{0}_T) \text{ with } \beta \in (0,1) \tag{2.28}$$

for the antiquark-collinear region. In a general multi-loop diagram, the solutions to Landau equation form a multidimensional *pinch surface* in the (real-valued) loop momentum space. Illustrated in Fig. 2.3(a) is a generic pinch surface for the Sudakov form factor. This pinch surface is characterized by a set of soft momenta, $k_s^i = 0$, a set of collinear momenta along the quark direction, $k_q^i = (\alpha_i\, p_1^+, 0^-, \mathbf{0}_T)$, and along the antiquark direction, $k_{\bar{q}}^j = (0^+, \beta_j\, p_2^-, \mathbf{0}_T)$, and a set of hard momenta in the hard subgraph H whose virtualities are of order Q^2.

As discussed in Sec. 2.2, the Libby-Sterman analysis relates the power counting of a diagram $I(Q, M)$ in the ratio M/Q of the hard scale to soft scale to the mass singularity of the same diagram at the limit of $M \to 0$. The mass singularity is in turn given by the pinch singularity of the massless theory, as determined by the Landau criterion. In the case with finite masses, the pinch singularity of the massless theory becomes inexact and regulated by the masses, as visualized by the simple examples in Sec. 2.2.1. Even though the loop momentum contour is no longer pinched by poles to give zero-virtuality lines, it is indeed trapped by pairs of close poles separated by distances much smaller than Q, which forbids it from being arbitrarily deformed. The maximum virtualities of the pinched propagators in this region are still much smaller than Q^2, which lead to a large integrand. As a result, the region around the pinch surface is likely to give an important contribution to the integral, in the sense of having a leading power counting behavior in M/Q in Eq. (2.15). However, this is not necessarily true, because the numerator and integration measure of the Feynman integral may rescue the singular behavior and reduce the power counting. Therefore, locating the pinch surfaces is only necessary but not sufficient to determine the mass singularities in the massless integral, or the leading power counting contributions in the massive integral. We need to further formulate a power counting rule for the divergence degree around the pinch

surface.

Around the pinch surface, we define a set of intrinsic coordinates to describe the points on that surface, and a set of normal coordinates to characterize the deviations from the surface. As an example, for the quark-collinear pinch surface in Eq. (2.27), we can use α as the intrinsic coordinate, and $(k^-, \boldsymbol{k}_T)$ as the (three-dimensional) normal coordinates. In contrast, for the soft pinch "surface" in Fig. 2.2(e), there is no intrinsic degree of freedom; any nonzero component k^μ is a normal coordinate. The integration of normal coordinates leads to the singularity. Since it is the virtualities of pinched propagators that cause a large integrand, we further redefine the normal coordinates as a radial coordinate λ and angular coordinates, such that for a fixed λ, the virtualities stays constant.

Around the pinch surface in Eq. (2.27), k^- and k_T are much smaller than k^+, which is of order Q, the pinched quark and gluon propagators have virtualities

$$(p_1 + k)^2 = 2(1+\alpha)p_1^+ k^- - k_T^2, \tag{2.29}$$

$$k^2 = 2\alpha p_1^+ k^- - k_T^2, \tag{2.30}$$

which are linear with k^- but quadratic with k_T. So we choose the radial coordinate λ such that

$$k^- = \lambda^2 \bar{k}^- / p_1^+, \quad \boldsymbol{k}_T = \lambda \bar{\boldsymbol{k}}_T, \tag{2.31}$$

where λ has the mass dimension, and $\bar{k}^-$ and $\bar{\boldsymbol{k}}_T$ are (two-dimensional) dimensionless angular variables subject to the condition $|\bar{k}^-| + |\bar{\boldsymbol{k}}_T|^2 = 1$ if we choose the radial coordinate λ as

$$\lambda = \sqrt{|p_1^+ k^-| + |k_T|^2}. \tag{2.32}$$

Note that Eqs. (2.32) and (2.31) are just a change of variables from a flat coordinate system into an angular coordinate system. For a fixed nonzero α and λ, the integration of the angular variables $\bar{k}^-$ and $\bar{\boldsymbol{k}}_T$ do not touch any singularities, so gives a regular result. The two propagators in Eq. (2.29) together with the integration $d^4k \sim \lambda^3 d\lambda$ (modulo the α and angular integrations) gives an integral

$$\int_0^{\lesssim Q} \frac{\lambda^3 d\lambda}{(\lambda^2)^2} = \int_0^{\lesssim Q} \frac{d\lambda}{\lambda}. \tag{2.33}$$

The collinear pinch means that the singularity at $\lambda = 0$ cannot be avoided. Eq. (2.33) then has a divergence degree $p = 0$ for a logarithmic divergence.

This analysis is for a massless theory, for the massive case with both the quark having a mass m, the pinch becomes inexact, and we can avoid the pole by order of m, so that λ never reaches 0. This smoothly cuts off the integral in Eq. (2.33) at $\lambda \to 0$, and gives

$$\int_{\gtrsim m}^{\lesssim Q} \frac{d\lambda}{\lambda} \sim \ln\left(\frac{Q}{m}\right), \tag{2.34}$$

which manifests the logarithmic divergence. This massive discussion can be used to analyze the form factor in QED with a massive electron, but obviously not to the real QCD. In QCD, partons never appear as external on-shell lines, which must be replaced by hadrons. The quarks are indeed massive, but the light quark masses are much less than $\Lambda_{\rm QCD}$, so the mass regulation to the pinch singularity does not come into play before the nonperturbative dynamics kicks in. Hence we should regard the mass scale in Eq. (2.33) as of the same order as $\Lambda_{\rm QCD}$, i.e., the scale $\lambda \lesssim \Lambda_{\rm QCD}$ should be controlled by nonperturbative QCD.

Similarly, around the soft pinch in Fig. 2.2(e), we have $|k^\mu| \ll Q$. The gluon propagator

$k^2 = 2k^+k^- - k_T^2$ is quadratic with both (k^+, k^-) and k_T. So we choose the radial coordinate λ_S as

$$k^\mu = \lambda_S \bar{k}^\mu, \quad \text{with} \quad \lambda_S = \sum_\mu |k^\mu|, \tag{2.35}$$

where the $\bar{k}^\mu$ is a (three-dimensional) dimensionless angular coordinates subject to the constraint $\sum_\mu |\bar{k}^\mu| = 1$. Then the three pinched propagators have the scaling

$$k^2 = \lambda_S^2(2\bar{k}^+\bar{k}^- - \bar{k}_T^2) \qquad = \mathcal{O}\Big(\lambda_S^2\Big), \tag{2.36a}$$

$$(p_1 + k)^2 = 2p_1^+k^- + k^2 = 2\lambda_S\, p_1^+\bar{k}^- + \lambda_S^2(2\bar{k}^+\bar{k}^- - \bar{k}_T^2) \qquad = \mathcal{O}(\lambda_S Q), \tag{2.36b}$$

$$(p_2 - k)^2 = -2p_2^-k^+ + k^2 = -2\lambda_S\, p_2^-\bar{k}^+ + \lambda_S^2(2\bar{k}^+\bar{k}^- - \bar{k}_T^2) \qquad = \mathcal{O}(\lambda_S Q). \tag{2.36c}$$

We note that now the collinear lines have higher virtualities than the soft line, being much larger than λ_S^2 but still much smaller than Q^2. This is because it is the large momentum components of the collinear lines, p_1^+ or p_2^-, that interact with the soft gluon. Together with the integration measure $d^4k \sim \lambda_S^3 d\lambda_S$, Eq. (2.36) gives the scaling for the soft region,

$$\int_0^{\lesssim Q} \frac{\lambda_S^3 d\lambda_S}{\lambda_S^2\,(\lambda_S Q)^2} \propto \int_0^{\lesssim Q} \frac{d\lambda_S}{\lambda_S}, \tag{2.37}$$

which is logarithmically divergent, for a divergence degree $p = 0$, similarly to Eq. (2.33).

Now in the massive theory, suppose both the quark and gluon carry masses, m_q and m_g, respectively. If the quark and antiquark are on shell, $p_1^2 = p_2^2 = m_q^2$, the same scalings in Eqs. (2.36b)(2.36c) hold, but the gluon propagator becomes $\mathcal{O}\big(\lambda_S^2\big) + m_g^2$, which smoothly cuts off the $\lambda_S \to 0$ region and brings Eq. (2.37) to a form like Eq. (2.34) with m replaced by m_g.

On the other hand, if the gluon is massless but the quark and antiquark are off shell by

$\mathcal{O}\left(\Lambda^2_{\rm QCD}\right)$, their virtualities would become $\mathcal{O}(\lambda_S^2)$ and $\mathcal{O}(\lambda_S Q) + \mathcal{O}\left(\Lambda^2_{\rm QCD}\right)$ for the gluon and quark/antiquark, respectively. This situation resembles the real QCD more since the partons are never on shell. But this brings a more intricate power counting. Compared to the hard region in Fig. 2.2(b), which has the same power counting as the leading-order (LO) diagram, the soft region has a power counting

$$I_S = Q^2 \int_0^{\lesssim Q} \frac{\lambda_S^3 d\lambda_S}{\lambda_S^2 \left(\lambda_S Q + \Lambda^2_{\rm QCD}\right)^2} = \int_0^{\lesssim Q} \frac{\lambda_S d\lambda_S}{\left(\lambda_S + \Lambda^2_{\rm QCD}/Q\right)^2}. \tag{2.38}$$

Now we examine three subregions in the soft region,

- $\lambda_S \ll \Lambda^2_{\rm QCD}/Q$, where $I_S \ll \mathcal{O}(1)$ is power suppressed;
- $\lambda_S \sim \mathcal{O}\left(\Lambda^2_{\rm QCD}/Q\right)$, which gives $I_S \sim \mathcal{O}(1)$;
- $\mathcal{O}\left(\Lambda^2_{\rm QCD}/Q\right) \ll \lambda_S \lesssim \mathcal{O}\left(\Lambda_{\rm QCD}\right)$, which gives $I_S \sim \mathcal{O}(1)$,

where we stop at $\lambda_S \lesssim \mathcal{O}\left(\Lambda_{\rm QCD}\right)$ beyond which all the three propagators have virtualities much greater than $\Lambda^2_{\rm QCD}$, and start entering the hard region. We found that the whole region $\Lambda^2_{\rm QCD}/Q \lesssim \lambda_S \lesssim \Lambda_{\rm QCD}$ gives a leading-power contribution. In the low end with $\lambda_S \sim \mathcal{O}\left(\Lambda^2_{\rm QCD}/Q\right)$, the quark propagators have virtualities of order $\Lambda^2_{\rm QCD}$, but the gluon has $\Lambda^4_{\rm QCD}/Q^2 \ll \Lambda^2_{\rm QCD}$. In the high end with $\lambda_S \sim \mathcal{O}\left(\Lambda_{\rm QCD}\right)$, the gluon propagator has a virtuality of order $\Lambda^2_{\rm QCD}$, but the quarks have $Q\,\Lambda_{\rm QCD} \gg \Lambda^2_{\rm QCD}$. Given the fourth assumption in Sec. 2.1.2, the whole soft region $\lambda_S \lesssim \Lambda_{\rm QCD}$ is in the nonperturbative regime. But for the perturbative analysis, we usually make the second assumption in Sec. 2.1.2 to convert the sum over final hadron states into a sum over parton states, so on-shell partons do appear in the final states, for which the region $\lambda_S \ll \Lambda^2_{\rm QCD}/Q$ also becomes important and contribute to soft divergences. In such cases, we need to show that the whole soft region

is cancelled. Therefore, since factorization is rooted in a perturbative analysis, we need to consider the whole soft region $\Lambda_{\rm QCD}^2/Q \lesssim \lambda_S \lesssim \Lambda_{\rm QCD}$.

Such complication arises because in the soft region, the collinear lines and soft lines have different virtualities, which causes an extra scale $\Lambda_{\rm QCD}^2/Q$. In contrast, the power counting analysis of the collinear region is much simpler because all collinear lines have virtualities $\mathcal{O}(\lambda^2)+\mathcal{O}\Big(\Lambda_{\rm QCD}^2\Big)$, and hence only the region $\lambda \sim \Lambda_{\rm QCD}$ needs to be considered. In a more complicated diagram, we can have (multiple) soft and collinear momenta at the same time. Each collinear momentum scales as

$$k_c = (k_c^+, k_c^-, \boldsymbol{k}_{cT}) \sim (Q, \frac{\lambda^2}{Q}, \lambda), \quad \text{with} \quad \lambda \sim \mathcal{O}\big(\Lambda_{\rm QCD}\big), \tag{2.39}$$

and each soft momentum has the scaling

$$k_s = (k_s^+, k_s^-, \boldsymbol{k}_{sT}) \sim (\lambda_S, \lambda_S, \lambda_S), \quad \text{with} \quad \frac{\lambda^2}{Q} \lesssim \lambda_S \lesssim \lambda. \tag{2.40}$$

Eqs. (2.39) and (2.40) constitute the *canonical scaling* for the pinched regions, with λ and λ_S being the radial normal coordinates parametrizing the distance from the pinch surfaces.

2.3.2 Power counting

Now we derive the power counting around the pinch surface, based on the canonical scaling in Eqs. (2.39) and (2.40), with $\lambda_S = \mathcal{O}\big(\lambda^2/Q\big)$. I will take a simpler approach than the treatment in Ref. [Collins(2013)] by examining the power counting with respect to the leading-order diagrams. The derivation is for a generic quantum field theory (QFT), and we work in the Feynman gauge for a gauge theory involving a vector boson.

Each pinched momentum belongs either to a collinear sector or the soft sector, so a general pinch surface represented by a reduced diagram is decomposed into a hard subgraph H, a set of collinear subgraphs C_i, and a soft subgraph S. Normally we work in the CM frame of the hard subgraph H, a momentum k_H in which has all its components of order Q. Each collinear subgraph C_i is defined by one (or more collinear) external hard particle p_i and is connected to the hard subgraph H via a set of collinear lines $\{k_{iH}\}$. We include all the propagators of $\{k_{iH}\}$ and their integrations $\prod_{k_{iH}} \int d^4k_{iH}$ in C_i. Within each C_i, the collinear lines can interact with each other in all arbitrary ways under the constraints of fixed $\{k_{iH}\}$ and p_i. The soft subgraph S, which may contain one or more connected parts, is connected to each collinear subgraph C_i and/or hard subgraph H by soft lines, $\{k_{iS}\}$ and/or $\{k_{HS}\}$, respectively. Similarly, all the propagators and integrations of $\{k_{iS}\}$ and/or $\{k_{HS}\}$ are included in S. A concrete example is given by the Sudakov form factor in Fig. 2.3(a), but the discussion in this section applies more generally.

2.3.2.1 Leading order and hard region

First, for a given process, the leading-order diagram can be easily worked out, whose power counting in the scaling limit $Q \to \infty$ is determined by its dimension. For example, the Sudakov form factor Γ^μ has dimension one, so it simply scales as Q^1 at leading order. Some complications arise when there are observed hadrons in the initial or final states, which we shall discuss later. The purely hard region, as illustrated in Fig. 2.2(b) where all internal propagator denominators are of order Q^2, has the same structure as the leading order and gives the same power counting. This is the feature of a renormalizable quantum field theory, as is the case of QCD, for which the coupling is dimensionless; otherwise, we would have a suppression from a power of $g/Q^{\dim(g)}$.

2.3.2.2 Collinear subgraph

For ease of notation, now we look at a particular collinear subgraph and denote it as C, In the simplest case, C only comprises a single line of the external particle, which does not cause additional power counting analysis beyond the previous discussion. This situation can be trivially generalized to the case where C is connected to H by a single propagator but with an arbitrary two-point function included in C. If an extra line of the field $\Phi(x)$ connects C to H, their conlution will be modified to

$$\begin{aligned}
&\int \frac{d^4k_{CH}^{\Phi}}{(2\pi)^4} H^{\alpha}(k_{CH}^{\Phi})\, C^{\alpha}(k_{CH}^{\Phi}) \\
&\quad = \int \frac{d^4k_{CH}^{\Phi}}{(2\pi)^4} H^{\alpha}(k_{CH}^{\Phi}) \left[\int d^4x\, e^{-ik_{CH}^{\Phi}\cdot x} \langle C|T\{\cdots \Phi^{\alpha}(x)\cdots\}|0\rangle \right],
\end{aligned} \tag{2.41}$$

where we have only explicitly indicated the extra dependence on the new particle Φ, k_{CH}^{Φ} is its momentum, and α describes its spin quantum number. The extra dimensions of C and H due to the appearance of Φ are

$$\Delta C^{\alpha} = -4 + \dim(\Phi), \quad \Delta H^{\alpha} = -\dim(\Phi), \tag{2.42}$$

where $\dim(\Phi)$ is the dimension of the field $\Phi(x)$, which is 1 for a scalar or vector field, and 3/2 for a fermion field. The dependence of C^{α} on α can be easily worked out using a boost analysis. If we choose the direction of C as the z axis, then each collinear momentum in C scales as in Eq. (2.39). Now we consider boosting C back to its rest frame, which causes the C-collinear momenta to scale as $(\lambda, \lambda, \lambda)$. Hence each component of α should scale in the

same way, and the power counting C^α is simply given by its dimension,

$$C^\alpha \simeq \lambda^{\dim(C)} \text{ for each } \alpha \text{ in } C \text{ rest frame.} \tag{2.43}$$

Then we boost C^α back to the lab frame, where it is highly boosted along the z direction. This gives an enhancement $(Q/\lambda)^s$ to the largest component of C^α, with s being the spin of Φ. In contrast, each component of H^α scales the same, being $Q^{\dim(H)}$. Including the power counting $d^4k^\Phi_{CH} \sim \lambda^4$, we then have the extra power counting due to Φ:

- $\Phi = \phi$ (scalar): $\dim(\phi) = 1$ and $s = 0$, leading to $Q^{-1} \cdot \lambda^1 = \lambda/Q$; (Note that this case also applies to ghost fields.)
- $\Phi^\alpha = \psi^\alpha$ (fermion): $\dim(\psi) = 3/2$ and $s = 1/2$, leading to $Q^{-3/2} \cdot \lambda^{3/2} \cdot \sqrt{Q/\lambda} = \lambda/Q$;
- $\Phi^\alpha = A^\alpha$ (vector boson): $\dim(A) = 1$ and $s = 1$, leading to $Q^{-1} \cdot \lambda^1 \cdot (Q/\lambda) = 1$. This only applies to the unphysical A^+ component which is proportional to its momentum. The physical transverse polarization $A^\perp$ receives no enhancement from the boost, so gives a power counting λ/Q, the same as the scalar case. The remaining component A^- undergoes a suppression λ/Q by the boost, so gives the power counting $(\lambda/Q)^2$.

Therefore, attaching a collinear subgraph to the hard subgraph by a scalar, fermion, or transversely polarized vector boson brings a power suppression by λ/Q, while by a longitudinally polarized vector boson brings no power suppression.

2.3.2.3 Soft subgraph connection to a collinear subgraph

Now we consider the power counting due to soft lines. Adding an extra line of the field $\Phi^\alpha(x)$ between the soft subgraph S and some collinear subgraph C (taken to be along the z

direction) changes their convolution to

$$\int \frac{d^4k_{CS}^\Phi}{(2\pi)^4} C^\alpha(k_{CS}^\Phi)\, S^\alpha(k_{CS}^\Phi) = \int \frac{d^4k_{CS}^\Phi}{(2\pi)^4} C^\alpha(k_{CS}^\Phi) \left[\int d^4x\, e^{-ik_{CS}^\Phi \cdot x} \langle 0|T\{\cdots \Phi^\alpha(x) \cdots\}|0\rangle \right], \tag{2.44}$$

where k_{CS}^Φ is the soft momentum that scales as $(\lambda^2/Q, \lambda^2/Q, \lambda^2/Q)$, and α is the spin index. This new attachment changes the dimensions of S^α and C^α by

$$\Delta S^\alpha = -4 + \dim(\Phi), \quad \Delta C^\alpha = -\dim(\Phi). \tag{2.45}$$

This is similar to Eq. (2.42) with H replaced by C and C by S, but now the collinear subgraph C^α has different scalings for different α components. So we count Eq. (2.44) as

$$\begin{aligned} \Delta \left[\int \frac{d^4k_{CS}^\Phi}{(2\pi)^4} C^\alpha(k_{CS}^\Phi)\, S^\alpha(k_{CS}^\Phi) \right] &\sim \left(\frac{\lambda^2}{Q}\right)^{\dim(\Phi)} \times \left[\lambda^{-\dim(\Phi)} \cdot (\text{spin enhancement})\right] \\ &\sim \left(\frac{\lambda}{Q}\right)^{\dim(\Phi)} \times (\text{spin enhancement}), \end{aligned} \tag{2.46}$$

where in the first step, the first factor is from the soft subgraph and the integration measure, and the second factor is from the collinear subgraph. By the same boost argument as in the previous situation, C^α receives a power enhancement for fermions and vector bosons.

- $\Phi = \phi$ (scalar) or $A^\perp$ (transversely polarized vector boson), $\dim(\Phi) = 1$ without boost enhancement, leading to a λ/Q suppression; (Note that this case also applies to ghost fields.)

- $\Phi = \psi$ (fermion), $\dim(\Phi) = 3/2$ with a boost enhancement $\sqrt{Q/\lambda}$, leading to a λ/Q suppression;

- $\Phi = A^+$ (longitudinally polarized vector boson), $\dim(\Phi) = 1$ with a boost enhancement Q/λ, leading to a power counting of 1.

Therefore, attaching the soft subgraph to a collinear subgraph by a scalar, fermion, or transversely polarized vector boson brings a power suppression by λ/Q, while by a longitudinally polarized vector boson brings no power suppression.

2.3.2.4 Soft subgraph connection to the hard subgraph

Adding an extra soft line to the hard subgraph H works in a similar way and leads to the power counting formula

$$\Delta(S \otimes H) \sim \left(\frac{\lambda^2}{Q}\right)^{\dim(\Phi)} \cdot Q^{-\dim(\Phi)} = \left(\frac{\lambda}{Q}\right)^{2\dim(\Phi)} . \tag{2.47}$$

Compared to Eq. (2.46), the power factor $Q^{-\dim(\Phi)}$ instead of $\lambda^{-\dim(\Phi)}$ generally suppresses the soft connections to H, and there is power enhancement from the boost. Therefore, attaching the soft subgraph to the hard subgraph by a scalar or vector boson brings a power suppression by $(\lambda/Q)^2$, while by a fermion brings a power suppression $(\lambda/Q)^3$.

To conclude, we list in Table 2.1 the power counting rules for adding an extra line in a certain reduced diagram. The rules work in a fashion of construction so give the power counting relative to a certain diagram, e.g., the leading-order diagram. As an example, for the Sudakov form factor in Fig. 2.3(a), the external $q\bar{q}$ lines dictate the two collinear subgraphs to be connected to H by at least a fermion line separately. From our power counting rules, having additional line connections generally brings power suppressions except for longitudinally polarized gluons connecting $C_{q,\bar{q}}$ to H or S. This leads to the reduced diagram in Fig. 2.3(b) that has the same power counting as the leading-order diagram or

Table 2.1: The counting of the (λ/Q) power associated with each extra line attachment between a collinear subgraph C and the hard subgraph H, the soft subgraph S and C, or S and H. In the second and third columns, we take S to refer to the soft region with the momentum scaling $(\lambda^2/Q, \lambda^2/Q, \lambda^2/Q)$, while in the last two columns, S' refers to the soft region with the scaling $(\lambda, \lambda, \lambda)$. For S' we denote $\Delta n_{cs} = n_{cs} - 1$ as the number of collinear propagators that the soft momentum flows through with respect to the minimal configuration ($n_{cs} = 1$).

	C-H	S-C	S-H	S'-C	S'-H
$\phi, c, \bar{c}$	1	1	2	$1 + \Delta n_{cs}$	1
ψ	1	1	3	$1/2 + \Delta n_{cs}$	3/2
A^+	0	0	2	$0 + \Delta n_{cs}$	1
$A^\perp$	1	1	2	$1 + \Delta n_{cs}$	1
A^-	2	2	2	$1 + \Delta n_{cs}$	1

the pure hard region. Any other pinch surfaces give more suppressed power counting. So it is called the *leading region*.

2.4 Power counting for alternative soft scalings

The previous subsection assumes the soft gluon momenta scale by a uniform scaling $\lambda_S \sim \lambda^2/Q$. Such soft momenta do not change the collinear propagator virtualities when flowing through the latter. In general, we can have λ_S to vary between λ^2/Q and λ, for $\Lambda_{\rm QCD} \lesssim \lambda \ll Q$. This generic soft scaling does not affect the power counting for the collinear-to-hard coupling, but alters that for the soft attachments to the collinear and hard subgraphs.

When a soft momentum $k_s \sim (\lambda_S, \lambda_S, \lambda_S)$ flows along a collinear momentum $k_c \sim (Q, \lambda^2/Q, \lambda)$, it changes the virtuality to

$$(k_c{+}k_s)^2 = k_c^2{+}k_s^2{+}2k_c{\cdot}k_s \sim \lambda^2{+}\lambda_S^2{+}\lambda_S Q \sim \max(\lambda^2, \lambda_S Q) = \lambda^2{\cdot}\max(1, \lambda_S Q/\lambda^2). \quad (2.48)$$

Thus if this soft momentum flows through n_{cs} collinear propagators, the collinear subgraph

gains an extra factor $\left[1/\max(1,\lambda_S Q/\lambda^2)\right]^{n_{cs}}$ apart from the dimensional counting $\lambda^{-\dim(\Phi)}$ times a boost enhancement factor in Eq. (2.46). Since we take $\lambda_S \gtrsim \lambda^2/Q$, the term $\lambda_S Q/\lambda^2$ is at least of order 1, so we can simplify $\max(1,\lambda_S Q/\lambda^2)$ to $\lambda_S Q/\lambda^2$. The power counting of the soft subgraph should also be modified by λ_S. Therefore, an extra soft attachment between S and a collinear subgraph leads to an additional power counting

$$\Delta(C\otimes S) \sim \left(\frac{\lambda_S}{\lambda}\right)^{\dim(\Phi)} \cdot \left(\frac{Q}{\lambda}\right)^{s} \cdot \left(\frac{\lambda^2}{\lambda_S Q}\right)^{n_{cs}} = \left(\frac{\lambda}{Q}\right)^{\dim(\Phi)-s} \left(\frac{\lambda_S}{\lambda^2/Q}\right)^{\dim(\Phi)-n_{cs}} \tag{2.49}$$

where s is the spin of Φ. This introduces an extra factor $(\lambda_S Q/\lambda^2)^{\dim(\Phi)-n_{cs}}$ with respect to Eq. (2.46). For $\lambda_S = \lambda^2/Q$, it recovers the same counting. As λ_S increases, we gain a power enhancement if $\dim(\Phi) > n_{cs}$, which can only happen for fermion case with $n_{cs} = 1$, but otherwise a suppression. The minimal configuration $n_{cs} = 1$ yields a power counting

$$\left(\frac{\lambda}{Q}\right)^{\dim(\Phi)-s} \left(\frac{\lambda_S}{\lambda^2/Q}\right)^{\dim(\Phi)-1}, \quad (n_{cs}=1) \tag{2.50}$$

which does not affect the power counting for scalar and vector bosons, but changes the fermion case to $\sqrt{\lambda_S/Q}$, enhancing the λ/Q counting in Table 2.1 if $\lambda_S \sim \lambda$. For $n_{cs} \geq 2$, a large $\lambda_S \gg \lambda^2/Q$ leads to a suppression for all cases. Hence, for the leading region, one usually needs $n_{cs} = 1$ for the large scaling.

For the soft momentum k_s flowing into H, we can still neglect it in H since $\lambda_S \ll Q$. Then Eq. (2.47) is modified to

$$\Delta(S\otimes H) \sim \lambda_S^{\dim(\Phi)} \cdot Q^{-\dim(\Phi)} = \left(\frac{\lambda_S}{Q}\right)^{\dim(\Phi)}, \tag{2.51}$$

which enhances the counting in Eq. (2.47) if $\lambda_S \gg \lambda^2/Q$.

To summarize, we include in the last two columns of Table 2.1 the power counting for the high end of soft region S' with $\lambda_S = \mathcal{O}(\lambda)$, and with $n_{cs} = 1$. Since the soft attachments still lead to power suppression except for longitudinally polarized gluons, the leading region graph for Sudakov form factor takes the same form as Fig. 2.3, now for the whole soft region with $\lambda^2/Q \lesssim \lambda_S \lesssim \lambda$.

2.5 Basic approximation for each single region

It is the regions around the pinch surfaces that give important power contributions to the Feynman integrals. Having identified the pinch surfaces that are associated with leading power contributions, we may then make certain approximations to extract those contributions based on the power counting of the related momenta in Eqs. (2.39) and (2.40).

As shown in Table 2.1, the major complication from the gauge theory is that there is no penalty from adding arbitrarily many vector boson lines attaching the collinear subgraphs to the hard or soft subgraphs. But the polarizations must be proportional to the collinear momenta. This is the key for the factorization of gauge theory as it will allow the use of Ward identity.

To present the approximators, it is helpful to confine ourselves to a particular process or amplitude. So in the following discussions, I will mainly be using the Sudakov form factor as an example, but other processes like DIS will also be referred to for completeness.

2.5.1 Approximation of collinear-to-hard connections

In the Sudakov form factor, each collinear subgraph C_i is connected to the hard subgraph H by one quark line and a series of gluon lines. They are convoluted by the integrations of

the loop momenta, which can be written as

$$C_q \otimes H \otimes C_{\bar{q}} = \int \frac{d^4k_q}{(2\pi)^4}\frac{d^4k_{\bar{q}}}{(2\pi)^4}\left[\prod_{i=1}^{n}\frac{d^4k_i}{(2\pi)^4}\right]\left[\prod_{j=1}^{m}\frac{d^4l_j}{(2\pi)^4}\right] \times C_{q,\alpha,\mu_1\cdots\mu_n}(k_q,k_1,\cdots,k_n)\cdot g^{\mu_1\nu_1}\cdots g^{\mu_n\nu_n} \times H_{\alpha,\nu_1\cdots\nu_n;\beta,\sigma_1\cdots\sigma_m}(k_q,k_1,\cdots,k_n;l_{\bar{q}},l_1,\cdots,l_m) \times g^{\sigma_1\rho_1}\cdots g^{\sigma_m\rho_m}\cdot C_{\bar{q},\beta,\rho_1\cdots\rho_m}(l_{\bar{q}},l_1,\cdots,l_m) \tag{2.52}$$

for a certain region of some diagram that has n and m collinear gluons connecting C_q and $C_{\bar{q}}$ to H, respectively. In Eq. (2.52), α (k_q) and β ($l_{\bar{q}}$) are the spinor indices (loop momenta) of the quark and antiquark respectively, and $\{\mu_i\}$ ($\{k_i\}$) and $\{\nu_j\}$ ($\{k_j\}$) are the Lorentz indices (loop momenta) of the C_q- and $C_{\bar{q}}$-collinear gluons, respectively. All the collinear (pinched) propagators have been included in C_q or $C_{\bar{q}}$, and we will eventually include the loop integrations into them as well.

We take the quark and antiquark to move along the $\pm z$ directions, respectively. Around the pinch surface, the collinear momenta scale as

$$k_i \sim (Q,\lambda^2/Q,\lambda),\ (i=q,1,\cdots,n), \quad \text{and} \quad l_j \sim (\lambda^2/Q,Q,\lambda),\ (j=\bar{q},1,\cdots,m). \tag{2.53}$$

These momenta circulate between the hard subgraph H and collinear subgraphs. The propagators inside H are not pinched, and proper deformations can be done to make them have high virtualities of order Q^2. Then we may expand each of them with respect to the small parameter λ without encountering any singularities. The leading-power contribution can be

simply obtained by neglecting λ in H, so we approximate H by

$$H(\{k_i\};\{l_j\}) \to H(\{\hat{k}_i\};\{\hat{l}_j\}), \tag{2.54}$$

with

$$\hat{k}_i^\mu = (k_i^+, 0^-, \mathbf{0}_T) = (k_i \cdot n)\,\bar{n}^\mu, \quad \hat{l}_j^\mu = (0^+, l_j^-, \mathbf{0}_T) = (l_j \cdot \bar{n})\,n^\mu, \tag{2.55}$$

where $i = q, 1, \cdots, n$, $j = \bar{q}, 1, \cdots, m$, and we have introduced two lightlike auxiliary vectors

$$n^\mu = (0^+, 1^-, \mathbf{0}_T) = \frac{1}{\sqrt{2}}(1, -\vec{z}), \quad \bar{n}^\mu = (1^+, 0^-, \mathbf{0}_T) = \frac{1}{\sqrt{2}}(1, \vec{z}). \tag{2.56}$$

For the spinor contraction between C_q and H, the boosted factor C_q has a large component in the spinor space, which can be projected out by [Collins(2013)]

$$C_{q,\alpha}(k) \to C_{q,\delta}(k)\,\mathcal{P}_{\delta\alpha} = C_{q,\delta}(k) \left[\frac{\gamma \cdot n \sum_s u_s(\hat{k})\bar{u}_s(\hat{k})}{2\hat{k}\cdot n}\right]_{\delta\alpha} = C_{q,\delta}(k) \left[\frac{\gamma^+\gamma^-}{2}\right]_{\delta\alpha}, \tag{2.57}$$

where k stands for a generic collinear momentum along the z direction and $u_s(\hat{k})$ is the massless spinor with momentum $\hat{k} = (k\cdot n)\bar{n}$ and spin s. The projector $\mathcal{P}_{\delta\alpha}$ has the property

$$\mathcal{P}^2 = \mathcal{P},\ \bar{u}_s(\hat{k})\mathcal{P} = \bar{u}_s(\hat{k}),\ \text{and}\ \mathcal{P}(\gamma\cdot\hat{k}) = 0, \tag{2.58}$$

such that it projects $C_q(k)$ onto a massless spinor along the z direction. Perturbatively, the fermion propagator numerator $\not{k} + m$ contracted with $\mathcal{P}$ keeps its large component $k^+\gamma^-$ intact, so $\mathcal{P}$ keeps the leading-power accuracy. $\mathcal{P}$ inserting between C_q and H contracts the massless spinor $\bar{u}_s(\hat{k})$ with H to give the hard factor a physical interpretation of massless quark interaction.

Similarly, for the spinor contraction between H and $C_{\bar{q}}$, we insert a projector

$$C_{\bar{q},\beta}(l) \to \bar{\mathcal{P}}_{\beta\kappa} C_{\bar{q},\kappa}(l) = \left[\frac{\sum_s u_s(\hat{l})\bar{u}_s(\hat{l})\gamma\cdot\bar{n}}{2\hat{l}\cdot\bar{n}}\right]_{\beta\kappa} C_{\bar{q},\kappa}(l) = \left[\frac{\gamma^+\gamma^-}{2}\right] C_{\bar{q},\kappa}(l), \tag{2.59}$$

which is the same as $\mathcal{P}$. After these two approximations, Eq. (2.52) becomes

$$\begin{aligned} C_q \otimes H \otimes C_{\bar{q}} \simeq \int \frac{d^4k_q}{(2\pi)^4}\frac{d^4k_{\bar{q}}}{(2\pi)^4}\left[\prod_{i=1}^{n}\frac{d^4k_i}{(2\pi)^4}\right]\left[\prod_{j=1}^{m}\frac{d^4l_j}{(2\pi)^4}\right] \\ \times C_{q,\alpha,\mu_1\cdots\mu_n}(k_q,k_1,\cdots,k_n)\cdot g^{\mu_1\nu_1}\cdots g^{\mu_n\nu_n} \\ \times \mathcal{P}_{\alpha\delta}\, H_{\delta,\nu_1\cdots\nu_n;\kappa,\sigma_1\cdots\sigma_m}(\hat{k}_q,\hat{k}_1,\cdots,\hat{k}_n;\hat{l}_{\bar{q}},\hat{l}_1,\cdots,\hat{l}_m)\,\mathcal{P}_{\kappa\beta} \\ \times g^{\sigma_1\rho_1}\cdots g^{\sigma_m\rho_m}\cdot C_{\bar{q},\beta,\rho_1\cdots\rho_m}(l_{\bar{q}},l_1,\cdots,l_m), \end{aligned} \tag{2.60}$$

where the hard factor H is surrounded by two $\mathcal{P}$'s which amputate and put on-shell the two quark lines connected to H. This fact will be important when applying Ward identity to the collinear gluons.

Based on our power counting rules, only the longitudinal polarizations of the collinear gluons connecting C_q or $C_{\bar{q}}$ to H are of leading power. This means that we shall have $\nu_i = +$ and $\sigma_j = -$ in Eq. (2.62), which extracts the g^{-+} components for all the metric tensors. So we make the approximations

$$g^{\mu_i\nu_i} \mapsto \frac{n^{\mu_i}\,\hat{k}_i^{\nu_i}}{\hat{k}_i\cdot n} = \frac{n^{\mu_i}\,\hat{k}_i^{\nu_i}}{k_i\cdot n}, \quad g^{\sigma_j\rho_j} \mapsto \frac{\hat{l}_j^{\sigma_i}\,\bar{n}^{\rho_j}}{\hat{l}_j\cdot\bar{n}} = \frac{\hat{l}_j^{\sigma_i}\,\bar{n}^{\rho_j}}{l_j\cdot\bar{n}}. \tag{2.61}$$

These are equivalent to $g^{\mu\nu} \mapsto n^\mu\bar{n}^\nu$, but writing as Eq. (2.61) has the advantage that the gluon connection to the hard factor H will be replaced by its momentum contracted with

H,

$$
\begin{aligned}
C_q \otimes H \otimes C_{\bar{q}} \simeq & \int \frac{d^4k_q}{(2\pi)^4}\frac{d^4k_{\bar{q}}}{(2\pi)^4}\left[\prod_{i=1}^{n}\frac{d^4k_i}{(2\pi)^4}\right]\left[\prod_{j=1}^{m}\frac{d^4l_j}{(2\pi)^4}\right] \\
& \times C_{q,\alpha,\mu_1\cdots\mu_n}(k_q,k_1,\cdots,k_n)\cdot\left[\prod_i \frac{n^{\mu_i}}{k_i\cdot n}\right] \\
& \times \left(\prod_i \hat{k}_i^{\nu_i}\right)\left[\mathcal{P}_{\alpha\delta}\, H_{\delta,\nu_1\cdots\nu_n;\kappa,\sigma_1\cdots\sigma_m}(\hat{k}_q,\hat{k}_1,\cdots,\hat{k}_n;\hat{l}_{\bar{q}},\hat{l}_1,\cdots,\hat{l}_m)\,\mathcal{P}_{\kappa\beta}\right]\left(\prod_j \hat{l}_j^{\sigma_j}\right) \\
& \times \left[\prod_j \frac{\bar{n}^{\rho_j}}{l_j\cdot\bar{n}}\right]\cdot C_{\bar{q},\beta,\rho_1\cdots\rho_m}(l_{\bar{q}},l_1,\cdots,l_m),
\end{aligned}
\tag{2.62}
$$

which will in turn allow the use of Ward identity.

2.5.2 Approximation of soft-to-collinear connections

From the power counting rules in Table 2.1, soft connections are generally power suppressed except for soft gluons that are attached to collinear subgraphs with polarizations proportional to the collinear momenta. For the leading region graph in Fig. 2.3(b), a soft momentum k_s scales as $(\lambda_S,\lambda_S,\lambda_S)$ and can be taken to circulate from S to C_q, to H, to $C_{\bar{q}}$, and then back to S. When k_s flows through H, each of its component is much smaller than Q, so we can neglect it in H to the leading-power accuracy. When it flows through C_q along a collinear line with momentum k_i, it modifies the momentum to k_i+k_s, which does not change the leading component $(k_i+k_s)^+ = k_i^+ = \mathcal{O}(Q)$ thus does not change the collinear propagator numerator, but it modifies the propagator denominator by

$$
(k_i+k_s)^2 - m^2 = (k_i^2-m^2) + 2k_i\cdot k_s + k_s^2. \tag{2.63}
$$

Since k_s has a uniform scaling λ_S for all components, it is the term $2k_i^+ k_s^- = \mathcal{O}(Q\lambda_S)$ that is the most important among all k_s-related terms. Therefore, we may only keep k_s^- when k_s flows through C_q, which gives the approximation,

$$k_{qs}^\mu \mapsto \hat{k}_{qs}^\mu = (k_{qs} \cdot \bar{n}) n^\mu, \tag{2.64}$$

where k_{qs} denotes the soft momentum flowing through C_q. This applies for the whole range of $\lambda_S \in (\lambda^2/Q, \lambda)$. Even though for $\lambda_S \sim \lambda$, the whole quark propagator is dominated by $2k_i^+ k_s^- = \mathcal{O}(Q\lambda)$, we do not modify the term $(k_i^2 - m^2)$ in order for a unified approximation. Similarly, for a soft momentum $k_{\bar{q}s}$ flowing in $C_{\bar{q}}$, we approximate it by

$$k_{\bar{q}s}^\mu \mapsto \hat{k}_{\bar{q}s}^\mu = (k_{\bar{q}s} \cdot n) \bar{n}^\mu. \tag{2.65}$$

Those soft momentum approximation decouples the soft momenta from the hard subgraph and simplifies the soft-collinear couplings to

$$\begin{aligned} C_q \otimes S \otimes C_{\bar{q}} \simeq \int \left[\prod_i \frac{d^4 k_{qs,i}}{(2\pi)^4}\right] \left[\prod_j \frac{d^4 k_{\bar{q}s,j}}{(2\pi)^4}\right] & C_{q;\mu_1\cdots\mu_n}(\{\hat{k}_{qs,i}\}) g^{\mu_1\nu_1} \cdots g^{\mu_n\nu_n} \\ & \times S_{\nu_1,\cdots,\nu_n;\sigma_1,\cdots,\sigma_m}(\{k_{qs,i}\}, \{k_{\bar{q}s,j}\}) \\ & \times g^{\sigma_1\rho_1} \cdots g^{\sigma_m\rho_m} C_{\bar{q};\rho_1\cdots\rho_m}(\{\hat{k}_{\bar{q}s,j}\}), \end{aligned} \tag{2.66}$$

where we have suppressed the collinear momentum dependence, and $\hat{k}_{qs,i}$ and $\hat{k}_{\bar{q}s,j}$ are defined as Eqs. (2.64) and (2.65), respectively. The soft factor S includes all the soft gluon propagators. Here we are separately examining the soft momenta attaching to C_q and $C_{\bar{q}}$, which are related by necessary delta functions included in S; eventually we will also include

the soft integrations into S. Similar to the collinear gluon coupling C_i to H, here only the g^{-+} components of all the metric tensors give leading-power contributions. So we make the approximations,

$$g^{\mu_i\nu_i} \mapsto \frac{\hat{k}_{qs,i}^{\mu_i}\,\bar{n}^{\nu_i}}{\hat{k}_{qs,i}\cdot\bar{n}} = \frac{\hat{k}_{qs,i}^{\mu_i}\,\bar{n}^{\nu_i}}{k_{qs,i}\cdot\bar{n}}, \quad g^{\sigma_j\rho_j} \mapsto \frac{n^{\sigma_j}\,\hat{k}_{\bar{q}s,j}^{\rho_j}}{n\cdot\hat{k}_{\bar{q}s,j}} = \frac{n^{\sigma_j}\,\hat{k}_{\bar{q}s,j}^{\rho_j}}{n\cdot k_{\bar{q}s,j}}. \tag{2.67}$$

Similar to Eq. (2.61), this is equivalent to $g^{\mu\nu} \mapsto n^\mu\bar{n}^\nu$. It simplifies Eq. (2.68) to

$$\begin{aligned} C_q \otimes S \otimes C_{\bar{q}} \simeq \int &\left[\prod_i \frac{d^4k_{qs,i}}{(2\pi)^4}\right]\left[\prod_j \frac{d^4k_{\bar{q}s,j}}{(2\pi)^4}\right] C_{q;\mu_1\cdots\mu_n}(\{\hat{k}_{qs,i}\})\left(\prod_i \hat{k}_{qs,i}^{\mu_i}\right) \\ &\times\left[\prod_i \frac{\bar{n}^{\nu_i}}{k_{qs,i}\cdot\bar{n}}\right] S_{\nu_1\cdots\nu_n;\sigma_1\cdots\sigma_m}(\{k_{qs,i}\},\{k_{\bar{q}s,j}\})\left[\prod_j \frac{n^{\sigma_j}}{n\cdot k_{\bar{q}s,j}}\right] \\ &\times\left(\prod_j \hat{k}_{\bar{q}s,j}^{\rho_j}\right) C_{\bar{q};\rho_1\cdots\rho_m}(\{\hat{k}_{\bar{q}s,j}\}). \end{aligned} \tag{2.68}$$

The soft gluon couplings to the collinear factors are replaced by their approximated momenta in the collinear subgraphs, which will allow the use of Ward identity.

2.5.3 K gluons as G gluons

The previous two subsections have covered almost all the needed approximations to the leading power. One remaining case is when the collinear subgraph is connected to the hard subgraph only by gluons. This does not happen for the Sudakov form factor due to the external quark legs, but can happen for processes involving hadrons, like DIS. In this subsection, we examine this remaining case using DIS as an example.

The related leading region is shown in Fig. ??.

2.6 Glauber region and modified approximations

The previous discussion on the soft momenta all relies on the uniform scaling in Eq. (2.40), assuming the integration of the angular variable $\bar{k}^\mu$ in Eq. (2.35) has a uniform bound in its whole range. This includes the power counting rules, determination of leading regions, and the soft approximations. The missing regions surrounding the soft pinch surface concern two types:

- $|k_s^+ k_s^-| \sim k_{sT}^2 \ll Q^2$ but $|k_s^+| \gg |k_s^-|$ or vice versa. An example is $k_s \sim (\lambda, \lambda^3/Q^2, \lambda^2/Q)$. This is still a soft momentum but with a large rapidity $y \sim \ln(Q/\lambda)$, so it is also collinear to the quark. We can call this scaling soft-collinear scaling. When it flows through C_q, it is no longer a good approximation to only keep k_s^- as in Eq. (2.64). As we will see later, a correct treatment needs to consider k_s as a collinear momentum here.

- $Q^2 \gg |k_s^+ k_s^-| \gg k_{sT}^2$. This does not raise any new issue compared to the uniform scaling and soft-collinear scaling.

- $|k_s^+ k_s^-| \ll k_{sT}^2 \ll Q^2$. This transverse-component-dominated region is called *Glauber region*, to which we now turn our discussion.

2.6.1 Glauber region

The Glauber region $|k_s^+ k_s^-| \ll k_{sT}^2 \ll Q^2$ is a subset of the soft region. A typical Glauber momentum scaling is

$$k_s^{\text{Glauber}} \sim (\lambda^2/Q, \lambda^2/Q, \lambda), \tag{2.69}$$

where the plus and minus components are taken of the same order. When it flows through the collinear subgraphs $C_{q,\bar{q}}$, it does not change the virtualities of collinear lines,

$$\begin{aligned}(k_q + k_s^{\text{Glauber}})^2 &\simeq k_q^2 - (\boldsymbol{k}_{sT}^{\text{Glauber}})^2 + 2k_q^+ (k_s^{\text{Glauber}})^- - \boldsymbol{k}_{qT} \cdot \boldsymbol{k}_{sT}^{\text{Glauber}} \simeq \mathcal{O}\Big(\lambda^2\Big), \\ (k_{\bar{q}} - k_s^{\text{Glauber}})^2 &\simeq k_{\bar{q}}^2 - (\boldsymbol{k}_{sT}^{\text{Glauber}})^2 - 2k_{\bar{q}}^- (k_s^{\text{Glauber}})^+ + \boldsymbol{k}_{\bar{q}T} \cdot \boldsymbol{k}_{sT}^{\text{Glauber}} \simeq \mathcal{O}\Big(\lambda^2\Big), \end{aligned} \tag{2.70}$$

where we only retained the terms of the highest scaling. The soft propagator also has the same scaling

$$(k_s^{\text{Glauber}})^2 \sim (k_{sT}^{\text{Glauber}})^2 \sim \mathcal{O}\Big(\lambda^2\Big). \tag{2.71}$$

In this way, the Glauber region also makes a leading-power contribution. But it is clear from Eq. (2.70) that the transverse component of the soft momentum becomes non-negligible in the collinear subgraphs, so that the approximations in Eqs. (2.64) and (2.65) are no longer valid. Even though we may still take the approximations in Eq. (2.67), the soft momentum $\hat{k}_s$ that couples to collinear subgraphs is not the same soft momentum that flows in them. As a result, the Glauber region violates the soft approximations that allow the exact use of Ward identities.

As we will see, it is crucial for the use of Ward identities to factorize soft gluons from collinear subgraphs in a gauge theory. So the presence of the Glauber region endangers factorization, which we must deal with particularly.

2.6.2 Contour deformation

The Glauber region (or any other soft region) is in the neighborhood of the soft pinch surface, but is not itself a pinch surface. When getting away from the pinch surface, the momentum

contour is no longer exactly pinched at a singular point to give zero virtualities. But if we are close to the pinch surface, the contour deformation is normally still restricted to keep the virtualities from getting too large. Therefore, we need to investigate whether the contour is pinched in the Glauber region. If not, we may still deform the contour to avoid the Glauber region.

Since the characteristics of the Glauber region is that the longitudinal components $k_s^{\pm}$ are much smaller than the transverse component k_{sT}, we would identify the poles of $k_s^{\pm}$ around 0 given k_{sT}. First, the denominators of C_q-collinear propagators

$$\begin{aligned}(k_{qi}+k_s)^2+i\epsilon &= 2(k_{qi}^+ + k_s^+)(k_{qi}^- + k_s^-) - (\boldsymbol{k}_{qi,T}+\boldsymbol{k}_{sT})^2 + i\epsilon \\ &\simeq 2k_{qi}^+(k_{qi}^- + k_s^-) - (\boldsymbol{k}_{qi,T}+\boldsymbol{k}_{sT})^2 + i\epsilon \end{aligned} \tag{2.72}$$

contribute to poles of k_s^- on the lower half plane, of the order λ^2/Q. Since all the C_q-collinear lines propagate from H to the future with large positive plus momenta, and we can always choose k_s to flow along C_q-collinear lines in the same direction without detouring back and forth inside C_q, all the C_q-collinear lines only contribute to small k_s^- on the lower half plane. Similarly, all the denominators of $C_{\bar{q}}$-collinear propagators only contribute to k_s^+ poles on the upper half plane,

$$\begin{aligned}(k_{\bar{q}j}-k_s)^2+i\epsilon &= 2(k_{\bar{q}j}^+ - k_s^+)(k_{\bar{q}j}^- - k_s^-) - (\boldsymbol{k}_{\bar{q}j,T}+\boldsymbol{k}_{sT})^2 + i\epsilon \\ &\simeq 2k_{\bar{q}j}^-(k_{\bar{q}j}^+ - k_s^+) - (\boldsymbol{k}_{\bar{q}j,T}+\boldsymbol{k}_{sT})^2 + i\epsilon, \end{aligned} \tag{2.73}$$

of order λ^2/Q. Both these k_s^+ and k_s^- poles are in the Glauber region, but only on the same half plane respectively, and not pinched. Around those poles, the gluon propagator

also contribute to poles for k_s^+ and k_s^-, but of order $k_{sT}^2/k_s^\pm \sim \mathcal{O}(Q)$, which is far away.

Therefore, we can deform the contour of $k_s^\pm$ such that their magnitudes stay much greater than λ^2/Q. Due to the k_s^- poles from C_q propagators, we deform the k_s^- contour to the upper half plane,

$$k_s^- \mapsto k_s^- + i\, v(k_s^-), \tag{2.74}$$

where $v(k_s^-) > 0$ kicks in when $k_s^- \sim \mathcal{O}(\lambda)$ and keeps k_s^- on the deformed contour to be at least of order λ. A simple choice can be, e.g.,

$$v(k) = \lambda\, e^{-k^2/2\lambda^2}, \tag{2.75}$$

which only modifies the Glauber region. This deformation does not change the k_s^+ poles from the $C_{\bar{q}}$ propagators, but changes the k_s^+ pole from the gluon propagator to the order $k_{sT}^2/k_s^- \sim \mathcal{O}(\lambda)$. Hence, it is still compatible to deform the k_s^+ contour to the lower half plane by $\mathcal{O}(\lambda)$,

$$k_s^+ \mapsto k_s^+ - i\, v(k_s^+), \tag{2.76}$$

where we chose the same deformation function in Eq. (2.75), which is not necessary.

Eqs. (2.74) and (2.76) deform the contours of k_s^+ and k_s^- by the same amount. This is called symmetrical deformation. To avoid possible obstruction from the poles of the gluon propagator, the maximum extent of the symmetrical deformation is $\mathcal{O}(\lambda)$. Symmetrical deformation is not always necessary. We will also see that in certain cases, symmetrical deformation is not allowed by a partial pinch in the Glauber region. There it is sufficient to only deform k_s^+ *or* k_s^-.

The deformations in Eqs. (2.74) and (2.76) are only applied to the Glauber region, but

not necessary to the other soft subregions. One may devise a uniform deformation formula for the whole soft region, e.g.,

$$k_s^- \mapsto k_s^- + i\,\rho\left(\frac{2k_s^+k_s^-}{k_{sT}^2}\right) v(k_s^-), \quad k_s^+ \mapsto k_s^+ - i\,\rho\left(\frac{2k_s^+k_s^-}{k_{sT}^2}\right) v(k_s^+), \tag{2.77}$$

where $\rho(x)$ has the property that $\rho(x) \simeq 1$ as $|x| \ll 1$ and $\rho(x) \to 0$ as $|x| \gtrsim 1$. One simple choice is

$$\rho(x) = \frac{(\lambda/Q)^2}{x^2 + (\lambda/Q)^2}. \tag{2.78}$$

After this deformation, the components (k_s^+, k_s^-, k_{sT}) are of the same order, restoring the uniform scaling [Eq. (2.40)]. Then the soft approximations in Eqs. (2.64) and (2.65) can be applied.

2.6.3 Modified approximations

The soft approximations can be applied only after the contour deformation, so it is important that they do not introduce any poles that obstruct the contour deformations in Eq. (2.77). Therefore, for the approximations in Eq. (2.67), we need to carefully specify an $i\epsilon$ prescription for the soft poles introduced around 0. For soft gluon momenta $\hat{k}_{qs,i}$ and $\hat{k}_{\bar{q}s,j}$ flowing *into* S from C_q and $C_{\bar{q}}$, respectively, we modify Eq. (2.67) to

$$g^{\mu_i\nu_i} \mapsto \frac{\hat{k}_{qs,i}^{\mu_i}\,\bar{n}^{\nu_i}}{\hat{k}_{qs,i}\cdot\bar{n} + i\epsilon} = \frac{\hat{k}_{qs,i}^{\mu_i}\,\bar{n}^{\nu_i}}{k_{qs,i}\cdot\bar{n} + i\epsilon}, \qquad g^{\sigma_j\rho_j} \mapsto \frac{n^{\sigma_j}\,\hat{k}_{\bar{q}s,j}^{\rho_j}}{n\cdot\hat{k}_{\bar{q}s,j} + i\epsilon} = \frac{n^{\sigma_j}\,\hat{k}_{\bar{q}s,j}^{\rho_j}}{n\cdot k_{\bar{q}s,j} + i\epsilon}. \tag{2.79}$$

Thus introduced poles for $k_s^\pm$ are all on the same half plane as those from the $C_{\bar{q},q}$ propagators.

The collinear approximations in Eq. (2.61) also introduce poles of the gluon momenta at

0. Even though they are designed only for the collinear region, as we will see in Sec. 2.7, after applying those approximations, we extend the loop momenta to all regions, including the soft and hard regions as well. The overlap with the soft region will be subtracted to avoid double counting. The subtraction term is obtained by first applying the soft approximation in Eqs. (2.64)(2.65)(2.79), and then applying the collinear approximation. Since the soft approximation is applied to the deformed contour, it is necessary that the collinear approximation be compatible with such deformation when the same gluon momentum enters the soft region. The same collinear gluon momentum k_i entering C_q from H can also enter the soft region, where it flows from $C_{\bar{q}}$ into S and has soft poles on the lower half plane for its plus momentum component. Similarly, for the collinear gluon momentum l_j entering $C_{\bar{q}}$ from H, we need to avoid the soft pole on the lower half plane for its minus momentum component. Therefore, we need to modify Eq. (2.61) to

$$g^{\mu_i\nu_i} \mapsto \frac{n^{\mu_i}\,\hat{k}_i^{\nu_i}}{\hat{k}_i\cdot n+i\epsilon}=\frac{n^{\mu_i}\,\hat{k}_i^{\nu_i}}{k_i\cdot n+i\epsilon},\quad g^{\sigma_j\rho_j} \mapsto \frac{\hat{l}_j^{\sigma_i}\,\bar{n}^{\rho_j}}{\hat{l}_j\cdot \bar{n}+i\epsilon}=\frac{\hat{l}_j^{\sigma_i}\,\bar{n}^{\rho_j}}{l_j\cdot \bar{n}+i\epsilon}. \tag{2.80}$$

In this way, the necessity of contour deformation to get out of the Glauber region dictates the $i\epsilon$ prescriptions in the soft and collinear approximations. The direction of the deformation is determined only by the causal structure of the scattering process, so are the $i\epsilon$ prescriptions, which will give correct causal properties for each factor in the factorization result.

2.7 Subtraction method and factorization

The leading power contribution of a certain amplitude or cross section does not *a priori* correspond to a factorized expression. The latter is motivated by the fact that the leading

regions have distinct momentum scales, hard, collinear, and soft, as given by the Libby-Sterman analysis. By choosing proper approximations as in Sec. 2.5, the different momentum scales detach so as to imply a factorized expression.

As a necessary condition for factorization, the simplest nontrivial diagram that only has a single leading region with two distinct momentum scales should simply factorize as a result of the approximations, e.g., the leading-order DIS diagram as in Fig. 2.4(a). If the whole amplitude or cross section only had one single region, then factorization would come as a direct result of proper approximations. However, as a renormalizable gauge theory, each process in QCD has an infinite number of diagrams with arbitrarily complicated leading regions. A proper treatment must take into account all possible regions of all diagrams, with careful avoidance of double counting between neighboring regions. The factorization is then a highly nontrivial result, which is very intricate and fragile.

In this section, I briefly review the subtraction formalism used in the treatment of multiple regions in the derivation of factorization. First, I will ...

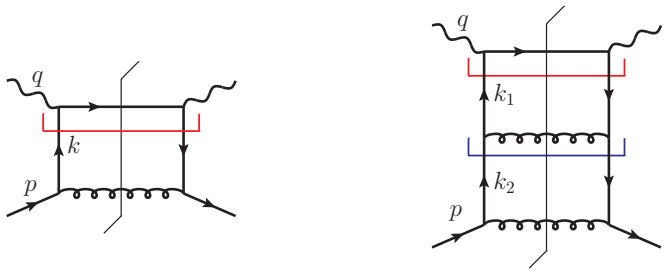

(a) (b)

Fig. 2.4: Examples of DIS diagrams for an elementary target. (a) is the LO diagram, with one single leading region indicated by the red hooked line. (b) is an NLO diagram, with two leading regions indicated by the red and blue hooked lines, respectively.

2.7.1 A particular DIS diagram as an example

Each leading region of a DIS diagram contains only two subgraphs, one hard subgraph H connected to the virtual photon lines, and one collinear subgraph C attaching to the external target. The two subgraphs are joined by a set of collinear lines whose propagators we include in the collinear subgraph. Fig. 2.4 shows two diagrams for an elementary target, which we take as on on-shell quark with a small mass m to cutoff collinear divergences, with no concern for confinement issues. Taking the kinematics

$$p = \left(p^+, \frac{m^2}{2p^+}, \mathbf{0}_T\right), \quad q = \left(-xp^+, \frac{Q^2}{2xp^+}, \mathbf{0}_T\right), \tag{2.81}$$

for the target and photon, respectively, with $Q \gg m$, the lines in the hard subgraph have virtualities of order Q^2, and those in the collinear subgraph have virtualities of order m^2. The leading regions are represented by the massless reduced diagrams, obtained by taking $m \to 0$, which yields $p \to \hat{p} = (p^+, 0^-, \mathbf{0}_T)$.

In this section, we work in the light-cone gauge, where the gluon propagator denominator is

$$-g_\perp^{\mu\nu} = -g^{\mu\nu} + n^\mu \bar{n}^\nu + n^\nu \bar{n}^\mu, \tag{2.82}$$

with n and $\bar{n}$ defined in Eq. (2.56); This suppresses the longitudinal polarization so that the leading regions only have two quark or transversely polarized gluon lines joining C to H. The approximation can be easily devised, following the spirit in Sec. 2.5, as

- for each collinear momentum k_i flowing into the hard subgraph H, we approximate it

by only keeping its plus component,

$$k_i \mapsto \hat{k}_i = (k_i \cdot n)\bar{n}, \tag{2.83}$$

where n and $\bar{n}$ are defined the same as Eq. (2.56);

- for each quark line entering (leaving) H, insert the spinor projector $\mathcal{P} = \gamma^-\gamma^+/2$ ($\bar{\mathcal{P}} = \gamma^+\gamma^-/2$);
- for each gluon line connecting C to H, insert the Lorentz tensor $g_\perp^{\mu\nu}$ to project out the transverse polarization.

Denoting the effect of such approximation by

$$H \otimes C \equiv \int [dk] H(k) C(k) \;\mapsto\; \int [dk] H(k)\, \hat{T}\, C(k), \tag{2.84}$$

where k collectively denotes all the collinear momenta, and $\hat{T}$ acts on the integrand, inserting certain projectors between H and C and neglecting certain momenta in H to its left.

The LO diagram Γ_0 in Fig. 2.4(a) has two leading regions, (1) one with $k = \alpha\, \hat{p}$ ($0 < \alpha < 1$) collinear to the target, so that the reduced diagram has one hard subgraph and one collinear subgraph, separated by the red hooked line, which inserts necessary projectors and approximates on shell the collinear momenta passing it. (2) and the other with $k^2 \sim \mathcal{O}(Q^2)$, so that the whole diagram is the hard subgraph, to which the external photon and quark lines attach. For the discussion in this section, we assume the second region is power suppressed by some nonperturbative effect, so that we only have the first leading region. Factorization

then follows trivially from the fact that only k^+ flows through H, and this leads to

$$\Gamma_0 = \int \frac{d^4k}{(2\pi)^4} H_0(k)\,\hat{T}\,C_0(k) = \int dk^+ H_0(\hat{k}) \left[\int \frac{dk^- d^2\boldsymbol{k}_T}{(2\pi)^4} \mathcal{P}\,C_0(k)\,\bar{\mathcal{P}}\right], \tag{2.85}$$

up to power suppressed contribution. We will deal with the spin and color projectors in more detail later.

The NLO diagram Γ_1 in Fig. 2.4(b) is more complicated. We have two leading regions: (1) region R_1: k_1 is in H with a large virtuality, while $k_2 = \beta\hat{p}$ $(0 < \beta < 1)$ is collinear, as indicated by the blue hooked line; and (2) region R_2: both k_1 and k_2 are collinear to the target, with

$$k_1 = \alpha k_2, \quad k_2 = \beta\hat{p}, \quad 0 < \alpha, \beta < 1, \tag{2.86}$$

which is indicated by the red hooked line in Fig. 2.4(b). The topology of the region R_1 is defined in the momentum space as $k_1^2 \neq 0$ and $k_2 = \beta\hat{p}$. Apparently, its closure contains R_2 as a subset. This relation between the two leading regions is denoted as $R_1 > R_2$. R_1 is greater than R_2 in the sense that it has more lines with hard virtualities, while R_2 has more lines in the collinear subgraph.

To move forward, we first define the diagram Fig. 2.4(b) as

$$\Gamma_1 = \int \frac{d^4k_1}{(2\pi)^4} \frac{d^4k_2}{(2\pi)^4} \left[H_0(q;k_1) \cdot K_0(k_1,k_2) \cdot C_0(p;k_2)\right]. \tag{2.87}$$

The factor $H_0(q;k_1)$ includes the quark line on the top and the two photon vertices, $K_0(k_1,k_2)$ includes the propagators of k_1, the gluon line of $(k_2 - k_1)$, and their vertices, and $C_0(p;k_2)$ includes the rest of the diagram. These three factors are convoluted in momenta k_1 and k_2, which has been explicitly written, and spinor and color indices, implicitly implied by the dot

notation.

To extract the leading contribution from R_2, we can insert the approximator $\hat{T}$ between H_0 and K_0, formally written as

$$C_{R_2}\Gamma_1 = T_{R_2}\Gamma_1 = \int \frac{d^4k_1}{(2\pi)^4}\frac{d^4k_2}{(2\pi)^4}\left[H_0(q;k_1)\hat{T}K_0(k_1,k_2)\cdot C_0(p;k_2)\right], \tag{2.88}$$

which projects k_1 in H_0 by $\hat{k}_1$ according to Eq. (2.83) and inserts the spinor projectors $\mathcal{P}$ and $\bar{\mathcal{P}}$. This expression simply factorizes into

$$C_{R_2}\Gamma_1 = \int dk^+ H_0(q;\hat{k})\left[\int \frac{dk^-d^2\boldsymbol{k}_T}{(2\pi)^4}\frac{d^4k_2}{(2\pi)^4}\mathcal{P}\left(K_0(k,k_2)\cdot C_0(p;k_2)\right)\bar{\mathcal{P}}\right], \tag{2.89}$$

which adds to Eq. (2.85) with the same hard coefficient, but as an NLO correction to the collinear factor.

Now we consider the contribution from R_1. Naively, $C_{R_1}\Gamma_1$ is obtained by

$$\begin{aligned} C_{R_1}\Gamma_1 \sim T_{R_1}\Gamma_1 &= \int \frac{d^4k_1}{(2\pi)^4}\frac{d^4k_2}{(2\pi)^4}\left[H_0(q;k_1)\cdot K_0(k_1,k_2)\,\hat{T}\,C_0(p;k_2)\right] \\ &= \int \frac{d^4k_1}{(2\pi)^4}\frac{d^4k_2}{(2\pi)^4}\left[H_0(q;k_1)\cdot K_0(k_1,\hat{k}_2)\cdot\left(\mathcal{P}C_0(p;k_2)\bar{\mathcal{P}}\right)\right], \end{aligned} \tag{2.90}$$

which seems to factorize into a hard factor $H_0(q;k_1)\cdot K_0(k_1,\hat{k}_2)$ and a collinear factor $\mathcal{P}C_0(p;k_2)\bar{\mathcal{P}}$. Now the hard factor includes the integration of k_1, which should be constrained to the hard region. However, this is technically hard to define, given also the need to deform the contour when the unpinched propagators become close to the on-shell poles. It would be ideal to have the k_1 integration in the hard factor to extend to all regions. Then it can unavoidably reach the collinear region where $k_1 = \alpha\hat{k}_2$. This is still a leading region

in the hard subgraph. But such contribution has been included in the region R_1. This reflects a general fact that a larger region R_1 has overlap with smaller regions $R_2 < R_1$, such that the approximator T_{R_1} alone is not sufficient to only extract the contribution from R_1 when acting on the graph Γ. Therefore, when applying T_{R_1}, one should first subtract the contribution from smaller regions, such that

$$\begin{aligned} C_{R_1}\Gamma_1 &= T_{R_1}(\Gamma_1 - C_{R_2}\Gamma_1) = T_{R_1}(1 - T_{R_2})\Gamma_1 \\ &= \int \frac{d^4k_1}{(2\pi)^4}\frac{d^4k_2}{(2\pi)^4}\left[H_0(q;k_1)\,(1-\hat{T})\,K_0(k_1,k_2)\,\hat{T}\,C_0(p;k_2)\right] \\ &= \int dk^+\left[\int \frac{d^4k_1}{(2\pi)^4} H_0(q;k_1)\,(1-\hat{T})\,K_0(k_1,\hat{k})\right]\left[\int \frac{dk^- d^2\boldsymbol{k}_T}{(2\pi)^4}\mathcal{P}C_0(p;k)\bar{\mathcal{P}}\right], \end{aligned} \tag{2.91}$$

where in the third line we gave the factorization expression, which adds onto Eq. (2.85) with the same collinear factor, but as an NLO correction to the hard factor.

Adding the leading contribution from R_1 and R_2, we have the total leading-power contribution of Γ_1,

$$\begin{aligned} \sum_R C_R\Gamma_1 &= C_{R_2}\Gamma_1 + C_{R_1}\Gamma_1 = T_{R_2}\Gamma_1 + T_{R_1}(1 - T_{R_2})\Gamma_1 \\ &= T_{R_2}\Gamma_1 + T_{R_1}\Gamma_1 - T_{R_1}T_{R_2}\Gamma_1, \end{aligned} \tag{2.92}$$

where in the second line, we have separated all terms of different approximator applications. By construction, T_{R_2} gives a good approximation to Γ_1 when both k_1 and k_2 have low virtualities, but gives a poor description when either of them is hard. (Recalling our assumption that the region with both momenta having hard virtualities is suppressed, so T_{R_2} is bad when k_1 is hard but k_2 is collinear.) Also, T_{R_1} gives a good approximation to Γ_1 only when k_1 is hard and k_2 is collinear. Now, in the region R_2, among the three terms in the second

line of Eq. (2.92), the first term $T_{R_2}\Gamma_1$ gives a good approximation of Γ_1. The other two terms combine into $T_{R_1}(1-T_{R_2})\Gamma_1$, which is suppressed in this region due to the $(1-T_{R_2})$ factor that suppresses the low virtuality region of k_1. Since T_{R_1} keeps k_1 unchanged, it does not affect such suppression. In the region R_1, the second term gives a good approximation of Γ_1. The other two terms combine into $(1-T_{R_1})T_{R_2}\Gamma_1$, which is suppressed due to the factor $(1-T_{R_1})$ that suppresses the hard virtuality region of k_1.

Now we examine how well Eq. (2.92) can approximate the graph Γ_1, by constructing the error term,

$$r_1 \equiv \Gamma_1 - \sum_R C_R\Gamma_1 = (1-T_{R_1})(1-T_{R_2})\Gamma_1. \tag{2.93}$$

The factor $(1-T_{R_2})$ accounts for the error introduced by neglecting k_{1T} with respect to Q, so gives

$$(1-T_{R_2})\Gamma_1 = \mathcal{O}\left(\frac{k_{1T}}{Q}\right)\Gamma_1. \tag{2.94}$$

The other factor $(1-T_{R_1})$ accounts for the error introduced by neglecting k_{2T} with respect to k_{1T} and Q, so

$$r_1 = \mathcal{O}\left(\frac{k_{2T}}{k_{1T}}, \frac{k_{2T}}{Q}\right)\mathcal{O}\left(\frac{k_{1T}}{Q}\right)\Gamma_1 = \mathcal{O}\left(\frac{k_{2T}}{Q}, \frac{k_{1T}k_{2T}}{Q^2}\right)\Gamma_1. \tag{2.95}$$

Since we always have $k_{2T} \simeq m \ll Q$ and $k_{1T} \lesssim Q$, the error is power suppressed,

$$r_1 = \mathcal{O}\left(\frac{m}{Q}\right)\Gamma_1. \tag{2.96}$$

In fact, the argument of the subtraction formalism [Eq. (2.92)] can start with the error term Eq. (2.93). Successively applying $(1-T_R)$ on Γ_1 must yield a power suppressed result,

since it successively suppresses all the leading regions. Therefore, we have

$$r_1 \equiv (1 - T_{R_1})(1 - T_{R_2})\Gamma_1 = \mathcal{O}\left(\frac{m}{Q}\right). \tag{2.97}$$

This can be reorganized as

$$r_1 = (1 - T_{R_2})\Gamma_1 - T_{R_1}(1 - T_{R_2})\Gamma_1 = \Gamma_1 - T_{R_2}\Gamma_1 - T_{R_1}(1 - T_{R_2})\Gamma_1, \tag{2.98}$$

which gives the subtraction formula

$$\Gamma_1 = T_{R_2}\Gamma_1 + T_{R_1}(1 - T_{R_2})\Gamma_1 + \mathcal{O}\left(\frac{m}{Q}\right), \tag{2.99}$$

where the power suppressed term is from r_1. Such subtraction formalism systematically extracts the leading-power contributions from all regions, with loop momenta extending to all regions and without double counting. Our analysis of the DIS diagrams up to NLO should motivate that summing over all regions and diagrams can lead to a factorization result, which we will discuss in Sec. 2.7.3.

2.7.2 Subtraction formalism

Generally, a diagram Γ can contain multiple leading regions, R_i. In the Sudakov form factor example Fig. 2.3(b), different regions of a particular diagram differ by having different lines or different numbers of lines in the hard, A-collinear, B-collinear, or soft subgraphs. In the DIS example, different regions of the diagram Γ_1 differ by having different numbers of ladders in the hard of collinear subgraphs. In each region R_i, we design suitable approximator T_{R_i} that acts on the integrand and gives a proper approximation for the integral in that region.

The leading power contribution of each region is iteratively defined as

$$C_R\Gamma = \begin{cases} T_R\Gamma, & \text{if no region } R_i \text{ of } \Gamma \text{ is smaller than } R; \\ T_R\left(\Gamma - \sum_{R'<R} C_{R'}\Gamma\right), & \text{otherwise.} \end{cases} \tag{2.100}$$

And then summing over all regions gives an approximation to the original diagram Γ up to power suppressed corrections,

$$\Gamma = \sum_R C_R\Gamma + \text{p.s.} \tag{2.101}$$

This is the general subtraction formalism of extracting the leading-power contribution from a diagram Γ.

No attempt will be given here to prove Eq. (2.101).[2] We simply motivate it by examining a simple case where the leading regions are strictly nested, i.e., all the leading regions R_i of any graph Γ have the strict ordering $R_1 > R_2 > \cdots > R_n$. This is true for diagrams with only two kinds of subgraphs, such as DIS diagrams which only have collinear and hard subgraphs (but not for Sudakov form factor which has four subgraphs). Similar to Eq. (2.97), by successively subtracting all the leading region contributions, the remainder

$$r = (1 - T_{R_1})(1 - T_{R_2}) \cdots (1 - T_{R_n})\Gamma \tag{2.102}$$

[2] A formal argument can be found in [Collins(2013)].

is power suppressed. Then by reorganizing Eq. (2.102), we have

$$\begin{aligned}
\Gamma &= \Gamma - r + \text{p.s.} \\
&= \Gamma - (1 - T_{R_2}) \cdots (1 - T_{R_n})\Gamma + T_{R_1}(1 - T_{R_2}) \cdots (1 - T_{R_n})\Gamma + \text{p.s.} \\
&= \Gamma - (1 - T_{R_3}) \cdots (1 - T_{R_n})\Gamma + T_{R_2}(1 - T_{R_3}) \cdots (1 - T_{R_n})\Gamma \\
&\quad + T_{R_1}(1 - T_{R_2}) \cdots (1 - T_{R_n})\Gamma + \text{p.s.} \\
&= T_{R_n}\Gamma + T_{R_{n-1}}(1 - T_{R_n})\Gamma + \cdots + T_{R_1}(1 - T_{R_2}) \cdots (1 - T_{R_n})\Gamma + \text{p.s.} \\
&= C_{R_n}\Gamma + C_{R_{n-1}}\Gamma + \cdots + C_{R_1}\Gamma + \text{p.s.},
\end{aligned} \tag{2.103}$$

where in the last step we defined

$$C_{R_i} = T_{R_i}(1 - T_{R_{i+1}}) \cdots (1 - T_{R_n})\Gamma, \tag{2.104}$$

which agrees with the general definition in Eq. (2.100).

In a general Feynman diagram, the relations among all the leading regions form an ordered graph, starting from the largest region where all loop momenta have hard virtualities, and ending at the smallest region where as many loop momenta as possible are in the soft (or collinear, when there is no soft subgraph) region. Then the contribution $C_R\Gamma$ of any region

R has the formal structure

$$\begin{aligned} C_R\Gamma &= T_R\Gamma - \sum\nolimits_{R'<R} T_R C_{R'}\Gamma \\ &= T_R\Gamma - \sum\nolimits_{R'<R} T_R T_{R'}(\Gamma - \sum\nolimits_{R''<R} C_{R''}\Gamma) \\ &= T_R\Gamma + T_R \sum\nolimits_{R'<R}(-T_{R'})\Gamma + T_R \sum\nolimits_{R'<R}(-T_{R'}) \sum\nolimits_{R''<R}(-T_{R''})\Gamma + \cdots \\ &= T_R\Gamma + T_R \sum_{\{R'_i\}} \prod_i (-T_{R'_i})\Gamma, \end{aligned} \tag{2.105}$$

where in the last line the sum is over all possible nestings of regions smaller than R: $R > R'_1 > R'_2 > \cdots > R'_n$, and

$$\prod_i (-T_{R'_i}) = (-T_{R'_1})(-T_{R'_2}) \cdots (-T_{R'_n}), \tag{2.106}$$

with the approximators for larger regions on the left.

Eq. (2.105) gives a general formula for the subtraction terms in $C_R\Gamma$. They are given by successively applying $-T_{R'}$ for smaller regions $R' < R$, and then applying T_R. In order for the presence of subtraction not to affect the argument of the approximation T_R, especially the application of Ward identities that follows the soft and collinear approximators defined in Eqs. (2.79) and (2.80), the same simplifications following $T_R\Gamma$ should also apply to the subtraction terms $T_R \sum_{R'<R} C_{R'}\Gamma$. Furthermore, due to the presence of subtraction terms, it is necessary that the approximators for larger regions do not affect the contour deformations needed for the approximators of smaller regions, which explains the $i\epsilon$ choices in Eq. (2.80).

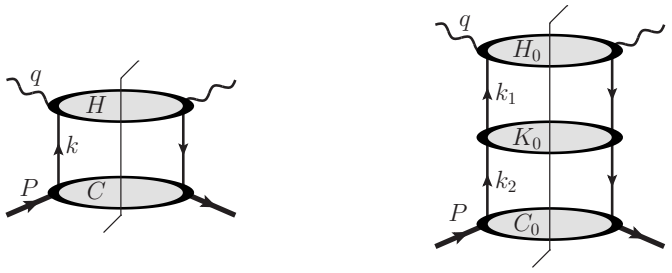

(a) (b)

Fig. 2.5: (a) A general leading region for a DIS cut diagram in light-cone gauge is divided into a hard subgraph H and a collinear subgraph C, joined by two collinear quark or gluon lines. (b) The ladder expansion for a certain DIS cut diagram is decomposed into a series of 2PI subdiagrams connected by two quark or gluon lines. The thick external lines represent hadron targets.

2.7.3 Factorization of DIS in light-cone gauge

Now we extend to all orders the discussion in Sec. 2.7.1 of the DIS factorization in light-cone gauge, as a simple application and illustration of the subtraction formalism in Sec. 2.7.2. We will replace the elementary quark target by a physical on-shell hadron target, such as a proton, of momentum P and mass M.

In the light-cone gauge, the general leading region for DIS contains a hard subgraph and a collinear subgraph, which are joined by two collinear quark or gluon lines, as shown in Fig. 2.5(a). For a given graph, a larger region has more lines in H and fewer in C. This motivates the ladder expansion of a general DIS diagram, as shown in Fig. 2.5(b), where each unit of H_0, K_0, and C_0 is two-particle-irreducible (2PI), which means that they cannot be divided into two parts by only cutting two propagators, such that they cannot have further ladder expansion. We denote H_0, K_0, and C_0 as the sums of all possible 2PI subgraphs, each being a function of external momenta, spin indices, and color indices. So then the sum

of all DIS diagrams is given by

$$\begin{aligned} W &= D_0 + H_0 \cdot C_0 + H_0 \cdot K_0 \cdot C_0 + H_0 \cdot K_0 \cdot K_0 \cdot C_0 + \cdots \\ &= D_0 + \sum_{n=0}^{\infty} H_0 \cdot K_0^n \cdot C_0, \end{aligned} \tag{2.107}$$

where D_0 is the minimal graph which is itself 2PI and has no ladder decomposition. We stress that each factor represents an all-order sum of 2PI *perturbative* diagrams, by the assumption (1) in Sec. 2.1.2, with the hadron-parton vertex described by some hadron wavefunction which we will not need to make clear.

By directly coupling the hadron to the virtual photon, D_0 has all lines being highly virtual, so it is power suppressed, by the assumption (1) in Sec. 2.1.2.

A graph Γ_n with n ladders (n is the number of K_0 factor in Eq. (2.107)) has $n+1$ leading regions, $R_0 > R_1 > \cdots R_n$, with R_i referring to the region with i lower K_0 ladders belonging to the collinear subgraph. Then following the discussion in Eqs. (2.102) - (2.104), the leading contribution of each region R_i is

$$C_{R_i}\Gamma_n = T_{R_i}(1 - T_{R_{i+1}}) \cdots (1 - T_{R_n})\Gamma_n = H_0 \cdot \left[(1-\hat{T})K_0\right]^{n-i} \hat{T}\left[K_0\right]^i \cdot C_0, \tag{2.108}$$

which factorizes into a hard factor $H_0 \cdot \left[(1-\hat{T})K_0\right]^{n-i}$ and a collinear factor $\mathcal{P}\left[K_0\right]^i \cdot C_0\bar{\mathcal{P}}$, similar to the low-order examples in Eqs. (2.85)(2.89) and (2.91). Summing over i from 0 to n and then over n from 0 to ∞ amounts to summing over the ladders in the hard and

collinear factors separately,

$$\begin{aligned}\hat{W} &= \sum_{n=0}^{\infty}\sum_{i=0}^{n} C_{R_i}\left[H_0 \cdot K_0^n \cdot C_0\right] \\ &= \sum_{n=0}^{\infty}\sum_{i=0}^{n} H_0 \cdot \left[(1-\hat{T})K_0\right]^{n-i} \hat{T}\left[K_0\right]^i \cdot C_0 \\ &= \sum_{i=0}^{\infty}\sum_{j=0}^{\infty} H_0 \cdot \left[(1-\hat{T})K_0\right]^{i} \hat{T}\left[K_0\right]^j \cdot C_0 \\ &= H_0 \cdot \frac{1}{1-(1-\hat{T})K_0}\hat{T}\frac{1}{1-K_0} \cdot C_0. \end{aligned} \tag{2.109}$$

This factorizes into a hard factor

$$H(q;\hat{k}) = H_0 \cdot \frac{1}{1-(1-\hat{T})K_0}, \tag{2.110}$$

and a collinear factor

$$C(P,k) = \mathcal{P}\left[\frac{1}{1-K_0}\cdot C_0\right]\bar{\mathcal{P}}. \tag{2.111}$$

They are convoluted in the momentum k and in color and spin indices. Eq. (2.109) approximates W in Eq. (2.107) with the remainder term

$$r = W - \hat{W} = D_0 + \sum_{n=0}^{\infty} H_0 \cdot \left[(1-\hat{T})K_0\right]^n \cdot (1-\hat{T})C_0, \tag{2.112}$$

where both terms are power suppressed. Therefore, we get the factorized result of the DIS cross section

$$W = \int dk^+ H(q;\hat{k})\left[\int \frac{dk^- d^2\boldsymbol{k}_T}{(2\pi)^4} C(P,k)\right] + \mathcal{O}\left(\frac{M}{Q}\right). \tag{2.113}$$

We will deal with the spin and color connections later.

We note that the sum over regions (i) and graphs (n) is converted to two independent sums over each subgraph, which leads to the factorized expression. But it is the subtraction of smaller regions from larger regions that separates different momentum scales. In this way, the hard factor defined in Eq. (2.110) has removed all contributions from the regions where any of the loop momenta become collinear. In terms of perturbative Feynman amplitudes, it is free from collinear singularity, and the corresponding Feynman integrals are only sensitive to the hard scale Q, so we are allowed to use perturbative descriptions due to the asymptotic freedom, and it is safe to neglect the parton masses and virtualities therein, as is encoded in the approximator $\hat{T}$. The collinear factor defined in Eq. (2.111) collects all the pinch singularities in perturbative diagrams, so parton momenta in it are trapped in the low-virtuality regions. It thus becomes not perturbatively tractable, but the all-order sum in Eq. (2.111) can be *formally* defined nonperturbatively. Then the perturbative pinch singularities are interpreted to be reflecting the sensitivity to nonperturbative dynamics. Even though the result is obtained by perturbative diagram expansion, the overall sum, regardless of its convergence issue, is still assumed to reflect the correct reality, by the assumption (3) in Sec. 2.1.2. Its actual value can be obtained by fitting it to experimental data, by virtue of its universality.

In this way, the subtraction formalism together with the sum over regions and graphs factorizes the DIS cross section into hard and collinear factors, with the former only sensitive to dynamics at a hard scale Q, and the latter only to the nonperturbative soft scale m. The separation of distinct scales is the essence of factorization.

Chapter 3

QCD Factorization of exclusive processes

In the previous section, we have reviewed the main principles and methodology of QCD factorization, which applies to hadronic scattering processes with one hard scale Q much greater than $\Lambda_{\rm QCD}$. Normally, this would localize the interaction to become sensitive to the partonic degrees of freedom in the hadron(s). To the leading power in $\Lambda_{\rm QCD}/Q$, only one parton enters[1] the hard interaction. This breaks the incoming hadron into colored objects, which exchange soft gluons to neutralize the colors. The final state is then a series of hard jets surrounded by soft hadrons. Any query about a specific soft hadron would touch the non-perturbative dynamics and go beyond the control of a perturbative method. Hence in such situations it is more sensible to study inclusive observables, which "inclusively sums over" (which is another way of saying "neglecting") anything else besides the directly observed hard particles or quantities, and the related processes are called inclusive processes. As we have demonstrated in the preceding section, the inclusive sum cancels the soft gluon exchanges between different collinear sectors and establishes universal parton density functions or fragmentation functions. The universality of those nonperturbative functions gives QCD factorization predictive power, and allows them to be measured to reveal certain aspects of

[1] A similar story holds for the inclusive hadron production process where one parton leaves the hard interaction and initializes a jet of hadrons.

the hadron structures.

It should be noted that inclusiveness is not the absolutely necessary condition for well-defined observables in hadronic scattering, but more of a practically convenient choice against our inability to deal with the nonperturbative soft regime. This is in contrast to the soft divergences in QED; there the massless photons pose infrared divergences in both virtual and real processes, and it is only inclusive observables that are well defined, given that arbitrarily soft photons can never be detected by an equipment of a finite size. In QCD, however, due to the color confinement, all final-state particles can in principle be captured by detectors — no soft gluons elude the observation. That means, it is in principle sensible to talk about the amplitude or cross section of the production of a certain number of particles. Such processes are termed *exclusive processes*.

In practice, including the context of this paper, exclusive processes usually refer to a narrower class of processes in which hadrons are *unbroken*, given that the multiple soft radiations from broken hadrons are easily intractable even in experiments. In this sense, we divide the exclusive processes to be discussed in this paper into three types:

- *large-angle scattering*, referring generally to a hadronic $2 \to n$ process in which the final-state hadronic particles are hard and well separated, and no hadrons are found in the direction(s) of the hadron beam(s),

- *single-diffractive scattering*, which is similar to the previous case, but has one diffracted hadron in one of the hadron beam directions, and

- *double-diffractive scattering*, which has one diffracted hadron in both hadron beam directions.

We only discuss at most $2 \to 2$ processes for the large-angle scattering, with $n > 2$ a trivial

generalization. The minimal configuration involves only one hadron, and the maximal one is the scattering of two hadrons into two other hadrons. We will show that in the hard scattering case, the soft gluons are cancelled, leading the *amplitudes* to be factorized into hadron *distribution amplitudes* (DAs). For the single-diffractive scattering, we can similarly show the soft cancellation, and then the diffraction subprocess is factorized into generalized parton distributions (GPDs). For the double-diffractive scattering and beyond, however, we will show that soft gluons can be pinched in the Glauber region, which prohibits a factorization theorem to be derived.

By the nature of exclusive processes, each hadron is connected to the hard scattering by at least two partons. This causes exclusive processes to be more power suppressed than inclusive processes, by the power counting rules in Table 2.1. Hence, exclusive processes are more suitably studied at low energy scattering, while as the colliding energy increases, hadrons are more likely to break, leading to the inclusive regime. Nevertheless, the universal parton correlation functions, the DAs and GPDs, obtained from the factorization of exclusive processes, provide valuable information on the hadron structures complementary to the correlation functions obtained from inclusive processes, as will be discussed in more details in the next section.

3.1 Large-angle exclusive meson scattering

We confine our discussion within large-angle $2 \to 2$ exclusive meson scattering,

$$A(p_1) + B(p_2) \to C(q_1) + D(q_2), \tag{3.1}$$

in which we always take A as a meson. The processes can be categorized according to the particle type of the beam B, and we look at three types of processes: (1) electron-meson scattering, with $B = e^-$, (2) photon-meson scattering, with $B = \gamma$, and (3) meson-meson scattering, with $B =$ meson. The factorization discussion can be trivially adapted to other processes with no mesons in the initial states or processes involving baryons.

3.1.1 Large-angle electron-meson scattering

For electron-meson scattering, the beam particle B stands for an electron. To the leading order in QED, it will be scattered into the final state, which we take as $C = e^-$. The other particle D can be either a photon or a meson, for which we discuss sequentially.

3.1.1.1 Single-meson process: $D = \gamma$

Electric charge conservation constrains the meson A to be neutral, so for simplicity, we take $A = \pi^0$ to be the charge-neutral pion. The scattering $\pi^0(p_1) + e(p_2) \to e(q_1) + \gamma(q_2)$ thus gives the π-γ transition form factor [Lepage and Brodsky(1980)]. As usual, we define the Mandelstam variables

$$s = (p_1 + p_2)^2, \quad t = (p_1 - q_1)^2, \quad u = (p_1 - q_2)^2. \tag{3.2}$$

We work in the center-of-mass (CM) frame, where A always moves along the $+\hat{z}$ direction, and $e(q_1)$ has a transverse momentum $\vec{q}_T$. In the limit $s \to \infty$ while t/s and u/s stay constant, i.e., $s \to \infty$ with $q_T/\sqrt{s}$ constant, the pion is connected to the hard scattering via a set of collinear lines, as shown by the reduced diagram in Fig. 3.1(a). From the Landau criterion in Sec. 2.2.3, this represents a general pinch surface in the parton loop momentum

space that possibly gives mass divergences. The most general pinch surface here can also have arbitrarily many soft lines connecting A and H, but they are power suppressed by the general power counting rule in Sec. 2.3, so are neglected. The power counting rule for the collinear lines, as discussed in Sec. 2.3, can be summarized as (1) one collinear fermion line or transversely polarized gluon line is associated with a power λ/Q, where $Q = \mathcal{O}(q_T) = \mathcal{O}(\sqrt{s})$ and $\lambda = \mathcal{O}(\Lambda_{\rm QCD}) = \mathcal{O}(m_\pi, f_\pi)$, with m_π and f_π the pion mass and decay constant, respectively, and (2) a longitudinally polarized gluon line is associated with a power $(\lambda/Q)^0$. Hence, the leading region should have two collinear quark or transversely polarized gluon lines connecting A to H, together with arbitrarily many longitudinally polarized gluons. However, having purely gluon lines violates the isospin symmetry. So we only have one type of leading regions, with one collinear subgraph and a hard subgraph, joined by a pair of quark lines and arbitrarily many gluon lines of longitudinal polarization. One example of the leading-order (LO) diagram is shown in Fig. 3.1(c), where the scattered electron exchanges a highly-virtual photon γ^*_{ee} with the quark. The latter is then excited to a high virtuality. After a short lifetime, it annihilates with the antiquark to emit a real photon. Exchanging the roles of quark and antiquark gives the other LO diagram.

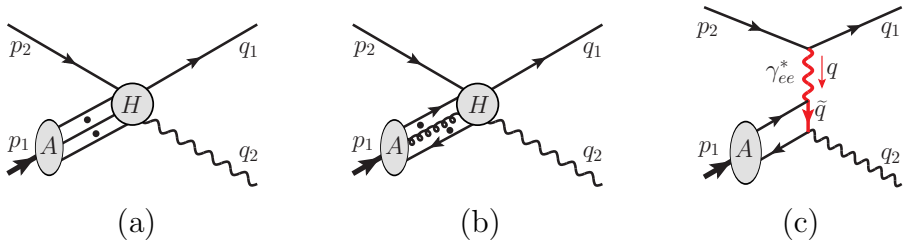

Fig. 3.1: (a) Reduced diagram for a general pinch surface of the exclusive scattering process $\pi^0(p_1)+e(p_2) \to e(q_1)+\gamma(q_2)$. The dots represent an arbitrary number of collinear lines. (b) is the leading region, where the dots alongside the gluon line represent an arbitrary number of collinear longitudinally polarized gluons. (c) is one leading-order diagram. Reversing the fermion arrow gives the other LO diagram.

One can immediately notice the difference of exclusive processes from the inclusive pro-

cesses in Fig. **??** that now a collinear subgraph is connected to the hard subgraph by at least two parton lines. This is because the hadrons participating in the exclusive processes must be color singlets. To keep intact, they must only exchange a color singlet state with the hard interaction. As a result, the leading power for the exclusive amplitude $\pi^0(p_1) + e(p_2) \to e(q_1) + \gamma(q_2)$ already counts as $(\lambda/Q)^1$.

The factorization works in a way similar to DIS treated in **??**. We include all the collinear propagators in the collinear subgraph C. For each k_i flowing in H, which scales as

$$k_i \sim (Q, \lambda^2/Q, \lambda), \tag{3.3}$$

we approximate it by only retaining the plus component,

$$k_i \to \hat{k}_i = (k_i \cdot n)\bar{n}, \tag{3.4}$$

where we introduced the light-like auxiliary vectors, $\bar{n} = (1, \hat{z})/\sqrt{2}$ and $n = (1, -\hat{z})/\sqrt{2}$. We project on shell the quark and antiquark lines external to H by inserting the Dirac matrices, respectively,

$$\mathcal{P}_A = \frac{\gamma \cdot \bar{n}\gamma \cdot n}{2} = \frac{\gamma^-\gamma^+}{2}, \quad \text{and} \quad \bar{\mathcal{P}}_A = \frac{\gamma \cdot n\gamma \cdot \bar{n}}{2} = \frac{\gamma^+\gamma^-}{2}. \tag{3.5}$$

Each gluon has its polarization dominantly proportional to its momentum, so we approximate its connection to H by

$$H_{\mu_i}(k_i) g^{\mu_i\nu_i} C_{\nu_i}(k_i) \mapsto H_{\mu_i}(\hat{k}_i) \frac{\hat{k}_i^{\mu_i} n^{\nu_i}}{k_i \cdot n - i\epsilon} C_{\nu_i}(k_i), \tag{3.6}$$

for a particular gluon of momentum k_i flowing into H. Since there is no soft region here, the $i\epsilon$ is not important; we added it only for convention.

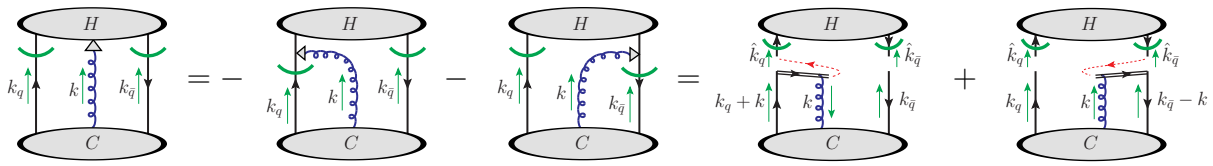

Fig. 3.2: Graphic representation of the two steps to detach a longitudinally polarized collinear gluon from the collinear subgraph C to the hard subgraph H, and reconnect it to corresponding gauge links of the C. The red thin dashed lines represent the color flows.

The approximator defined in Eqs. (3.4)-(3.6) can be collectively denoted as $\hat{T}$. It acts on one leading region R_Γ, which has the decomposition into a hard subgraph H_n and and a collinear subgraph C_n as in Fig. 3.1(b), of a certain diagram Γ, where n is the number of gluons connecting H_n and C_n alongside the quark and antiquark lines. The leading-power contribution from the region R_Γ can be obtained by applying $\hat{T}$, with the contribution from smaller regions subtracted,

$$C_{R_\Gamma}\Gamma = H_n^{\text{sub}} \cdot \hat{T} \cdot C_n, \tag{3.7}$$

where H_n^{sub} is the hard subgraph with subtraction for smaller regions, and $\hat{T}$ acts to the left on H_n^{sub} by neglecting small components of collinear momenta (as specified in Eq. (3.4)) and inserting spinor and Lorentz projectors (as specified in Eqs. (3.5) and (3.6)). The subtraction terms in H_n^{sub} can be further written in a form like Eq. (3.7). By our assumptions (1) and (3) in Sec. 2.1.2, the amplitude of $\pi^0(p_1) + e(p_2) \to e(q_1) + \gamma(q_2)$ is given by the sum over all graphs. Each region R_Γ of a graph Γ is uniquely specified by the hard subgraph H and collinear subgraph C. Varying H with a given C or vice versa corresponds to a different graph. Summing over all regions of all diagrams is equivalent to summing over the

subgraphs H and C individually. And for each given subgraph H, the associated subtraction for smaller regions is also uniquely determined. Now for a given C_n, we sum over all possible attachments of the collinear gluons onto the hard subgraph, which amounts to summing over H_n at a given n and perturbative order. This, together with the $H(\hat{k})\cdot\hat{k}$ structure after the approximation in Eq. (3.6), allows the use of Ward identity for the collinear gluons, which also equally applies to each subtracted term in $H_n^{\rm sub}$. Due to the presence of two quark lines, the Ward identity results in two gauge links that collect all the collinear gluons, different from the inclusive processes. This can be easily demonstrated for $n = 1$. As shown in Fig. 3.2, each quark is connected by a gauge link that goes along the lightcone direction n to ∞ in the future, and the gluon can be connected to either one. The result can be generalized by mathematical induction to an arbitrary n, for which all possible ways to attach the n gluons to the two gauge links are included. The vertices and propagators along the gauge links are the same as that can be obtained from the operator[2]

$$\int d^4y e^{ik\cdot x}\left[\bar{\psi}_q(0)\Phi^\dagger(\infty,0;n)\right]_j\left[\Phi(\infty,y;n)\psi_q(y)\right]_i, \tag{3.8}$$

expanded to the n-th order in g, where ψ_q is the quark field of flavor q, $\Phi(\infty,y;n)$ is the Wilson line from y to ∞ along n,

$$\Phi(\infty,y;n) = \mathcal{P}\exp\left\{-ig\int_0^\infty d\lambda\, n^\mu A_\mu^a(y+\lambda n)t^a\right\}, \tag{3.9}$$

and i, j are color indices in the fundamental representation. The hard subgraph then only has two external quark lines, with momenta k and $p_1 - k$, respectively. So we can write

[2] Eq. (3.8) only specifies the momentum k going out from the quark-to-Wilson-line vertex. The momentum from the antiquark-to-Wilson-line vertex is $p_1 - k$, determined by momentum conservation.

Eq. (3.7) as

$$C_{R_\Gamma}\Gamma = H^{\rm sub}(\hat{k}, \hat{p}_1 - \hat{k}) \otimes \left[\hat{T}_w \cdot C_n\right](k; p_1), \tag{3.10}$$

where $\hat{T}_w$ acting on C_n is not different from $\hat{T}$, but just refers to the fact that Ward identity has been used to attach all collinear gluons onto gauge links that only belong to C_n. Then summing over all possible diagrams for H_n and C_n gives a factorized result,

$$\sum_{R,\Gamma} C_{R_\Gamma}\Gamma = \int \frac{d^4k}{(2\pi)^4} \mathcal{H}_{\beta\alpha;ji}(\hat{k}, \hat{p}_1 - \hat{k})\, \mathcal{C}_{\alpha\beta;ij}(k; p_1), \tag{3.11}$$

where we have left explicit the momentum convolution, and the dependence on colors and spinor indices. In Eq. (3.11), $\mathcal{H} = \sum_H H^{\rm sub}$ is the subtracted hard subgraph with gluons factored out, and $\mathcal{C} = \hat{T}_w \sum_C C$ is the collinear subgraph, both being summed over all diagrams. Since there is no any subtraction involved in the collinear subgraph, we can write it as a matrix element form, by extending Eq. (3.8) to all orders,

$$\begin{aligned}\mathcal{C}_{\alpha\beta;ij}(k; p_1) =& \mathcal{P}_{A,\alpha\alpha'} \int d^4y e^{ik\cdot y} \langle 0|\mathcal{T}\left\{\left[\bar{\psi}_{q,\beta'}(0)\Phi^\dagger(\infty, 0; n)\right]_j\right. \\ & \left.\times \left[\Phi(\infty, y; n)\psi_{q,\alpha'}(y)\right]_i\right\} |\pi^0(p_1)\rangle \bar{\mathcal{P}}_{A,\beta'\beta},\end{aligned} \tag{3.12}$$

where we have explicitly left the dependence on colors and spinor indices, and have included the spinor projectors in Eq. (3.5). By construction, Eq. (3.11) approximates the amplitude of $\pi^0(p_1) + e(p_2) \to e(q_1) + \gamma(q_2)$ at the leading power.

Now $\mathcal{H}$ is only convoluted with $\mathcal{C}$ by (1) color indices i and j, (2) spinor indices α and β, and (3) the plus component of the quark (or antiquark) momentum k. Since the pion is color neutral, only the color singlet component of $\mathcal{C}_{\alpha\beta;ij}$ is nonzero, so we can define a gauge

invariant factor $\mathcal{C}_{\alpha\beta}$ by summing over the color diagonal elements,

$$\mathcal{C}_{\alpha\beta;ij}(k;p_1) = \frac{1}{N_c}\delta_{ij}\,\mathcal{C}_{\alpha\beta}(k;p_1). \tag{3.13}$$

By expanding $\mathcal{C}_{\alpha\beta}(k;p_1)$ in terms of the 16 independent Dirac matrices, we can see that only the γ^-, $\gamma_5\gamma^-$, and $\sigma^{-\perp}$ components survive under the projection of $\mathcal{P}_A$ and $\bar{\mathcal{P}}_A$. The pseudoscalar nature of π^0 further kills the γ^- and $\sigma^{-\perp}$ components, so we end up with only one spinor structure,

$$\mathcal{C}_{\alpha\beta}(k;p_1) = \left(\frac{\gamma_5\gamma\cdot\bar{n}}{2}\right)_{\alpha\beta}\mathcal{C}(k;p_1) \tag{3.14}$$

with the scalar coefficient in both color and spinor space,

$$\mathcal{C}(k;p_1) = \int d^4y e^{ik\cdot y}\langle 0|\mathcal{T}\left\{\left[\bar{\psi}_{q,\alpha}(0)\Phi^\dagger(\infty,0;n)\right]_i\frac{\gamma\cdot n\gamma_5}{2}\left[\Phi(\infty,y;n)\psi_{q,\alpha}(y)\right]_i\right\}|\pi^0(p_1)\rangle. \tag{3.15}$$

Finally, for the momentum convolution, since the hard part $\mathcal{H}$ only depends on $k\cdot n$, we insert into Eq. (3.11) the factor

$$1 = \int dx\,\delta\left(x - \frac{k\cdot n}{p_1\cdot n}\right) = (p_1{\cdot}n)\int dx\,\delta\left(x\,p_1\cdot n - k\cdot n\right) = (p_1{\cdot}n)\int dx\int\frac{d\lambda}{2\pi}e^{i\lambda(x\,p_1\cdot n - k\cdot n)}. \tag{3.16}$$

Together with the color and spinor factors in Eqs. (3.13) and (3.14), the convolution in Eq. (3.11) becomes

$$\int dx\left[(p_1\cdot n)\frac{1}{N_c}\delta_{ij}\left(\frac{\gamma_5\gamma\cdot\bar{n}}{2}\right)_{\alpha\beta}\mathcal{H}_{\beta\alpha;ji}(x\hat{p}_1,(1-x)\hat{p}_1)\right] \times\left[\int\frac{d\lambda}{2\pi}\int\frac{d^4k}{(2\pi)^4}e^{i\lambda(x\,p_1\cdot n - k\cdot n)}\mathcal{C}(k;p_1)\right], \tag{3.17}$$

This completes the derivation of factorization for the amplitude,

$$\mathcal{M}_{\pi^0 e\to e\gamma} = \sum_q \int dx\, D_{q/\pi^0}(x)\, \mathcal{H}_q(x,\vec{q}_T,s) + \mathcal{O}\big(\Lambda_{\rm QCD}/q_T\big), \tag{3.18}$$

where we have left explicit the sum over the quark flavor q, and changed the notation $\mathcal{C}$ to define the DA for π^0,

$$\begin{aligned} D_{q/\pi^0}(x) &= \int \frac{d\lambda}{2\pi} \int \frac{d^4k}{(2\pi)^4} e^{i\lambda(x\,p_1\cdot n - k\cdot n)} \mathcal{C}(k;p_1) \\ &= \int_{-\infty}^{\infty} \frac{d\lambda}{2\pi} e^{i\lambda x\, p_1\cdot n} \langle 0|\mathcal{T}\left\{\left[\bar\psi_q(0)\Phi^\dagger(\infty,0;n)\right]\frac{\gamma\cdot n\gamma_5}{2}\left[\Phi(\infty,\lambda n;n)\psi_q(\lambda n)\right]\right\}|\pi^0(p_1)\rangle \\ &= \int_{-\infty}^{\infty} \frac{d\lambda}{2\pi} e^{i\lambda x\, p_1\cdot n} \langle 0|\mathcal{T}\left\{\bar\psi_q(0)\frac{\gamma\cdot n\gamma_5}{2}\Phi(0,\lambda n;n)\psi_q(\lambda n)\right\}|\pi^0(p_1)\rangle. \end{aligned} \tag{3.19}$$

The integration of k^- and $\vec{k}_T$ sets the operator on the negative light cone, along which the operators have canonical commutation relations. Then we can equivalently remove the time ordering in Eq. (3.19). It can also be shown by the analyticity properties of $\mathcal{C}(k;p_1)$ as a scattering amplitude under the integration of k^- [Diehl and Gousset(1998)], following the assumption (3) in Sec. 2.1.2 and that the analyticity properties are the same as the corresponding perturbative Feynman diagrams. This would allow the insertion of physical states,

$$\begin{aligned} D_{q/\pi^0}(x) = \sum_X \int_{-\infty}^{\infty} \frac{d\lambda}{2\pi} e^{i\lambda x\, p_1\cdot n} &\langle 0|\left[\bar\psi_q(0)\Phi^\dagger(\infty,0;n)\right]|X\rangle \frac{\gamma\cdot n\gamma_5}{2} \\ &\times \langle X|\left[\Phi(\infty,\lambda n;n)\psi_q(\lambda n)\right]|\pi^0(p_1)\rangle \\ = \sum_X \delta\left(p_X\cdot n - (1-x)p_1\cdot n\right) &\langle 0|\left[\bar\psi_q(0)\Phi^\dagger(\infty,0;n)\right]|X\rangle \frac{\gamma\cdot n\gamma_5}{2} \\ &\times \langle X|\left[\Phi(\infty,0;n)\psi_q(0)\right]|\pi^0(p_1)\rangle, \end{aligned} \tag{3.20}$$

where momentum conservation constrains the plus component of the total momentum of the state X,

$$p_X^+ = (1-x)p_1^+. \tag{3.21}$$

For X to be a physical state, we must require $p_X^+ \geq 0$, so that $x \leq 1$. On the other hand, by using the canonical commutation relation for ψ and $\bar{\psi}$, Eq. (3.20) can also be written as

$$\begin{aligned} D_{q/\pi^0}(x) &= -\sum_X \int_{-\infty}^{\infty} \frac{d\lambda}{2\pi} e^{i\lambda x\, p_1\cdot n} \,\mathrm{Tr}\left\{ \frac{\gamma\cdot n\gamma_5}{2} \langle 0| \left[\Phi(\infty,\lambda n;n)\psi_q(\lambda n)\right] |X\rangle \right. \\ &\qquad \left. \times \langle X| \left[\bar{\psi}_q(0)\Phi^\dagger(\infty,0;n)\right] |\pi^0(p_1)\rangle \right\} \\ &= -\sum_X \delta\left(p_X\cdot n - x\, p_1\cdot n\right) \mathrm{Tr}\left\{ \frac{\gamma\cdot n\gamma_5}{2} \langle 0| \left[\Phi(\infty,0;n)\psi_q(0)\right] |X\rangle \right. \\ &\qquad \left. \times \langle X| \left[\bar{\psi}_q(0)\Phi^\dagger(\infty,0;n)\right] |\pi^0(p_1)\rangle \right\}, \end{aligned} \tag{3.22}$$

where Tr takes the spinor trace. Now we have

$$p_X^+ = x\, p_1^+ \geq 0, \tag{3.23}$$

which requires $x \geq 0$. Together, we must have $x \in [0,1]$ for the DA to be nonzero. Therefore, we should constrain the x integration in Eq. (3.18) to be from 0 to 1.

Such constraint is not mandatory condition inherent from factorization, but as a result of having the operator on light cone in collinear factorization and setting $x = k^+/p_1^+$ on the real axis. This then causes a problem of endpoint singularity. However, we note that the above approximations $\hat{T}$ defined in Eqs. (3.4)-(3.6) is true only for the scaling in Eq. (3.3), which corresponds to the pinch surface whose surrounding region gives the leading-power contribution to the amplitude. In principle, one should keep the scaling $k_i^+ \sim \mathcal{O}(Q)$ through-

out the factorization analysis. Nevertheless, in the result of factorization, Eq. (3.18), the variable x is integrated from 0 to 1, so that we have to include the region where one of the active partons has momentum $k_i^+ \ll Q$. Perturbatively, this does not lead to a pinch, so we should have deformed the contour of k_i^+ by $\mathcal{O}(Q)$ to make the associated propagator in the hard subgraph to have high virtuality. For example, as shown later in Eq. (**??**), the leading-order hard coefficient contains a term that is proportional to $1/(x - i\varepsilon)Q^2$ which becomes soft as $x \to 0$, and we should deform the contour of x to the lower half complex plane to make $\mathrm{Im}\, x \sim \mathcal{O}(1)$. Similar issue arises as $x \to 1$. However, since the DA only has support in $x \in [0, 1]$, such deformation is forbidden by the end points of the z integration. Therefore, the validity of the DA factorization in Eq. (3.18) needs to be supplemented with an additional assumption that the end point region should be strongly suppressed by the DA, which we refer to as the *soft-end suppression*.

So far, we have been working with the bare DA and hard coefficient, without caring for the possible UV divergences introduced by the approximator $\hat{T}$. The original amplitude $\mathcal{M}_{\pi^0 e\to e\gamma}$ contains no UV divergence. But the approximator $\hat{T}$ short-circuits the integration of k^- and $\vec{k}_T$ into $\mathcal{C}$ in Eq. (3.17), and extends the integration to infinity. This introduces an (artificial) UV divergence. However, since the hard coefficient $\mathcal{H}$ is defined with subtraction of lower regions, which are themselves factorized in the same way the DA is factorized, whatever UV divergences introduced by $\hat{T}$ in the DA has been compensated by the subtraction in $\mathcal{H}$. In this way, both the DA and $\mathcal{H}$ contain UV divergences, which cancel each other and make up a finite convolution result in Eq. (3.18). Nevertheless, it would be nice to define a *renormalized* DA by taking off the UV divergences therein. This procedure would

be discussed later in Sec. **??**, and it results in a multiplicative renormalization,

$$D_{q/\pi^0}(x,\mu) = \int_0^1 dz\, Z(x,z;\alpha_s(\mu);\epsilon^{-1}) D^{\text{bare}}_{q/\pi^0}(z;\epsilon^{-1}), \tag{3.24}$$

with an invertible renormalization coefficient

$$D^{\text{bare}}_{q/\pi^0}(x;\epsilon^{-1}) = \int_0^1 dz\, Z^{-1}(x,z;\alpha_s(\mu);\epsilon^{-1}) D_{q/\pi^0}(z,\mu). \tag{3.25}$$

This introduce a factorization scale μ dependence in the renormalized DA, which will lead to an evolution equation. Here we have explicitly indicated the UV divergence in the bare DA, which is polynomials of ϵ^{-1} in dimensional regularization. The renormalized DA depends on μ through the running coupling $\alpha_s(\mu)$ in the renormalization coefficient. We note that due to the lack of gluon mediated channel, the DA renormalization has no mixing between the quark and gluon or between different quark flavors. Restoring the "bare" notation in Eq. (3.18) and substituting Eq. (3.25) for the bare DA, we get the factorization formula for the amplitude, in terms of UV renormalized DA and infrared (and UV) finite hard coefficient

$$\mathcal{M}_{\pi^0 e\to e\gamma} = \sum_q \int_0^1 dx\, D_{q/\pi^0}(x,\mu)\, \mathcal{H}_q\left(x; \frac{\vec{q}_T}{\sqrt{s}}, \frac{q_T}{\mu}\right) + \mathcal{O}\big(\Lambda_{\text{QCD}}/q_T\big), \tag{3.26}$$

which looks like Eq. (3.18) but has an extra factorization scale dependence. The renormalized hard coefficient is related to the bare one by

$$\mathcal{H}_q\left(x; \frac{\vec{q}_T}{\sqrt{s}}, \frac{q_T}{\mu}\right) = \int_0^1 dz\, Z^{-1}(x,z;\alpha_s(\mu);\epsilon^{-1})\, \mathcal{H}^{\text{bare}}(z;\vec{q}_T,s;\epsilon^{-1}). \tag{3.27}$$

Then we finished proving the factorization for the amplitude of $\pi^0 e \to e\gamma$. We have not

only obtained the operator definition for the pion DA, given in Eqs. (3.19) and renormalized in (3.24), but also given a practical procedure for calculating the hard coefficient to all perturbative orders. By projecting the pion state in Eq. (3.26) to an on-shell parton-pair state, we can expand both sides order by order and obtain the hard coefficient at each order by an iterative matching.

3.1.1.2 Double-meson process: $D =$ meson

Now we discuss the electron induced meson production. Similarly, the electromagnetic current does not change the flavor of the meson, so for concreteness let us take $A = D = \pi^+$, with the scattering of other mesons generalized in a trivial way. The process $\pi^+(p_1)+e(p_2) \to e(q_1) + \pi^+(q_2)$ probes the electromagnetic pion form factor [**?**]. The kinematics are also defined as in Eq. (3.2). We work in the CM frame with the $\pi^+(p_1)$ along $+\hat{z}$ direction, under the limit $q_T \gg m_\pi$ and $q_T/\sqrt{s} = \mathcal{O}(1)$.

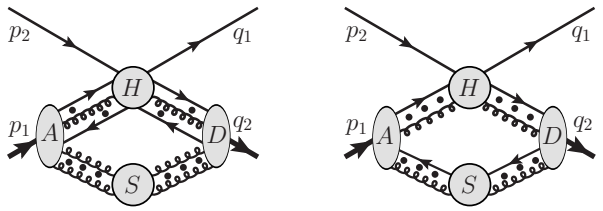

Fig. 3.3: Leading regions of the exclusive scattering process $\pi^+(p_1)+e(p_2) \to e(q_1)+\pi^+(q_2)$.

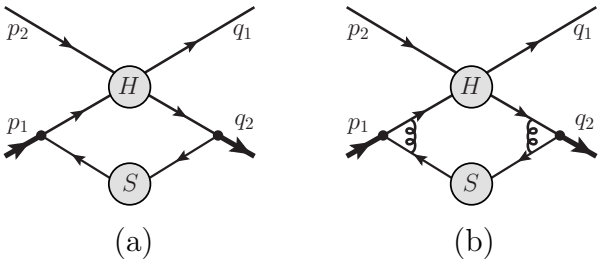

Fig. 3.4: Two examples for the leading region (b) in Fig. 3.3.

Following the same procedure, we can list the leading region diagrams for the meson production amplitude, shown in Fig. 3.3. Immediately, one can notice the differences from the real photon production process discussed above

(1) there are two collinear subgraphs now, which are connected by an extra soft subgraph, and

(2) there are two kinds of leading regions, shown in Figs. 3.3(a) and 3.3(b), which we denote as region (a) and region (b). For region (b), only one active quark parton enters the hard interaction, and the other one is soft and only transmits the needed quantum number.

Region (b) raises some theoretical difficulty for factorization argument. However, we note that such leading regions are obtained based on the soft scaling in Eq. (2.40) with $\lambda_S = \mathcal{O}(\lambda^2/Q)$. In this region, a soft parton has virtuality of order λ^4/Q^2, well below the nonperturbative threshold, so we consider such ultrasoft region to be cut off by nonperturbative dynamics. As argued in Sec. 2.3.1, considering $\lambda_S \lesssim \lambda^2/Q$ is more important for inclusive processes where we replace the sum over final-state hadrons by the sum over final-state on-shell partons. Here we are dealing with exclusive processes, and all partons are directly connected to hadrons, so we confine our discussion within $\lambda_S \gtrsim \lambda$, for which the power counting rules are given by the last two columns of Table 2.1. We note the suppression from having soft momenta flowing through more than one collinear lines. This constrains the diagrams for region (b) to be at very low order due to the continuity of fermion lines, while for region (a), we must require the soft gluons to attach to the collinear lines right before they enter the hard part.

While it is likely not well defined, the lowest-order diagram for region (b) can be con-

ceived as in Fig. 3.4(a), where the two quark lines directly attach to the "pion wavefunction". In this case, the two collinear lines have virtualities λQ, while the soft subgraph has a power counting λ^3, so it gives the power counting λ/Q in total, which is one power higher than the counting $(\lambda/Q)^2$ for region (a). However, this assumes the bare quark-pion coupling to scale as 1. In the kinematical regime when the pion is highly boosted, it is hardly conceivable that all the pion momentum is carried by one of the two valence partons. So we add into the *soft-end suppression assumption* made for the $e\pi^0 \to e\gamma$ process that diagrams like Fig. 3.3(b) receive a high enough suppression from the nonperturbative hadron wavefunction such that they are power suppressed compared to the region in Fig. 3.3(a). This assumption is supported by high-order QCD corrections. As shown in Fig. 3.4(b), when there are gluon connections between the soft and collinear partons, the whole diagram becomes power suppressed compared to Fig. 3.3(a), by the counting rule in Table 2.1. Also as indicated by the suppression of Fig. 3.4(b), one may expect that a resummation of the gluon exchanges can lead to a suppression for region (b). We leave a detailed study to future work. For now, we simply note that the soft-end suppression brings the leading regions down to the one in Fig. 3.3(a).

To simplify the following discussion, we note that by virtue of the large q_T, one can always boost to the frame where A is moving along $+z$ direction and D is moving along $-z$ direction, as was done in Refs. [**?**, Nayak et al.(2005)Nayak, Qiu, and Sterman], which brings the discussion similar to the Sudakov form factor in Ch. 2. This can be achieved in a covariant way by defining two sets of light-cone vectors

$$w_A^\mu = \frac{1}{\sqrt{2}}(1,\hat{z})\,, \quad \bar{w}_A^\mu = \frac{1}{\sqrt{2}}(1,-\hat{z})\,, \quad w_D^\mu = \frac{1}{\sqrt{2}}(1,\hat{w})\,, \quad \bar{w}_D^\mu = \frac{1}{\sqrt{2}}(1,-\hat{w})\,, \tag{3.28}$$

where $\hat{w} = (\sin\theta\cos\phi, \sin\theta\sin\phi, \cos\theta)$ is the direction of the final-state meson D. Then any momentum four-vector r can be expanded in the w_A-w_D frame as

$$r^\mu = r^+ w_A^\mu + r^- w_D^\mu + r_T^\mu, \tag{3.29}$$

where $r^\pm = (r \cdot w_{D,A})/(w_A \cdot w_D)$ are the longitudinal components, and $w_A \cdot w_D \sim \mathcal{O}(1)$ does not affect the power counting. Under this notation, we have

$$r^2 = 2\, r^+ r^- w_A \cdot w_D - \boldsymbol{r}_T^2, \tag{3.30}$$

where $\boldsymbol{r}_T^2 = -g_{\mu\nu} r_T^\mu r_T^\nu$. The A-collinear momentum k_A and D-collinear momentum k_D have dominant components along w_A and w_D, respectively,

$$\begin{aligned} k_A^\mu &= \left(k_A^+, k_A^-, \boldsymbol{k}_{A,T}\right)_{AD} \sim (Q, \lambda^2/Q, \lambda), \\ k_D^\mu &= \left(k_D^+, k_D^-, \boldsymbol{k}_{D,T}\right)_{AD} \sim (\lambda^2/Q, Q, \lambda), \end{aligned} \tag{3.31}$$

where the subscript "AD" refers to light-front coordinates in the w_A-w_D frame. A soft momentum k_s exchanged between the A- and D-collinear subgraphs is in the central rapidity region with respect to the w_A-w_D frame, so we have

$$k_s^\mu = \left(k_s^+, k_s^-, \boldsymbol{k}_{s,T}\right)_{AD} \sim (\lambda_S, \lambda_S, \lambda_S), \tag{3.32}$$

with λ_S varying between λ^2/Q and λ. In the following discussion of this subsection, we will stay in this frame and omit the subscripts "AD".

As noted in Sec. 2.6, however, the Glauber region of the soft gluons requires special care,

where the soft momentum k_s has the scaling

$$k_s^{\text{Glauber}} \sim (\lambda^2/Q, \lambda^2/Q, \lambda). \tag{3.33}$$

Similar to the Sudakov form factor case detailed in Sec. 2.6.2, there is no pinch that traps the soft momentum in the Glauber region. So we can deform the contour to stay away from the Glauber region. For a soft momentum k_s flowing from A into S and then into D, its minus component only receives poles from the A-collinear lines, which all lie on the upper half plane, whereas its plus component only has poles from the D-collinear lines and lie on the upper half plane. Hence, in this region, we deform the contour as

$$k_s^+ \mapsto k_s^+ - i\,v(k_s^+), \quad k_s^- \mapsto k_s^- - i\,v(k_s^-), \tag{3.34}$$

where $v(k_s^\pm)$ is a positive real function defined in Sec. 2.6.2. Such deformation deforms the Glauber momenta back to the uniform soft scaling in Eq. (3.32). Then we can define the approximator $\hat{T}$ for a leading region R:

(a) For a soft momentum k_{SA} (k_{SD}) flowing in A (D), we approximate it by

$$k_{SA} \mapsto \hat{k}_{SA} = \frac{k_{SA}\cdot w_A}{w_A\cdot w_D} w_D, \quad k_{SD} \mapsto \hat{k}_{SD} = \frac{k_{SD}\cdot w_D}{w_A\cdot w_D} w_A. \tag{3.35}$$

(b) For a soft momentum k_{SA} flowing from A *into* S, we include its propagator in S and approximate its coupling with A by

$$J_\mu^A(k_A; k_{SA})\, g^{\mu\nu}\, S_\nu(k_{SA}) \mapsto J_\mu^A(k_A; \hat{k}_{SA})\, \frac{\hat{k}_{SA}^\mu w_A^\nu}{k_{SA}\cdot w_A - i\epsilon}\, S_\nu(k_{SA}), \tag{3.36}$$

where k_A stands for some A-collinear momentum, and the $i\epsilon$ prescription makes the artificially introduced pole at $k_{SA}^- = 0$ on the upper half plane, compatible with the needed deformation in Eq. (3.34).

(c) For a soft momentum k_{SD} flowing from D *into* S, we include its propagator in S and approximate its coupling with D by

$$J_\mu^D(k_D; k_{SD})\, g^{\mu\nu}\, S_\nu(k_{SD}) \mapsto J_\mu^D(k_D; \hat{k}_{SD})\, \frac{\hat{k}_{SD}^\mu w_D^\nu}{k_{SD}\cdot w_D + i\epsilon}\, S_\nu(k_{SD}), \tag{3.37}$$

Note that we flipped the soft momentum flow relative to that in Eq. (3.34).

(d) For an A (D) collinear momentum k_{AH} (k_{DH}) flowing in H, we approximate it by

$$k_{AH} \mapsto \hat{k}_{AH} = (k_{AH}\cdot \bar{w}_A) w_A, \quad k_{DH} \mapsto \hat{k}_{DH} = (k_{DH}\cdot \bar{w}_D) w_D. \tag{3.38}$$

Here we project k_{AH} (k_{DH}) against $\bar{w}_A$ ($\bar{w}_D$), instead of w_D (w_A), such that after factoring the collinear subgraphs out of H, each collinear subgraph is independent of each other. Such replacement keeps the leading momentum components, so does not affect the leading-power accuracy.

(e) For a collinear gluon attaching A to H, its polarization is dominantly longitudinal. We include its propagator in C_A and approximate its coupling with H by

$$H_\mu(k_H; k_{AH})\, g^{\mu\nu}\, J_\nu^A(k_{AH}) \mapsto H_\mu(k_H; \hat{k}_{AH})\, \frac{\hat{k}_{AH}^\mu \bar{w}_A^\nu}{k_{AH}\cdot \bar{w}_A + i\epsilon}\, J_\nu^A(k_{AH}), \tag{3.39}$$

where k_H is some hard momentum in H, and we take k_{AH} to flow from H *into* A. This introduces a pole at $k_{AH}\cdot\bar{w}_A = 0$. The $i\epsilon$ is introduced to make it compatible

with the deformation in Eq. (3.34), as explained in Sec. 2.6.3. The same momentum k_{AH} can reach the soft region, where it flows from S into A, through H, into B, and back to S. The deformation in Eq. (3.34) is then adapted to

$$\Delta k_{AH}^{S} = +i\,\mathcal{O}(\lambda)(w_A + w_D), \tag{3.40}$$

which deforms the denominator $k_{AH} \cdot \bar{w}_A$ by

$$\Delta k_{AH}^{S} \cdot \bar{w}_A = +i\,\mathcal{O}(\lambda), \tag{3.41}$$

into the upper half plane. So we need the $+i\epsilon$ prescription in Eq. (3.39). This will lead to a future-pointing Wilson line along $\bar{w}_A$.

(f) For a collinear gluon attaching D to H, we include its propagator in C_D and approximate its coupling with H by

$$H_\mu(k_H; k_{DH})\, g^{\mu\nu}\, J_\nu^D(k_{DH}) \mapsto H_\mu(k_H; \hat{k}_{DH})\, \frac{\hat{k}_{DH}^\mu \bar{w}_D^\nu}{k_{DH} \cdot \bar{w}_D - i\epsilon}\, J_\nu^D(k_{DH}), \tag{3.42}$$

where we take k_{DH} to flow from H *into* D. The $i\epsilon$ is introduced in a similar way to Eq. (3.39). This will lead to a past-pointing Wilson line along $\bar{w}_D$.

(g) For the quark and antiquark lines entering H from A, we insert the spinor projectors

$$\mathcal{P}_A = \frac{\gamma \cdot w_A\, \gamma \cdot \bar{w}_A}{2}, \quad \bar{\mathcal{P}}_A = \frac{\gamma \cdot \bar{w}_A\, \gamma \cdot w_A}{2}, \tag{3.43}$$

respectively. For the quark and antiquark lines leaving H to D, we insert the spinor

projectors

$$\bar{\mathcal{P}}_D = \frac{\gamma \cdot \bar{w}_D \, \gamma \cdot w_D}{2}, \quad \mathcal{P}_D = \frac{\gamma \cdot w_D \, \gamma \cdot \bar{w}_D}{2}, \tag{3.44}$$

respectively.

A region R for a graph Γ is specified by the set of collinear and soft gluons (and the two pairs of collinear quark lines by default); any other lines belong to the hard subgraph H. We denote the graph contribution in such a region as

$$H_{n_1,n_2} \otimes C_{A,n_1;m_1} \otimes C_{B,n_2;m_2} \otimes S_{m_1,m_2}, \tag{3.45}$$

where n_1 and n_2 are the number of collinear gluons connecting H to A and B, respectively, and m_1 and m_2 are the number of soft gluons connecting S to A and B, respectively. The symbol $\otimes$ refers collectively to the momentum convolutions and color and spinor contractions. For the same graph Γ, there may be smaller regions R' than R, which have fewer lines in H and/or $C_{A,D}$, and/or more lines in S. The contribution from the region R is then extracted by applying $\hat{T}$ after the subtraction of smaller region contributions,

$$C_{R_\Gamma}\Gamma = \hat{T}\left(\Gamma - \sum_{R'<R} C_{R'_\Gamma}\Gamma\right), \tag{3.46}$$

where the contribution $C_{R'_\Gamma}\Gamma$ is obtained by iterative use of Eq. (3.46). The subtraction terms in Eq. (3.46) also have $\hat{T}$ acted in front. They are obtained by treating the lines in the same way as in R, with certain lines belonging to H, certain lines to A, etc., even though the approximators for R' have been applied that treat those lines in some other (smaller) regions. Therefore, the subtraction terms in Eq. (3.46) have the same structure as Eq. (3.45), with different factors H, C_A, and C_D, but the same S. Those subtraction terms can be uniquely

determined once R is specified.

The approximator $\hat{T}$ modifies certain momenta some Lorentz and spinor projectors in a way that the use of Ward identity for soft and collinear gluons is exact. This applies to both $\hat{T}\Gamma$ and the subtracted terms $C_{R'_\Gamma}\,\Gamma$ (which is obtained after applying their approximators) in Eq. (3.46). Acting $\hat{T}$ on the latter further modifies the momenta and introduces projectors that makes a further use of Ward identity exact. Therefore, after applying $\hat{T}$ in Eq. (3.46), we can use Ward identity for both Γ and the subtracted terms in an exact way. Then we sum over all possible diagrams with the same region specification as Eq. (3.45), with H having a fixed order N_h of α_s. Among them, the sum of those with the same subgraphs A, D and S but different H allows the use of Ward identity for the A and D collinear gluons. This factorizes the collinear gluons out of H, and simplifies Eq. (3.45) to

$$H^{(N_h)} \otimes \hat{T}_w \left[C_{A,n_1;m_1} \otimes S_{m_1,m_2} \otimes C_{D,n_2;m_2} \right], \tag{3.47}$$

where $\hat{T}_w$ is the same as $\hat{T}$ but just refers to the fact that the collinear gluons are now collected by two pairs gauge links. This is shown graphically in Fig. **??**. Eq. (3.47) applies to both terms in Eq. (3.46), so the factorized result also extends to the subtracted factors,

$$H^{(N_h)}_{\rm sub} \otimes \hat{T}_w \left[C_{A,n_1;m_1} \otimes S_{m_1,m_2} \otimes C_{D,n_2;m_2} \right]_{\rm sub}, \tag{3.48}$$

Now $H^{(N_h)}$ is only specified by two pairs of external amputated collinear quarks, at a given order N_h of α_s. Summing over H is then independent of the other factors, and each given H determines uniquely the subtracted terms within. So the sum over H yields the partially

factorized result,

$$H_{\rm sub} \otimes \hat{T}_w \left[C_{A,n_1;m_1} \otimes S_{m_1,m_2} \otimes C_{D,n_2;m_2} \right]_{\rm sub} , \tag{3.49}$$

which applies for any values of n_1 and n_2. Here

$$H_{\rm sub} = \sum_{N_h} \sum_i \left[H_i^{(N_h)} - (\text{subtraction for smaller regions}) \right] , \tag{3.50}$$

with $H_i^{(N_h)}$ denoting the i-th graph at N_h-th order for the two pairs of external collinear quarks.

Then we sum over all subdiagrams for A and D at a given order N_a and N_d of α_s, respectively, and for fixed n_1 and n_2. This allows the use of Ward identities for the soft gluons to factorize them out of the collinear subgraphs. Again, this applies to both A and D themselves and the subtracted terms therein, so we have

$$H_{\rm sub} \otimes \left[C^{(N_a)}_{A,n_1;{\rm sub}} \otimes S_{m_1,m_2} \otimes C^{(N_d)}_{D,n_2;{\rm sub}} \right] , \tag{3.51}$$

which is graphically shown in Fig. **??**, where the soft gluons are collected by two pairs of gauge links, one along w_A and the other along w_D. Then we can sum over n_1, n_2, N_a and N_d, independently. The result converts the two collinear factors into matrix element

definitions,

$$C^{\text{unsub}}_{A,\alpha\beta,ij}(k) = \int d^4z\, e^{ik\cdot z}\mathcal{P}_{A,\alpha\alpha'}\,\langle 0|\mathcal{T}\left\{\left[\Phi(\infty,z;\bar{w}_A)\psi_{1,\alpha'}(z)\right]_i \times\left[\bar{\psi}_{2,\beta'}(0)\Phi^\dagger(\infty,0;\bar{w}_A)\right]_j\right\}|\pi^+\rangle\bar{\mathcal{P}}_{A,\beta'\beta}, \tag{3.52a}$$

$$C^{\text{unsub}}_{D,\gamma\delta,mn}(l) = \int d^4z\, e^{-il\cdot z}\mathcal{P}_{D,\gamma\gamma'}\,\langle \pi^+|\mathcal{T}\left\{\left[\Phi(-\infty,0;\bar{w}_D)\psi_{2,\gamma'}(0)\right]_m \times\left[\bar{\psi}_{1,\delta'}(z)\Phi^\dagger(-\infty,z;\bar{w}_D)\right]_n\right\}|0\rangle\bar{\mathcal{P}}_{D,\delta'\delta}, \tag{3.52b}$$

where the subscript "unsub" means that these factors have not included the subtraction for smaller regions (where some of the lines go soft), $(\alpha,\beta,\gamma,\delta)$ are spinor indices, (i,j,m,n) are color indices in the fundamental representation, and we keep the general notations ψ_1 and ψ_2, which are u and d quark fields for π^+.

Sum over all possible soft subdigrams and over m_1 and m_2 can be done independently and converts it into a matrix element definition,

$$S_{i'i,j'j;m'm,n'n} = \langle 0|\mathcal{T}\left\{\Phi_{i'i}(0,-\infty;w_A)\Phi^\dagger_{jj'}(0,-\infty;w_A) \times\Phi^\dagger_{m'm}(\infty,0;w_D)\Phi_{nn'}(\infty,0;w_D)\right\}|0\rangle, \tag{3.53}$$

where the color indices (i,j,m,n) match the ones for the collinear factors in Eq. (3.52), and (i',j',m',n') are to contract with those of the hard factor $H_{i'j',m'n'}$. The soft subgraph contains no subtraction for smaller regions, so Eq. (3.53) is the final result.

Now for the same reason as Eq. (3.13), the collinear factors in Eq. (3.52) are color singlets, such that

$$C^{\text{unsub}}_{A,\alpha\beta,ij}(k) = \frac{1}{N_c}\delta_{ij}\,C^{\text{unsub}}_{A,\alpha\beta}(k), \quad C^{\text{unsub}}_{D,\gamma\delta,mn}(l) = \frac{1}{N_c}\delta_{mn}\,C^{\text{unsub}}_{D,\gamma\delta}(l), \tag{3.54}$$

and their contraction with the soft factor renders the latter into an identity matrix,

$$\delta_{ij}\, S_{i'i,j'j;m'm,n'n}\delta_{mn} = \delta_{i'j'}\delta_{m'n'}. \tag{3.55}$$

Hence all the exchanges of soft gluons are cancelled. This also applies to the subtraction terms in A and D subgraphs. Those smaller regions where some of the gluon lines turn soft are cancelled after summing over graphs. Therefore, the unsubtracted collinear factors in Eq. (3.52) are the same as the subtracted ones.

We note that the choices of lightlike vectors for the soft approximations in Eqs. (3.36) and (3.37) could have introduced rapidity divergences if the soft factor does not reduce to unity. In that case, one needs to choose some non-lightlike vectors to use in the soft approximations, which does not affect the result that $S = 1$. The cancellation of soft gluons for the exclusive processes is a direct result of the scattered particles being color singlets, which itself is the consequence of color confinement. This is in contrast to the inclusive processes, where soft cancellation is a result of unitarity, due to the sum over final states. If we also compare QCD to non-confined gauge theories like QED, the latter have bare charges that can emit and absorb soft (and/or collinear) gauge bosons (photons for QED), which can introduce corresponding divergences to the amplitudes. A finite cross section is achieved only after a proper sum over the final (and/or initial) states, as a result of unitarity. Hence, exclusive processes are only well defined for a confined gauge theory like QCD, but not for non-confined ones, where only inclusive processes are sensibly defined.

After a similar spinor and momentum decomposition as in Eqs. (3.14) and (3.16), we get

the factorized expression for the amplitude of $\pi^+ + e \to e + \pi^+$,

$$\mathcal{M}_{\pi^+ e\to e\pi^+} = \int_0^1 dx\, dy\, D_{u/\pi^+}(x,\mu)\bar{D}_{u/\pi^+}(y,\mu)\mathcal{H}\left(x,y;\frac{\vec{q}_T}{\sqrt{s}},\frac{q_T}{\mu}\right), \tag{3.56}$$

where we have used the multiplicative renormalization to convert each factor into the renormalized one. Here the two bare DAs are defined as

$$\begin{aligned} D^{\rm bare}_{u/\pi^+}(x) &= \int \frac{d\lambda}{2\pi}\, e^{i\lambda x p_1\cdot\bar{w}_A}\, \langle 0|\mathcal{T}\left\{\bar{\psi}_2(0)\frac{\gamma\cdot\bar{w}_A\gamma_5}{2}\Phi(0,\lambda\bar{w}_A;\bar{w}_A)\psi_1(\lambda\bar{w}_A)\right\}|\pi^+(p_1)\rangle, \\ \bar{D}^{\rm bare}_{u/\pi^+}(y) &= \int \frac{d\lambda}{2\pi}\, e^{-i\lambda y q_2\cdot\bar{w}_D}\, \langle \pi^+(q_2)|\mathcal{T}\left\{\bar{\psi}_1(\lambda\bar{w}_D)\frac{\gamma\cdot\bar{w}_D\gamma_5}{2}\Phi(\lambda\bar{w}_D,0;\bar{w}_D)\psi_2(0)\right\}|0\rangle, \end{aligned} \tag{3.57}$$

where the time ordering can be deleted, as in Eq. (3.19). It can be easily shown that the value of DA does not depend on the momentum direction of the hadron, and the final-state pion DA differs from the initial-state one by a complex conjugate,

$$\bar{D}_{u/\pi^+}(x) = \left[D_{u/\pi^+}(x)\right]^*, \tag{3.58}$$

which applies to both the bare and renormalized DAs. The hard coefficient is defined as the scattering of two pairs of collinear color-singlet quark and antiquark,

$$\mathcal{H}\left(x,y;\frac{\vec{q}_T}{\sqrt{s}},\frac{q_T}{\mu}\right) = \frac{1}{N_c^2}\left[\left(\frac{\gamma_5\gamma\cdot w_A}{2}\right)_{\alpha\beta} H_{\beta\alpha,\delta\gamma}\left(x,y;\frac{\vec{q}_T}{\sqrt{s}},\frac{q_T}{\mu}\right)\left(\frac{\gamma_5\gamma\cdot w_D}{2}\right)_{\gamma\delta}\right], \tag{3.59}$$

with subtraction for smaller region contributions.

Eq. (3.56) can be readily extended to other mesons and baryons, just with a proper change of the DA and hard coefficients [Lepage and Brodsky(1980)].

3.1.1.3 Choice of Glauber deformation for the double-meson process

In the discussion of Sec. 3.1.1.2, the contour deformation to get the soft gluon momentum k_s out of the Glauber region is symmetric with k_s^+ and k_s^-, as was employed for the Sudakov form factor in Sec. 2.6.2. This is, nevertheless, not the unique choice [Collins and Metz(2004)], as it is sufficient to get rid of the Glauber region as long as $|k_s^+ k_s^-| \gtrsim |k_{sT}^2|$. By examining the contour of k_s^+, we note that while all the k_s^+ poles from the D-collinear lines are of $\mathcal{O}(\lambda^2/Q)$ and lie on the same half plane, the poles from the A-collinear lines and soft lines are of order Q in the Glauber region. Hence one may choose to only deform the contour of k_s^+, but now by a magnitude of $\mathcal{O}(Q)$,

$$k_s^+ \mapsto k_s^+ + i\,\mathcal{O}(Q), \tag{3.60}$$

when k_s flows from D into S. This deforms a Glauber gluon momentum into the A-collinear region with the scaling $(Q, \lambda^2/Q, \lambda)$, and then one can perform usual approximations and apply Ward identities for the rest of the soft gluon momenta. In this way, although the Glauber region will not be treated accurately by the soft approximation, it will be by the collinear approximation.

The soft gluons factorized from D are attached to two Wilson lines along w_D, and the A-collinear longitudinally polarized gluons are collected by two Wilson lines along $\bar{w}_A$; both of the two sets of Wilson lines point to the future. Since we do not deform the contour of k_s^-, it does not matter what $i\varepsilon$ prescription we assign to the approximator $1/k_s^-$; the $+i\varepsilon$ choice leads to same result[3] as the symmetric deformation in Sec. 3.1.1.2, with soft Wilson lines along w_A and collinear Wilson lines along $\bar{w}_D$ both pointing from/to the past, but the

[3]Here k_s is the same as in Eq. (3.60), flowing from D to S and then to A.

$-i\varepsilon$ choice would have both point to the future.

Similarly, one may also choose to only deform k_s^- as $k_s^- \mapsto k_s^- - i\mathcal{O}(Q)$ when it flows out of A-collinear lines into S, and then the $i\varepsilon$ prescription for k^+ is not important as long as every k_s^- is associated with the same prescription as in $1/(k_s^- + i\varepsilon)$.

This gives some freedom in choosing the suitable $i\varepsilon$ prescriptions to achieve universal definitions for the soft factor and collinear factors when compared with other processes [Collins and Metz(2004)]. Within collinear factorization framework, the soft factor cancels no matter what prescription is used, and the Wilson lines associated with the collinear factors also become straight lines on the light cone due to unitarity of the Wilson lines, so that universality is a trivial property in the collinear factorization for exclusive processes. However, such freedom as in Eq. (3.60) is necessary for the factorization of diffractive processes, as we will discuss in Sec. 3.2.2.2.

3.1.2 Large-angle photon-meson scattering

For photon-meson scattering, the beam particle B stands for a photon. The final-state particles CD can take (1) $(CD) = (l^+l^-)$, (2) $(CD) = (\gamma\gamma)$, (3) $(CD) = (\gamma, \text{meson})$, or (4) $(CD) = (\text{meson}, \text{meson})$. The first three cases do not raise new issues in factorization, which we will briefly remark, while the last case requires a generalization of our factorization argument for the electron-meson scattering in Sec. 3.1.1.

3.1.2.1 Single-meson process: $(CD) = (l^+l^-)$ or $(\gamma\gamma)$.

For the dilepton or diphoton production, the color structure does not differ from the pion-photon transition in Sec. 3.1.1.1. The leading region in QCD thus takes the same form as

Fig. 3.1(b) with a mere change of external lines.

At LO in QED, the dilepton production happens via the decay of a timelike virtual photon of invariant mass $Q = m_{ll}$, as shown in Fig. **??**, so this process is probing the *timelike* meson-photon transition form factor [**?**]. This can only happen for a charge-neutral meson with an even charge-conjugation parity (C-even), such as π^0. In this case, the hard scale for factorization is provided by the high virtuality Q, which is guaranteed by the condition of large q_T. However, the factorization holds as long as $Q \gg \Lambda_{\rm QCD}$, even when q_T is small. Therefore, we have a factorization formula as Eq. (3.26), with the same DA definition and a proper change of the hard coefficient. The power suppressed correction is now $\mathcal{O}\big(\Lambda_{\rm QCD}/m_{ll}\big)$.

In contrast, for the diphoton production, all the three photons directly couple to the quark line, as shown by the LO diagram in Fig. **??**. In this case, the hard scale is necessarily provided by the large q_T. The same factorization cannot extend to the forward kinematic region. Now that the meson is coupled to three photons, such process can only happen to charge-neutral C-odd mesons, such as the ρ vector meson. Since we neglect the quark masses in the hard part, the collinear $q\bar{q}$ state from the meson must have zero helicity, so the vector meson must be longitudinally polarized. The factorization formula therefore is extended from Eq. (3.26) to

$$\mathcal{M}_{\rho_L\gamma\to\gamma\gamma} = \sum_q \int_0^1 dx\, D_{q/\rho_L}(x,\mu)\, \mathcal{H}_q\left(x; \frac{\vec{q}_T}{\sqrt{s}}, \frac{q_T}{\mu}\right) + \mathcal{O}\big(\Lambda_{\rm QCD}/q_T\big). \tag{3.61}$$

Here the bare DA defined as

$$D^{\rm bare}_{q/\rho_L}(x) = \int_{-\infty}^{\infty} \frac{d\lambda}{2\pi} e^{i\lambda x\, p_1\cdot n} \langle 0|\mathcal{T}\left\{\bar{\psi}_q(0)\frac{\gamma\cdot n}{2}\Phi(0,\lambda n; n)\psi_q(\lambda n)\right\}|\rho_L(p_1)\rangle, \tag{3.62}$$

with n the same as in Eq. (3.4), and the bare hard coefficient is the scattering $[q\bar{q}](p_1) + \gamma(p_2) \to \gamma(q_1) + \gamma(q_2)$, defined as

$$\mathcal{H}_q^{\text{bare}}\left(x; \frac{\vec{q}_T}{\sqrt{s}}\right) = (p_1 \cdot n)\frac{1}{N_c}\delta_{ij}\left(\frac{\gamma \cdot \bar{n}}{2}\right)_{\alpha\beta}\mathcal{H}_{\beta\alpha;ji}(x\hat{p}_1, (1-x)\hat{p}_1), \tag{3.63}$$

up to subtraction for smaller regions.

3.1.2.2 Double-meson process: $(CD) = (\gamma, \textbf{meson})$.

The photon-meson pair production has the same color structure as the elastic electron-meson scattering in Sec. 3.1.1.2, so the leading region differs from Fig. 3.3 only by changing the external electron lines by photon lines. By the same argument (including the soft-end suppression assumption), we can obtain a factorization formula like Eq. (3.56). However, we need to note that now the LO diagrams have both of the external photons attaching to the quark lines, such that there are three propagators in the hard part, as shown in Fig. **??**. The calculation of the hard coefficient thus becomes more involved, but it also has a richer structure.

First, for diagrams like Fig. **??**(b), the two photons attach to two different quark lines. The mediating gluon propagator is then not attached to two on-shell lines. As a result, it leads to a pole in the middle of the integration in the (x, y) convolution. This introduces an imaginary part to the amplitude even at LO. Second, as will be elaborated in the next section, the hard coefficient cannot factor into an (x, y) dependent factor and a q_T dependent factor. Their entanglement will lead to a nontrivial sensitivity to the x dependence of the DA.

3.1.2.3 Triple-meson process: $(CD) = (\text{meson}, \text{meson})$. Symmetric deformation.

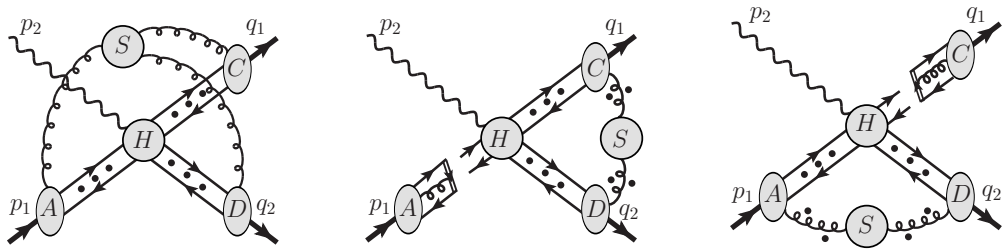

Fig. 3.5: (a) Leading-region graphs for the photoproduction of a light meson pair. There can be any numbers of soft gluons connecting S to each collinear subgraph. The regions with S connecting to one or more collinear subgraphs via quark lines or transversely polarized gluon lines are omitted. Depending on the quantum numbers, the collinear quark lines may be replaced by transversely polarized gluon lines. The dots represent arbitrary numbers of longitudinally polarized collinear gluons. (b) The result of factorizing the collinear subgraph A out of the hard subgraph H, with the soft gluons coupled to A canceled. (c) The result of factorizing the collinear subgraph C out of the hard subgraph H, with the soft gluons coupled to C canceled.

The process $M_A(p_1) + \gamma(p_2) \to M_C(q_1) + M_D(q_2)$ has three hadrons in three different directions, among them arbitrary soft gluon exchanges can happen. The leading region is shown in Fig. 3.5(a). The regions where the soft subgraph is connected to any two collinear subgraphs via quark lines or transversely polarized gluon lines are omitted, which are power suppressed by the soft-end suppression.

In such a three-meson process, each of the final-state mesons exchanges soft gluons with both initial-state and final-state mesons. This causes difficulty for a uniform contour deformation to get the soft gluons away from the Glauber regions. To put forward a formal discussion, we work in the CM frame and define some auxiliary vectors, by extending

Eq. (3.28),

$$
\begin{aligned}
w_A^\mu &= \frac{1}{\sqrt{2}}(1,\hat{z}), & \bar{w}_A^\mu &= \frac{1}{\sqrt{2}}(1,-\hat{z}),\\
w_C^\mu &= \frac{1}{\sqrt{2}}(1,\hat{n}) = \bar{w}_D^\mu, & \bar{w}_C^\mu &= \frac{1}{\sqrt{2}}(1,-\hat{n}) = w_D^\mu,
\end{aligned}
\tag{3.64}
$$

where $\hat{z}$ and $\hat{n}$ are normalized three-vectors along the directions of the initial-state meson M_A and final-state meson M_C. Basically, $w_{A,C,D}$ are the light-cone vectors along the directions of meson A, C and D, respectively, and the corresponding vectors with bars refer to the conjugate light-cone vectors along the opposite directions.

The essential point is that any soft gluon momentum k_s can be routed to only flow through two collinear subgraphs. For this, we introduce the notation $k_s^{(ij)}$ to be a soft gluon momentum that leaves the collinear subgraph i into S, then into the collinear subgraph j, through the hard subgraph H and back to i. Apparently, we have $k_s^{(ij)} = -k_s^{(ji)}$, with $i,j = A,C,D$ and $i \neq j$.

When considering the soft gluon momentum $k_s^{(ij)}$, we expand it in the w_i-w_j frame as defined in Eq. (9.20),[4]

$$
k_s^{(ij)} = w_i \frac{k_s^{(ij)} \cdot w_j}{w_i \cdot w_j} + w_j \frac{k_s^{(ij)} \cdot w_i}{w_i \cdot w_j} + k_{sT}^{(ij)} \,, \tag{3.65}
$$

where all the three terms on the right are of the same size, $\mathcal{O}(\lambda_s Q)$. When it flows in the collinear subgraph i, whose momenta are dominantly along w_i, the $k_s^{(ij)}$ can be approximated

[4]While we may define the plus and minus components in each w_i-w_j frame like Eqs. (9.20)-(3.31), having multiple such frames makes the notation cumbersome, so we stick to the covariant notations.

by only retaining the w_j component,

$$k_s^{(ij)} \simeq \hat{k}_s^{(ij)} = w_j \frac{k_s^{(ij)} \cdot w_i}{w_i \cdot w_j} \,. \tag{3.66}$$

Moreover, the coupling of this soft gluon to the collinear subgraph J^i can be approximated as

$$J^i_\mu(k_i, k_s^{(ij)})\, g^{\mu\nu}\, S_\nu(k_s^{(ij)}) \simeq J^i_\mu(k_i, \hat{k}_s^{(ij)})\, \frac{\hat{k}_s^{(ij)\mu}\, w_i^\nu}{k_s^{(ij)} \cdot w_i}\, S_\nu(k_s^{(ij)}) \,, \tag{3.67}$$

because it is the component g^{-+} of $g^{\mu\nu}$, which is given by $w_j^\mu w_i^\nu / w_i \cdot w_j$, that provides the dominant contribution. In Eq. (3.67), k_i stands for some collinear momentum in the subgraph i. This approximation will allow the use of Ward identity to factorize the soft gluons out of the collinear subgraphs.[5]

While this is a good approximation for the central soft region, it is not for the Glauber region in which

$$|k_s^{(ij)} \cdot w_i|\, |k_s^{(ij)} \cdot w_j| \ll |k_{sT}^{(ij)}|^2\, w_i \cdot w_j \,. \tag{3.68}$$

Now because all the collinear lines in the subgraph i or j only give poles for $k_s^{(ij)} \cdot w_i$ or $k_s^{(ij)} \cdot w_j$ on the same half complex plane, the integration contour of $k_s^{(ij)}$ is not pinched in the Glauber region, and a proper deformation can get it out of the Glauber region. However, if we take the symmetric deformation as in Eq. (2.77), we need to deform in opposite ways the soft momenta coupling A to C and those coupling D to C. Specifically, for $k_s^{(AC)}$, it receives poles on the upper half plane for both the component $k_s^{(AC)} \cdot w_A$ from A-collinear

[5] We should note that the argument given here is equivalent to Refs. [?, Nayak et al.(2005)Nayak, Qiu, and Sterman] that boost into the rest frame of two collinear subgraphs. The underlying reason is that any two distinct collinear subgraphs are well separated in rapidity; in the language here, it is $w_i \cdot w_j \simeq \mathcal{O}(1)$.

lines, and $k_s^{(AC)} \cdot w_C$ from C-collinear lines. So we need to deform its contour as

$$k_s^{(AC)} \mapsto k_s^{(AC)} - i\mathcal{O}(\lambda) w_C - i\mathcal{O}(\lambda) w_A, \tag{3.69}$$

following the expansion in Eq. (3.65). On the other hand, the soft momentum $k_s^{(DC)}$ has poles for $k_s^{(DC)} \cdot w_D$ on the lower half plane, so the deformation is

$$k_s^{(DC)} \mapsto k_s^{(DC)} + i\mathcal{O}(\lambda) w_C - i\mathcal{O}(\lambda) w_D. \tag{3.70}$$

While such sign difference is for different soft momentum attachments so does not pose any difficulty like a Glauber pinch, it does imply that a C-collinear longitudinally polarized gluon k_C has soft subtraction terms with different contour deformation. If we take k_C to flow from H to C, then we approximate k_C by

$$k_C \to \hat{k}_C = (k_C \cdot \bar{w}_C) w_C \tag{3.71}$$

in H, and its coupling to H by

$$H_\mu(k_H, k_C)\, g^{\mu\nu}\, J_\nu^C(k_C) \simeq H_\mu(k_H, \hat{k}_C)\, \frac{\hat{k}_C^\mu\, \bar{w}_C^\nu}{k_C \cdot \bar{w}_C}\, J_\nu^C(k_C)\,. \tag{3.72}$$

This introduces a pole at $k_C \cdot \bar{w}_C = 0$, which can potentially obstruct the deformations in Eqs. (3.69) and (3.70) in the soft subtraction terms. The latter would need to deform this denominator by

$$\Delta(k_C^{(A)} \cdot \bar{w}_C) = -i\mathcal{O}(\lambda) w_C \cdot \bar{w}_C - i\mathcal{O}(\lambda) w_A \cdot \bar{w}_C = -i\mathcal{O}(\lambda), \tag{3.73}$$

when k_C reaches the soft region and attaches to A, or by

$$\Delta(k_C^{(D)} \cdot \bar{w}_C) = +i\mathcal{O}(\lambda) w_C \cdot \bar{w}_C - i\mathcal{O}(\lambda) w_D \cdot \bar{w}_C = +i\mathcal{O}(\lambda), \tag{3.74}$$

when k_C reaches the soft region and attaches to D. Therefore, there is not a uniform $i\epsilon$ choice for the collinear gluon approximation [Eq. (3.72)] to respect the soft deformations in the corresponding subtraction terms.

To avoid this difficulty, we note that the collinear subgraph A only couples to final-state mesons by the soft gluons. So we can first factorize A out of the the hard part. To do that, we approximate all A-collinear momenta k_A by

$$k_A \to \hat{k}_A = (k_A \cdot \bar{w}_A) w_A \tag{3.75}$$

when they flow in H. We insert proper spinor or Lorentz projectors for the collinear quark or transversely polarized gluon lines. The coupling of each A-collinear longitudinally polarized gluon to H is approximated by

$$H_\mu(k_H, k_A)\, g^{\mu\nu}\, J_\nu^A(k_A) \simeq H_\mu(k_H, \hat{k}_A)\, \frac{\hat{k}_A^\mu\, \bar{w}_A^\nu}{k_A \cdot \bar{w}_A}\, J_\nu^A(k_A)\,. \tag{3.76}$$

By taking k_A to flow from H into A, the soft subtraction terms contain the regions $k_A = k_A^{(C)} \sim k_s^{(CA)}$ and $k_A = k_A^{(D)} \sim k_s^{(DA)}$. These require the deformations

$$\Delta k_A^{(C)} = +i\mathcal{O}(\lambda)(w_A + w_C), \quad \Delta k_A^{(D)} = +i\mathcal{O}(\lambda)(w_A + w_D), \tag{3.77}$$

which change the denominator $k_A \cdot \bar{w}_A$ in the collinear approximation [Eq. (3.76)] by

$$\Delta(k_A^{(C)} \cdot \bar{w}_A) = +i\mathcal{O}(\lambda), \quad \Delta(k_A^{(D)} \cdot \bar{w}_A) = +i\mathcal{O}(\lambda), \tag{3.78}$$

respectively. Therefore, it is possible to introduce a $+i\epsilon$ prescription to Eq. (3.76) to be compatible with such deformations. This leads to future-pointing Wilson lines along $\bar{w}_A$ to collect the A-collinear longitudinal gluons.

In contrast, it is easy to choose the $i\epsilon$ prescriptions for all soft gluons to make the approximation in Eq. (3.67) compatible with the deformations. We choose the $-i\epsilon$ when $i = A$ and $+i\epsilon$ when $i = C$ or D. As a result, the soft gluons attached to A will be collected by a pair of Wilson lines along w_A that come from the past infinity, and those attached to C (D) by a pair of Wilson lines along w_C (w_D) that go to the future infinity.

Then following the same procedure as Sec. 3.1.1.2, we can factorize the A subgraph out of H, and soft gluons out of A. This Ward-identity argument applies equally to the approximated region itself and to the subtracted smaller regions, to which the same approximator applied. Then because the meson M_A is a color singlet state, the same soft cancellation happens as Eqs. (3.54) and (3.55). That is, the two infinitely long Wilson lines associated with the A subgraph are joined to a connected one with a finite length, and the soft gluons coupling to A are cancelled. Although the argument in Eqs. (3.54) and (3.55) is for the whole Wilson lines to all orders, it applies to each finite perturbative order as well.

The result is shown in Fig. 3.5(b). The remaining gluons only couple to C and D, which are both in the final state. Then the symmetric deformation to get the gluons out of Glauber

region works in the same way as the Sudakov form factor in Eq. (2.77), namely,

$$k_s^{(CD)} \mapsto k_s^{(CD)} + i\mathcal{O}(\lambda)(w_D - w_C). \tag{3.79}$$

The following factorizations of collinear subgraphs and soft gluons work a similar way to the Sudakov form factor, so will not be repeated here. The resultant soft Wilson lines are cancelled in the same way as those coupling to A, as a result of M_C and M_D being color neutral mesons.

Therefore, we end up with the factorization result of the amplitude,

$$\mathcal{M}_{M_A\gamma\to M_C M_D} = \sum_{i,j,k} \int_0^1 dxdydz\, D_{i/A}(x,\mu)\, H_{i\gamma\to jk}\left(x,y,z;\frac{\vec{q}_T}{\sqrt{s}},\frac{q_T}{\mu}\right) \times \bar{D}_{j/C}(y,\mu)\,\bar{D}_{k/D}(z,\mu), \tag{3.80}$$

where the sum is over all possible parton flavors, and we have used the multiplicative renormalization of DAs to write each factor as the renormalized one. The hard coefficient H is the scattering of photon off a collinear pair of on-shell massless partons i, into two pairs of partons j and k. Note that the soft cancellation applies also to the subtractio.n terms in A, C, D, and H, so the unsubtracted DA factors are the same as the subtracted ones, and the H only contains collinear subtractions. The operator definitions for the (bare) DAs can be written in a similar way as Eq. (3.57) for pseudoscalar mesons. The DAs for other kinds of mesons can be extended straightforwardly.

3.1.2.4 Triple-meson process: $(CD) = (\text{meson}, \text{meson})$. Asymmetric deformation.

The factorization procedure for the process $M_A + \gamma \to M_C + M_D$ is based on the symmetric deformation. Its feasibility relies on there only being one collinear subgraph A in the initial state, which only exchanges soft gluons with final-state particles. The strategy does not apply to the process $M_A + M_B \to M_C + M_D$ which involves two widely separated mesons in both initial and final states. On the other hand, we cannot extend the proof to the single diffractive case where the meson M_A is replaced by a diffracted hadron h, which enters the hard interaction with γ but also produces another hadron h' in the nearly forward direction. As we will see in Sec. **??**, there exists a kinematic region where the momentum component $k_s \cdot w_A$ is pinched in the Glauber region when the soft gluon k_s is exchanged between the diffracted hadron and final-state mesons. It then forbids the symmetric deformation such as Eq. (3.69). Therefore, a different approach is needed for extending the proof. Now, we explore the possibility of asymmetric deformation.

Given the above consideration of allowing to generalize the factorization proof to the single diffractive process, we choose not to deform the contour of $k_s^{(Aj)} \cdot w_A$ when a soft momentum $k_s^{(Aj)}$ flows in the A-collinear subgraph, and will instead try to factorize soft interactions from the collinear subgraphs C and D.

The needed deformations can be motivated by examining a single soft gluon exchange between different collinear subgraphs. We first consider the collinear subgraph C that has one soft gluon $k_s^{(CA)}$ and $k_s^{(CD)}$ exchange with the A-collinear subgraph and D-collinear subgraph, respectively. Since $k_s^{(CA)}$ flows in C in the same direction as the C-collinear lines,

the poles of $k_s^{(CA)} \cdot w_C$ are all on the lower half plane, so we deform the contour of $k_s^{(CA)}$ by

$$k_s^{(CA)} \to k_s^{(CA)} + i\, w_A\, \mathcal{O}(Q)\,, \tag{3.81}$$

when it is in the Glauber region, similar to Eq. (3.60). Similarly, we deform the contour of $k_s^{(CD)}$ by

$$k_s^{(CD)} \to k_s^{(CD)} + i\, w_D\, \mathcal{O}(Q)\,. \tag{3.82}$$

Such deformations get the soft gluon momenta from the Glauber region all the way into the A or D collinear region, which will be properly treated by collinear approximations.

In order for the approximator in Eq. (3.67) not to obstruct such deformations, we modify it to

$$J_\mu^C(k_C, k_s^{(CA)})\, g^{\mu\nu}\, S_\nu(k_s^{(CA)}) \simeq J_\mu^C(k_C, \hat{k}_s^{(CA)})\, \frac{\hat{k}_s^{(CA)\mu}\, w_C^\nu}{k_s^{(CA)} \cdot w_C + i\varepsilon}\, S_\nu(k_s^{(CA)})\,, \tag{3.83a}$$

$$J_\mu^C(k_C, k_s^{(CD)})\, g^{\mu\nu}\, S_\nu(k_s^{(CD)}) \simeq J_\mu^C(k_C, \hat{k}_s^{(CD)})\, \frac{\hat{k}_s^{(CD)\mu}\, w_C^\nu}{k_s^{(CD)} \cdot w_C + i\varepsilon}\, S_\nu(k_s^{(CD)})\,, \tag{3.83b}$$

where only the relevant arguments are written explicitly. Both approximations in Eq. (3.83) have the structure

$$J_\mu^C(k_C, k_s)\, g^{\mu\nu}\, S_\nu(k_s) \simeq J_\mu^C(k_C, \hat{k}_s)\, \frac{\hat{k}_s^\mu\, w_C^\nu}{k_s \cdot w_C + i\varepsilon}\, S_\nu(k_s)\,, \tag{3.84}$$

where the structure $\hat{k}_s^\mu\, J_\mu^C(k_C, \hat{k}_s)$ allows the use of Ward identity in a uniform way, no matter which other collinear subgraph k_s flows through. The $+i\varepsilon$ choice will lead to future-pointing soft Wilson lines.

Now we consider the collinear longitudinally polarized gluons attaching C to H. Similarly,

the approximation can be obtained by examining a single gluon, whose momentum k_C flows from H into C and can be expanded in the w_C-$\bar{w}_C$ frame,

$$k_C = w_C \,(k_C \cdot \bar{w}_C) + \bar{w}_C \,(k_C \cdot w_C) + k_{C,T}\,, \tag{3.85}$$

where among the three terms on the right, the w_C component dominates and scales as $\mathcal{O}(Q)$. Then we approximate k_C in H by

$$k_C \to \hat{k}_C = w_C \,(k_C \cdot \bar{w}_C)\,, \tag{3.86}$$

and the coupling of the collinear gluon to H by

$$H_\mu(k_H, k_C)\, g^{\mu\nu}\, J_\nu^C(k_C) \simeq H_\mu(k_H, \hat{k}_C)\, \frac{\hat{k}_C^\mu\, \bar{w}_C^\nu}{k_C \cdot \bar{w}_C - i\varepsilon}\, J_\nu^C(k_C)\,, \tag{3.87}$$

where only the relevant argument dependence is written explicitly and k_H stands for some hard momentum in H.

The $-i\varepsilon$ in Eq. (3.87) is chosen in order to be compatible with the deformations in Eqs. (3.81) and (3.82). Even though we are approximating the collinear region, which does not suffer from the Glauber region problem, Eq. (3.87) is applied to the whole diagram with deformed contours. Furthermore, the same gluon k_C considered in Eq. (3.87) can also go into the soft region, attaching to A- or D-collinear subgraph, for which we will change the notation k_C to $k_C^{(A)}$ or $k_C^{(D)}$,whose contribution has already been included in the soft approximations defined in Eq. (3.83). A subtraction is needed from Eq. (3.87) to avoid such double counting, which is obtained by first applying the soft approximation [Eq. (3.83)] and then applying the collinear approximation [Eq. (3.87)]. Since the subtraction mixes the collinear and soft

approximations for the same gluons, and the latter require deformation of contours, we do need the $i\varepsilon$ prescription in Eq. (3.87) not to obstruct the contour deformations in Eqs. (3.81) and (3.82). Since we need the deformations[6]

$$\Delta k_C^{(A)} = -i\, w_A\, \mathcal{O}(Q), \quad \Delta k_C^{(D)} = -i\, w_D\, \mathcal{O}(Q), \tag{3.88}$$

which means that the denominator in Eq. (3.87) needs to be compatible with the deformations

$$\begin{aligned} \Delta k_C^{(A)} \cdot \bar{w}_C &= -i\,(w_A \cdot \bar{w}_C)\,\mathcal{O}(Q) = -i\,\mathcal{O}(Q)\,, \\ \Delta k_C^{(D)} \cdot \bar{w}_C &= -i\,(w_D \cdot \bar{w}_C)\,\mathcal{O}(Q) = 0\,. \end{aligned} \tag{3.89}$$

This explains the $-i\varepsilon$ choice in Eq. (3.87). After applying Ward identity, it leads to collinear Wilson lines pointing to the past.

Eqs. (3.83) and (3.87) constitute the needed approximations related to the collinear subgraph C. Even though we only considered a single soft or collinear gluon connection, they generalize to multiple gluon connections in an obvious way: one just applies Eq. (3.83) to every soft gluon connecting C to A or D, and (3.87) to every collinear longitudinally polarized gluon connecting H to C. Then by applying suitable on-shell projections to the C-collinear quark lines or transversely polarized gluon lines, and summing over all possible attachments of the collinear gluons, we can factorize the collinear longitudinally polarized gluons out of the hard part H onto two Wilson lines along $\bar{w}_C$ pointing to the past, and the soft gluons out of C onto two Wilson lines along w_C pointing to the future.

[6]Note that now the soft momentum direction is reversed compared to the convention of $k_s^{(CA)}$ and $k_s^{(CD)}$, which are used in Eqs. (3.81) and (3.82).

We should note that by choosing lightlike auxiliary vectors w_C in the soft approximation Eq. (3.83), the resultant soft factor contains rapidity divergences. This can be remedied by a different vector n_C that differs from w_C by being slightly off light cone, as in Refs. [Collins(2013), Qiu and Yu(2022)] for example, which does not affect the argument. Since the soft gluons eventually cancel whether we use w_C or n_C, the problem of rapidity divergence does not affect our argument of collinear factorization, and we will simply use the lightlike vector w_C.

The subsequent argument follows the same line as Secs. 3.1.1.2 and 3.1.2.3. By the color neutrality of M_C, the soft gluons factorized out of C are cancelled order by order, which is proved by identifying the Wilson line structure that they form. This reduces the graph in Fig. 3.5(a) to the partly factorized one in Fig. 3.5(c), in which only the two collinear subgraphs A and D are coupled to the hard subgraph H, and the soft subgraph S is only coupled to A and D subgraphs.

With the C-collinear subgraph factorized out, the leading-region graph in Fig. 3.5(c) is similar to that in Fig. 3.3(a), whose factorization is shown in Sec. 3.1.1.2. Again, in the treatment of the soft region, one only needs to deform the contour of soft gluon $k_s^{(DA)}$ by

$$k_s^{(DA)} \to k_s^{(DA)} + i\, w_A\, \mathcal{O}(Q), \tag{3.90}$$

regardless of the poles of $k_s^{(DA)} \cdot w_A$ provided by the A-collinear propagators. By the same argument as for the C subgraph, the soft gluons coupling to D are canceled, and the D subgraph is factorized out of H into the DA for M_D. Then the soft gluons are only coupled to the A subgraph and no longer pinched. They can then be deformed into the A-collinear region and grouped into a part of A-collinear subgraph, which can be further factorized from

H into the DA of the M_A.

The soft cancellation applies equally to the subtracted terms for smaller regions, so this procedure leads to the same factorization in Eq. (3.80). Even though the Wilson lines associated with the collinear factors point to different directions from the ones in Sec. 3.1.2.3 with symmetric deformations, due to the cancellation of soft gluons, the Wilson line pair for each collinear factor join together into a finite-length Wilson line, with the segments pointing to infinity cancelled. So, the resultant DA definitions are universal and do not depend on the specific deformation ways. This is a property of collinear factorization.

3.1.3 Large-angle meson-meson scattering

For meson-meson scattering, the beam particle B is also a meson. The final-state particles CD can take (1) $(CD) = (l^+l^-)$, (2) $(CD) = (\gamma\gamma)$, (3) $(CD) = (\gamma, \text{meson})$, or (4) $(CD) = (\text{meson}, \text{meson})$. The first three cases do not raise new issues in factorization, which we will briefly remark on, and the last case only requires a simple generalization of our factorization argument for the photon-meson scattering in Sec. 3.1.2.4.

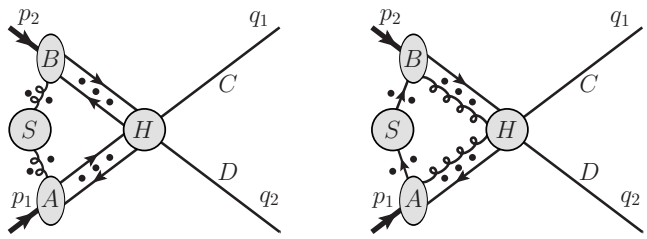

Fig. 3.6: Leading regions of the exclusive scattering process $M_A(p_1)+M_B(p_2) \to C(q_1)D(q_2)$, with (CD) being colorless particles, (l^+l^-) or $(\gamma\gamma)$. The quark lines can be replaced by transversely polarized gluons, and the dots refer to arbitrary numbers of gluon lines with longitudinally polarized gluons.

3.1.3.1 Double-meson process: $(CD) = (l^+l^-)$ or $(\gamma\gamma)$.

The processes $M_A M_B \to l^+l^-$ and $M_A M_B \to \gamma\gamma$ have similar color structures as the meson electroproduction (discussed in Sec. 3.1.1.2) and photoproduction (discussed in Sec. 3.1.2.2), respectively, except that both mesons are now in the initial state. They thus have similar leading regions, as shown in Fig. 3.6, where the final-state lines refer to colorless particles, $(CD) = (l^+l^-)$ or $(\gamma\gamma)$. As usual, the region (b) is assumed to be power suppressed by the soft-end suppression.

At LO in QED, the dilepton production happens via the production and decay of a time-like virtual photon of invariant mass $Q = m_{ll}$. An example is $\pi^+\pi^-(\to \gamma^*) \to l^+l^-$. This property means that it is the invariant mass Q that provides the hard scale for factorization, regardless of the transverse momentum q_T of the leptons, similar to the dilepton photoproduction in Sec. 3.1.2.1. On the other hand, in the diphoton production, both photons directly attach to the quark parton lines, and the large q_T is necessary for factorization. Examples are $\pi^+\pi^- \to \gamma\gamma$ or $\pi^0\pi^0 \to \gamma\gamma$.

Factorization for the region (a) works in a similar way to the meson electroproduction and photoproduction discussed before. One can use either symmetric or asymmetric deformation to avoid the Glauber region. They give different soft and collinear Wilson lines in intermediate steps, but result in the same soft cancellation and the same collinear factor definitions, as a property of collinear factorization. The asymmetric deformation is particularly important for later generalization to single diffractive scattering. For a soft gluon momentum k_s flowing from B to A, we first expand it as

$$k_s = \frac{k_s \cdot w_A}{w_A \cdot w_B} w_B + \frac{k_s \cdot w_B}{w_A \cdot w_B} w_A + k_{sT}, \tag{3.91}$$

with w_A defined as in Eq. (3.64) and $w_B = \bar{w}_A$ in the CM frame, and deform its contour by

$$k_s \mapsto k_s - i\mathcal{O}(Q) w_A. \tag{3.92}$$

This then determines all necessary $i\epsilon$ prescriptions for the soft and collinear approximations.

In the end, we get a factorization formula for the scattering amplitude,

$$\begin{aligned}&\mathcal{M}_{M_A M_B \to l^+ l^-/\gamma\gamma} \\ &\quad = \sum_{i,j} \int_0^1 dx dy\, D_{i/A}(x,\mu)\, D_{j/B}(y,\mu)\, H_{ij\to l^+l^-/\gamma\gamma}\left(x, y; \frac{\vec{q}_T}{\sqrt{s}}, \frac{q_T}{\mu}\right),\end{aligned} \tag{3.93}$$

where the DAs are for initial-state meson annihilations, and the hard coefficient H is for the scattering of two pairs of collinear partons i and j into l^+l^- or $\gamma\gamma$. We have used their multiplicative renormalization to convert each factor to renormalized ones, which introduces the factorization scale μ.

3.1.3.2 Triple-meson process: $(CD) = (\gamma, \textbf{meson})$.

The triple-meson process $M_A M_B \to \gamma M_D$ exactly resembles the meson pair photoproduction in Secs. 3.1.2.3 and 3.1.2.4, just with the exchange of the photon and one meson. As there, both symmetric and asymmetric deformation are applicable to deal with the Glauber region. The symmetric one starts with the factorization of D-collinear subgraph, which reduces the leading region to Fig. 3.6, discussed in Sec. 3.1.3.1. The asymmetric deformation keeps intact the soft gluon momentum components flowing along A-collinear subgraph, but deforms the other components in B or D collinear subgraphs by an order of Q. The soft gluons cancel in both cases as a result of the mesons being color neutral. Finally, the amplitude is factorized

into

$$\mathcal{M}_{M_A M_B \to \gamma M_D} = \sum_{i,j,k} \int_0^1 dx dy dz\, D_{i/A}(x,\mu) D_{j/B}(y,\mu) \times H_{ij\to\gamma k}\left(x, y, z; \frac{\vec{q}_T}{\sqrt{s}}, \frac{q_T}{\mu}\right) \bar{D}_{k/D}(z,\mu). \tag{3.94}$$

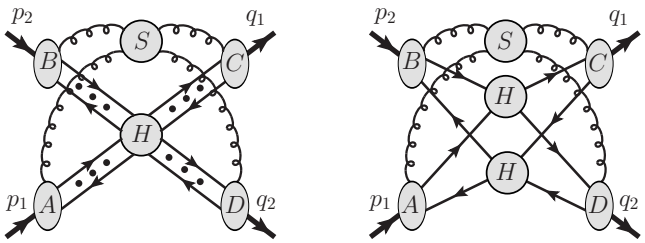

(a) (b)

Fig. 3.7: Leading regions of the exclusive scattering process $M_A(p_1)+M_B(p_2) \to C(q_1)D(q_2)$, with (CD) being colorless particles, (l^+l^-) or $(\gamma\gamma)$. The quark lines can be replaced by transversely polarized gluons, and the dots refer to arbitrary numbers of gluon lines with longitudinally polarized gluons.

3.1.3.3 Quadruple-meson process: $(CD) = (\textbf{meson}, \textbf{meson})$.

The quadruple-meson process $M_A M_B \to M_C M_D$ has two collinear sectors in both initial and final states. The leading region is shown in Fig. 3.7(a). The symmetric deformation out of Glauber region does not trivially apply, as explained in Sec. 3.1.2.3. So we will simply employ the asymmetric deformation in Sec. 3.1.2.4.

For a soft gluon momentum $k_s^{(Cj)}$ flowing from the collinear subgraph C to some other one j, we expand it as

$$k_s^{(Cj)} = \frac{k_s^{(Cj)} \cdot w_C}{w_C \cdot w_j} w_j + \frac{k_s^{(Cj)} \cdot w_j}{w_C \cdot w_j} w_C + k_{sT}. \tag{3.95}$$

When it flows through the C-collinear subgraph, we approximate it by

$$k_s^{(Cj)} \mapsto \hat{k}_s^{(Cj)} = \frac{k_s^{(Cj)} \cdot w_C}{w_C \cdot w_j} w_j. \tag{3.96}$$

This component receives poles from the C-collinear lines, which are all on the lower half plane. So we choose to deform its contour by

$$k_s^{(Cj)} \mapsto k_s^{(Cj)} + i\mathcal{O}(Q) w_j. \tag{3.97}$$

Thus its coupling to the C-collinear subgraph is approximated by

$$J_\mu^C(k_c, k_s^{(Cj)})\, g^{\mu\nu}\, S_\nu(k_s^{(Cj)}) \mapsto J_\mu^C(k_c, \hat{k}_s^{(Cj)})\, \frac{\hat{k}_s^{(Cj)\,\mu} w_C^\nu}{k_s^{(Cj)} \cdot w_C + i\epsilon}\, S_\nu(k_s^{(Cj)}). \tag{3.98}$$

This will allow use of Ward identity to factorize soft gluons out of J^C into a pair of Wilson lines along w_C pointing into the future.

For a C-collinear momentum k_C, we expand it as

$$k_C = (k_C \cdot w_C)\bar{w}_C + (k_C \cdot \bar{w}_C) w_C + k_{C,T}, \tag{3.99}$$

and only keep the large component $k_C \cdot \bar{w}_C$ in the hard part H,

$$k_C \mapsto \hat{k}_C = (k_C \cdot \bar{w}_C) w_C. \tag{3.100}$$

The coupling of a collinear longitudinally polarized gluon k_C to H is approximated by

$$H_\mu(k_H;k_C)\,g^{\mu\nu}\,J^C_\nu(k_C) \mapsto H_\mu(k_H;\hat{k}_C)\,\frac{\hat{k}^\mu_C \bar{w}^\nu_C}{k_C\cdot\bar{w}_C - i\epsilon}\,J^C_\nu(k_C), \tag{3.101}$$

for k_C to flow from H into J^C. The $-i\epsilon$ is uniquely determined to be compatible with the deformation [Eq. (3.97)], given the need of soft subtraction. This will lead to a pair of past-pointing Wilson lines along $\bar{w}_C$ to collect all C-collinear gluons with longitudinal polarization.

After factorizing C-collinear subgraph from H, and soft gluons out of C, one can easily identify the soft Wilson lines as an identity by the color neutrality of the meson M_C. This soft cancellation applies to both the approximated region and the subtracted smaller regions. Thus we have a factorized DA for M_C, whose unsubtracted version is the same as the soft subtracted one, convoluted with the rest of the graph, which has the same color structure as the triple-meson process $M_AM_B\to\gamma M_D$ in Sec. 3.1.3.2 and which factorizes in the same manner. All the soft deformations leave the components $k_s\cdot w_A$ unchanged. Eventually, we have the factorized expression for the amplitude,[7]

$$\begin{aligned}\mathcal{M}_{M_AM_B\to M_CM_D} = \sum_{i,j,k,l}\int_0^1 dxdydzdw\, D_{i/A}(x,\mu)D_{j/B}(y,\mu)\\ \times H_{ij\to kl}\left(x,y,z,w;\frac{\vec{q}_T}{\sqrt{s}},\frac{q_T}{\mu}\right)\bar{D}_{k/C}(z,\mu)\bar{D}_{l/D}(w,\mu),\end{aligned} \tag{3.102}$$

where the sum is over all parton flavors and their spin structures, and the hard coefficient H is the scattering of two pairs of collinear partons i and j into another two pairs k and l. Again, the hard coefficient contains subtraction of collinear regions for each of the four

[7] Note the symbol D has been used to denote both the DA and the particle D in the $2\to2$ scattering, which should not cause confusion.

mesons, and we have used the multiplicative renormalization of DAs to convert all factors into renormalized ones, which introduced the factorization scale μ.

The leading regions that contain soft quark or physically polarized gluon lines to directly couple any of the collinear subgraphs to the soft subgraph are assumed to be power suppressed, by the same soft-end suppression assumption that applies to all the processes discussed before. However, for the quadruple-meson scattering process, there is one different type of regions that have more leading power counting. This is given by the reduced diagram [Fig. 3.7(b)] that has two separated hard scattering subgraphs. **[ZT: Give some comments.]** Discussion of such multiple hard scattering case is beyond the scope of this paper, for which we refer to [Landshoff(1974), Botts and Sterman(1989)]. In this paper, we assume that all processes are dominated by one single hard scattering.

3.2 Single diffractive hard exclusive processes

Now we generalize the $2 \to 2$ large-angle meson scattering processes by allowing one extra hadron h' in the final state along the direction of one of the initial-state hadrons h. The extra hadron h' is the *diffraction* of the initial-state hadron h. To allow perturbative QCD study, we further require a hard scale in the scattering process, so we take the two particles C and D in the final state to have hard transverse momentum q_T, with respect to the collision axis. Thus the minimal configuration we study is a generic $2 \to 3$ process that we call *single diffractive hard exclusive process* (SDHEP),

$$h(p) + B(p_2) \to h'(p') + C(q_1) + D(q_2), \tag{3.103}$$

where h of momentum p is the hadron we would like to study, B of momentum p_2 is a colliding lepton, photon or meson, and C and D of momentum q_1 and q_2, respectively, are two final-state particles, which can be a lepton, photon or meson, with large transverse momenta,

$$q_{1T} \sim q_{2T} \gg \sqrt{-t}\,, \tag{3.104}$$

with $t \equiv (p - p')^2$. In the lab frame with h along $+\hat{z}$ and B along $-\hat{z}$, the scattering configuration is illustrated in Fig. 3.8(a).

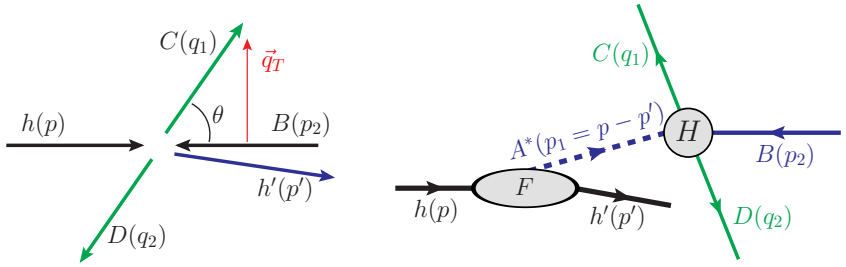

Fig. 3.8: (a) Illustration of the kinematic configuration of the SDHEP in the lab frame. (b) The two-stage paradigm of the SDHEP.

There are two distinct scales involved in the SDHEP, one soft scale $\sqrt{-t}$ characterizing the diffraction subprocess, and one hard scale $Q = \mathcal{O}(q_T)$ characterizing the production of the particles C and D. Then the SDHEP can be pictured as a two-stage process, as shown in Fig. 3.8(b), being a combination of a diffractive production of a single long-lived state $A^*(p_1)$,

$$h(p) \to A^*(p_1) + h'(p'), \quad \text{with } p_1 = p - p', \tag{3.105}$$

and a hard exclusive $2 \to 2$ scattering between the two nearly head-on states $A^*(p_1)$ and $B(p_2)$,

$$A^*(p_1) + B(p_2) \to C(q_1) + D(q_2). \tag{3.106}$$

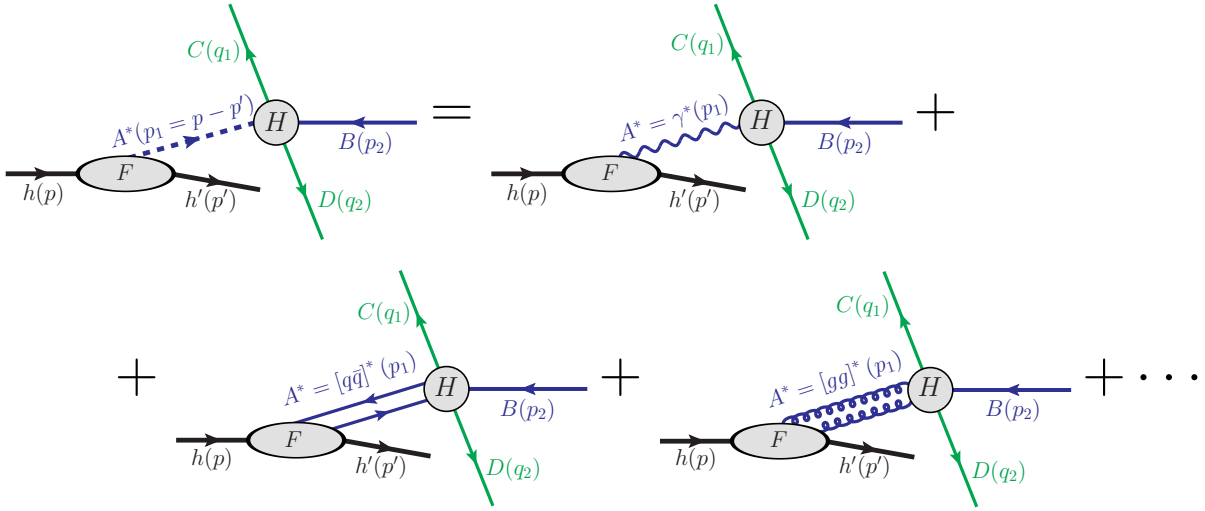

Fig. 3.9: The representation of the SDHEP in terms of all possible exchanged channels of the virtual state $A^*(p_1)$ between the single diffractive $h \to h'$ transition and the $2 \to 2$ hard exclusive process. The two gluons in gg channel have physical polarizations. The $q\bar{q}$ and gg channels can be accompanied by arbitrary numbers of collinear longitudinally polarized gluons. The "$\cdots$" refers to the channels with more than two physically polarized partons, which are power suppressed compared to the two-parton case.

In the CM frame of A^* and B, as a necessary condition for the factorization, the transverse momentum q_T of C or D is required to be much greater than the invariant mass of A^* or B.

The $2 \to 2$ hard exclusive process H in Fig. 3.8(b) takes place at a short distance $1/Q \ll 1/\Lambda_{\rm QCD} \sim 1 \sim$ fm and is sensitive to the partonic structure of the exchanged state $A^*(p_1)$. The scattering amplitude of the SDHEP should include a sum of all possible partonic states, as illustrated in Fig. 3.9, which can be schematically described as

$$\mathcal{M}_{hB\to h'CD} = \sum_{n=1}^{\infty} \sum_{f} F^{fn}_{h\to h'}(p,p') \otimes C_{fnB\to CD}, \tag{3.107}$$

where n and f represent the number and flavor of particles included in the exchanged state A^*, respectively, $F^{fn}_{h\to h'}(p,p')$ is a "form factor" responsible for the $h \to h'$ transition, and $C_{fnB\to CD}$ represents the scattering amplitude of the hard part H, along with the sum

running over all possible exchanged states characterized by n and f. For the discussion in this paper, we keep the scattering amplitude $C_{f_n B\to CD}$ at the lowest order in the QED coupling constant for given exchanged state f_n and particle types of B, C, and D, while we explore contributions from QCD at all orders in its coupling constant.

For $n = 1$, the only possible case is a virtual photon exchange, i.e., $f_1 = \gamma^*$, which is like the Bethe-Heitler process for the DVCS (see [Ji(1997a)] for example). Instead of probing the partonic structure of h, this channel only gives an access to the electromagnetic form factor of h evaluated at a relatively soft scale t. As discussed below, the γ^*-mediated subprocess gives the "superleading power" background for the $n \geq 2$ channels, and should not be excluded even if they are suppressed by higher orders of QED coupling, unless it is forbidden by the symmetry. The scattering amplitude of the SDHEP should be expanded in inverse powers of the hard scale, and then followed by a perturbative factorization for the leading power contribution (and subleading power contribution if needed, see, e.g., [Kang et al.(2014)Kang, Ma, Qiu, and Sterman]). If the $n = 1$ subprocess is forbidden (as discussed below), then the scattering amplitude of the SDHEP starts with $n = 2$ subprocesses.

For $n = 2$, we can have QCD subprocesses with $f_2 = [q\bar{q}']$ or $[gg]$. This gives the leading-power contribution that, as shown in the following subsections, can be factorized into GPDs with corresponding hard coefficients. The channels with $n \geq 3$ belong to high-twist subprocesses that are suppressed by powers of $\sqrt{-t}/Q$ and will be neglected in the following analysis.

3.2.1 General discussion of the γ^*-mediated channel

Before providing the detailed arguments for QCD factorization of SDHEPs, initiated by a lepton, photon or meson beam, respectively, in next three subsections, we give a general discussion for the γ^*-mediated hard subprocesses, corresponding to the $n = 1$ channel in Eq. (3.107), independent of the particle types of B, C and D. More detailed discussion for specific processes will be given in later sections.

One difference between the $n = 1$ and $n \geq 2$ subprocesses is that the virtual photon momentum is fully determined by the diffraction of the hadron h. The amplitude of the γ^*-mediated subprocess can be trivially factorized into the electromagnetic form factor of the hadron h,

$$\begin{aligned}\mathcal{M}^{(1)} &= \frac{ie^2}{t}\langle h'(p')|J^\mu(0)|h(p)\rangle\,\langle C(q_1)D(q_2)|J_\mu(0)|B(p_2)\rangle \\ &\equiv \frac{ie^2}{t}F^\mu(p,p')\,\mathcal{H}_\mu(p_1,p_2,q_1,q_2),\end{aligned} \tag{3.108}$$

where the superscript "(1)" refers to the contribution to the SDHEP amplitude from the $n = 1$ channel, and $J^\mu = \sum_{i\in q} Q_i\bar{\psi}_i\gamma^\mu\psi_i$ is the electromagnetic current of quarks, summing over flavor "i" and weighted by their fractional charges Q_i. We defined the form factor,

$$F^\mu(p,p') = \langle h'(p')|J^\mu(0)|h(p)\rangle = F_1^h(t)\,\bar{u}(p')\gamma^\mu u(p) + F_2^h(t)\,\bar{u}(p')\frac{i\sigma^{\mu\nu}p_{1\nu}}{2m_h}u(p), \tag{3.109}$$

which has the leading component $F^+ \sim \mathcal{O}(Q)$ as the h-h' system is highly boosted along $\hat{z}$ direction.[8] However, when this component is contracted with $\mathcal{H}_\mu$, which scales as $\mathcal{O}(Q^0)$

[8] We define the light-front components of a vector $V^\mu = (V^+, V^-, \boldsymbol{V}_T)$ as $V^\pm = (V^0 \pm V^3)/\sqrt{2}$ and $\boldsymbol{V}_T = (V^1, V^2)$.

for each component, we have

$$F^+\mathcal{H}^- = \frac{1}{p_1^+}\,F^+\left(p_1^+\,\mathcal{H}^-\right) = \frac{1}{p_1^+}\,F^+\left(p_1\cdot\mathcal{H} + \boldsymbol{p}_{1T}\cdot\boldsymbol{\mathcal{H}}_T - p_1^-\mathcal{H}^+\right), \tag{3.110}$$

where in the bracket, the first term vanishes by the Ward identity of QED, and the other two scale as $\sqrt{-t}$ and t/p_1^+ respectively. So the leading power of $F\cdot\mathcal{H}$ scales as $\sqrt{-t}$ and is given by the transverse polarization of the virtual photon. Therefore, the power counting of $\mathcal{M}^{(1)}$ is of the order $1/\sqrt{-t}$, which is higher than the $n=2$ channel by one power of $Q/\sqrt{-t}$.

One caution should be noted that it is not appropriate to only keep p_1^+ in the amplitude $\mathcal{H}_\mu(p_1,p_2,q_1,q_2)$ because the approximation introduces an error of order $\sqrt{-t}/Q$. While this is power suppressed comparing to the leading contribution from the $n=1$ channel, it could scale at the same order as the contribution from the $n=2$ channel since both of them have the power counting $1/Q$. By neglecting all the $n\geq 3$ channels, our approximation to the full SDHEP amplitude is up to the error at $\mathcal{O}\big(\sqrt{-t}/Q^2\big)$, so that the $1/Q$ part should be kept as exact when evaluating the contribution from the $n=1$ channel.

We note one further subtlety of the case when the γ^*-mediated subprocess involves light mesons in $\mathcal{H}$. The conventional practice is to factorize it into meson distribution amplitudes (DAs). While this is true to the leading power at $\mathcal{O}\big(1/\sqrt{-t}\big)$, it neglects the power correction of $\mathcal{O}\big(\Lambda_{\rm QCD}/Q\big)\cdot\mathcal{O}\big(1/\sqrt{-t}\big) = \mathcal{O}(1/Q)$, which is of the same order as the $n=2$ channels, i.e., the GPD channels. Keeping the exact $1/Q$ contribution thus requires the subleading-power (or, twist-3) factorization for the γ^*-mediated subprocess that involves any mesons, which is beyond the scope of this paper.

There are two cases in which the γ^*-channel is forbidden. The first is for a flavor-changing

channel with $h \neq h'$ that cannot be achieved by the electromagnetic interaction, like the pion-nucleon scattering processes in [Berger et al.(2001)Berger, Diehl, and Pire, Qiu and Yu(2022)] which can involve the proton-neutron transition. The second case is for particular combinations of the particle types of B, C and D that require $\mathcal{H}_\mu(p_1, p_2, q_1, q_2) = 0$ by some symmetries. Apart from these two cases, we should generally include the γ^*-mediated subprocess.

For example, for the photoproduction of diphoton process considered in [Pedrak et al.(2017)Pedrak, Pire one should include the γ^*-channel that involves photon-photon scattering in $\mathcal{H}_\mu$. Even though this is suppressed by $\alpha_{\rm em}$ compared to the GPD subprocess that corresponds to the $n = 2$ channel, the γ^*-channel at $n = 1$ is power enhanced by $Q/\sqrt{-t}$. In such cases, we need to carefully compare the contributions from these two channels, and to develop an experimental approach to remove the background due to the γ^*-channel in order to extract GPDs from the experimental data. One common approach by using azimuthal correlations will be briefly discussed in Sec. **??**.

3.2.2 SDHEP with a lepton beam

For single diffractive hard exclusive electroproduction processes, we have $B = C = e$. The other particle D can be a photon γ or a light meson M_D. Both of these two processes allow the γ^*-initialized channel with $n = 1$. For the $n = 2$ channel, the $D = \gamma$ case leads to the deeply virtual Compton scattering (DVCS) process [Ji(1997a), Radyushkin(1997)], and the case for $D =$ light meson corresponds to the deeply virtual meson production (DVMP) process [Brodsky et al.(1994)Brodsky, Frankfurt, Gunion, Mueller, and Strikman, Frankfurt et al.(1996)Frankfurt, Koepf, and Strikman]. Both of these two processes have been proved to be factorized into GPDs [Collins and Freund(1999), Collins et al.(1997)Collins, Frankfurt, a

Here, we will switch the theoretical perspective from [Collins and Freund(1999), Collins et al.(1997)Collins, by fitting them into the general SDHEP type of processes. The proof follows the two-stage paradigm depicted in Eqs. (3.105)-(3.107). This approach incorporates the γ^*-initialized $n = 1$ channel naturally, and for the $n = 2$ channel, it leads to a direct analogy to the large-angle meson scattering processes in Eq. (3.106) by having A^* being some meson state carrying the quantum number of the $[q\bar{q}']$ or $[gg]$ state. Our strategy for the proof follows a two-step process introduced in [Qiu and Yu(2022), Qiu and Yu(2023)]: (1) justify the factorization for a simpler $2 \to 2$ hard exclusive process in Eq. (3.106), which has been done in Sec. 3.1, and (2) extend the factorization to the full SDHEP in Eq. (4.134) by addressing extra complications, including especially the difficulty from Glauber gluons. As expected, we will reproduce the proofs in [Collins and Freund(1999), Collins et al.(1997)Collins, Frankfurt, and Strikman].

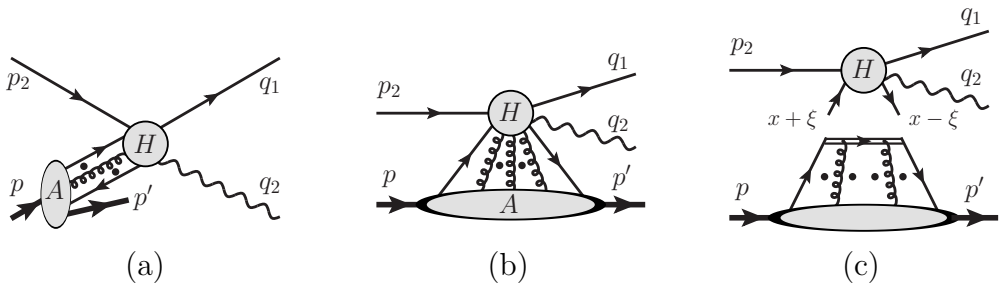

Fig. 3.10: Leading-region graphs of the DVCS for the (a) ERBL region and (b) DGLAP region of the GPD. (c) illustrates the result after factorizing the collinear subgraph out of H into a GPD. The two quark lines can be replaced by two transverse gluon lines.

3.2.2.1 Real photon production: $D = \gamma$

For $n = 1$, this gives the Bethe-Heitler process, and the amplitude $\mathcal{H}^\mu$ in Eq. (3.108) is the scattering amplitude of $\gamma^*(p_1) + e(p_2) \to e(q_1) + \gamma(q_2)$ with $q_{1T}^2 \gg |p_1^2| = |t|$.

For $n = 2$, the state A^* can be either a collinear $q\bar{q}$ or gg pair, which interacts with the electron beam by exchanging a virtual photon γ_{ee}^* with momentum $q = p_2 - q_1$, which

is similar to Fig. 3.1(c). This channel is therefore referred to as deeply virtual Compton scattering (DVCS). The $[q\bar{q}]$ and $[gg]$ state can be accompanied by an arbitrary number of longitudinally polarized collinear gluons. The traditional treatments all work in the Breit frame of the virtual photon γ^*_{ee} and hadron beam h [Collins and Freund(1999), Collins et al.(1997)Collins, Frankfurt, and Strikman]. Here, we follow the kinematic setup of the SDHEP in Eq. (4.134) to work in the CM frame of the initial-state hadron and electron with the hadron along the $\hat{z}$ axis. The requirement of a high virtuality $Q^2 = -q^2$ for the γ^*_{ee} is equivalent to the requirement of hard transverse momenta q_T for the final-state electron and photon in this frame, since $Q^2 \propto q_T^2$. Hence, the virtual photon γ^*_{ee} has a short lifetime and belongs to the hard part, and therefore we have the leading-region diagrams as in Fig. 3.10(a)(b).

Due to the presence of the diffraction, now we have two types of leading regions. In the first region [Fig. 3.10(a)], all the h-collinear parton lines go into the hard scattering H with positive plus momenta. This region is greatly similar to the leading region of meson scattering, e.g., Fig. 3.1(b). We call it ERBL region. In the other region [Fig. 3.10(b)], however, we also have some of the h-collinear parton lines go out of H with positive plus momenta and merge with the beam remnants to form the diffracted hadron h'. This region is called DGLAP region. It has no analogy in the large-angle meson scattering so represents the new feature of the diffractive scattering. In the DGLAP region, not only do we have long-lived propagating partons lines connecting the collinear subgraph to the hard subgraph H, but also have long-lived remnant particles propagating along the collinear direction of h as spectators of the hard interaction. Therefore, one has an opened color object lasting for a long time throughout the whole scattering. Soft gluons can be exchanged between the spectators and colored lines along other collinear directions. This will lead to the problem

of Glauber pinch that we will discuss in detail below.

Luckily, the Glauber region does not cause any issue for the real photon electroproduction process here, since there is only one collinear subgraph and so no soft subgraph exists. Therefore, the factorization proof can be directly built on that of the corresponding meson scattering process treated in Sec. 3.1.1.1.

For both the ERBL and DGLAP regions, the collinear momenta k_i^μ are pinched for their minus components if $\sqrt{-t} \ll p_1^+ \sim q_T$. Introducing the scaling variable $\lambda = \sqrt{-t} \ll q_T$, the collinear momentum scaling is the same as in Eq. (3.3). And then the same approximations as in Eqs. (3.4)-(3.6) can be made to factorize the collinear subgraph from the hard subgraph for quark-initiated process. For the diffractive scattering, one no longer has isospin symmetry to forbid the gluon-initiated channel, so the leading region in Fig. 3.10 contains an extra case when all collinear parton lines are gluons. Then we replace each gluon coupling by

$$H_\mu(k_i; k_H)\, g^{\mu\nu}\, C_\nu(k_i) = H_\mu(k_i; k_H)\, (K^{\mu\nu}(k_i, n) + G^{\mu\nu}(k_i, n))\, C_\nu(k_i), \tag{3.111}$$

with

$$K^{\mu\nu}(k_i, n) = \frac{k_i^\mu n^\nu}{k_i \cdot n - i\epsilon}, \quad G^{\mu\nu}(k_i, n) = g^{\mu\nu} - \frac{k_i^\mu n^\nu}{k_i \cdot n - i\epsilon}. \tag{3.112}$$

Note that no replacement of $k_i \to \hat{k}_i$ as Eq. (3.4) has been made in H. A gluon with its coupling replaced by the K (G) factor is called a K-gluon (G-gluon). When all or all but one gluons are K-gluons, we get a super-leading power contribution. The region with two G-gluons and all the others being K-gluons corresponds to the leading power. When there are three or more gluons being G-gluons, one receives a power suppression. As demonstrated in [Collins and Rogers(2008)], the super-leading power contribution is cancelled, but the regions with all or all but one gluons being K-gluons still give nonzero contribution at leading power,

which combines with the contribution from the leading region to give the full leading-power contribution.

After use of Ward identities and sum over regions and graphs, the collinear lines are factorized out of the hard part, as in Eq. (3.11),

$$\mathcal{M}^{(2)}_{he\to h'e\gamma} = \int \frac{d^4k}{(2\pi)^4} \left[\sum_q \mathcal{H}^q_{\beta\alpha;ji}(\hat{k}, \hat{p}_1 - \hat{k})\, \mathcal{C}^q_{\alpha\beta;ij}(k;p,p') \right. \\ \left. + \mathcal{H}^g_{\nu\mu;ba}(\hat{k}, \hat{p}_1 - \hat{k})\, \mathcal{C}^g_{\mu\nu;ab}(k;p,p') \right] \tag{3.113}$$

up to terms suppressed by powers of λ/q_T, where the superscript "(2)" refers to the contribution to the SDHEP amplitude from the $n = 2$ channel. We have included the contributions from both quark and gluon channels. The collinear factor $\mathcal{C}^q$ for the quark parton differs from Eq. (3.12) only in the external hadron states,

$$\mathcal{C}^q_{\alpha\beta;ij}(k;p,p') = \mathcal{P}_{A,\alpha\alpha'} \int d^4y e^{ik\cdot y} \langle h'(p')|\mathcal{T} \left\{ \left[\bar{\psi}_{q,\beta'}(0) \Phi^\dagger(\infty, 0; n) \right]_j \right. \\ \left. \times \left[\Phi(\infty, y; n) \psi_{q,\alpha'}(y) \right]_i \right\} |h(p)\rangle \bar{\mathcal{P}}_{A,\beta'\beta}, \tag{3.114}$$

but now we are allowed to have more spin structures,

$$\mathcal{C}^q_{\alpha\beta;ij}(k;p,p') = \frac{\delta_{ij}}{N_c} \left[\mathcal{C}^{q,+}(k;p,p') \frac{\gamma^-}{2} + \widetilde{\mathcal{C}}^{q,+}(k;p,p') \frac{\gamma_5\gamma^-}{2} + \sum_{i=1,2} \mathcal{C}^{q,+i}_\perp(k;p,p') \frac{\sigma^{i-}}{2} \right]_{\alpha\beta}, \tag{3.115}$$

with each factor defined as

$$\left(\mathcal{C}^{q,+},\widetilde{\mathcal{C}}^{q,+},\mathcal{C}_{\perp}^{q,+i}\right)(k;p,p') = \int d^4y e^{ik\cdot y}\langle h'(p')|\mathcal{T}\left\{\bar{\psi}_q(0)\Phi^{\dagger}(\infty,0;n)\right. \\ \left.\times\left(\frac{\gamma^+}{2},\frac{\gamma^+\gamma_5}{2},\frac{\sigma^{+i}}{2}\right)\Phi(\infty,y;n)\psi_q(y)\right\}|h(p)\rangle. \quad (3.116)$$

The collinear factor for the gluon parton is

$$\mathcal{C}_{ab}^{g,\mu\nu}(k;p,p') = \frac{1}{k^+(k-p_1)^+}\int d^4y e^{ik\cdot y}\langle h'(p')|\mathcal{T}\left\{\left[G^{+\nu}(0)\Phi_A^{\dagger}(\infty,0;n)\right]_b\right. \\ \left.\times\left[\Phi_A(\infty,y;n)G^{+\mu}(y)\right]_a\right\}|h(p)\rangle, \quad (3.117)$$

where $G_a^{\mu\nu} = \partial^\mu A_a^\nu - \partial^\nu A_a^\mu - g f^{abc} A_b^\mu A_c^\nu$ is the gluon field strength tensor, and Φ_A is the Wilson line in the adjoint representation,

$$\Phi_{A,ab}(\infty,y;n) = \mathcal{P}\exp\left\{-g\int_0^\infty d\lambda\, n_\mu\, A_c^\mu(y+\lambda n)\,(f^{cab})\right\}, \quad (3.118)$$

obtained by replacing t^a in Eq. (3.9) by $T_A^a = -i(f^{abc})$. Due to the antisymmetry of $G_a^{\mu\nu}$, only the components of $\mathcal{C}_{ab}^{g,\mu\nu}$ with $\mu,\nu = 1,2$ are nonzero, so $\mathcal{C}_{ab}^{g,\mu\nu}$ also has four independent Lorentz structures, similar to Eq. (3.115),

$$\mathcal{C}_{ab}^{g,ij} = \frac{\delta_{ab}}{2(N_c^2-1)}\left[\mathcal{C}^{g,\bar{i}\bar{i}}\delta^{ij} + \left(\mathcal{C}^{g,ij} - \mathcal{C}^{g,ji}\right) + \left(\mathcal{C}^{g,ij} + \mathcal{C}^{g,ji} - \mathcal{C}^{g,\bar{i}\bar{i}}\delta^{ij}\right)\right], \quad (3.119)$$

where the repeated index $\bar{i}$ is summed over, and the quantities $\mathcal{C}$ without color subscripts a,b have traced over them. We may rewrite Eq. (3.119) by abusing the notations of Pauli

matrices $\sigma_k = (\sigma_k^{ij})$ $(k = 1, 2, 3)$,

$$\mathcal{C}_{ab}^{g,ij} = \frac{\delta_{ab}}{2(N_c^2 - 1)} \left[\mathcal{C}_0 \, \delta^{ij} + \sum_{k=1}^{3} \mathcal{C}_k \, \sigma_k^{ij}, \right], \tag{3.120}$$

with the coefficients determined as

$$\begin{aligned} \mathcal{C}_0 &= \mathrm{tr}\,(\mathcal{C}^g) = \mathcal{C}^{g,11} + \mathcal{C}^{g,22}, & \mathcal{C}_2 &= \mathrm{tr}\,(\mathcal{C}^g \sigma_2) = -i(\mathcal{C}^{g,21} - \mathcal{C}^{g,12}), \\ \mathcal{C}_1 &= \mathrm{tr}\,(\mathcal{C}^g \sigma_1) = \mathcal{C}^{g,12} + \mathcal{C}^{g,21}, & \mathcal{C}_3 &= \mathrm{tr}\,(\mathcal{C}^g \sigma_3) = \mathcal{C}^{g,11} - \mathcal{C}^{g,22}. \end{aligned} \tag{3.121}$$

Define the kinematics associated with the collinear factors,

$$P = (p + p')/2, \quad \Delta = p_1 = p - p', \quad \xi = \frac{(p - p')^+}{(p + p')^+}, \quad k^+ = (x + \xi) P^+, \tag{3.122}$$

and so

$$p^+ = (1 + \xi) P^+, \quad p'^+ = (1 - \xi) P^+, \quad (k - p_1)^+ = (x - \xi) P^+. \tag{3.123}$$

Then because only the plus parton momentum flows in H, the momentum integration in Eq. (3.113) can be disentangled into a mere convolution in k^+, which can be converted to x. This then factorizes the whole amplitude into GPDs that captures the infrared sensitivity,

$$\begin{aligned} \mathcal{M}^{(2)}_{he \to h' e \gamma} = \sum_f \int_{-1}^{1} dx \Big[& F^f(x, \xi, t) H^f(x, \xi) + \widetilde{F}^f(x, \xi, t) \widetilde{H}^f(x, \xi) \\ & + \sum\nolimits_{i=1,2} F_T^{f,i}(x, \xi, t) H_T^{f,i}(x, \xi) \Big], \end{aligned} \tag{3.124}$$

which sums over the parton flavors $f = q, g$, as illustrated in Fig. 3.10(c). We have defined the quark and gluon GPDs, obtained by integrating Eqs. (3.116) and (3.117) over $\boldsymbol{k}_T$ and

k^-,

$$\left(F^q, \widetilde{F}^q, F_T^{q,1}, F_T^{q,2}\right)(x,\xi,t) = \int \frac{dy^-}{4\pi} e^{i(x+\xi)P^+ y^-} \tag{3.125}$$
$$\times \langle h'(p')|\mathcal{T}\left\{\bar{\psi}_q(0)\Phi(0,y^-;n)\left(\gamma^+, \gamma^+\gamma_5, \sigma^{+1}, \sigma^{+2}\right)\psi_q(y^-)\right\}|h(p)\rangle,$$
$$\left(F^g, \widetilde{F}^g, F_T^{g,1}, F_T^{g,2}\right)(x,\xi,t) = \int \frac{dy^-}{2\pi P^+} e^{i(x+\xi)P^+ y^-} \tag{3.126}$$
$$\times \left(\delta^{ij}, -\sigma_2^{ij}, \sigma_3^{ij}, \sigma_1^{ij}\right)\langle h'(p')|\mathcal{T}\left\{G^{+j}(0)\Phi_A(0,y^-;n)G^{+i}(y^-)\right\}|h(p)\rangle$$

for the unpolarized, (longitudinally) polarized, and transversity ones. The corresponding hard coefficients are,

$$\left(H^q, \widetilde{H}^q, H_T^{q,1}, H_T^{q,2}\right)(x,\xi) = \frac{1}{2N_c}\left(\gamma^-, \gamma_5\gamma^-, \sigma^{1-}, \sigma^{2-}\right)_{\alpha\beta} H^q_{\beta\alpha;\bar{i}i}(\hat{k}, \hat{p}_1 - \hat{k}), \tag{3.127}$$
$$\left(H^g, \widetilde{H}^g, H_T^{g,1}, H_T^{g,2}\right)(x,\xi) = \frac{1}{2(N_c^2-1)}\frac{1}{x^2-\xi^2}\left(\delta^{ij}, -\sigma_2^{ij}, \sigma_3^{ij}, \sigma_1^{ij}\right) H^g_{ji;\bar{a}a}(\hat{k}, \hat{p}_1 - \hat{k}),$$

where the spinor indices $\alpha\beta$ and transverse Lorentz indices ij are summed over. Note that the factor $1/(x^2-\xi^2)$ in the gluon hard coefficient does not raise problems for the x integration at $x = \pm\xi$ because such poles are introduced by the artificial use of the field strength tensor in the gluon GPD definition. The latter contains zeros at $x = \pm\xi$, which cancel the poles at the hard coefficients.

For the DVCS, however, transversity GPDs do not contribute because the massless parton approximation renders the corresponding hard coefficients to vanish. Then Eq. (3.124) only has the first line. By a similar argument as Eqs. (3.20)-(3.23), the time ordering can be dropped [Diehl and Gousset(1998)] in Eq. (3.125), allowing for insertion of physical states.

Then we have the support conditions for the GPDs,

$$p^+ - k^+ = (1-x)P^+ \geq 0, \quad p^+ - (p_1 - k)^+ = (1+x)P^+ \geq 0, \tag{3.128}$$

such that GPDs are only nonzero when $x \in [0,1]$, which explains the integration range in Eq. (3.124). Due to the amplitude nature, the GPDs are (non-local) matrix elements between two *pure* hadron state. There is no way for the hadron spin average to come in before we square the amplitude. So all possible GPDs should be kept unless they are forbidden by symmetries. This is different from the collinear factorization of inclusive processes such as DIS, for which the polarization state of partons is dependent on the target spins state, and polarized PDFs are nonzero only when the targets are polarized. Also, we note that the flavor sum in Eq. (3.124) is only over all possible quark flavors and gluon, not antiquarks. Because the x is integrated from -1 to 1, there is no need to introduce antiquark GPDs separately.

Due to the absence of soft subgraph, the collinear factors in Eq. (3.125) do not need further subtraction. The factorization result in Eq. (3.124) is obtained mainly by use of Ward identities, which applies equally to the leading region R under approximation and to the subtracted smaller regions $R' < R$, effectively contained in H. So the hard coefficients in Eq. (3.124) contain subtractions of smaller regions when some lines become collinear, which can be dealt with recursively using the same factorization procedure.

However, the GPDs defined in Eq. (3.125), as well as the corresponding hard coefficients due to collinear subtractions, contain artificial UV divergences, as a result of short circuiting the $\boldsymbol{k}_T$ integration in the collinear factors. They thus need additional renormalization. It can be shown that the GPDs can be multiplicatively renormalized, just as the DAs. This

can be used to convert each factor in Eq. (3.124) to a renormalized version, with the same factorization structure. All the renormalized factors depend additionally on the factorization scale μ,

$$\mathcal{M}^{(2)}_{he\to h'e\gamma} = \sum_f \int_{-1}^{1} dx \left[F^f(x,\xi,t;\mu) H^f(x,\xi;\mu) + \widetilde{F}^f(x,\xi,t;\mu) \widetilde{H}^f(x,\xi;\mu) \right], \quad (3.129)$$

which implies a set of evolution equations that can be used to improve the factorization predictivity.

Compared to the corresponding DA factorization in Sec. 3.1.1.1, the soft parton issue can also arise here, i.e., some of the parton momenta may have $k_i^+ \ll Q$, which violates the scaling in Eq. (3.3), and thus the corresponding approximations. This is termed the "breakpoint" issue in [Collins et al.(1997)Collins, Frankfurt, and Strikman]. However, since the region $k_i^+ \sim 0 \ll Q$ is not pinched, we can deform the contour of k^+ integration by $k^+ \mapsto k^+ \pm i\mathcal{O}(Q)$ [Collins et al.(1997)Collins, Frankfurt, and Strikman]. Because the breakpoint only lies on the boundary between the ERBL and DGLAP regions, but not at the GPD end points, this deformation is allowed. Perturbatively, the soft parton singularity appears in Eq. (3.129) at $x = \pm\xi$. For example, the leading-order DVCS hard coefficient contains a term that is proportional to $1/(x \pm \xi \mp i\varepsilon)$, and we can deform the x contour to avoid the poles at $\mp\xi$; in practical calculations, this is achieved by

$$\frac{1}{x \pm \xi \mp i\varepsilon} = P\frac{1}{x \pm \xi} \pm i\pi\,\delta(x \pm \xi), \quad (3.130)$$

where P denotes principal-value integration.

3.2.2.2 Light meson production: D =meson

Similarly, the single diffractive hard electroproduction of a light meson M_D can be built on the large-angle meson electron scattering process in Sec. 3.1.1.2. We keep the same definitions in Eqs. (3.28)-(3.33), and use the same approximations in Eqs. (3.35)-(3.44) except the Eqs. (3.36) and (3.39), which will be explained below. We will also rely on the asymmetric deformation discussed in Sec. 3.1.1.3 and extensively used in Secs. 3.1.2.4 and 3.1.3.3.

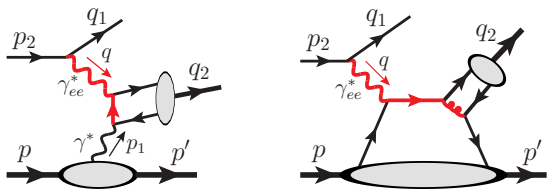

Fig. 3.11: Examples of leading-order diagrams for the light meson production in the SDHEP with an electron beam, for (a) the $n = 1$ channel and (b) the $n = 2$ channel for $[q\bar{q}']$ case, where the red thick lines indicate those with hard q_T flow and high virtualities.

First, the $n = 1$ γ^*-initialized channel exists for a neutral meson production, which gives the subprocess

$$\gamma^*(p_1) + e(p_2) \to e(q_1) + M_D(q_2). \tag{3.131}$$

One leading-order diagram is shown in Fig. 3.11(a). The slightly off-shell photon $\gamma^*(p_1)$ scatters with the highly virtual photon $\gamma^*_{ee}(q = p_2 - q_1)$ to produce the meson M_D. Eq. (3.131) is just the reversed process of the large-angle real photon production in electron-meson scattering, discussed in Sec. 3.1.1.1, although now the photon γ^* is virtual. As in Sec. 3.1.1.1, we can also factorize the amplitude of the process [Eq. (3.131)] into the DA of M_D to the leading power of m_D/q_T, similar to Eq. (3.26). As noted in Sec. 3.2.1, however, this approximation is only valid at leading power of the process in Eq. (3.131), which is of one power higher (super-leading) than the $n = 2$ GPD channel of our main interest. A more consistent

treatment needs to factorize the process in Eq. (3.131) to subleading power, which is beyond the scope of this paper. Alternatively, one may choose to parametrize the amplitude by the $\gamma^*\gamma^*_{ee} \to M_D$ form factor, without use of factorization. The $n = 1$ channel would be forbidden for the production of a charged meson like $\pi^\pm$, or of a neutral meson with odd C parity, such as ρ and J/ψ.

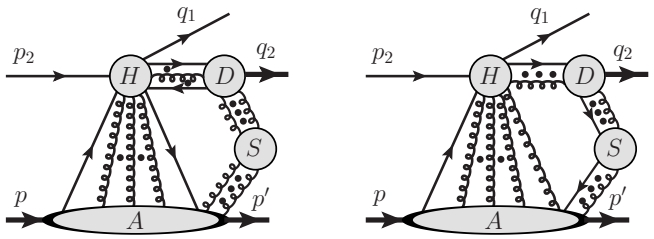

Fig. 3.12: Leading-region graphs (a)(b) for producing a light meson from the SDHEP with a lepton beam. Depending on the quantum numbers, the quark lines may be replaced by transversely polarized gluon lines. (c) is the result after factorizing it into the DA and GPD.

For the $n = 2$ channel, the diffracted hadron h can exchange a collinear $[q\bar{q}']$ or $[gg]$ state with the hard scattering. The latter only holds when M_D is charge neutral. One leading-order diagram for the quark channel is shown in Fig. 3.11(b). The hard electron scattering still happens by exchanging a highly virtual photon γ^*_{ee}, and so this (sub)process is referred to as deeply virtual meson production (DVMP). The leading regions are shown in Fig. 3.12(a) and Fig. 3.12(b). In region (b) physically polarized quarks or gluons are attaching the collinear subgraphs to the soft subgraph; it is power suppressed by the soft-end suppression with respect to the meson wavefunction, as explained in Sec. 3.1.1.2.

As for the DVCS in Sec. 3.2.2.1, the diffractive kinematics introduces the extra DGLAP region, compared to the meson scattering case in Sec. 3.1.1.2. While this does not cause problems for the DVCS, it does lead to obstacles in factorizing soft gluons out of the A-collinear subgraph. This is illustrated in a simple model theory in Fig. 3.13, where we have

indicated the chosen soft momentum flows by the thin curved arrowed lines. We make the following observations:

(1) DGLAP region has active collinear parton lines both before and after the hard interactions, and the soft gluons can attach to both, as shown in Figs. 3.13(a) and 3.13(b). With the soft momentum flows as indicated, attaching to the initial-state collinear parton gives a pole of k_s^- at $\mathcal{O}(\lambda^2)/Q - i\epsilon$, while the final-state one gives a pole of k_s^- at $\mathcal{O}(\lambda^2)/Q + i\epsilon$;

(2) DGLAP region also has some spectator partons going in the forward direction. When the soft gluon attaches to the spectator lines, as shown in Fig. 3.13(c), it flows both in the same and opposite directions as the target-collinear lines, so that one single diagram gives both $\mathcal{O}(\lambda^2)/Q \pm i\epsilon$ poles for k_s^- contour.[9]

Diagrams like Fig. 3.13(c) pinch the k_s^- contour at small values, such that for a Glauber gluon with the momentum scaling as in Eq. (3.33), one cannot deform the k_s^- contour to get out of the Glauber region, as was allowed by the corresponding $2 \to 2$ meson scattering in Eq. (3.34). While the diagrams in Figs. 3.13(a) and 3.13(b) do not directly cause pinch in the Glauber region, they cannot be trivially dealt with, either. Note that factorizing the soft gluons from the A-collinear lines requires to first deform soft gluons out of the Glauber region and then apply Ward identities. Even though we can deform the k_s^- contour to get out the Glauber region for both diagrams, the deformation directions are opposite. For Fig. 3.13(a), we need to replace the gluon coupling by

$$J_\mu^A(k_s, k_A)\, g^{\mu\nu}\, S_\nu(k_s) \mapsto J_\mu^A(\hat{k}_s, k_A)\, \frac{\hat{k}_s^\mu w_A^\nu}{k_s \cdot w_A + i\epsilon}, \tag{3.132}$$

[9] Rerouting the soft momentum flow can change the situation (1) such that it also flows through the spectators and leads to both kinds of poles.

whereas for Fig. 3.13(b), we need to flip the $i\epsilon$ sign. This would forbid use of Ward identity for the soft gluons, since different terms do not combine and cancel. This feature is closely related to the existence of Glauber pinch for k_s^- in Fig. 3.13(c).

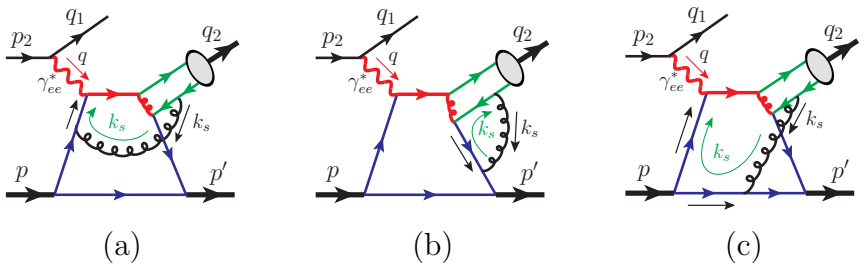

Fig. 3.13: Three example diagrams illustrating the soft gluon exchange between the collinear subgraphs along the diffractive hadron and the final-state meson, for the DGLAP region of the GPD in a simple model theory. The green thin curved lines indicate the soft momentum flows.

The way out is to note that all the soft k_s^+ poles come from the D-collinear lines, and lie on the lower half plane when k_s flows from D into S. One may thus deform k_s^+ as $k_s^+ \mapsto k_s^+ + i\mathcal{O}(Q)$ while keeping k_s^- contour unchanged, as was done in Eq. (3.60). While it is a free choice for the $2 \to 2$ hard exclusive scattering, this deformation is necessary here due to the pinch in the DGLAP region of the diffractive process, and it moves all Glauber gluon momenta to the A-collinear region. For the same reason as discussed in Sec. 3.1.1.3, the $i\epsilon$ prescription for k^- does not matter so it can be chosen in an arbitrary but consistent way.

Then by a similar discussion to Sec. 3.1.2.4, we can first factorize the D-collinear subgraph out of H, and soft gluons out of D. The same line of arguments applies here for the neutrality of meson D, the soft cancellation, and that the pair of collinear Wilson lines associated with D is joined into a finite-length Wilson line along $\bar{w}_D$. This applies to both the approximated region in Fig. 3.12(a) and smaller regions for subtraction, and reduces the leading region to Fig. 3.14(a). Then by only attaching to the collinear subgraph A, soft gluons are no

longer pinched. Because all the k_s^+ poles are of order Q, one may deform the k_s^+ contour by order Q to make it a A-collinear momentum. We can thus group the soft subgraph into the A-collinear subgraph. Then Fig. 3.14(a) is exactly similar to Fig. 3.10(a)(b) for the single diffractive real photon electroprodcution, and we can follow the same procedure to factorize the collinear subgraph associated with the diffracted hadron out of H into the GPD.

Finally, we achieve the factorization of the amplitude,

$$\mathcal{M}^{(2)}_{he\to h'eM_D} = \sum_{i,j} \int_{-1}^{1} dx \int_0^1 dz\, F^i_{hh'}(x,\xi,t;\mu) C_{ie\to ej}(x,\xi;z;\boldsymbol{q}_T,\mu)\, \bar{D}_{j/D}(z,\mu), \quad (3.133)$$

up to $1/q_T$ power suppressed terms, as diagrammatically shown in Fig. 3.14(b). The hard coefficient is a scattering of a collinear and on-shell parton pair i along w_A off the electron into another collinear and on-shell parton pair j along w_D. It contains collinear subtractions from both the GPD $F^i_{hh'}$ and DA $\phi_{j/D}$, but the latter two do not contain further soft subtractions, as a feature of collinear factorization. We have used the multiplicative renormalizations of GPD and DA to convert each factor to a renormalized one, which introduces a factorization scale μ and the associated evolution equations. The sum over i and j runs over all possible flavors and spin structures.

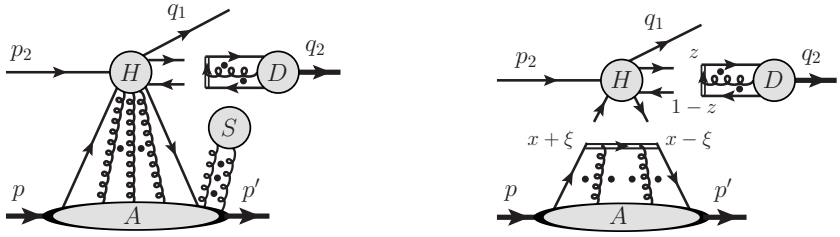

Fig. 3.14: (a) Factorization of soft subgraph from the collinear subgraph of the final-state meson. (b) Factorization of the A-collinear subgraph out of the hard subgraph into GPD.

For example, the charged pion π^+ production $pe \to ne\pi^+$ only supports the channel

$i = j = [u\bar{d}]$, which gives the factorization formula,

$$\mathcal{M}^{(2)}_{pe\to ne\pi+} = \int_{-1}^{1} dx \int_{0}^{1} dz\, \widetilde{F}^{u}_{pn}(x,\xi,t;\mu) C_{[u\bar{d}]e\to e[u\bar{d}]}(x,\xi;z;\boldsymbol{q}_T,\mu)\, \bar{D}_{u/\pi+}(z,\mu). \quad (3.134)$$

To the leading order of QED, the hard coefficient is only nonzero for the polarized GPD $\widetilde{F}^{u}_{pn}$ due to the QED Ward identity,

$$C_{[u\bar{d}]e\to e[u\bar{d}]} \propto \bar{u}(q_1)\gamma_\mu u(p_2)\frac{-ig_{\mu\nu}}{q^2}(\hat{p}_1 + \hat{q}_2)^\nu, \quad (3.135)$$

which requires a γ from the GPD. The bare flavor-changing GPD $\widetilde{F}^{u}_{pn}$ is defined as

$$\widetilde{F}^{u,\text{bare}}_{pn}(x,\xi,t) = \int \frac{dy^-}{4\pi} e^{i(x+\xi)P^+ y^-} \langle n(p')|\bar{\psi}_d(0)\Phi(0,y^-;n)\gamma^+\gamma_5\psi_u(y^-)|p(p)\rangle. \quad (3.136)$$

The neutral pion π^0 production $pe \to pe\pi^0$, on the other hand, supports both quark and gluon channels,

$$\mathcal{M}^{(2)}_{pe\to pe\pi 0} = \sum_{i=u,d,g}\sum_{j=u,d}\int_{-1}^{1} dx \int_{0}^{1} dz\, \widetilde{F}^{i}_{p}(x,\xi,t;\mu) C_{[i\bar{i}]e\to e[j\bar{j}]}(x,\xi;z;\boldsymbol{q}_T,\mu)\, \bar{D}_{j/\pi 0}(z,\mu). \quad (3.137)$$

The flavor-changing GPD $\widetilde{F}^{u}_{pn}$ can be related to the flavor-conserving ones by isospin symmetry.

3.2.2.3 Extending to virtual photon or heavy quarkonium production

The DVCS and DVMP differ in how the observed particle couples to the hard interaction: the photon of the DVCS couples directly to the hard collision while the light meson of

DVMP couples to the hard collision via two collinear partons. The factorization proof for the DVCS should apply equally to the case of producing a virtual photon γ_f^* with high q_T and low virtuality Q'^2 that decays into a pair of charged leptons. Even if $q_T \gg Q'$, there is no large logarithm of q_T/Q' that spoils perturbation theory, contrary to the inclusive process [Berger et al.(2002a)Berger, Qiu, and Zhang], because such logarithms are associated with diagrams' collinear sensitivity, which require two collinear parton lines to connect the low mass virtual photon to the hard part, which is suppressed by one power of Q'/q_T compared to the direct photon attachment. In contrast, the DVMP amplitude has large logarithms of q_T/m_D, due to the long-distance evolution of the collinear parton lines. Such logarithms are incorporated by the evolution equation associated with the factorization formula in Eqs. (3.56) and (3.133).

For a virtual photon γ_f^* with its virtuality Q' of the same order as q_T (but, sufficiently away from masses of heavy quarkonia), it should belong to the short-distance hard part, and the whole process becomes $e^- + h \to h' + 2e^- + e^+$. This is no longer a $2 \to 3$ SDHEP-type process, but we can still relate it to the SDHEP type by considering the kinematic regime where one of the final-state electrons has a high transverse momentum q_T, balanced by the other e^+e^- pair, which also has a large invariant mass $Q' \sim q_T$.

First of all, the γ^*-mediated channel at $n = 1$ is allowed, with the hard scattering $e^- + \gamma^* \to 2e^- + e^+$. Second, the $n = 2$ channel does not unambiguously lead to the double DVCS (DDVCS) process [Guidal and Vanderhaeghen(2003)] because it is not possible to distinguish which of the final-state electrons comes from the scattering of the initial-state electron. By labeling the final-state electrons and positron as $\left(e_1^-, e_2^-, e^+\right)$, we find that a single configuration of $\left(e_1^-, e_2^-, e^+\right)$ could correspond to both high-Q' and low-Q' processes. Specifically, let us consider the following three kinematic cases:

(1) All the (e_1^-, e_2^-, e^+) have high transverse momenta, of order $q_T \gg \sqrt{-t}$, and the two invariant masses $(m_{e_1^- e^+}, m_{e_2^- e^+})$ are large, of the same order of q_T. This case leads unambiguously to DDVCS, and the factorization of DVCS can be trivially generalized here. But one needs to consider both diagrams with either e_1^- or e_2^- coming from the decay of the virtual photon γ_f^*.

(2) All the (e_1^-, e_2^-, e^+) have high transverse momenta, of order $q_T \gg \sqrt{-t}$, but one of the invariant lepton-pair masses, say $m_{e_1^- e^+}$, is much less than q_T, and the other pair has a large invariant mass, i.e., $q_T \sim m_{e_2^- e^+} \gg m_{e_1^- e^+}$. In this case, one can have (a) (e_1^-, e^+) comes from the decay of a low-virtuality γ_f^*, and (b) (e_2^-, e^+) comes from the decay of a high-virtuality γ_f^*. While both correspond to the DDVCS processes, it is the case (a) with a low-mass electron pair that contributes at a leading power.

(3) (e_2^-, e^+) have high transverse momenta, of order $q_T \gg \sqrt{-t}$, and e_1^- has a low transverse momentum, much less than q_T. Automatically, we have both $(m_{e_1^- e^+}, m_{e_2^- e^+})$ to be large. This gives two different cases: (a) e_1^- comes from the diffraction of the initial-state electron, which gives out a quasireal photon γ_{ee}^* that scatters with the diffractive hadron h and produces a highly virtual photon γ_f^* that decays into the (e_2^-, e^+) pair; (b) e_2^- comes from the hard scattering of the initial-state electron, whose interaction with the diffractive hadron h produces a highly virtual photon γ_f^* with a high transverse momentum, which decays into the (e_1^-, e^+) pair. Now only the case (b) corresponds to the DDVCS process, and case (a) gives a subprocess of (quasi)real photon scattering with the hadron, whose factorization will be proved later in Sec. **??**. While both subprocesses are factorizable, it is the subprocess (a) that gives the leading power contribution.

Of course, if the virtual photon γ_f^* decays into a lepton pair of other flavors, like a $\mu^+\mu^-$ pair, then it unambiguously leads to the DDVCS process and can be factorized in the same way as the DVCS.

When the γ_f^* virtuality Q' becomes much greater than q_T, one starts entering the two-scale regime. Whether there will be large logarithms of Q'/q_T that requires a new factorization theorem to be developed is not a trivial problem based on our analysis so far. We leave that discussion to the future.

For a heavy quarkonium production, unfortunately, it is not obvious that the factorization in Sec. 3.2.2.2 can be easily generalized. The key points to the factorization are

(i) there is a pinch singularity that forces a collinear momentum to have the scaling in Eq. (3.3), with a leading component and two smaller components;

(ii) soft gluons can be factorized from the collinear lines.

The exclusive production of a heavy quarkonium naturally has the most contribution from producing a heavy quark pair with an invariant mass $M_H \sim 2m_Q$, where $m_Q \gg \Lambda_{\rm QCD}$ is the heavy quark mass. Since the corresponding heavy quark GPD in h-h' transition is suppressed, we do not suffer from the extra region like Fig. 3.12(b). When the transverse momentum q_T of the heavy quarkonium is much greater than m_Q, the heavy quark can be thought of as the active parton line associated with the observed particle D in Fig. 3.12(a), and the heavy quarkonium is attached to the hard part by a pair of nearly collinear heavy quark lines, whose momenta scale as

$$k_Q \sim \left(\lambda_Q^2, 1, \lambda_Q\right) q_T, \quad \text{with } \lambda_Q = m_Q/q_T, \tag{3.138}$$

when the heavy quarkonium moves along the minus direction. This pinches the plus momentum components to be small, and for a soft gluon k_s attached to such heavy quark lines, one may keep only the k_s^+ component, which allows us to factorize the soft gluon out of the collinear lines. Hence, for $q_T \gg m_Q \gg \Lambda_{\rm QCD}$, one can still factorize the heavy quarkonium production amplitude into the heavy quarkonium DA, up to the error of $\mathcal{O}\big(m_Q/q_T\big)$. See [Kang et al.(2014)Kang, Ma, Qiu, and Sterman] for a similar discussion of the inclusive production of a heavy quarkonium.

When $m_Q \sim q_T \gg \Lambda_{\rm QCD}$, the error estimated above becomes $\mathcal{O}(1)$, which invalidates the factorization into heavy quarkonium DA. However, if $M_H/2 - m_Q \ll m_Q \sim q_T$, the formation of the heavy quarkonium from the produced heavy quark pair might be treated in terms of the color singlet model [Einhorn and Ellis(1975), Chang(1980), Berger and Jones(1981)] or the velocity expansion of nonrelativistic QCD with color singlet long-distance matrix elements [Bodwin et al.(1995)Bodwin, Braaten, and Lepage]. For this exclusive production, the soft gluon interaction from the diffractive hadron with the heavy quark pair at $q_T \sim m_Q \gg \Lambda_{\rm QCD}$ is expected to be suppressed by powers of $m_Q v/q_T \sim v$ with v being the heavy quark velocity in the quarkonium's rest frame. More detailed study for the heavy quarkonium production when $q_T \lesssim m_Q$ will be presented in a future publication.

3.2.3 SDHEP with a photon beam

For single diffractive hard exclusive photoproduction processes, we have $B = \gamma$. The other particles C and D can be two elementary particles, one elementary particle and one light meson, or two light mesons. So we consider the three cases, (1) massive dilepton $(CD) = (l^+l^-)$ [Berger et al.(2002b)Berger, Diehl, and Pire, **?**] or diphoton $(\gamma\gamma)$ production [Pedrak et al.(2017)Pedrak, Pire, Szymanowski, and Wagner, Grocholski et al.(2021)Grocholski, Pire,

Grocholski et al.(2022)Grocholski, Pire, Sznajder, Szymanowski, and Wagner], (2) real photon and light meson pair $(CD) = (\gamma M_D)$ production [Boussarie et al.(2017)Boussarie, Pire, Szymanowski, a Duplančić et al.(2018)Duplančić, Passek-Kumerički, Pire, Szymanowski, and Wallon], and (3) light meson pair $(CD) = (M_C M_D)$ production [**?**]. These are similar to the large-angle photon-meson scattering treated in Sec. 3.1.2. In this section, we generalize the factorization arguments there to the corresponding single diffractive processes, following the same two-stage paradigm as the single-diffractive lepton-hadron scattering in Sec. 3.2.2.

3.2.3.1 Dilepton or diphoton production: $(CD) = (l^+l^-)$ or $(\gamma\gamma)$

Both production processes allow the γ^*-mediated $n = 1$ subprocesses. For the dilepton production, we have the partonic process $\gamma\gamma^* \to l^+l^-$, starting at $\mathcal{O}(e^2)$ in terms of the QED coupling e, while we have $\gamma\gamma^* \to \gamma\gamma$ for the diphoton production, starting at $\mathcal{O}(e^4)$. Since this γ^*-mediated $n = 1$ channel has a power enhancement of $\mathcal{O}(q_T/\sqrt{-t})$ compared to the $n = 2$ channel, it cannot be simply neglected even though its scattering amplitude might require a higher power in QED coupling. A careful quantitive comparison in size between γ^*-mediated $n = 1$ and GPD-sensitive $n = 2$ subprocesses is needed in practical evaluation.

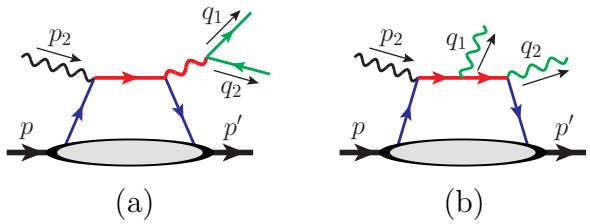

Fig. 3.15: Examples of leading-order diagrams in the $n = 2$ (GPD) channel for the single diffractive hard exclusive photoproduction of massive (a) dilepton and (b) diphoton processes.

For $n = 2$ channel, these two processes share the same color structure as the DVCS, and thus the same leading-region graphs in Fig. 3.10 with a proper change of the external lines,

because B, C, and D are all elementary colorless particles. The argument for factorization into GPDs works in the same way as for the DVCS in Sec. 3.2.2.1 and will not be repeated here. The process with $(CD) = (l^+l^-)$ happens by producing a timelike photon γ'^* in the exclusive $\gamma h \to \gamma'^* h'$ process followed by the decay $\gamma'^* \to l^+l^-$, which is thus called timelike Compton scattering (TCS), as shown in Fig. 3.15(a). For the process with $(CD) = (\gamma\gamma)$, all the three photons couple to the quark lines, as illustrated in Fig. 3.15(b). In both processes, it is the high q_T that provides the hard scale for factorizability, by creating high virtualities through the invariant mass of the virtual photon in the dilepton case or having the q_T flow through the quark lines in the diphoton case.

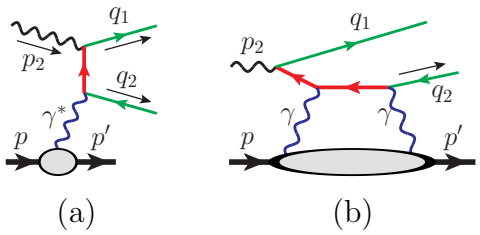

Fig. 3.16: (a) The sample diagram for the γ^*-mediated channel of the photoproduction of a massive lepton pair, where the internal lepton propagator (in red) has a hard virtuality only when q_T is large. (b) At large m_{ll} but small q_T, the forward scattering diagrams with two photon exchanges between the diffractive hadron and the quasireal lepton can become important and compete with the TCS mechanism in Fig. 3.15(a).

It is important to note that in general, the requirement of a high invariant mass for the pair of particles (CD) is not the same as requiring a hard q_T. This is similar to the large-angle photon-meson scattering in Sec. 3.1.2.1. For the TCS, it is the invariant mass of the lepton pair m_{ll} that provides the hard scale for the partonic collision, and hence keeping m_{ll} large is sufficient for TCS to be factorized into GPD, independent of the magnitude of q_T of the observed lepton. However, a hard q_T is needed to guarantee the γ^*-mediated $n = 1$ subprocess $\gamma\gamma^* \to l^+l^-$ to be a hard scattering process, as illustrated in Fig. 3.16(a). If q_T is too low, then this amplitude introduces another enhancement factor of $\mathcal{O}(m_{ll}/q_T)$,

in addition to the $m_{ll}/\sqrt{-t}$ enhancement of the $n = 1$ channel, as correctly pointed out in [Berger et al.(2002b)Berger, Diehl, and Pire]. Then, this could allow other subprocesses to happen that may compete with the TCS subprocess in magnitude. For example, one may have an $n = 2$ channel mediated by $f_2 = [\gamma\gamma]$, as shown in Fig. 3.16(b), which is suppressed by e^2 and one power of $\sqrt{-t}/m_{ll}$ compared to the $n = 1$ channel, but is still one power $\mathcal{O}(m_{ll}/q_T)$ higher than the TCS channel. The relative order comparison is then too complicated to be obvious, and the extraction of GPDs from the TCS amplitude becomes even harder.

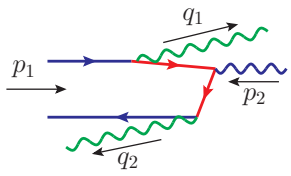

Fig. 3.17: A sample diagram for the photoproduction of diphoton process at low q_T, where the photon q_1 is radiated collinearly by the incoming quark.

On the other hand, if q_T is too low in the diphoton production process, some quark lines could have low virtualities of order q_T, as the photons could be radiated from the quark lines (see Fig. 3.17) almost collinearly, introducing the long-distance physics into the "hard probe", which invalidates our factorization arguments.

3.2.3.2 Real photon and light meson pair production: $(CD) = (\gamma M_D)$

For $(CD) = (\gamma M_D)$ with M_D being a light meson, the $n = 1$ channel corresponds to the subprocess $\gamma^*\gamma \to \gamma M_D$. This is forbidden for a charged meson like $\pi^\pm$, as considered in [Duplančić et al.(2018)Duplančić, Passek-Kumerički, Pire, Szymanowski, and Wallon], or for a neutral meson with even C-parity, like π^0, η, etc. In the high-q_T scattering, the $n = 1$ amplitude can be factorized into the DA of M_D.

The $n = 2$ channel has the same color structure as the DVMP process in Sec. 3.2.2.2, and the leading region is also as in Fig. 3.12 just with the proper change of the external electron lines by photon lines. The argument for factorization then works in the same way, and is not to be repeated here. For the same reason as the diphoton production process in the previous subsection, we emphasize the necessity of the hard transverse momentum q_T, which is not equivalent to requiring a large invariant mass of the γM_D pair.

3.2.3.3 Light meson pair production: $(CD) = (M_C M_D)$

The single diffractive photoproduction with $(CD) = (M_C M_D)$ differs from the electroproduction of a light meson in Sec. 3.2.2.2 by having one more hadron in the final state. This leads to one more collinear subgraph in another direction but does not make the factorization proof very different. As for the DVMP, generalizing the proof of the corresponding meson scattering in Sec. 3.1.2.3 to the diffractive case encounters the trouble of Glauber pinch for gluons attaching to the diffracted hadron. As a result, we will need to use the asymmetric contour deformation in Sec. 3.1.2.4.

First, the $n = 1$ channel is given by the subprocess $\gamma^*\gamma \to M_C M_D$, which may or may not happen depending on the quantum numbers of M_C and M_D. This was considered first in [**?**]. The t-channel crossing process $M_A\gamma \to \gamma M_D$ is briefly discussed in Sec. 3.1.2.2. The time-reversal process $M_A + M_B \to \gamma\gamma$ was also studied in [Qiu and Yu(2022)]. Its amplitude can be factorized into the DAs of M_C and M_D, as a simple generalization of the factorization proof for the process in Sec. 3.1.1.2.

For the $n = 2$ channel, the leading regions is shown in Fig. 3.18(a), where all lines in the hard part "H" are off shell by order of the hard scale $Q \sim q_T$, which effectively makes the contribution from attaching soft gluons to H power suppressed. There could be

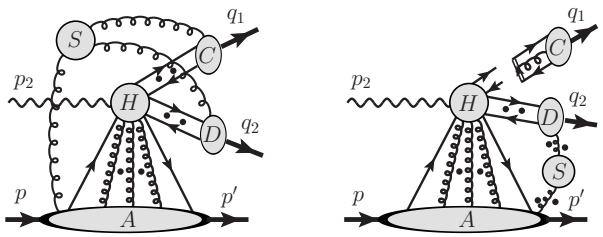

Fig. 3.18: (a) Leading-region graphs for the single diffractive hard photoproduction of a light meson pair. (b) is obtained as an intermediate step after factorizing the C-collinear subgraph out of the hard subgraph H and soft subgraph S.

additional leading regions in which one or more of the collinear subgraph is connected to the soft subgraph by one quark or transversely polarized gluon line, while connecting to the hard subgraph by the other quark or transversely polarized gluon line. Following the same assumption that such soft end point region is strongly suppressed by the nonperturbative QCD dynamics from the meson distribution amplitude, we neglect them and consider only the leading regions in Fig. 3.18(a).

Extending the factorization of the meson scattering process to the corresponding single diffractive process is trivial. The only complication arises from the extra DGLAP region in the single diffractive channel of the hadron $h \to h'$, which causes the momentum k_s of the soft gluon coupling to the A-collinear subgraph to be pinched in the Glauber region for its component $k_s \cdot w_A$, as explained in Sec. **??**. This makes the use of symmetric deformation as in Sec. 3.1.2.3 not possible. But the asymmetric deformation strategy in Sec. 3.1.2.4 applies here with no change, because we never deformed the contour of $k_s \cdot w_A$ when k_s flows through the A-collinear subgraph. The important step of factorizing the C-collinear subgraph is shown in Fig. 3.18(b). In the end, the diffractive amplitude is factorized into

the hadron GPD and meson DAs,

$$\mathcal{M}^{(2)}_{h\gamma\to h' M_C M_D} = \sum_{i,j,k} \int_{-1}^{1} dx \int_0^1 dz_C\, dz_D F^i_{hh'}(x,\xi,t;\mu) \times C_{i\gamma\to jk}(x,\xi;z_C,z_D;\boldsymbol{q}_T,\mu)\, \phi_{j/C}(z_C,\mu)\, \phi_{k/D}(z_D,\mu), \tag{3.139}$$

up to $1/q_T$ power suppressed terms, where the sum over i, j, and k runs over all possible flavors and spin structures.

3.2.4 SDHEP with a meson beam

For the SDHEP with a meson beam, we have B being some meson M_B, which is usually a pion or kaon. Similar to the case with a photon beam, we consider three cases for the particles C and D: (1) massive dilepton $(CD) = (l^+l^-)$ or diphoton $(\gamma\gamma)$ production; (2) real photon and light meson pair $(CD) = (\gamma M_D)$ production; and (3) light meson pair $(CD) = (M_C M_D)$ production. The dilepton and diphoton production processes have been studied in [Berger et al.(2001)Berger, Diehl, and Pire, Qiu and Yu(2022)], respectively, and their factorizations are similar to the DVMP process. The processes (2) and (3) have not been considered in the literature. In this section, we address the factorization of these processes in the framework of the SDHEP within the two-stage paradigm.

3.2.4.1 Massive dilepton or diphoton production: $(CD) = (l^+l^-)$ or $(\gamma\gamma)$

The SDHEPs of massive dilepton and diphoton productions are

$$h(p) + M_B(p_2) \to h'(p') + l^-(q_1) + l^+(q_2), \tag{3.140}$$

and

$$h(p) + M_B(p_2) \to h'(p') + \gamma(q_1) + \gamma(q_2), \tag{3.141}$$

respectively. Both processes have C and D being colorless elementary particles, and they are similar to the meson production in the SDHEP with a lepton beam in Sec. 3.2.2.2 and the meson-photon pair production in the SDHEP with a photon beam in Sec. 3.2.3.2, respectively. The difference comes from switching the final-state meson with the initial-state lepton or photon. The argument for the factorization works in essentially the same way, with only a slight change due to the meson being in the initial state instead of final state. In reality, only charged light meson beams such as $\pi^{\pm}$ or $K^{\pm}$ are readily accessible in experiments, so we will consider only those beams. Then charge conservation implies a flavor change of the diffractive hadron, i.e., $h' \neq h$, which forbids the γ^*-mediated $n = 1$ channel. Therefore, the leading-power contributions to the amplitudes in Eqs. (3.140) and (3.141) start with the $n = 2$ channels, which are factorized into the GPDs associated with the hadron transition $h \to h'$, as in [Berger et al.(2001)Berger, Diehl, and Pire, Qiu and Yu(2022)].

For the process in Eq. (3.140), at the lowest order in QED, the high-q_T lepton pair is produced via a timelike photon γ^*_{ll} with a high virtuality $Q \sim \mathcal{O}(q_T)$, when it is sufficiently away from the resonance region of a heavy quarkonium. This process can hence be referred to as exclusive Drell-Yan process [**?**]. It is this highly virtual photon that couples directly to the parton lines from the h-M_B interaction, whose virtuality Q provides the hard scale that localizes the parton interactions. This is sufficient for the factorization argument. Furthermore, due to the lack of γ^*-mediated $n = 1$ subprocess, the requirement of the high invariant mass for the lepton-pair is a sufficient condition for factorization, allowing us to release the high q_T requirement, which is contrary to the requirement for the lepton-pair production in

the SDHEP with a photon beam, as discussed in Sec. 3.2.3.1.

In contrast, the process in Eq. (3.141) has the two final-state photons directly couple to the parton lines, and the hard scale is solely provided by their high transverse momentum q_T, which is both the sufficient and necessary condition for collinear factorization. In the low-q_T regime, one starts to have two widely separated scales in the same process, $q_T^2 \ll \hat{s} = (p - p' + p_2)^2$, just as the photoproduction of diphoton process in Sec. 3.2.3.1, the factorization for which needs further study.

3.2.4.2 Real photon and light meson pair production: $(CD) = (\gamma M_D)$

Now we consider the process

$$h(p) + M_B(p_2) \to h'(p') + \gamma(q_1) + M_D(q_2), \tag{3.142}$$

which differs from the photoproduction of a meson pair process in Sec. **??** by switching the initial-state photon with one of the final-state mesons. The $n = 1$ channel corresponds to the subprocess $\gamma^*(p_1) + M_B(p_2) \to \gamma(q_1) + M_D(q_2)$, which has been discussed in Sec. 3.1.2.2. Depending on the quantum numbers of M_B and M_D, this channel may or may not be present. The amplitude can be factorized into the DAs of M_B and M_D.

The amplitude of $n = 2$ channel can be factorized into a GPD and two DAs, whose proof can be adapted from Sec. 3.1.2.4 with straightforward modifications: one can first factorize the D-collinear subgraph and the soft gluons attached to it, and then do the same thing for B, which is sufficient to complete the proof.

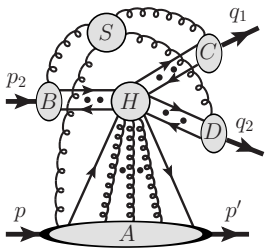

Fig. 3.19: Leading-region graphs for the single diffractive hard mesoproduction of two mesons. There can be any numbers of soft gluons connecting S to each collinear subgraph. Depending on the quantum numbers, the quark lines may be replaced by transversely polarized gluon lines. The dots represent arbitrary numbers of longitudinally polarized collinear gluons.

3.2.4.3 Light meson pair production: $(CD) = (M_C M_D)$

Now we consider the process

$$h(p) + M_B(p_2) \to h'(p') + M_C(q_1) + M_D(q_2), \tag{3.143}$$

whose corresponding $2 \to 2$ hard meson scattering is discussed in Sec. 3.1.3.3. The $n = 1$ channel, $\gamma^*(p_1) + M_B(p_2) \to M_C(q_1) + M_D(q_2)$, which may or may not contribute depending on the quantum numbers, can be analyzed in the same way as the photon-meson scattering in Secs. 3.1.2.3 and 3.1.2.4. The $n = 2$ channel has leading regions shown in Fig. 3.19, under the assumptions of strong soft-end suppression *and* a single hard scattering in which all the parton lines are off shell by the hard scale. Compared to the meson pair photoproduction process in Sec. 3.2.3.3, there is one more collinear subgraph in the initial state, and factorization works with a simple generalization. In Fig. 3.19 one does not deform the contours of soft gluon momenta k_s for their components $k_s \cdot w_A$ when they flow in the A-collinear subgraph. We first factorize C, D, and B from H sequentially, together with the soft gluons attached to them, and then group the soft gluons into the A-collinear subgraph to complete

the proof in a way similar to Sec. 3.2.3.3. Consequently, the amplitude of the diffractive process in Eq. (3.143) can be factorized into the GPD and DAs,

$$\mathcal{M}^{(2)}_{hM_B\to h'M_CM_D} = \sum_{i,j,k,l}\int_{-1}^{1} dx \int_0^1 dz_B\, dz_C\, dz_D F^i_{hh'}(x,\xi,t;\mu)\,\phi_{j/B}(z_B,\mu) \times C_{ij\to kl}(x,\xi;z_B,z_C,z_D;\boldsymbol{q}_T,\mu)\,\phi_{k/C}(z_C;\mu)\,\phi_{l/D}(z_D;\mu), \tag{3.144}$$

up to $1/q_T$ power suppressed terms, where where the sum over i, j, and k runs over all possible flavors and spin structures, and the hard coefficient $C_{ij\to kl}(x,\xi;z_B,z_C,z_D;\boldsymbol{q}_T,\mu)$ can be calculated as the scattering of two collinear parton pairs i and j into another two pairs k and l.

3.3 Further discussion on single diffractive processes

In this section, we give a few general remarks on the properties of SDHEPs, and their factorizability and sensitivities for extracting GPDs.

3.3.1 Two-stage paradigm and factorization

We have presented the arguments to prove the factorization of SDHEPs with different colliding beams and different types of final-state particles. Our proofs follow a unified two-stage approach by taking advantage of the unique feature of SDHEPs, which can be effectively separated into two stages, as specified in Eqs. (3.105) and (3.106). By requiring $q_T \gg \sqrt{-t}$, we effectively force the exchanged state A^* between the single diffractive transition of $h \to h'$ and the hard exclusive $2 \to 2$ scattering to be a low-mass and long-lived state in comparison to the timescale $\sim \mathcal{O}(1/q_T)$ of the hard exclusive process, and effectively reduce the SDHEP

into two stages: single diffractive (SD) + hard exclusive (HE) with the quantum interference between these two subprocesses suppressed by powers of $\sqrt{-t}/q_T$. As emphasized earlier, requiring large transverse momenta for the final-state particles C and D is not equivalent to requiring a large invariant mass of them, $m_{CD} \gg \sqrt{-t}$; the latter does not necessarily guarantee a hard collision.

This two-stage paradigm gives a unified picture for the microscopic mechanism of the SDHEPs, described in Eq. (3.107) and Fig. 3.9. It accounts for the γ^*-mediated $n = 1$ channel in a coherent framework, which is usually regarded as a "byproduct" of the GPD channel in the literature and can be easily forgotten but which is in fact one power higher than the GPD channel and should be incorporated unless it is forbidden by some quantum number conservation.

Furthermore, this two-stage paradigm leads to a simple methodology for proving factorization of the SDHEPs in Eq. (4.134), in particular, for the $n = 2$ channel. By treating the long-lived exchanged state A^* as a "meson" capturing the quantum number of $h \to h'$ transition, we make the corresponding scattering $A^* + B \to C + D$ effectively a $2 \to 2$ exclusive process with a single hard scale, whose factorization is relatively easier to prove. In this way, the factorization proof of the SDHEP can focus on its differences from the $2 \to 2$ hard exclusive process.

The only difference between the factorization of the $2 \to 2$ hard exclusive process and the full SDHEP is that the GPD channel supports both ERBL and DGLAP regions, and a Glauber pinch can exist for the DGLAP region. However, since we only have one diffractive hadron, only one component $k_s \cdot w_A$ of the soft gluon momentum k_s is pinched in the Glauber region. The factorizability of the corresponding $2 \to 2$ exclusive process implies that soft gluons coupling to B, C, and/or D are canceled, which applies equally to the

situation of SDHEPs. The rest of the soft gluons only couple to the diffracted hadron and can be grouped into the collinear subgraph of the diffractive hadron $h \to h'$; see Fig. 3.20 as an illustration. The factorization of soft gluons leads to the independence among different collinear subgraphs, and help to establish the factorization of the collinear subgraph of the diffractive hadron into a universal GPD, and the other collinear subgraphs into universal meson DAs.

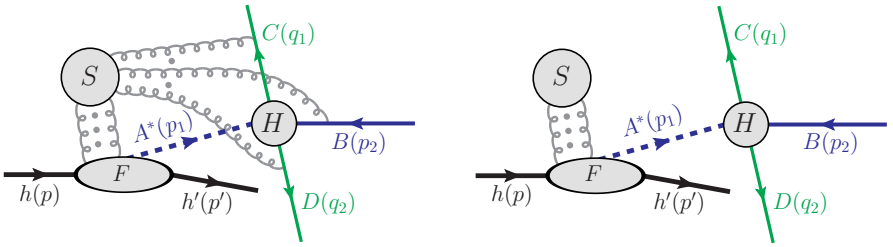

Fig. 3.20: (a) SDHEP in the general case, with all possible soft gluon connections. (b) The result of soft cancellation in (a). The cancellation of the soft gluons in the $2 \to 2$ hard exclusive scattering implies the same cancellation of the soft gluons that couple to B, C, and/or D.

3.3.2 Assumptions for the exclusive factorization

The keys to collinear factorization are the cancellation of soft subgraphs that connect to different collinear subgraphs and the factorization of all collinear subgraphs from the infrared-safe short-distance hard part.

The first assumption that we made is that the leading active quark lines or transversely polarized gluon lines from the mesons must be coupled to the hard interaction, but not to the soft subgraph, for which we effectively assume that we could get an additional suppression from the expected end point behavior of meson wave function, when one of the active quarks (or gluons) has a soft momentum, which we have referred to as the soft-end suppression. The

result of this assumption is that, to the leading power, the soft subgraph is only connected to collinear subgraphs by gluon lines that are longitudinally polarized, for which Ward identity can be applied to factorize them onto Wilson lines. The soft Wilson lines are only connected to the rest of the graph by colors, and can be disentangled and factorized from the collinear subgraphs because the collinear subgraphs are in color singlet states, which is an important feature of exclusive processes. Consequently, the soft cancellation for the factorization of SDHEPs is very different from typical soft cancellation for the factorization of inclusive processes [Collins et al.(1989)Collins, Soper, and Sterman].

Another consequence of the soft-end suppression is that we are allowed to constrain the light-cone parton momenta of the mesons on the real axis and arrive at a definition of meson DA, $\phi(z)$ with $0 < z < 1$, as argued at the end of Sec. 3.2.2.1.

This assumption was also applied to most factorizations of exclusive processes involving high-momentum mesons, notably for the pion form factor and large-angle production processes; see the review [Brodsky and Lepage(1989)]. Even though the soft-end region was conjectured to be Sudakov suppressed in [Brodsky and Lepage(1989)], which is more than the power suppression taken as our assumption, a more extensive discussion on this issue is still lacking in the literature.

The second assumption that we implicitly made is that there is only one single hard interaction in which all the parton lines are effectively off shell by the hard scale. This applies especially to the mesoproduction of a meson pair process in Secs. 3.1.3.3 and 3.2.4.3. It is well known that the exclusive hadron-hadron scattering into large-angle hadrons can happen via multiple hard interactions, which has an enhanced power counting with respect to the single hard interaction [Landshoff(1974), Botts and Sterman(1989)]. We have shown the factorization for the hard exclusive $2 \to 2$ meson-meson scattering and the correspond-

ing SDHEP with a meson beam for the single hard interaction case. Within the two-stage paradigm, it is unclear to us whether the factorization of the large-angle meson-meson scattering via multiple hard interactions can imply a corresponding factorization for the SDHEP with a meson beam; it is left for future study.

One may also consider representing A^* as a sum over virtual hadronic states, instead of the expansion in terms of partonic states like $[q\bar{q}']$ and $[gg]$. However, the exchanged state A^* in the SDHEP enters a hard collision, which has a resolution scale $1/Q$ much smaller than the typical hadronic scale, and therefore it is the partonic degrees of freedom inside the virtual hadronic state or the diffractive hadron that are probed. For example, the leading-power contribution from a virtual hadronic state should also be mediated by two active parton lines, just as in Figs. 3.1(b), 3.3(a), 3.5(a), 3.6(a), and 3.7(a), along with the same short-distance hard part as the $n = 2$ partonic channel in connection with GPDs. In principle, to this power, one should add all the two-parton-mediated contributions from all possible virtual hadronic states of the same diffractive hadron, which could possibly recover the full contributions from the corresponding GPDs of the same hadron, but, only from their ERBL region. GPDs also contain the DGLAP region, which cannot be covered by the subprocesses mediated by virtual hadronic states. The approach of taking out a virtual meson A^* from the $h \to h'$ transition, described by some form factor $F^A_{h\to h'}(t)$, followed by extracting two parton lines via its distribution amplitude, should also be captured by the GPD of $h \to h'$ transition in a more general sense. The choice to represent A^* by a single virtual meson state, like the Sullivan process, is therefore an additional approximation. On the other hand, the expansion in terms of the number of partons, n, is an expansion in powers of $1/Q$.

3.3.3 Non-factorizability of double diffractive processes

From the procedure for proving factorization in the two-stage paradigm, it is easy to understand the importance of the *single* diffraction for factorizability of the exclusive process. The whole difficulty from the diffraction is the DGLAP region that pinches one component of the soft gluon momentum in the Glauber region, and we get away with it by only deforming the other components associated with other mesons. After factorizing out all the other mesons, the rest of the soft gluons are only coupled to the diffracted hadron and can be grouped together into this hadron's GPDs.

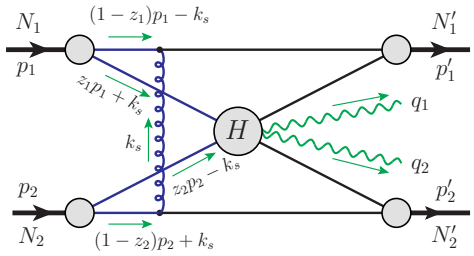

Fig. 3.21: Diphoton production in a double diffractive hard exclusive scattering process between two head-on hadrons N_1 and N_2 along the z axis.

If we consider the double diffractive process, as shown in Fig. 3.21, the soft gluon k_s exchanged between the remnants along opposite directions is pinched in the Glauber region for both k_s^+ and k_s^-, and thus no deformation can be done to get it out. As a result, this process cannot be factorized, even if we do have a hard scale provided by the transverse momentum q_T of the final-state photon pair.

Similar conclusion holds for the *inclusive* diffractive processes [Soper(1997), Collins(1998)]. The observation of the diffracted hadron anchors the inclusive sum over the final state and forbids the use of unitarity to cancel the Glauber gluon exchanges. While the soft gluon momentum can be deformed out of the Glauber region for single diffractive inclusive processes [Collins(1998)], in a similar way to the exclusive processes discussed in this paper, it

does not work for inclusive diffractive hadron-hadron scattering [Landshoff and Polkinghorne(1971), Henyey and Savit(1974), Cardy and Winbow(1974), DeTar et al.(1975)DeTar, Ellis, and Landshoff, Collins et al.(1993)Collins, Frankfurt, and Strikman, Soper(1997)].

This phenomenon is very similar to the factorization of Drell-Yan process at high twists [Qiu and Sterma Qiu and Sterman(1991b)], where the hadron connected by more than two active partons to the hard part is analogous to the diffracted hadron here. Even though the extra transversely polarized gluon lines at a high twist may be confused by soft gluons and endangers factorization, this is still factorizable as one can first factorize soft gluons out of the other hadron at the leading twist, similar to the procedure for the single diffractive process here that we first factorize the soft gluons out of the other mesons. This can only be done at the *first* subleading twist for which one of the two hadrons still has a twist-2 PDF involved, and so the Drell-Yan process is not factorizable beyond the first nonvanishing subleading twist, similar to the nonfactorizability of double diffractive processes.

3.3.4 Comparison to high-twist inclusive processes

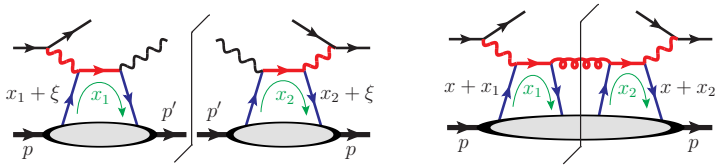

(a) (b)

Fig. 3.22: Sample leading-order cut diagrams for (a) DVCS amplitude squared and (b) inclusive DIS cross section at twist-4. The red thick lines indicate the hard parts, and the blue lines are collinear partons.

The factorization of exclusive processes at the amplitude level shares many common features with the inclusive process factorization at a high twist. Taking the leading-order DVCS amplitude as an example, we show the amplitude square as a cut diagram in Fig. 3.22(a),

which is compared with one of the leading-order diagrams of the inclusive DIS at twist-4 in Fig. 3.22(b). They only differ in that the cut line for the DVCS forces an exclusive final state. Both diagrams have two collinear parton lines connecting the hadron-collinear subgraph to the hard part, in both the amplitude to the left of the cut and conjugate amplitude to the right. In this sense, the DVCS amplitude squared corresponds to a twist-4 contribution to the cross section of the real photon electroproduction process. On the other hand, the amplitude squared of the $n = 1$ channel for the γ^*-mediated subprocess corresponds to a twist-2 contribution [see Fig. 3.23(a)], and the interference between the $n = 1$ and $n = 2$ channels corresponds to a twist-3 contribution [see Fig. 3.23(b)].

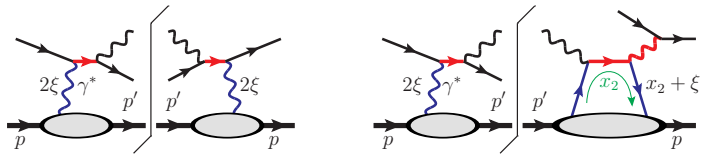

(a) (b)

Fig. 3.23: Sample cut diagrams of the amplitude squared of the real photon electroproduction process for (a) the γ^*-mediated channel, and (b) the interference between the γ^*-mediated channel and GPD channel. The red thick lines indicate the hard parts, and the blue lines are collinear partons or photons.

In the DVCS amplitude in Fig. 3.22(a), the two partons carry momenta $(x_1 + \xi)P^+$ and $(x_1 - \xi)P^+$ (following the directions indicated by the curved arrow), with x_1 integrated in $[-1, 1]$. In its conjugate amplitude, the two partons carry momenta $(x_2 \pm \xi)P^+$ with x_2 integrated in the same range. Similarly, for the twist-4 DIS diagram in Fig. 3.22(b), the amplitude part has two collinear partons with momenta $(x + x_1)p^+$ and $x_1\, p^+$, with x_1 integrated in $[-1, 1 - x]$. The conjugate amplitude part has two collinear partons with momenta $(x + x_2)p^+$ and $x_2\, p^+$, with x_2 integrated in the same range. In both cases, the x_1 and x_2 integrations are not related and to be integrated independently. Only the total momentum of the two partons, which is $2\xi P^+$ for the DVCS and xp^+ for the twist-4 DIS,

is observable, whose dependence is probed by the experiment.

On the other hand, there are soft breakpoint poles of x_1 (or x_2), given by the situations when one of the two partons has zero momentum, which is $x_1 = \pm\xi$ for DVCS and $x_1 = 0$ or $-x$ for twist-4 DIS. However, those poles are not pinched and they happen at the middle part of the x_1 integration range. As a result, we can deform the contour of x_1 to avoid them, just as discussed around Eq. (3.130). This situation is contrary to the DA factorization, for which the soft poles happen at the end points of the DA integration and cannot be deformed away, which requires us to make the soft-end suppression assumption in Sec. 3.3.2.

Chapter 4

Generalized parton distributions

The generalized parton distributions (GPDs) resulting from factorization of single diffractive exclusive scattering processes are important nonperturbative parton correlation functions that reveal many aspects of the confined partonic structures of hadrons. By their universal operator definitions, GPDs can be studied by themselves. Their values can be obtained by nonperturbative calculation methods like Lattice QCD [**?**], which will not be discussed in this paper, or by fitting to experimental data by virtue of the factorization theorem discussed in Sec. 3. Nevertheless, the exclusive nature of the GPD factorization poses substantial challenges for the fitting programs, which makes the extraction of GPDs, especially their x dependence, from experimental data, extremely difficult. This is our focus in this section. First, we will first review some important properties of GPDs, especially their roles in unveiling the hadron structures. And then we will discuss various processes that can be used to probe the x dependence of GPDs. We will introduce a type of processes that can provide enhanced sensitivity to the x dependence, and demonstrate how well they can help determine the latter. We will close this section by proposing a global analysis of all types of observables that can be used for the task of determining GPDs.

4.1 GPD properties

4.1.1 Definitions and spin dependence

As remarked below Eq. (3.128), the GPDs defined in Eq. (3.125) contain full dependence on the hadron spin states. This shall be separated by decomposing the matrix elements into independent form factors,

$$\begin{aligned} F^q(x,\xi,t) &= \int \frac{dy^-}{4\pi} e^{-ixP^+ y^-} \langle p',s'|\bar{\psi}_q\left(y^-/2\right)\,\gamma^+\,\psi_q\left(-y^-/2\right)|p,s\rangle \\ &= \frac{1}{2P^+}\bar{u}(p',s')\left[H^q(x,\xi,t)\gamma^+ - E^q(x,\xi,t)\frac{i\sigma^{+\alpha}\Delta_\alpha}{2m}\right]u(p,s), \qquad (4.1a) \\ \widetilde{F}^q(x,\xi,t) &= \int \frac{dy^-}{4\pi} e^{-ixP^+ y^-} \langle p',s'|\bar{\psi}_q\left(y^-/2\right)\,\gamma^+\gamma_5\,\psi_q\left(-y^-/2\right)|p,s\rangle \\ &= \frac{1}{2P^+}\bar{u}(p',s')\left[\widetilde{H}^q(x,\xi,t)\gamma^+\gamma_5 - \widetilde{E}^q(x,\xi,t)\frac{\gamma_5\Delta^+}{2m}\right]u(p,s), \qquad (4.1b) \end{aligned}$$

where we take the hadron states as protons for definiteness, and use the kinematic convention in Eq. (3.122). s and s' explicitly denote the spin states. The Δ differs from the usual convention [Diehl(2003)] by a sign, which has been compensated by the minus sign in front of E and $\widetilde{E}$ such that the GPDs are the same. We have dropped the time ordering and omitted the Wilson lines. This decomposition is done by Lorentz covariance, parity invariance, and

the Dirac matrix properties. The same decomposition applies to gluon GPDs,

$$
\begin{aligned}
F^g(x,\xi,t) &= \delta^{ij}\int\frac{dy^-}{2\pi P^+}e^{-ixP^+y^-}\langle p',s'|G^{+i}\left(y^-/2\right)G^{+j}\left(-y^-/2\right)|p,s\rangle \\
&= \frac{1}{2P^+}\bar{u}(p',s')\left[H^g(x,\xi,t)\gamma^+ - E^g(x,\xi,t)\frac{i\sigma^{+\alpha}\Delta_\alpha}{2m}\right]u(p,s), \qquad (4.2a)\\
\widetilde{F}^g(x,\xi,t) &= -i\epsilon_T^{ij}\int\frac{dy^-}{2\pi P^+}e^{-ixP^+y^-}\langle p',s'|G^{+i}\left(y^-/2\right)G^{+j}\left(-y^-/2\right)|p,s\rangle \\
&= \frac{1}{2P^+}\bar{u}(p',s')\left[\widetilde{H}^g(x,\xi,t)\gamma^+\gamma_5 - \widetilde{E}^g(x,\xi,t)\frac{\gamma_5\Delta^+}{2m}\right]u(p,s). \qquad (4.2b)
\end{aligned}
$$

It is the scalar coefficients $H^{q,g}$, $\widetilde{H}^{q,g}$, $E^{q,g}$, $\widetilde{E}^{q,g}$ that are usually referred to as GPDs, which are constrained to be real functions that are even in ξ. In this paper we loosely refer to both these coefficients and F's, $\widetilde{F}$'s as GPDs. There are also form factor decompositions for the transversity GPDs, but we will discuss them in this paper.

In the GPD definitions, the parton spin states are dictated by the spinor or tensor projectors, γ^+ and $\gamma^+\gamma_5$, or δ^{ij} and $-i\epsilon_T^{ij}$, whereas the proton spin structures are selected by the different form factors. However, it is not straightforward to quantitatively describe them. First, the partons in GPDs are not on-shell, but instead we have integrated out their transverse and minus momentum components (see the discussion above Eq. (3.125)). Second, the proton states are not both along the z direction, and one can even go to a frame where both p and p' are not along the z direction. On the other hand, the parton states in the hard scattering have been projected to be on-shell along the z direction, and their spin states can be chosen as the helicities. To unify the whole picture, we introduce the concept of light-cone helicity state.

4.1.1.1 Transverse boost and light-cone helicity

A *transverse boost* $\Lambda(\boldsymbol{v})$ is a special Lorentz transformation that transforms a momentum k to $k'^{\mu} = \Lambda^{\mu}{}_{\nu}(\boldsymbol{v})k^{\nu}$ by

$$k'^{+} = k^{+}, \quad \boldsymbol{k}'_{T} = \boldsymbol{k}_{T} + \sqrt{2}k^{+}\boldsymbol{v}, \quad k'^{-} = k^{-} + \sqrt{2}\boldsymbol{k}_{T}\cdot\boldsymbol{v} + k^{+}v^{2}, \tag{4.3}$$

where $\boldsymbol{v} = (v_1, v_2)$ is a transverse vector and $v^2 = v_1^2 + v_2^2$. This keeps the plus momentum invariant but shifts the transverse momentum (the k^- transformation is determined by requiring k^2 to be invariant). The transformation matrix $\Lambda(\boldsymbol{v})$ can be written in the Cartesian coordinate system as

$$\Lambda(\boldsymbol{v}) = (\Lambda^{\mu}{}_{\nu}(\boldsymbol{v})) = \begin{pmatrix} 1+v^2/2 & v_1 & v_2 & v^2/2 \\ v_1 & 1 & 0 & v_1 \\ v_2 & 0 & 1 & v_2 \\ -v^2/2 & -v_1 & -v_2 & 1-v^2/2 \end{pmatrix} \simeq 1 + \begin{pmatrix} 0 & v_1 & v_2 & 0 \\ v_1 & 0 & 0 & v_1 \\ v_2 & 0 & 0 & v_2 \\ 0 & -v_1 & -v_2 & 0 \end{pmatrix}. \tag{4.4}$$

In the last step, we have taken the small v approximation and thrown away higher power terms. This helps identify the transverse boost generators with the usual boost and rotation generators, $\boldsymbol{K} = (K_1, K_2, K_3)$ and $\boldsymbol{J} = (J_1, J_2, J_3)$, as $\boldsymbol{T} = (T_1, T_2)$,

$$T_1 = K_1 + J_2, \quad T_2 = K_2 - J_1. \tag{4.5}$$

The transverse boost can then be written as

$$\Lambda(\boldsymbol{v}) = e^{-i\boldsymbol{T}\cdot\boldsymbol{v}}. \tag{4.6}$$

This induces the transverse boost operator $\hat{U}(\boldsymbol{v}) = \exp\Big(-i\hat{\boldsymbol{T}}\cdot\boldsymbol{v}\Big)$ that acts on the quantum Hilbert space.

Using Eq. (4.5) and the Poincare algebra, we can get $[T_1, T_2] = 0$ and work out their commutation relations with the momentum operator $\hat{P}^\mu$,

$$[\hat{T}^i, \hat{P}^+] = 0, \quad [\hat{T}^i, \hat{P}^-] = -\sqrt{2}i\hat{P}^i, \quad [\hat{T}^i, \hat{P}^j] = -i\delta^{ij}\sqrt{2}\hat{P}^+, \tag{4.7}$$

where $i, j = 1, 2$ are the transverse indices, and we take $\hat{T}^i = \hat{T}_i$. By defining $\hat{P}^\mu(\boldsymbol{v}) = \hat{U}(\boldsymbol{v})\hat{P}^\mu\hat{U}^{-1}(\boldsymbol{v})$, we have

$$\frac{\partial}{\partial v^i}\hat{P}^\mu(\boldsymbol{v}) = \hat{U}(\boldsymbol{v})(-i)\left[\hat{T}^i, \hat{P}^\mu\right]\hat{U}^{-1}(\boldsymbol{v}), \tag{4.8}$$

which gives

$$\frac{\partial}{\partial v^i}\hat{P}^+(\boldsymbol{v}) = 0, \quad \frac{\partial}{\partial v^i}\hat{P}^j(\boldsymbol{v}) = -\delta^{ij}\sqrt{2}\hat{P}^+(\boldsymbol{v}), \quad \frac{\partial}{\partial v^i}\hat{P}^-(\boldsymbol{v}) = -\sqrt{2}\hat{P}^i(\boldsymbol{v}). \tag{4.9}$$

This gives the solution,

$$\hat{U}(\boldsymbol{v})\hat{P}^\mu\hat{U}^{-1}(\boldsymbol{v}) = \left(\hat{P}^+, \hat{P}^- - \sqrt{2}\hat{\boldsymbol{P}}\cdot\boldsymbol{v} + \hat{P}^+v^2, \hat{\boldsymbol{P}}_T - \sqrt{2}\hat{P}^+\boldsymbol{v}\right). \tag{4.10}$$

A one-particle state can be specified by its plus and transverse momentum, $|k^+, \boldsymbol{k}_T\rangle$, with its minus momentum component determined as $k^- = (k^2 + k_T^2)/(2k^+$. After acting on it a

transverse boost operation, we have

$$\begin{aligned}\hat{P}^\mu \hat{U}(\boldsymbol{v})|k^+, \boldsymbol{k}_T\rangle &= \hat{U}(\boldsymbol{v})\hat{P}^\mu(-\boldsymbol{v})|k^+, \boldsymbol{k}_T\rangle \\ &= \left(k^+, k^- + \sqrt{2}\boldsymbol{k}_T \cdot \boldsymbol{v} + k^+ v^2, \boldsymbol{k}_T + \sqrt{2}k^+\boldsymbol{v}\right) \hat{U}(\boldsymbol{v})|k^+, \boldsymbol{k}_T\rangle. \end{aligned} \tag{4.11}$$

Therefore,

$$\hat{U}(\boldsymbol{v})|k^+, \boldsymbol{k}_T\rangle = |k^+, \boldsymbol{k}_T + \sqrt{2}k^+\boldsymbol{v}\rangle \tag{4.12}$$

realizes the same momentum transformation as in Eq. (4.3).

The usual helicity state $|\boldsymbol{k}, \lambda\rangle$ is defined by transforming from the basic reference state $|k_0\hat{z}, \lambda\rangle$ by first boosting along the z direction such that it has the same energy as k, and then rotating around the y and z axes to reach the momentum $\boldsymbol{k}$ (see Ch. 7 for details),

$$|\boldsymbol{k}, \lambda\rangle \equiv U(R_z(\phi))U(R_y(\theta))U(\Lambda_z(\beta))|k_0\hat{z}, \lambda\rangle. \tag{4.13}$$

For such helicity state, the spin quantization axis is the momentum direction, which transforms as we rotate the momentum. A rotation around the z axis thus transforms $|\boldsymbol{k}, \lambda\rangle$ in a trivial way (see the discussion below Eq. (7.38) in Ch. 7),

$$U(R_z(\alpha))|\boldsymbol{k}, \lambda\rangle = |R_z(\alpha)\boldsymbol{k}, \lambda\rangle, \tag{4.14}$$

without any phase signifying a spin component along the z direction.

In a similar way, we define the light-cone helicity state $|k^+, \boldsymbol{k}_T, \lambda\rangle$ by transforming from the basic reference state $|k_0^+, \boldsymbol{0}_T, \lambda\rangle$. First boost along z to reach the plus momentum k^+.

Then perform a transverse boost with $\boldsymbol{v} = \boldsymbol{k}_T/(\sqrt{2}k^+)$, that is,

$$|k^+, \boldsymbol{k}_T, \lambda\rangle = U\left(\frac{\boldsymbol{k}_T}{\sqrt{2}k^+}\right)|k^+, \boldsymbol{0}_T, \lambda\rangle. \tag{4.15}$$

This applies to both massless and massive particle states. Since the transverse boosts form an Abelian subgroup, acting a transverse boost on $|k^+, \boldsymbol{k}_T, \lambda\rangle$ only changes the momentum component $\boldsymbol{k}_T$, but keeps k^+ and λ invariant. Also, by using $[\boldsymbol{T}, K_3] = i\boldsymbol{T}$ and thus

$$e^{-iK_3\beta}\,\boldsymbol{T}\,e^{iK_3\beta} = e^{-\beta}\boldsymbol{T}, \tag{4.16}$$

the light-cone helicity state transforms under a longitudinal boost as

$$\begin{aligned} e^{-iK_3\beta}|k^+, \boldsymbol{k}_T, \lambda\rangle &= \left(e^{-iK_3\beta}e^{-i\boldsymbol{T}\cdot\boldsymbol{v}}e^{iK_3\beta}\right)e^{-iK_3\beta}|k^+, \boldsymbol{0}_T, \lambda\rangle \\ &= e^{-i\boldsymbol{T}\cdot(e^{-\beta}\boldsymbol{v})}|e^{\beta}k^+, \boldsymbol{0}_T, \lambda\rangle \\ &= |e^{\beta}k^+, \boldsymbol{k}_T, \lambda\rangle, \end{aligned} \tag{4.17}$$

which keeps the light-cone helicity invariant. Similarly, under a rotation around the z direction, the state transforms as

$$\begin{aligned} e^{-iJ_3\alpha}|k^+, \boldsymbol{k}_T, \lambda\rangle &= \left(e^{-iJ_3\alpha}e^{-i\boldsymbol{T}\cdot\boldsymbol{v}}e^{iJ_3\alpha}\right)e^{-iJ_3\alpha}|k^+, \boldsymbol{0}_T, \lambda\rangle \\ &= e^{-i\lambda\alpha}e^{-i\boldsymbol{T}\cdot[R_z(\alpha)\boldsymbol{v}]}|k^+, \boldsymbol{0}_T, \lambda\rangle \\ &= e^{-i\lambda\alpha}|k^+, R_z(\alpha)\boldsymbol{k}_T, \lambda\rangle, \end{aligned} \tag{4.18}$$

which is obtained by using $[J_3, T_1] = iT_2$, $[J_3, T_2] = -iT_1$ and

$$e^{-iJ_3\alpha}\,\boldsymbol{T}\,e^{iJ_3\alpha} = R_z^{-1}(\alpha)\,\boldsymbol{T}. \tag{4.19}$$

Eqs. (4.17) and (4.18) establish the light-cone helicity λ with a physical interpretation of the spin component along the z direction.

We note the difference between the light-cone helicity state and the canonical spin state. The latter only applies to a massive state and is defined by boosting the basic reference state $|0, s\rangle$ along the momentum direction,

$$|\boldsymbol{k}, j, s\rangle = e^{-i\boldsymbol{K}\cdot\boldsymbol{\beta}}|0, j, s\rangle = U(R_3(\phi)R_2(\theta))e^{-iK_3\beta}U^{-1}(R_3(\phi)R_2(\theta))|0, j, s\rangle, \tag{4.20}$$

where $\boldsymbol{\beta} = \boldsymbol{k}/k^0$ and $\beta = |\boldsymbol{\beta}$. This is related to the helicity state by

$$|\boldsymbol{k}, j, s\rangle = e^{is\phi}\sum_{\lambda} d^j_{s\lambda}(\theta)\,|\boldsymbol{k}, j, \lambda\rangle. \tag{4.21}$$

Under a rotation around the z direction, this also transforms as $|\boldsymbol{k}, j, s\rangle \to e^{-is\alpha}|\boldsymbol{k}, j, s\rangle$. But under a boost along the z direction, s is not kept invariant. By using Eqs. (7.41) and (7.42), it transforms into

$$\begin{aligned} U(\Lambda_z(\beta))|\boldsymbol{k}, j, s\rangle &= e^{is\phi}\sum_{\lambda,\lambda'} d^j_{s\lambda}(\theta)\,|\Lambda_z(\beta)\boldsymbol{k}, j, \lambda'\rangle\, d^j_{\lambda'\lambda}\left(\chi(\beta, k)\right) \\ &= e^{is\phi}\sum_{\lambda} d^j_{s\lambda}\left(\theta - \chi(\beta, k)\right)|\Lambda_z(\beta)\boldsymbol{k}, j, \lambda\rangle \\ &= \sum_{s'} e^{is\phi}\, d^j_{ss'}\left(\theta - \chi(\beta, k) - \theta'(\Lambda k)\right)\, e^{-is'\phi}\,|\Lambda_z(\beta)\boldsymbol{k}, j, s'\rangle, \end{aligned} \tag{4.22}$$

where $\theta'(\Lambda k)$ is the polar angle of the momentum $\Lambda_z(\beta)\boldsymbol{k}$ after the boost, which is not equal to $\theta - \chi(\beta, k)$. Therefore, the canonical spin component s shall only be interpreted as the spin component along the z direction in the rest frame, but not in the boosted frame.

4.1.1.2 Light-front quantization

The light-cone helicity state defined in Eq. (4.15) applies to both massive and massless particles. One may designate such states into field decomposition and define single-particle creation and annihilation operators. For a fermion field, the amplitude for annihilating a state at some point x is given by

$$\langle 0|\psi(x)|k^+, \boldsymbol{k}_T, \lambda\rangle = u_\lambda(k^+, \boldsymbol{k}_T)e^{-ik\cdot x}, \tag{4.23}$$

which defines the spinor $u_\lambda(k^+, \boldsymbol{k}_T)$ associated with this state. By using the definition in Eq. (4.15), the left-hand side of Eq. (4.23) becomes

$$\begin{aligned}\langle 0|\psi(x)U(\boldsymbol{v})|k^+, \boldsymbol{0}_T, \lambda\rangle &= \langle 0|U^{-1}(\boldsymbol{v})\,\psi(x)\,U(\boldsymbol{v})|k^+, \boldsymbol{0}_T, \lambda\rangle \\ &= S(\boldsymbol{v})\langle 0|\psi\left(\Lambda^{-1}(\boldsymbol{v})x\right)|k^+, \boldsymbol{0}_T, \lambda\rangle = S(\boldsymbol{v})u_\lambda(k^+, \boldsymbol{0}_T)e^{-ik\cdot x},\end{aligned} \tag{4.24}$$

which therefore gives the definition for the spinor, in a similar way to the state definition,

$$u_\lambda(k^+, \boldsymbol{k}_T) = S(\boldsymbol{v})\,u_\lambda(k^+, \boldsymbol{0}_T). \tag{4.25}$$

Here $S(\boldsymbol{v})$ is the Lorentz group representation for the Dirac spinor associated with the transverse boost $\Lambda(\boldsymbol{v})$. It can be easily solved by using the generator definitions in Eq. (4.5),

and gives the explicit spinor definitions,

$$u_+(k^+,\boldsymbol{k}_T)=\left[\sqrt{2}k^+\right]^{1/2}\begin{pmatrix}\frac{m}{\sqrt{2}k^+}\begin{pmatrix}1\\0\end{pmatrix}\\ \begin{pmatrix}1\\ \frac{k_T\,e^{i\phi}}{\sqrt{2}k^+}\end{pmatrix}\end{pmatrix},\quad u_-(k^+,\boldsymbol{k}_T)=\left[\sqrt{2}k^+\right]^{1/2}\begin{pmatrix}\begin{pmatrix}-\frac{k_T\,e^{-i\phi}}{\sqrt{2}k^+}\\1\end{pmatrix}\\ \frac{m}{\sqrt{2}k^+}\begin{pmatrix}0\\1\end{pmatrix}\end{pmatrix},\tag{4.26}$$

where we took $\boldsymbol{k}_T=k_T(\cos\phi,\sin\phi)$. The spinors for antiparticles can be obtained in the same way, or by simply using charge conjugation relation $v_\lambda(k^+,\boldsymbol{k}_T)=i\gamma^2u^*_\lambda(k^+,\boldsymbol{k}_T)$,

$$v_+(k^+,\boldsymbol{k}_T)=\left[\sqrt{2}k^+\right]^{1/2}\begin{pmatrix}\begin{pmatrix}\frac{k_T\,e^{-i\phi}}{\sqrt{2}k^+}\\-1\end{pmatrix}\\ \frac{m}{\sqrt{2}k^+}\begin{pmatrix}0\\1\end{pmatrix}\end{pmatrix},\quad v_-(k^+,\boldsymbol{k}_T)=\left[\sqrt{2}k^+\right]^{1/2}\begin{pmatrix}\frac{m}{\sqrt{2}k^+}\begin{pmatrix}1\\0\end{pmatrix}\\ \begin{pmatrix}-1\\ -\frac{k_T\,e^{i\phi}}{\sqrt{2}k^+}\end{pmatrix}\end{pmatrix}.\tag{4.27}$$

It is straightforward to verify that the light-cone helicity spinors satisfy the usual normalization relations,

$$\begin{aligned}
&\bar u_\lambda(k^+,\boldsymbol{k}_T)\,u_{\lambda'}(k^+,\boldsymbol{k}_T)=2m\delta_{\lambda\lambda'},\quad \bar v_\lambda(k^+,\boldsymbol{k}_T)\,v_{\lambda'}(k^+,\boldsymbol{k}_T)=-2m\delta_{\lambda\lambda'},\\
&u^\dagger_\lambda(k^+,\boldsymbol{k}_T)\,u_{\lambda'}(k^+,\boldsymbol{k}_T)=2E\delta_{\lambda\lambda'},\quad v^\dagger_\lambda(k^+,\boldsymbol{k}_T)\,v_{\lambda'}(k^+,\boldsymbol{k}_T)=2E\delta_{\lambda\lambda'},\\
&\bar u_\lambda(k^+,\boldsymbol{k}_T)\,\gamma^\mu\,u_{\lambda'}(k^+,\boldsymbol{k}_T)=\bar v_\lambda(k^+,\boldsymbol{k}_T)\,\gamma^\mu\,v_{\lambda'}(k^+,\boldsymbol{k}_T)=2k^\mu\delta_{\lambda\lambda'},
\end{aligned}\tag{4.28}$$

with $E = (k^+ + k^-)/\sqrt{2}$, the orthogonality,

$$\bar{u}_\lambda(k^+, \boldsymbol{k}_T)\, v_{\lambda'}(k^+, \boldsymbol{k}_T) = \bar{v}_\lambda(k^+, \boldsymbol{k}_T)\, u_{\lambda'}(k^+, \boldsymbol{k}_T) = 0, \tag{4.29}$$

and the sum rules,

$$\sum_\lambda u_\lambda(k^+, \boldsymbol{k}_T)\, \bar{u}_\lambda(k^+, \boldsymbol{k}_T) = \not{k} + m, \quad \sum_\lambda v_\lambda(k^+, \boldsymbol{k}_T)\, \bar{v}_\lambda(k^+, \boldsymbol{k}_T) = \not{k} - m. \tag{4.30}$$

The same procedure can apply to a vector particle state, which is annihilated by the vector field by

$$\langle 0|A^\mu(x)|k^+, \boldsymbol{k}_T, \lambda\rangle = \epsilon^\mu_\lambda(k^+, \boldsymbol{k}_T) e^{-ik\cdot x}, \tag{4.31}$$

where the polarization vector $\epsilon^\mu_\lambda(k^+, \boldsymbol{k}_T)$ is defined by the transverse boost in a similar way to Eq. (4.25),

$$\epsilon^\mu_\lambda(k^+, \boldsymbol{k}_T) = \Lambda^\mu{}_\nu(\boldsymbol{v})\, \epsilon^\nu_\lambda(k^+, \boldsymbol{0}_T). \tag{4.32}$$

For massless vector bosons, the basic polarization vector is transverse, $\epsilon^\mu_\lambda(k^+, \boldsymbol{0}_T) = (0, \boldsymbol{\epsilon}_T, 0)$, where $\boldsymbol{\epsilon}_T = (\epsilon^1_T, \epsilon^2_T)$ is the transverse part. With the help of Eq. (4.4), this then gives the polarization vector for a general momentum,

$$\epsilon^\mu_\lambda(k^+, \boldsymbol{k}_T) = \left(\frac{\boldsymbol{k}_T\cdot\boldsymbol{\epsilon}_T}{\sqrt{2}k^+}, \boldsymbol{\epsilon}_T, -\frac{\boldsymbol{k}_T\cdot\boldsymbol{\epsilon}_T}{\sqrt{2}k^+}\right) = \left(0^+, \frac{\boldsymbol{k}_T\cdot\boldsymbol{\epsilon}_T}{k^+}, \boldsymbol{\epsilon}_T\right), \tag{4.33}$$

where the last expression is in light-front coordinates. We note that it has the same transverse component as the basic vector $\epsilon^\mu_\lambda(k^+, \boldsymbol{0}_T)$.

With the fixed definitions of the spinors and polarization vectors for arbitrary momenta, one can decompose the fields in terms of the light-cone helicity state creation and annihilation

operators. For a fermion field, one has

$$\psi(x) = \sum_{\lambda} \int \frac{dk^+ d^2\boldsymbol{k}_T}{(2\pi)^3\sqrt{2k^+}} \left[b(k^+, \boldsymbol{k}_T, \lambda)\, u_\lambda(k^+, \boldsymbol{k}_T)\, e^{-ik\cdot x} + d^\dagger(k^+, \boldsymbol{k}_T, \lambda)\, v_\lambda(k^+, \boldsymbol{k}_T)\, e^{ik\cdot x} \right], \tag{4.34}$$

where $b(k^+, \boldsymbol{k}_T, \lambda)$ and $d(k^+, \boldsymbol{k}_T, \lambda)$ respectively annihilate a fermion and an anti-fermion with momentum $(k^+, \boldsymbol{k}_T)$ and light-cone helicity λ, and the integration of k^+ is from 0 to ∞. And for a massless vector field, one has

$$A^\mu(x) = \sum_{\lambda} \int \frac{dk^+ d^2\boldsymbol{k}_T}{(2\pi)^3\sqrt{2k^+}} \left[a(k^+, \boldsymbol{k}_T, \lambda)\, \epsilon^\mu_\lambda(k^+, \boldsymbol{k}_T)\, e^{-ik\cdot x} + a^\dagger(k^+, \boldsymbol{k}_T, \lambda)\, \epsilon^{\mu *}_\lambda(k^+, \boldsymbol{k}_T)\, e^{ik\cdot x} \right], \tag{4.35}$$

where $\lambda = \pm 1$, and we have taken A to be a Hermitian field, as is the case for photons and gluons. The operators $a(k^+, \boldsymbol{k}_T, \lambda)$ and $a^\dagger(k^+, \boldsymbol{k}_T, \lambda)$ respectively annihilate and create a vector boson with momentum $(k^+, \boldsymbol{k}_T)$ and light-cone helicity λ. Then Eqs. (4.23) and (4.31) can be realized by the field decompositions in Eqs. (4.34) and (4.35) provided the single-particle definitions

$$|k^+, \boldsymbol{k}_T, \lambda\rangle = \sqrt{2k^+}\, a^\dagger(k^+, \boldsymbol{k}_T, \lambda)|0\rangle, \tag{4.36}$$

etc., and the commutation relations,

$$\left[a(k^+, \boldsymbol{k}_T, \lambda), a^\dagger(k'^+, \boldsymbol{k}'_T, \lambda') \right] = (2\pi)^3\, \delta(k^+ - k'^+)\, \delta^{(2)}(\boldsymbol{k}_T - \boldsymbol{k}'_T)\, \delta_{\lambda\lambda'}, \tag{4.37}$$

and similar anticommutation relations for the fermion operators.

Nevertheless, when converting such commutators among the creation and annihilation operators into the canonical commutators or anticommutators among the fields, one does

not get the "naturally conjectured" equal-x^+ commutation relations, but instead, at the last step one has to use $\int dk^+ d^2\boldsymbol{k}_T/2k^+ = \int d^3\boldsymbol{k}/2E_k$ to get the equal-time commutation relations. The existence of $\boldsymbol{k}_T$ and mass m in the spinors and polarization vectors forbids the derivation of an equal-x^+ commutation relation. The use of light-cone helicity states does not embed itself into a simply covariant formalism.

To overcome this problem, we introduce the light-front quantization. Instead of taking equal-time commutation relations plus time evolutions, one take, right in the beginning, equal-x^+ commutation relations, and evolve everything with respect to x^+, under the "Hamiltonian" P_+,

$$i\frac{\partial}{\partial x^+}O(x^+) = [O(x^+), P_+]. \tag{4.38}$$

Then one immediately notices from the QCD Lagrangian that there are some "bad" field components that are non-evolving or dynamically dependent on other components, and some "good" dynamically independent field components. In the light-cone gauge $A^+ = 0$, the good fields components are

$$\psi_G(x) = \frac{\gamma^-\gamma^+}{2}\psi(x), \quad \bar{\psi}_G(x) = \bar{\psi}(x)\frac{\gamma^+\gamma^-}{2}, \quad A^\perp(x) = (A^1(x), A^2(x)), \tag{4.39}$$

where the color indices are omitted.

The field decompositions for the good fields are particularly simple. We notice that the spinor projector $\gamma^-\gamma^+/2$ takes all the spinors in Eqs. (4.26) and (4.27) to their lightlike

versions,

$$\frac{\gamma^-\gamma^+}{2}u_\lambda(k^+,\boldsymbol{k}_T;m)=u_\lambda(k^+,\boldsymbol{0}_T;0)\equiv u_\lambda(k^+),$$
$$\frac{\gamma^-\gamma^+}{2}v_\lambda(k^+,\boldsymbol{k}_T;m)=v_\lambda(k^+,\boldsymbol{0}_T;0)\equiv v_\lambda(k^+). \tag{4.40}$$

Similarly, the transverse components of the polarization vectors are reduced to $\epsilon^\mu_\lambda(k^+,\boldsymbol{0}_T)$, for both massless and massive vector particles. Then, the decompositions in Eqs. (4.34) and (4.35) become,

$$\psi_G(x)=\sum_\lambda\int\frac{dk^+d^2\boldsymbol{k}_T}{(2\pi)^3\sqrt{2k^+}}\left[b(k^+,\boldsymbol{k}_T,\lambda)\,u_\lambda(k^+)\,e^{-ik\cdot x}+d^\dagger(k^+,\boldsymbol{k}_T,\lambda)\,v_\lambda(k^+)\,e^{ik\cdot x}\right], \tag{4.41a}$$

$$A^i(x)=\sum_\lambda\int\frac{dk^+d^2\boldsymbol{k}_T}{(2\pi)^3\sqrt{2k^+}}\left[a(k^+,\boldsymbol{k}_T,\lambda)\,\epsilon^i_\lambda(k^+)\,e^{-ik\cdot x}+a^\dagger(k^+,\boldsymbol{k}_T,\lambda)\,\epsilon^{i*}_\lambda(k^+)\,e^{ik\cdot x}\right], \tag{4.41b}$$

where $i=1,2$ and $x=(0^+,x^-,\boldsymbol{x}_T)$ is at the zero light-front time. Now there is no place for k^- to come in, and the good field components satisfy the equal-x^+ commutation relations,

$$\left\{\psi_G(x^+,x^-,\boldsymbol{x}_T),\bar\psi_G(x^+,x'^-,\boldsymbol{x}'_T)\right\}=\frac{\gamma^-}{2}\delta(x^--x'^-)\delta^{(2)}(\boldsymbol{x}_T-\boldsymbol{x}'_T), \tag{4.42}$$
$$\left[A^i(x^+,x^-,\boldsymbol{x}_T),\partial_-A^j(x^+,x'^-,\boldsymbol{x}'_T)\right]=\frac{i}{2}\delta(x^--x'^-)\delta^{(2)}(\boldsymbol{x}_T-\boldsymbol{x}'_T). \tag{4.43}$$

4.1.1.3 Parton spin structure

The parton spin structure is best understood in the light cone gauge $A^+=0$. The presence of the Wilson lines in the covariant gauge obscures the parton picture.

In the quark GPD definitions [Eq. (4.1)], the quark fields sandwich a γ^+ matrix. Since

$$\gamma^+ = \left(\frac{\gamma^+\gamma^-}{2}\right)\gamma^+\left(\frac{\gamma^-\gamma^+}{2}\right), \tag{4.44}$$

both the quark and antiquark fields are projected to be the good field components,

$$\bar{\psi}\gamma^+(1,\gamma_5)\psi = \bar{\psi}_G\gamma^+(1,\gamma_5)\psi_G. \tag{4.45}$$

Similarly, in the light-cone gauge, the gluon fields in the gluon GPD definitions [Eq. (4.2)] only have the transverse components, so are also good field components. Thus we can decompose the fields according to Eq. (4.41), with the partons interpreted as carrying light-cone helicities. Note that in this picture, the creation and annihilation operators are for on-shell partons, which may or may not be massless but whose light-cone helicity states are the same as the massless parton helicity states moving along the z direction.

4.1.1.4 Proton spin structure

In Eqs. (4.1)(4.2), each GPD is defined for a certain parton spin structure. The form factor decomposition for each GPD corresponds to different proton spin structure. Following the discussion above Sec. 4.1.1.1, we also describe the proton spin using light-cone helicity states. With the notation $\Gamma_{s,s'} = (2P^+)^{-1}\bar{u}(p',s')\Gamma u(p,s)$ and using the explicit spinor forms in Eq. (4.26), we have

$$\begin{aligned}
\left[\gamma^+\right]_{++} = \left[\gamma^+\right]_{--} = \sqrt{1-\xi^2}, \quad \left[\gamma^+\right]_{+-} = \left[\gamma^+\right]_{-+} = 0, \\
\left[\gamma^+\gamma_5\right]_{++} = -\left[\gamma^+\gamma_5\right]_{--} = \sqrt{1-\xi^2}, \quad \left[\gamma^+\gamma_5\right]_{+-} = \left[\gamma^+\gamma_5\right]_{-+} = 0,
\end{aligned} \tag{4.46}$$

for the helicity non-flipping structures, and

$$\begin{aligned}
&\left[\frac{-i\sigma^{+\alpha}\Delta_\alpha}{2m}\right]_{++} = \left[\frac{-i\sigma^{+\alpha}\Delta_\alpha}{2m}\right]_{--} = \frac{-\xi^2}{\sqrt{1-\xi^2}},\\
&\left[\frac{-i\sigma^{+\alpha}\Delta_\alpha}{2m}\right]_{+-} = -\left[\frac{-i\sigma^{+\alpha}\Delta_\alpha}{2m}\right]^*_{-+} = -e^{i\phi_\Delta}\cdot\frac{\sqrt{t_0-t}}{2m},\\
&\left[\frac{-\gamma_5\Delta^+}{2m}\right]_{++} = -\left[\frac{-\gamma_5\Delta^+}{2m}\right]_{--} = \frac{-\xi^2}{\sqrt{1-\xi^2}},\\
&\left[\frac{-\gamma_5\Delta^+}{2m}\right]_{+-} = \left[\frac{-\gamma_5\Delta^+}{2m}\right]_{-+} = -\xi\, e^{i\phi_\Delta}\cdot\frac{\sqrt{t_0-t}}{2m},
\end{aligned} \tag{4.47}$$

for the helicity flipping structures, where $t_0 = -4\xi^2 m^2/(1-\xi^2)$ is the maximum value of t at a given ξ. Here we describe the diffraction of $p \to p'$ by using the azimuthal angle ϕ_Δ of Δ.

In this way, the GPDs H and $\widetilde{H}$ are associated with proton helicity non-flipping channels, whereas the GPDs E and $\widetilde{E}$ are with proton helicity flipping ones. Since we are dealing with parton helicity non-flipping GPDs, the proton helicity flipping is compensated by a nonzero Δ_T, which is described in the lab frame by the factor

$$\sqrt{t_0-t} = \sqrt{\frac{1+\xi}{1-\xi}}\Delta_T \tag{4.48}$$

and the phases $e^{i\phi}\Delta$.

4.1.2 Moments and sum rules

Because GPDs only have support in $x \in [-1, 1]$, taking the x moments converts them into the matrix elements of local twist-2 operators,

$$\begin{aligned}
\int_{-1}^{1} dx\, x^n\, F^q(x,\xi,t) &= \int_{-\infty}^{\infty} dx x^n F^q(x,\xi,t) \\
&= \int_{-\infty}^{\infty} dx \int \frac{dy^-}{4\pi} \left[\left(\frac{i}{P^+} \frac{\partial}{\partial y^-} \right)^n e^{-ixP^+ y^-} \right] \langle p', s' | \bar{\psi}_q \left(y^-/2 \right) \gamma^+ \psi_q \left(-y^-/2 \right) | p, s \rangle \\
&= \int \frac{dy^-}{4\pi} \int_{-\infty}^{\infty} dx\, e^{-ixP^+ y^-} \left(\frac{-i}{P^+} \frac{\partial}{\partial y^-} \right)^n \langle p', s' | \bar{\psi}_q \left(y^-/2 \right) \gamma^+ \psi_q \left(-y^-/2 \right) | p, s \rangle \\
&= \int \frac{dy^-}{4\pi} (2\pi) \delta(P^+ y^-) \left(\frac{1}{P^+} \right)^n \langle p', s' | \bar{\psi}_q \left(y^-/2 \right) \gamma^+ (i \overleftrightarrow{\partial}^+)^n \psi_q \left(-y^-/2 \right) | p, s \rangle \\
&= \frac{1}{2(P^+)^{n+1}} \langle p', s' | \bar{\psi}_q (0) \gamma^+ (i \overleftrightarrow{\partial}^+)^n \psi_q (0) | p, s \rangle,
\end{aligned} \tag{4.49}$$

where $\overleftrightarrow{\partial}^+ = (\overrightarrow{\partial}^+ - \overleftarrow{\partial}^+)/2$ will become the covariant derivative $\overleftrightarrow{D}^+ = (\overrightarrow{D}^+ - \overleftarrow{D}^+)/2$ once the Wilson line is included. Similar relations apply to the other GPDs,

$$\begin{aligned}
\int_{-1}^{1} dx\, x^n\, \widetilde{F}^q(x,\xi,t) &= \frac{1}{2(P^+)^{n+1}} \langle p', s' | \bar{\psi}_q (0) \gamma^+ \gamma_5 (i \overleftrightarrow{D}^+)^n \psi_q (0) | p, s \rangle, \\
\int_{-1}^{1} dx\, x^{n-1}\, F^g(x,\xi,t) &= \frac{1}{(P^+)^{n+1}} \delta^{ij} \langle p', s' | G^{+i} (0) (i \overleftrightarrow{D}_A^+)^{n-1} G^{+j} (0) | p, s \rangle, \\
\int_{-1}^{1} dx\, x^{n-1}\, \widetilde{F}^g(x,\xi,t) &= \frac{1}{(P^+)^{n+1}} (-i\epsilon_T^{ij}) \langle p', s' | G^{+i} (0) (i \overleftrightarrow{D}_A^+)^{n-1} G^{+j} (0) | p, s \rangle,
\end{aligned} \tag{4.50}$$

where we weight the gluon GPDs by x^{n-1} instead of x^n such that the local twist-2 operators have spin $(n+1)$, similar to the quark case.

The off-forward matrix elements of the twist-2 operators can be decomposed into independent form factors based on Lorentz covariance, parity, and time reversal symmetries. Taking + for all the Lorentz indices then leads to important polynomiality properties for the

GPDs,

$$\int_{-1}^{1} dx\, x^n\, H^q(x,\xi,t) = \sum_{i=0,2,\cdots}^{n} (2\xi)^i\, A^q_{n+1,i}(t) + \mathrm{mod}(n,2)(2\xi)^{n+1}\, C^q_{n+1}(t), \tag{4.51a}$$

$$\int_{-1}^{1} dx\, x^n\, E^q(x,\xi,t) = \sum_{i=0,2,\cdots}^{n} (2\xi)^i\, B^q_{n+1,i}(t) - \mathrm{mod}(n,2)(2\xi)^{n+1}\, C^q_{n+1}(t), \tag{4.51b}$$

$$\int_{-1}^{1} dx\, x^{n-1}\, H^g(x,\xi,t) = \sum_{i=0,2,\cdots}^{n} (2\xi)^i\, A^g_{n+1,i}(t) + \mathrm{mod}(n,2)(2\xi)^{n+1}\, C^g_{n+1}(t), \tag{4.51c}$$

$$\int_{-1}^{1} dx\, x^{n-1}\, E^g(x,\xi,t) = \sum_{i=0,2,\cdots}^{n} (2\xi)^i\, B^g_{n+1,i}(t) - \mathrm{mod}(n,2)(2\xi)^{n+1}\, C^g_{n+1}(t), \tag{4.51d}$$

for the unpolarized GPDs, and

$$\int_{-1}^{1} dx\, x^n\, \widetilde{H}^q(x,\xi,t) = \sum_{i=0,2,\cdots}^{n} (2\xi)^i\, \widetilde{A}^q_{n+1,i}(t), \tag{4.52a}$$

$$\int_{-1}^{1} dx\, x^n\, \widetilde{E}^q(x,\xi,t) = \sum_{i=0,2,\cdots}^{n} (2\xi)^i\, \widetilde{B}^q_{n+1,i}(t), \tag{4.52b}$$

$$\int_{-1}^{1} dx\, x^{n-1}\, \widetilde{H}^g(x,\xi,t) = \sum_{i=0,2,\cdots}^{n} (2\xi)^i\, \widetilde{A}^g_{n+1,i}(t), \tag{4.52c}$$

$$\int_{-1}^{1} dx\, x^{n-1}\, \widetilde{E}^g(x,\xi,t) = \sum_{i=0,2,\cdots}^{n} (2\xi)^i\, \widetilde{B}^g_{n+1,i}(t). \tag{4.52d}$$

That is, the x moments of GPDs reduce to even polynomials of ξ. For unpolarized GPDs, the maximum power of ξ is equal to the spin of the corresponding twist-2 operator, whereas for polarized GPDs, it is the spin minus 1.

The low-order moments are related to the matrix elements of physical currents that can be probed in experiments. For $n = 0$, the twist-2 quark operators become the electric and axial currents,

$$J^\mu_q = \bar{\psi}_q \gamma^\mu \psi_q, \quad J^{5\mu}_q = \bar{\psi}\gamma^\mu\gamma_5\psi, \tag{4.53}$$

which can be accessed experimentally through electromagnetic and weak interactions, respectively, and give the Dirac and Pauli form factors,

$$\langle p'|J_q^\mu(0)|p\rangle = \bar{u}(p')\left[F_1^q(t)\,\gamma^\mu - F_2^q(t)\,\frac{i\,\sigma^{\mu\alpha}\Delta_\alpha}{2m}\right]u(p), \tag{4.54}$$

and the axial and pseudoscalar form factors,

$$\langle p'|J_q^{5\mu}(0)|p\rangle = \bar{u}(p')\left[g_A^q(t)\,\gamma^\mu\gamma_5 - g_P^q(t)\,\frac{\gamma_5\Delta^\mu}{2m}\right]u(p). \tag{4.55}$$

Taking $\mu = +$ then relates them to the form factors of GPDs in Eqs. (4.51) and (4.52),

$$\begin{aligned} A_{1,0}^q(t) &= \int_{-1}^{1} dx\, H^q(x,\xi,t) = F_1^q(t), \quad B_{1,0}^q(t) = \int_{-1}^{1} dx\, E^q(x,\xi,t) = F_2^q(t), \\ \widetilde{A}_{1,0}^q(t) &= \int_{-1}^{1} dx\, \widetilde{H}^q(x,\xi,t) = g_A^q(t), \quad \widetilde{B}_{1,0}^q(t) = \int_{-1}^{1} dx\, \widetilde{E}^q(x,\xi,t) = g_P^q(t). \end{aligned} \tag{4.56}$$

Since twist-2 gluon operators start from spin 2, there are no corresponding relations for gluon GPDs.

For $n = 1$, the spin-2 twist-2 operators are just the energy momentum tensor [Polyakov and Schweitzer(2

$$\begin{aligned} \int_{-1}^{1} dx\, x\, F^q(x,\xi,t) &= \frac{1}{2(P^+)^2}\langle p', s'|\bar{\psi}_q(0)\,\gamma^+\,(i\overleftrightarrow{D}^+)\psi_q(0)\,|p,s\rangle = \frac{1}{2(P^+)^2}\langle p', s'|T_q^{++}(0)|p,s\rangle, \\ \int_{-1}^{1} dx\, F^g(x,\xi,t) &= \frac{1}{2(P^+)^2}\langle p', s'|G^{+\alpha}(0)\,G_\alpha{}^+(0)\,|p,s\rangle = \frac{1}{2(P^+)^2}\langle p', s'|T_g^{++}(0)|p,s\rangle, \end{aligned} \tag{4.57}$$

where the energy momentum tensors are

$$T_q^{\mu\nu} = \frac{1}{2}\bar{\psi}_q \left(i \overleftrightarrow{D}^{\mu} \gamma^{\nu} + i \overleftrightarrow{D}^{\nu} \gamma^{\mu} \right) \psi_q - g^{\mu\nu} \bar{\psi}_q \left(i\gamma \cdot \overleftrightarrow{D} - m_q \right) \psi_q,$$
$$T_q^{\mu\nu} = G^{a,\mu\alpha} G^{a,}{}_{\alpha}{}^{\nu} + \frac{1}{4} g^{\mu\nu} (G^a_{\alpha\beta})^2. \tag{4.58}$$

The latter has the form factor decomposition,

$$\langle p', s' | T_i^{\mu\nu}(0) | p, s \rangle = \bar{u}'(p', s') \left[A_i(t) \frac{\gamma^{(\mu} P^{\nu)}}{2} - B_i(t) \frac{i P^{(\mu} \sigma^{\nu)\rho} \Delta_\rho}{4m} \right.$$
$$\left. + D_i(t) \frac{\Delta^\mu \Delta^\nu - g^{\mu\nu} \Delta^2}{4m} + m\, \bar{c}_i(t)\, g_{\mu\nu} \right] u(p, s), \tag{4.59}$$

where $i = q, g$, and we used the notation $a^{(\mu}\, b^{\nu)} = a^\mu\, b^\nu + a^\nu\, b^\mu$. Taking $\mu = \nu = +$ gives

$$\langle p', s' | T_i^{++}(0) | p, s \rangle = P^+\, \bar{u}'(p', s') \left[\Big(A_i(t) + \xi^2 D_i(t) \Big)\, \gamma^+ \right.$$
$$\left. - \Big(B_i(t) + \xi^2 D_i(t) \Big)\, \frac{i\sigma^{+\rho} \Delta_\rho}{2m} \right] u(p, s). \tag{4.60}$$

Compare this with Eqs. (4.57)(4.1a) and (4.1a), we have the sum rules,

$$\int_{-1}^{1} dx\, x\, H^q(x, \xi, t) = A_q(t) + \xi^2\, D_q(t), \quad \int_{-1}^{1} dx\, x\, E^q(x, \xi, t) = B_q(t) - \xi^2\, D_q(t),$$
$$\int_{-1}^{1} dx\, H^g(x, \xi, t) = A_g(t) + \xi^2\, D_g(t), \quad \int_{-1}^{1} dx\, E^g(x, \xi, t) = B_g(t) - \xi^2\, D_g(t), \tag{4.61}$$

which relate the energy momentum form factors to the GPD moments. While the former cannot be easily measured in experiments, the latter can in principle be measured (or calculated in lattice QCD) and give a probe to the energy momentum tensors. This can uncover certain global dynamic properties inside the hadrons. By combining the moments of H and

E in Eq. (4.61), the D terms cancel and we get the sum rule,

$$\begin{aligned}\int_{-1}^{1} dx\, x\, \left(H^q(x,\xi,t) + E^q(x,\xi,t)\right) &= A_q(t) + B_q(t) = 2J_q(t),\\ \int_{-1}^{1} dx\, \left(H^g(x,\xi,t) + E^g(x,\xi,t)\right) &= A_g(t) + B_g(t) = 2J_g(t),\end{aligned} \tag{4.62}$$

where the $J_a(t)$ form factor is related to the angular momentum sum of the parton a, normalized by

$$\sum_a J_a(0) = \frac{1}{2}. \tag{4.63}$$

Eq. (4.62) then gives the angular momentum sum rules for the partons inside a hadron [Ji(1997b)],

$$\begin{aligned}J_q &= \frac{1}{2}\lim_{t\to 0}\int_{-1}^{1} dx\, x\, \left(H^q(x,\xi,t) + E^q(x,\xi,t)\right),\\ J_g &= \frac{1}{2}\lim_{t\to 0}\int_{-1}^{1} dx\, \left(H^q(x,\xi,t) + E^q(x,\xi,t)\right).\end{aligned} \tag{4.64}$$

Therefore, the measurement of GPDs, especially the construction of the moments of their x distributions, gives important handles to the partonic dynamics inside a hadron.

4.2 The SDHEP frame

By the two-stage paradigm described at the beginning of Sec. 3.2, the most natural frame for the study of the SDHEP is the c.m. frame of the A^* and B with A^* along the z axis, which is shown in Fig. 9.5, where the diffraction process [Eq. (3.105)] happens in the blue plane, and the hard scattering process [Eq. (3.106)] happens in the orange plane. The x axis lies on the diffraction plane and points to the same direction as $\boldsymbol{p}_{1T} = \boldsymbol{\Delta}_T \equiv \boldsymbol{p}_T - \boldsymbol{p}'_T$ in the lab frame, as shown in Fig. 9.5. This frame can be obtained from the lab frame,

the c.m. frame of the colliding beams of h and B, by boosting along $-\boldsymbol{p}'$, as defined in [Berger et al.(2002b)Berger, Diehl, and Pire].

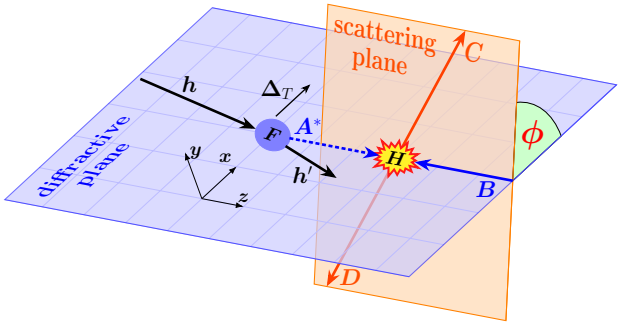

Fig. 4.1: The frame to study the SDHEP is the c.m. frame of A^* and B. F denotes the (nonperturbative) diffraction process $h \to h' + A^*$, which happens in the blue plane ("diffraction plane"), and H denotes the hard interaction between A^* and B to produce C and D, which happens in the orange plane ("scattering plane"). The two planes form an angle of ϕ and intersect at the collision axis between A^* and B, which is chosen as the z axis. $\boldsymbol{\Delta}_T$ denotes the transverse momentum of A^* in the lab frame, along which the x axis is chosen.

Each event of SDHEP can be described by five independent kinematic variables: the transverse momentum q_T (or equivalently, its polar angle θ) of one of the two back-to-back final-state particles (C or D) in their c.m. frame, which is our hard scale, the azimuthal angle variable ϕ of this particle in the same frame, which is directly connected to the angle between the diffractive plane and the scattering plane, the c.m. energy squared $\hat{s}$ of the hard collision between A^* and B, and the transverse momentum shift $\boldsymbol{\Delta}_T$ of the diffracted hadron in the lab frame. They can be equivalently transformed into $(\theta, \phi, \xi, t, \phi_\Delta)$, where ϕ_Δ is the azimuthal angle of $\boldsymbol{\Delta}_T$ in the lab frame. The distribution of ϕ_Δ is determined by the diffraction process, in particular, by the spin state of the initial state hadron h.

The angle ϕ describes the angular correlation between the diffraction and the hard collision. Its distribution is solely determined by the spin states of A^* and B. If we denote the helicities of A^* and B by λ_A and λ_B, respectively, then the ϕ dependence of the hard

scattering amplitude is captured by a phase factor

$$e^{i(\lambda_A - \lambda_B)\phi}. \tag{4.65}$$

For the $n = 1$ channel, $A^* = \gamma^*$ has three helicity states $(+1, 0, -1)$. For the $n = 2$ channel, the quark GPDs have three possible helicities $\lambda_A^q = 0$ or ± 1, where $\lambda_A^q = 0$ has two independent contributions from the unpolarized and polarized GPDs, while $\lambda_A^q = \pm 1$ is given by the two transversity GPDs. Similarly, the gluon GPDs also have three helicities $\lambda_A^g = 0$ or ± 2, with $\lambda_A^g = 0$ receiving contributions from both the unpolarized and polarized GPDs and $\lambda_A^g = \pm 2$ from the two transversity GPDs.

The interference between (λ_A, λ_B) and (λ'_A, λ'_B) leads to the azimuthal correlations

$$\cos(\Delta\lambda_A - \Delta\lambda_B)\phi, \quad \text{and/or} \quad \sin(\Delta\lambda_A - \Delta\lambda_B)\phi, \tag{4.66}$$

depending on details of the interaction, where $\Delta\lambda_{A,B} = \lambda_{A,B} - \lambda'_{A,B}$. Extracting different trigonometric components of the azimuthal distribution is a great way to disentangle different GPD contributions, in a way similar to using the angular modulations in the semi-inclusive DIS to extract different transverse momentum dependent PDFs, or TMDs [Bacchetta et al.(2007)Bacchetta, Diehl, Goeke, Metz, Mulders, and Schlegel]. Similarly, the angular distribution of the lepton pair in the Drell-Yan process [Lam and Tung(1978)] was studied to capture richer structures of QCD dynamics than the production rate alone. Because of the exclusive nature, the SDHEP cross section can receive contributions from the interferences among any two of $A^* = \gamma^*, [q\bar{q}']$ and $[gg]$ channels as well as their different polarization states.

4.3 A general discussion on the x dependence of different SDHEPs on GPDs

We are considering the sensitivity to the x-dependence of GPDs from the tree-level hard part $C(x, Q)$, where Q is the external observable not associated with the diffractive hadron.[1] We consider the two types of sensitivity:

(I) *Moment-type sensitivity*: $C(x, Q)$ factorizes into an x-dependent part and Q-dependent part,

$$C(x, Q) = G(x)\, T(Q). \tag{4.67}$$

In this case, the measurement of the Q distribution, which is fully captured by the predictable $T(Q)$, does not help in probing the x-dependence of GPDs, and all the sensitivity is in the moment-type quantity

$$\int_{-1}^{1} \mathrm{d}x\, G(x)\, F(x, \xi, t). \tag{4.68}$$

We call a process with only moment-type sensitivity a type-I process.

(II) *Enhanced sensitivity*: $C(x, Q)$ does not factorize, in the sense of Eq. (4.67). Then, the distribution of Q depends on the detailed x distribution in the GPD. To some extent, Q is the "conjugate variable" of x, and they are related in the amplitude

$$\mathcal{M}(Q) \sim \int_{-1}^{1} \mathrm{d}x\, C(x, Q)\, F(x, \xi, t) \tag{4.69}$$

[1] Even though the GPD variable ξ is also in the hard coefficient C and is directly observable from the diffracted hadron momentum, we do not consider it to be included in Q, but instead it always comes with x and is suppressed in $C(x, Q)$.

through the transformation kernel $C(x, Q)$, which is, in general, not invertible, of course. We call a process with enhanced sensitivity a type-II process.

Only having moment-type sensitivity is far from enough, even with next-to-leading-order hard coefficients and evolution effects included [Bertone et al.(2021)Bertone, Dutrieux, Mezrag, Moutarde, as also confirmed in practical fits of GPDs [Diehl et al.(2005)Diehl, Feldmann, Jakob, and Kroll, Hashamipour et al.(2020)Hashamipour, Goharipour, and Gousheh, Hashamipour et al.(2022)Hashamipou Guo et al.(2022)Guo, Ji, and Shiells]. Given the complicated functional dependence of the GPD on x plus its entanglement with ξ and t variables, one should have as much enhanced sensitivity as possible while having as many independent moment constraints. Among the processes that have been studied in the literature, only the DDVCS [Guidal and Vanderhaeghen(2003)], photoproduction of photon-meson pair [Boussarie et al.(2017)Boussarie, Pire, Szymanowski, and Wallon, Duplančić et al.(2018)Duplančić, Passek-Kumerički, Pire, Szymanowski, and Wallon], and meson-production of diphoton [Qiu and Yu(2022)] processes are type-II processes, and all the other processes [Ji(1997a), Radyushkin(1997), Brodsky et al.(1994)Brodsky, Frankfurt, Gunion, Mueller, and St Frankfurt et al.(1996)Frankfurt, Koepf, and Strikman, Berger et al.(2002b)Berger, Diehl, and Pire, Berger et al.(2001)Berger, Diehl, and Pire, Pedrak et al.(2017)Pedrak, Pire, Szymanowski, and Wagner] belong to type I.

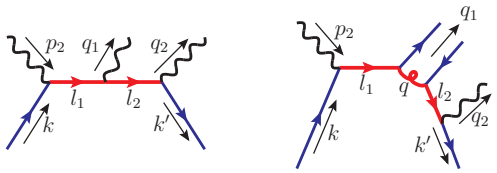

(a) (b)

Fig. 4.2: Sample diagrams for the hard scattering of the single diffractive (a) photoproduction of diphoton process, and (b) photoproduction of photon-meson pair process. The red thick lines indicate the propagators in the hard part, and the blue lines are amputated parton lines that are put on shell and massless.

A careful examination of the denominator structure of the leading-order hard part of the partonic scattering can help understand and identify the difference in the x-sensitivity from these two types of processes. The type-I processes have one common feature that every internal propagator can be made to have one end connect to two on-shell massless external lines, whether the external line is an amputated parton line or a real massless particle. Take the photoproduction of diphoton process, with one of its hard scattering diagrams in Fig. 4.2(a), as an example, the propagator of momentum l_1 is connected to an amputated parton line of on-shell momentum $k = (x+\xi)\hat{P}$ and the incoming photon line of momentum p_2, while the propagator of momentum l_2 is connected to an amputated parton line of momentum $k' = (x-\xi)\hat{P}$ and the outgoing photon line of momentum q_2. In the c.m. frame of the hard exclusive collision as defined in Fig. 9.5, we have

$$\begin{aligned} \hat{P}^\mu &= \left(P^+, 0^-, \mathbf{0}_T\right), \quad p_2^\mu = \left(0^+, p_2^-, \mathbf{0}_T\right), \\ \Delta^+ &= p_1^+ = 2\xi P^+ = p_2^- = \sqrt{\hat{s}/2}\,, \end{aligned} \tag{4.70}$$

and the final-state momenta q_1 and q_2, which define the hard scale q_T,

$$q_1^\mu = \frac{\sqrt{\hat{s}}}{2}(1, \boldsymbol{n}) = \left(\sqrt{\frac{\hat{s}}{2}}\frac{1+\cos\theta}{2}, \sqrt{\frac{\hat{s}}{2}}\frac{1-\cos\theta}{2}, \boldsymbol{q}_T\right), \tag{4.71a}$$

$$q_2^\mu = \frac{\sqrt{\hat{s}}}{2}(1, -\boldsymbol{n}) = \left(\sqrt{\frac{\hat{s}}{2}}\frac{1-\cos\theta}{2}, \sqrt{\frac{\hat{s}}{2}}\frac{1+\cos\theta}{2}, -\boldsymbol{q}_T\right), \tag{4.71b}$$

where we present them first in terms of Cartesian coordinates with $\boldsymbol{n}$ being a unit spatial vector defined as $\vec{q}_1/|\vec{q}_1|$ and then in light-front coordinates, and we also introduced the polar angle θ to represent q_T $(= \sqrt{\hat{s}}\,\sin\theta/2)$. With all external momenta defined in Eqs. (4.70)

and (4.71a), we can express the virtuality of the internal momentum l_1 as

$$l_1^2 = 2k \cdot p_2 = 2(x+\xi)\hat{P} \cdot p_2 = \frac{x+\xi}{2\xi}\,\hat{s} \equiv x_\xi\,\hat{s}\,, \tag{4.72}$$

where $x_\xi = (x+\xi)/2\xi$ is the same as the z_1 variable defined in Eq. (3.16) of Ref. [Qiu and Yu(2022)]. Similarly, we have the virtuality of the other internal momentum l_2 as

$$l_2^2 = 2k' \cdot q_2 = 2(x-\xi)\hat{P} \cdot q_2 = x'_\xi \cdot \cos^2(\theta/2)\,\hat{s}\,, \tag{4.73}$$

where $x'_\xi = (x-\xi)/2\xi = x_\xi - 1$. And then the hard coefficient of the diagram Fig. 4.2(a) takes a factorized form,

$$C(x,\xi,\cos\theta) \propto \frac{1}{(l_1^2+i\varepsilon)(l_2^2+i\varepsilon)} \propto \left[\frac{1}{(x_\xi+i\varepsilon)(x'_\xi+i\varepsilon)}\right] \cdot \frac{1}{\cos^2(\theta/2)} \tag{4.74}$$

in which the dependence on θ (or equivalently, q_T) is factorized from the momentum fraction x of the relative momentum of the active $[q\bar{q}]$ pair. This is an immediate consequence of having the internal propagator directly connected to two external on-shell massless particles. Generally, as a result of connecting to two on-shell massless lines with momenta e_1 and e_2, the virtuality of the internal propagator is just a product $e_1 \cdot e_2$, which simply factorizes into a GPD-x (or DA-z) dependent factor and a factor that depends on the external observable such as θ in Eq. (4.73). This example also indicates that the poles of x take place at $x_\xi = 0$ or $x'_\xi = 0$, that is, $x = \pm\xi$, which are at the boundary points between the DGLAP and ERBL regions.

In contrast, a type-II process has at least one internal line in the hard part that cannot be made to have either end connect to two on-shell massless lines. We take the photoproduction

of a photon-meson pair process as an example, for which one hard scattering diagram is shown in Fig. 4.2(b). The kinematics is the same as in Eqs. (4.70) and (4.71a), and two of the propagators, l_1 and l_2, are the same as the previous diphoton production example, given in Eqs. (4.72) and (4.73).

However, the gluon propagator q is connected to l_1 on one end and to l_2 one the other end, both of which are not on shell. Letting the outgoing quark line along q_1 have its momentum zq_1, we have the gluon momentum,

$$q = k + p_2 - zq_1 = (x + \xi)\hat{P} + p_2 - zq_1 \,, \tag{4.75}$$

which has the virtuality

$$q^2 = \hat{s}\left[x_\xi\left(1 - z\sin^2(\theta/2)\right) - z\cos^2(\theta/2)\right] \,. \tag{4.76}$$

This leads to a hard coefficient that does not take a simple factorized form to separate the (x_ξ, z) dependence from the observable θ, and therefore the distribution of θ contains extra sensitivity to the shape of x and z in the GPD and DA, respectively.

Compared to Eq. (4.74), the gluon propagator in Eq. (4.76) leads to some new poles of x, at

$$x_\xi = \frac{z\cos^2(\theta/2)}{1 - z\sin^2(\theta/2)} \in [0, 1], \quad \text{for } z \in [0, 1], \tag{4.77}$$

which corresponds to $x \in [-\xi, \xi]$, and thus lies in the ERBL region. These are not pinched poles, so do not pose any theoretical obstacles, but are just the regions where we need to deform the contour of x to avoid them.

Similarly, in Fig. 4.2(a), if we make the photon q_2 virtual in the diphoton production

process, the photon momenta in Eq. (4.71a) will become

$$q_1^\mu = \frac{\sqrt{\hat{s}}}{2}(1-\zeta)(1,\boldsymbol{n})\,, \qquad (4.78)$$
$$q_2^\mu = \frac{\sqrt{\hat{s}}}{2}(1+\zeta,-(1-\zeta)\boldsymbol{n})\,,$$

where $\zeta = Q'^2/\hat{s}$ with $Q'^2 = q_2^2$ being the virtuality of the photon q_2 that decays into a lepton pair. Then the propagator l_2 becomes

$$l_2^2 = \hat{s}\left\{x'_\xi\,\cos^2(\theta/2) + \zeta\left[1 + x'_\xi\,\sin^2(\theta/2)\right]\right\}\,, \qquad (4.79)$$

which differs from Eq. (4.73) by having an additional term proportional to ζ that introduces an extra scale dependence. By varying ζ and θ, one can get extra sensitivity to the x-dependence of the GPD. This is the same mechanism that gives the enhanced x-sensitivity as the DDVCS process [Guidal and Vanderhaeghen(2003)] which we discussed around Eq. (**??**). This propagator [Eq. (4.79)] leads to a new pole of x at

$$x'_\xi = \frac{-\zeta}{\cos^2(\theta/2) + \zeta\sin^2(\theta/2)} \in [-1,-\zeta], \quad \text{for } \theta\in[0,\pi], \qquad (4.80)$$

that is $x \in [-\xi,(1-2\zeta)\xi] \subset [-\xi,\xi]$, which is again inside the ERBL region.

By comparison, the type-I processes are usually topologically or kinematically simpler than the type-II processes, so their theoretical analysis and hard coefficient calculations are usually easier. The type-II processes introduce enhanced sensitivity to the x dependence by having extra scale dependence that entangles with the x flow. For the two type-II examples we have just examined, the photon-meson pair production process differs from the DVMP process by having one extra photon attaching to the active parton lines, while the virtual

photon production process differs from the real photon production process by having an extra scale Q' which is in turn achieved by having that photon decay into *two* leptons. In general, extra scale dependence is introduced by more complicated topology,[2] which is usually the necessary condition for enhanced sensitivity.

One important role that the SDHEP plays is that it sets a template for listing a number of processes, which we have categorized according to the beam types. We have shown the proof of factorization in a general sense. Within this framework, one shall study as many independent processes as possible, which should in turn constrain the x dependence of GPDs as much as possible.

4.4 Single diffractive hard exclusive diphoton mesoproduction

Having explained the main steps in factorizing the amplitude for the exclusive photon-pair production in the $\pi^+\pi^-$ annihilation, we now generalize the factorization formalism to an exclusive process involving diffractive scattering of a nucleon N of momentum p,

$$N(p) + \pi(p_2) \to N'(p') + \gamma(q_1) + \gamma(q_2), \tag{4.81}$$

where N can be a proton (p) or a neutron (n) and π can be π^- or π^+, making up various exclusive processes, such as, $p\,\pi^- \to n\gamma\gamma$, $n\,\pi^+ \to p\gamma\gamma$, $p\,\pi^- \to \Lambda^0\gamma\gamma$, and those that could be measured with a pion beam at J-PARC and other facilities. The pion beam can also be replaced by a kaon beam and makes up more processes. The exclusive process, $p\,\pi^- \to n\gamma\gamma$,

[2]Here, we consider virtual or massive particles as having more complicated topology than real massless particles, even in the case when the mass scale is not associated with virtual particle decay.

could be made analogous to the $\pi^+\pi^-$ collision by thinking of the $p \to n$ transition as taking a virtual π^+ out of the proton, carrying momentum $\Delta = p - p'$ and colliding with π^- to produce two hard photons exclusively.

4.4.1 Kinematics

In the lab frame, the nucleon (pion) is moving along $+\hat{z}$ ($-\hat{z}$) direction, carrying a large plus (minus) momentum. Two photons with large and opposite transverse momenta are produced in the final state, together with a recoiled nucleon, or a baryon in general. We focus on the region of phase space where $-t = -\Delta^2 \ll (q_1 + q_2)^2$. That is, we require that the proton be recoiled in an approximately collinear direction and the invariant mass of the momentum transfer Δ much smaller than the energy of this transfer. This is the condition that allows the scattering amplitude of the exclusive process in eq. (4.81) to be factorized into a transition GPD of the nucleon.

Since Δ carries a small transverse component and sufficiently large longitudinal component, it is convenient for our analysis to boost the lab frame into the CM frame of Δ and p_2 where $\vec{\Delta}$ is along $+\hat{z}$ direction, which is also the rest frame of q_1 and q_2, so that the Δ could mimic the momentum p_1 of π^+ in the Sec. **??**. We denote this frame as photon frame S_γ, distinguished from the lab frame $S_{\rm lab}$. The transformation from $S_{\rm lab}$ to S_γ can be done by first boosting along $\vec{\Delta}_T$ such that $\vec{\Delta}$ is in parallel and head-to-head with $\vec{p}_2$, followed by a rotation in the $\vec{\Delta}_T$-$\vec{p}_2$ plane to make $\vec{\Delta}$ along $+\hat{z}$ direction.

In the S_γ frame, we have the momentum conservation,

$$\Delta + p_2 = q_1 + q_2 \,, \tag{4.82}$$

and the CM collision energy square $\hat{s} \equiv (\Delta + p_2)^2 = (q_1 + q_2)^2 \gg \Lambda^2_{\rm QCD}$. For the leading power contribution, we can parametrize Δ and p_2 as

$$\begin{aligned}
\Delta &= \left(\Delta^+,\, \frac{t}{2\Delta^+},\, \mathbf{0}_T\right)_\gamma \simeq \left(\Delta^+,\, 0,\, \mathbf{0}_T\right)_\gamma \,, \\
p_2 &= \left(\frac{m_\pi^2}{2p_2^-},\, p_2^-, \mathbf{0}_T\right)_\gamma \simeq \left(0,\, p_2^-,\, \mathbf{0}_T\right)_\gamma \,,
\end{aligned} \tag{4.83}$$

where in the second step (and in the following) the "$\simeq$" means the neglect of small quantities suppressed by powers of m_π^2/Q^2 or t/Q^2 with the hard scale $Q \sim \mathcal{O}(q_T) \lesssim \sqrt{\hat{s}}$. In addition, we also implicitly take the *rescaled* light-like Δ and p_2 as the momenta entering the hard process, with

$$\Delta^+ = p_2^- = \sqrt{\frac{(\Delta + p_2)^2}{2}} = \sqrt{\frac{\hat{s}}{2}}\,, \tag{4.84}$$

to keep the momentum conservation manifest, which is useful for the factorization of this process.

The skewness in the lab frame is defined as

$$\xi = \frac{\Delta^+_{\rm lab}}{2P^+_{\rm lab}}, \tag{4.85}$$

where $P = (p + p')/2$. We then have $p^+_{\rm lab} = (1+\xi)P^+_{\rm lab}$, $p'^+_{\rm lab} = (1-\xi)P^+_{\rm lab}$, and

$$\hat{s} = (\Delta + p_2)^2 \simeq 2\Delta^+ p_2^- = \frac{2\xi}{1+\xi}(2p^+p_2^-)_{\rm lab} \simeq \frac{2\xi}{1+\xi}\, s\,, \tag{4.86}$$

which defines a unique role of the skewness, quantifying the momentum flowing into the hard process from the colliding hadron of momentum p.

The invariant mass squared of the momentum transfer, $t = \Delta^2$, can be related to ξ and

the transverse component of the momentum transfer Δ_T by

$$t = -\left(\frac{4\xi^2}{1-\xi^2}m_p^2 + \frac{1+\xi}{1-\xi}\Delta_T^2\right), \tag{4.87}$$

where m_p is the proton mass and we neglect the mass difference between proton and neutron. For a given small t, Δ_T is bounded to be small, and ξ is effectively constrained by

$$0 < \xi \leq \sqrt{\frac{-t/m_p^2}{4 - t/m_p^2}}\,. \tag{4.88}$$

Every event of the exclusive process in eq. (4.81) is specified by three momenta p', q_1 and q_2, which are constrained by on-shell conditions and momentum conservation, leading to $9-4=5$ degrees of freedom in kinematics. $\boldsymbol{\Delta}_T$ and ξ are sufficient to specify the neutron momentum. The photon momenta are to be described by $\boldsymbol{q}_T$ in the photon frame S_γ, where they are back-to-back. That is, $(\boldsymbol{\Delta}_T, \xi, \boldsymbol{q}_T)$ fixes all the kinematics. Our process is insensitive to azimuthal angle in either $\boldsymbol{\Delta}_T$ or $\boldsymbol{q}_T$, and we will integrate out these angles, leaving only three degrees of freedom, Δ_T, ξ and q_T, or equivalently, t, ξ and q_T as independent variables.

4.4.2 Factorization

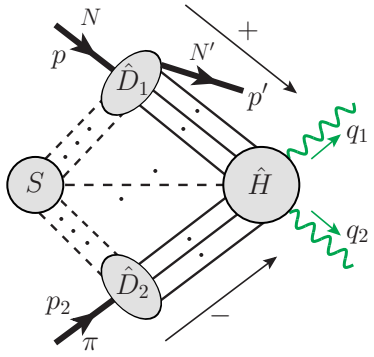

Fig. 4.3: The general pinch-singular surface for the process (4.81).

We generalize the factorization formula derived in Sec. **??** to describe the scattering amplitude of the exclusive process in eq. (4.81). As indicated by the general pinch-singular surface in figure 4.3, the initial-state nucleon momentum p and slightly recoiled hadron momentum p' define the direction of a collinear subgraph, $\hat{D}_1$, which is joined by a set of collinear parton lines to the hard subgraph, from which two photons with large transverse momenta are produced.

The power counting for a pinch surface is derived in the same way as what was done in the last section. The only difference is that the dimension for the $\hat{D}_1$ is reduced by 1 because we have an extra external final-state hadron line connected to $\hat{D}_1$ in figure 4.3. Like eq. (**??**), we obtain the scaling behavior for corresponding reduced diagram as

$$\mathcal{M}_{N\pi\to N'\gamma\gamma} \sim \hat{H} \otimes \hat{D}_1 \otimes \hat{D}_2 \otimes S \;\propto\; \lambda^{\alpha-1}\,, \tag{4.89}$$

where α is the same as that in eq. (**??**). With the minimum power $\alpha = 2$, we obtain the leading pinch surfaces to the scattering amplitude of exclusive process in eq. (4.81), as shown in figure 4.4, which are slightly modified from those in figure **??**. Due to the electric charge or isospin exchange, $\hat{D}_1$ or $\hat{D}_2$ must be connected to other subdiagrams by at least two quark lines. By the same argument at the end of Sec. **??**, the pinch surface in figure **??** is power suppressed compared to that in figure **??**.

4.4.2.1 Deformation out of Glauber region

Before we adopt the approximations listed in Sec. **??** to start our factorization arguments, we note one complication that distinguishes the diffractive meson-baryon process in eq. (4.81) from the $\pi^+\pi^-$ case discussed in the last section.

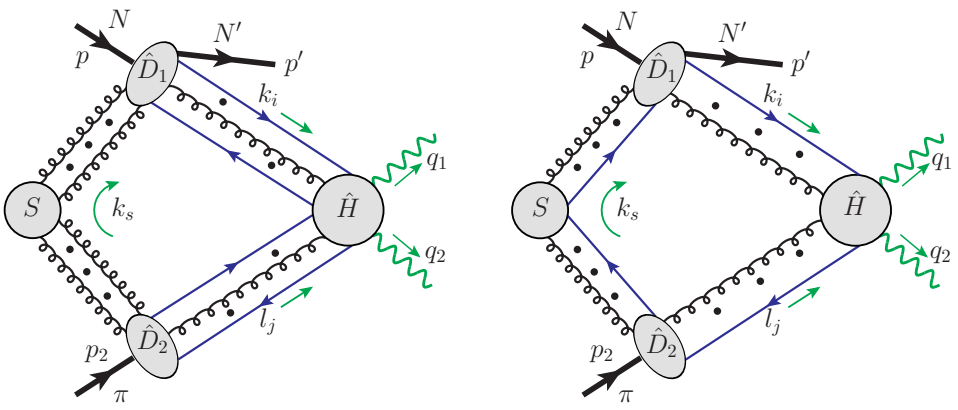

Fig. 4.4: Two possible leading regions for the process (4.81). Arbitrary number of gluons can connect to the collinear subgraphs $\hat{D}_1$ or $\hat{D}_2$ from S or $\hat{H}$, but they have to be longitudinally polarized.

The factorization proof of $\pi^+\pi^-$ process was simplified by the fact that all the collinear parton lines go from the *past* to *now* when the hard collision takes place, without going to the future as spectators, as shown in figure **??**. All the parton lines collinear to π^+ (π^-) have positive plus (minus) momenta, and the plus/minus momenta of the soft gluons are not trapped to be much smaller than their transverse components. We can get those soft gluons out of the Glauber region by deforming the contours of their momentum integrations, as discussed in Sec. **??**. However, in the πN case, or more specifically, in $p\pi^- \to n\gamma\gamma$ case, the proton-neutron transition can have either (i) all the collinear parton lines going from the proton *into* the hard part, as shown in figure **??**, or (ii) some parton lines going from the proton *into* the hard part, but others going to the future as spectators and merging with partons coming out the hard part to form a neutron, as shown in figure **??**. The type (i) corresponds to the ERBL region of GPD, and the type (ii) is for the DGLAP region.

For the ERBL region, the contour deformations and approximations made to the leading regions for every possible diagram are the same as those in Sec. **??**. But for the DGLAP region, the presence of proton spectator may trap the minus momenta of soft gluons at small

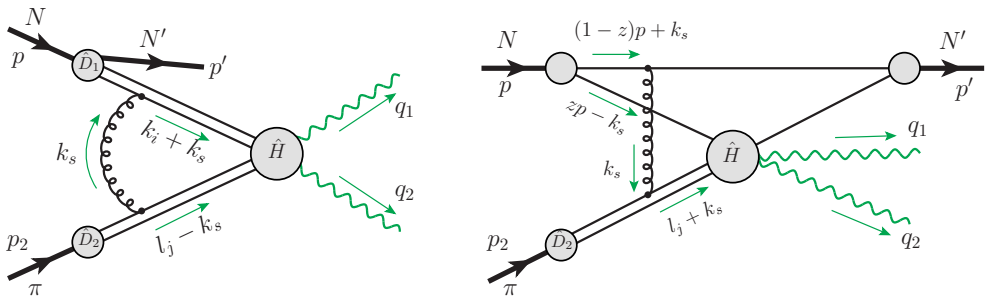

Fig. 4.5: Difference in soft gluon interaction between ERBL region (a) and DGLAP region (b) in the elastic πN process. In (a), the k_s^- integration is not pinched, while in (b), the k_s^- integration is pinched to be in the Glauber region.

values. For example, as shown in figure **??**, the attachment of a soft gluon of momentum k_s to a spectator of the colliding proton leads to two propagators with the denominators,

$$\begin{aligned}
&((1-z)p+k_s)^2+i\varepsilon \approx 2(1-z)p^+k_s^- - \boldsymbol{k}_{sT}^2 + i\varepsilon\,, \\
&\qquad\qquad \Rightarrow \quad k_s^- \text{ pole } \approx \frac{\boldsymbol{k}_{sT}^2}{2(1-z)p^+} - i\varepsilon \quad \to \quad \mathcal{O}(\lambda^2 Q) - i\varepsilon\,, \\
&(zp-k_s)^2+i\varepsilon \approx 2zp^+(-k_s^-) - \boldsymbol{k}_{sT}^2 + i\varepsilon\,, \\
&\qquad\qquad \Rightarrow \quad k_s^- \text{ pole } \approx -\frac{\boldsymbol{k}_{sT}^2}{2zp^+} + i\varepsilon \quad \to \quad -\mathcal{O}(\lambda^2 Q) + i\varepsilon\,,
\end{aligned} \tag{4.90}$$

which pinch the k_s^--integration of the soft gluon of momentum k_s to be $\mathcal{O}(\lambda^2 Q)$ when $k_{sT} = \mathcal{O}(\lambda Q)$ and trap the k_s^- in the Glauber region. The same conclusion arrives if we let k_s flow through $N'(p')$ in figure **??**. Therefore, the argument that we used in Sec. **??** to deform the contours of plus/minus components of soft gluon momenta to get them out of the Glauber region does not work for the soft minus components in the πN case when the nucleon N is moving in the "+" direction.

Luckily, the poles for the plus components of the soft momenta are solely provided by the collinear lines from the π, which all go *into* the hard part with positive minus momenta.

All the poles from $l_j + k_s$ lie on the same half plane, and therefore, we can deform k_s^+ as

$$k_s^+ \to k_s^+ + i\mathcal{O}(p^+), \tag{4.91}$$

when it lies in the Glauber region flowing into the $\hat{D}_2$ subgraph. This is the maximal extent that we can deform k_s^+, which leads the soft momentum k_s all the way into $\hat{D}_1$-collinear region. That is, the soft Glauber mode is deformed to be a collinear mode, which is only possible when all the collinear lines from the π flow into the hard part $\hat{H}$. Had we considered an exclusive double diffractive process: $pn \to pn\gamma\gamma$, with a pair of back-to-back high transverse momentum photons produced while the nucleons are slightly diffracted, we would have both plus and minus components of soft momenta pinched in the Glauber region, which forbids the double diffractive processes, like $pn \to pn\gamma\gamma$, $p\bar{p} \to p\bar{p} + \text{jet} + \text{jet}$, etc., to be factorized into two GPDs and a hard part [Soper(1997)], even though there is indeed a hard scale provided by the transverse momenta of the photons or the jets.

After the deformation of Glauber gluons, we can apply all the approximations in Sec. **??**. Since we will not deform k_s^- in DGLAP region, it does not matter what $i\varepsilon$ prescription we assign to k_s^-. We choose the same convention as in Sec. **??** to be compatible with ERBL region, for which we do need to deform k_s^-.

4.4.2.2 Soft cancellation and factorization

We first use the same arguments presented in the last section to factorize the collinear subgraph $\hat{D}_2$ from the hard part $\hat{H}$ and the soft factor S. The approximation in eqs. (**??**) and (**??**) allows us to use Ward identity to detach all longitudinally polarized collinear gluons of $\hat{D}_2$ from the hard part $\hat{H}$, and factorize them into Wilson lines along w_1, as shown in

figure 4.6. Like the $\pi^+\pi^- \to \gamma\gamma$ case in the last section, the Wilson lines connected to $\hat{D}_2$ point to the past due to the choice of $i\varepsilon$ in eq. (**??**).

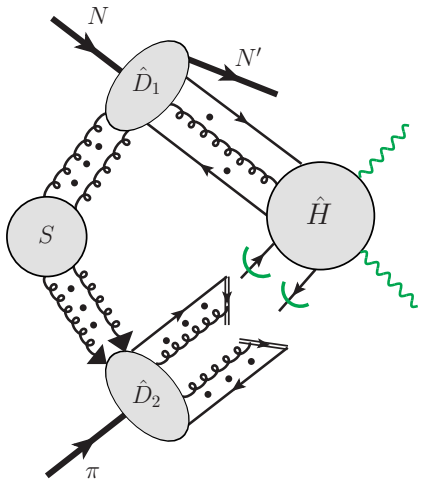

Fig. 4.6: The result of using Ward identity for $\hat{D}_2$-collinear gluons. The Wilson lines point along w_1 to the past. The notations are similar to figure **??**.

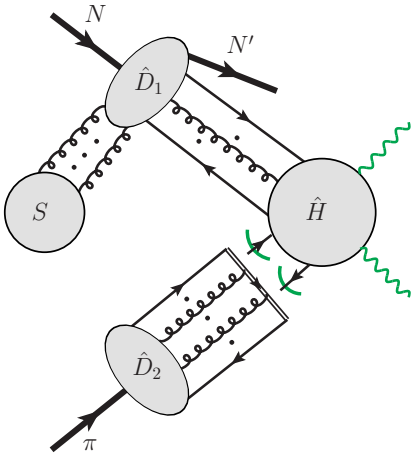

Fig. 4.7: The result of using Ward identity for soft gluons coupling to $\hat{D}_2$. Those gluons cancel. The Wilson line is along w_1.

Next, having eqs. (**??**) and (**??**), we can use Ward identity to factorize soft gluons out of the collinear factor $\hat{D}_2$. This leaves the collinear factor $\hat{D}_2$ uncoupled to $\hat{D}_1$, so that $\hat{D}_2$ ends up being color singlet. By the same method of Sec. **??**, the soft gluons coupling to $\hat{D}_2$ cancel. The rest of the soft gluons only couple to $\hat{D}_1$, as in figure 4.7, and can be grouped

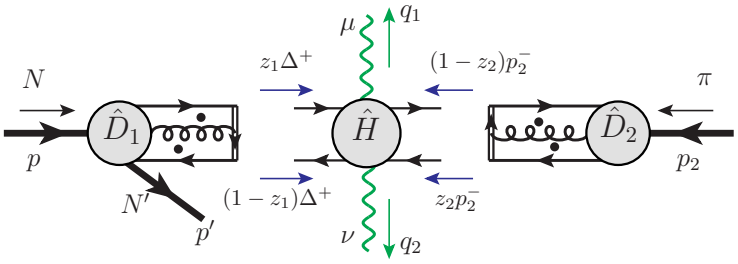

Fig. 4.8: The factorized form for the process (4.81).

into $\hat{D}_1$.

We can then use eqs. (**??**) and (**??**), and the Ward identity to factorize all longitudinally polarized collinear gluons of $\hat{D}_1$ out of the hard part $\hat{H}$. This step is similar to that of the $\pi^+\pi^-$ case, since the soft gluon connection to $\hat{D}_2$ has been canceled, which would have pinched the minus components of soft gluon momenta into the Glauber region. After factorizing the longitudinally polarized collinear gluons from the $\hat{H}$ into Wilson line, we get a color singlet $\hat{D}_1$. Therefore, we complete the factorization arguments and have a factorized result, as shown in figure 4.8. The color structure of the hard part takes the same form as in eq. (**??**). But, the spinor indices are still convoluted between $\hat{D}_1$ and $\hat{H}$, as well as between $\hat{D}_2$ and $\hat{H}$, and will be dealt with in next subsection.

4.4.2.3 Factorization formula

Similar to eq. (**??**), we derived the factorized formalism for the scattering amplitude of the exclusive process in (4.81), corresponding to the factorized diagram in figure 4.8,

$$\mathcal{M}^{\mu\nu}_{N\pi\to N'\gamma\gamma} = \int \mathrm{d}z_1\mathrm{d}z_2\,\mathrm{Tr}\Big\{[\mathcal{P}_A\,\hat{D}_1(z_1,p,p')\,\mathcal{P}_B][\mathcal{P}_B\,\hat{D}_2(z_2,p_2)\,\mathcal{P}_A] \times\Big[\frac{1}{N_c^2}\hat{H}^{\mu\nu}_{ii;mm}(k_1^+=z_1\,\Delta^+;k_2^-=z_2\,p_2^-;q_1,q_2;\mu)\Big]\Big\}, \tag{4.92}$$

where the repeated color indices, i and m are summed, and averaged with the factor $1/N_c^2$, and the "Tr" indicates the trace over all spinor indices between $\hat{D}_1$, $\hat{D}_2$, and $\hat{H}$. In eq. (4.92), $\mathcal{P}_A$, $\mathcal{P}_B$, and $\hat{D}_2(z_2, p_2)$ are the same as those in eq. (**??**), but $\hat{D}_1(z_1, p, p')$ is different, which now represents the transition GPD of the nucleon N,

$$\begin{aligned}\hat{D}_1(z_1, p, p')_{\alpha\beta} &= \int \frac{\mathrm{d}(\Delta^+ y^-)}{2\pi} e^{iz_1\Delta^+ y^-} \langle N'(p')|\bar{d}_\beta(0)\Phi(0, y^-; w_2)\, u_\alpha(y^-)|N(p)\rangle \qquad (4.93)\\ &= \int \frac{\mathrm{d}(\Delta^+ y^-)}{2\pi} e^{i(2z_1-1)\xi P^+ y^-} \langle N'(p')|\bar{d}_\beta\left(-\frac{y^-}{2}\right)\Phi\left(-\frac{y^-}{2}, \frac{y^-}{2}; w_2\right) u_\alpha\left(\frac{y^-}{2}\right)|N(p)\rangle\end{aligned}$$

where α, β are spinor indices, w_2 is as in eq. (**??**), color indices have been implicitly summed, and in the second line, we shifted the position of the operator to be consistent with the convention in [Diehl(2003)]. Now $\mathcal{P}_A$ and $\mathcal{P}_B$ sandwiching $\hat{D}_1$ picks out only the term proportional γ^-, $\gamma^-\gamma_5$ or $\gamma^-\gamma_5\gamma_i$. Because of helicity conservation, the transversity GPD associated with $\gamma^-\gamma_5\gamma_i$ does not contribute at leading power. Effectively, we have

$$\begin{aligned}&\left[\mathcal{P}_A\hat{D}_1(z_1, p, p')\mathcal{P}_B\right]_{\alpha\beta}\\ &\quad= \frac{1}{2\Delta^+}\mathrm{Tr}\left[\gamma^+\hat{D}_1\right]\left[\frac{1}{2}(\Delta^+\gamma^-)\right]_{\alpha\beta} + \frac{1}{2\Delta^+}\mathrm{Tr}\left[\gamma^+\gamma_5\hat{D}_1\right]\left[\frac{1}{2}\gamma_5(\Delta^+\gamma^-)\right]_{\alpha\beta}\\ &\quad\equiv \mathcal{F}^{ud}_{NN'}(z_1, \xi, t)\left[\frac{1}{2}(\Delta^+\gamma^-)\right]_{\alpha\beta} + \widetilde{\mathcal{F}}^{ud}_{NN'}(z_1, \xi, t)\left[\frac{1}{2}\gamma_5(\Delta^+\gamma^-)\right]_{\alpha\beta} \qquad (4.94)\end{aligned}$$

where $\mathcal{F}^{ud}_{NN'}(z_1,\xi,t)$ and $\widetilde{\mathcal{F}}^{ud}_{NN'}(z_1,\xi,t)$ are GPDs with different chirality characterizing the amplitude for the transition of hadron N to N',

$$\mathcal{F}^{ud}_{NN'}(z_1,\xi,t) = \int \frac{\mathrm{d}y^-}{4\pi} e^{iz_1\Delta^+ y^-} \langle N'(p')|\bar{d}(0)\gamma^+\Phi(0,y^-;w_2)\,u(y^-)|N(p)\rangle, \tag{4.95a}$$

$$= \int \frac{\mathrm{d}y^-}{4\pi} e^{i(2z_1-1)\xi P^+ y^-} \langle N'(p')|\bar{d}\left(-\frac{y^-}{2}\right)\gamma^+\Phi\left(-\frac{y^-}{2},\frac{y^-}{2};w_2\right)\,u\left(\frac{y^-}{2}\right)|N(p)\rangle,$$

$$= F^{ud}_{NN'}(x=(2z_1-1)\xi,\xi,t)\,; \tag{4.95b}$$

$$\widetilde{\mathcal{F}}^{ud}_{NN'}(z_1,\xi,t) = \int \frac{\mathrm{d}y^-}{4\pi} e^{iz_1\Delta^+ y^-} \langle N'(p')|\bar{d}(0)\gamma^+\gamma_5\Phi(0,y^-;w_2)\,u(y^-)|N(p)\rangle, \tag{4.95c}$$

$$= \int \frac{\mathrm{d}y^-}{4\pi} e^{i(2z_1-1)\xi P^+ y^-} \langle N'(p')|\bar{d}\left(-\frac{y^-}{2}\right)\gamma^+\gamma_5\Phi\left(-\frac{y^-}{2},\frac{y^-}{2};w_2\right)\,u\left(\frac{y^-}{2}\right)|N(p)\rangle,$$

$$= \widetilde{F}^{ud}_{NN'}(x=(2z_1-1)\xi,\xi,t)\,; \tag{4.95d}$$

where $F^{ud}_{NN'}(x,\xi,t)$ and $\widetilde{F}^{ud}_{NN'}(x,\xi,t)$ are the GPDs defined with the convention in Ref. [Diehl(2003)]. Note that we are using an unusual variable z_1 to label the momentum fraction of an active parton (u quark here), as indicated in figure 4.8, in order to have a direct analogy to the $\pi^+\pi^-$ process that we studied in the last section. As clearly indicated in eqs. (4.95b) and (4.95d), the momentum fraction z_1 is closely related to the common variables of GPDs, such as x and ξ,

$$z_1 = \frac{x+\xi}{2\xi}. \tag{4.96}$$

Consequently, the range of z_1 is different from $[0,1]$ for the nucleon side, as opposed to z_2 for the π, and is given by

$$z_m \equiv \frac{-1+\xi}{2\xi} \leq z_1 \leq \frac{1+\xi}{2\xi} \equiv z_M. \tag{4.97}$$

The choice of z_1 parameter highlights the so-called ERBL region, which lies between $-\xi < x < \xi$, and is now given by $0 < z_1 < 1$. In this region, a pair of quark and antiquark with positive momentum fractions enters the hard scattering. On the other hand, one of the DGLAP regions $\xi < x < 1$ with a quark scattering configuration corresponds to $1 < z_1 < (1+\xi)/2\xi$, while the other DGLAP region $-1 < x < -\xi$ with an antiquark scattering configuration becomes $-(1-\xi)/2\xi < z_1 < 0$.

Inserting eqs. (4.94) and (**??**) into eq. (4.92) we obtain the factorized scattering amplitude for the elastic process in eq. (4.81)

$$\mathcal{M}^{\mu\nu} = \int_{z_m}^{z_M} \mathrm{d}z_1 \int_0^1 \mathrm{d}z_2 \Big[\widetilde{\mathcal{F}}^{ud}_{NN'}(z_1,\xi,t) D_{\pi^-}(z_2) C^{\mu\nu}(z_1,z_2) + \mathcal{F}^{ud}_{NN'}(z_1,\xi,t) D_{\pi^-}(z_2) \widetilde{C}^{\mu\nu}(z_1,z_2) \Big] \tag{4.98}$$

where $C^{\mu\nu}$ is the same as that in eq. (**??**) with p_1^+ replaced by Δ^+, which has γ_5 attached on both proton and pion sides so is chiral even, while $\widetilde{C}^{\mu\nu}$ is given by

$$\widetilde{C}^{\mu\nu}(z_1,z_2) \equiv \mathrm{Tr}\left[\frac{\Delta^+\gamma^-}{2} H^{\mu\nu}(\hat{k}_1,\hat{k}_2;q_1,q_2;\mu) \frac{\gamma_5(p_2^-\gamma^+)}{2} \right], \tag{4.99}$$

which only has one γ_5 on the pion side and is referred as chiral odd. The correction to the factorized scattering amplitude in eq. (4.98) is suppressed by an inverse power of the high transverse momentum of observed photon q_T in S_γ.

The hard coefficients $C^{\mu\nu}$ and $\widetilde{C}^{\mu\nu}$, and the factorized formalism in eq. (4.98) are manifestly invariant under a boost along $\hat{z}$. Since the transformation from S_{lab} to S_γ is only by a boost along $\hat{z}$, up to a boost and rotation characterized by Δ_T, which is neglected at leading power, the factorization formula (4.98) takes the same form in the S_γ frame, and the hard

coefficients $C^{\mu\nu}$ and $\widetilde{C}^{\mu\nu}$ can be calculated in S_γ, in the same way as for $\pi^+\pi^-$ case.

If N = proton and N' = neutron, these transition GPDs can be related to the nucleon GPDs by isospin symmetry [**?**]

$$\begin{aligned}\mathcal{F}^{ud}_{pn}(z_1,\xi,t) &= \mathcal{F}^{u}_{p}(z_1,\xi,t) - \mathcal{F}^{u}_{n}(z_1,\xi,t),\\ \widetilde{\mathcal{F}}^{ud}_{pn}(z_1,\xi,t) &= \widetilde{\mathcal{F}}^{u}_{p}(z_1,\xi,t) - \widetilde{\mathcal{F}}^{u}_{n}(z_1,\xi,t).\end{aligned} \tag{4.100}$$

4.4.3 The leading-order hard coefficients

The leading-order diagrams are the same as those in figure **??** and **??**, except that now we have two sets of hard coefficients, obtained with different spinor projectors on the nucleon side. The calculation of the chiral-even coefficients is the same as $\pi^+\pi^-$ case, and the results are reorganized in a compact form in the Appendix with z_1 taking the value within $[z_m, z_M]$. From the parity constraint (**??**), the chiral-odd coefficient $\widetilde{C}^{\mu\nu}$ can be expanded into the P-odd gauge invariant tensor structures in eq. (**??**), with p_1 replaced by Δ. Similarly to eq. (**??**), we have

$$\widetilde{C}^{\mu\nu} = -\frac{e^2 g^2}{2\,\hat{s}^2}\frac{C_F}{N_c}\left(\widetilde{C}_1\,\widetilde{\Delta}^\mu \varepsilon_\perp^{\nu\rho} q_{T\rho} + \widetilde{C}_2\,\widetilde{p}_2^{\,\mu}\varepsilon_\perp^{\nu\rho} q_{T\rho} + \widetilde{C}_3\,\bar{\Delta}^\nu \varepsilon_\perp^{\mu\rho} q_{T\rho} + \widetilde{C}_4\,\bar{p}_2^{\,\nu}\varepsilon_\perp^{\mu\rho} q_{T\rho}\right). \tag{4.101}$$

where $\widetilde{\Delta}^\mu$ and $\bar{\Delta}^\nu$ are defined in the same way as $\widetilde{p}_1^{\,\mu}$ and $\bar{p}_1^{\,\nu}$ in eq. (**??**), respectively. The dimensionless scalar coefficients $\widetilde{C}_1$ to $\widetilde{C}_4$ can be extracted from the calculated result of each diagram by using eq. (4.101), and isolating the coefficient of the term proportional to Δ^μ, p_2^μ, Δ^ν and p_2^ν sequentially. The results are collected in the Appendix.

Following the discussion above eqs. (**??**) and (**??**), charge conjugation implies similar

relations for the chiral-odd coefficients, but with a minus sign, i.e.,

$$\{\widetilde{C}_{A1},\, \widetilde{C}_{A1'},\, \widetilde{C}_{A3},\, \widetilde{C}_{A4}\}^{\mu\nu}(z_1, z_2) = -\{\widetilde{C}_{A2'},\, \widetilde{C}_{A2},\, \widetilde{C}_{A3'},\, \widetilde{C}_{A4'}\}^{\mu\nu}(1-z_1, 1-z_2) \quad (4.102)$$

for Type-A diagrams, and

$$\begin{aligned}&\{\widetilde{C}_{B1},\, \widetilde{C}_{B1'},\, \widetilde{C}_{B2},\, \widetilde{C}_{B2'},\, \widetilde{C}_{B3},\, \widetilde{C}_{B3'}\}^{\mu\nu}(z_1, z_2)\Big|_{e_u \leftrightarrow e_d} \\ &\quad = -\{\widetilde{C}_{B4},\, \widetilde{C}_{B4'},\, \widetilde{C}_{B5},\, \widetilde{C}_{B5'},\, \widetilde{C}_{B6},\, \widetilde{C}_{B6'}\}^{\mu\nu}(1-z_1, 1-z_2) \end{aligned} \quad (4.103)$$

for Type-B diagrams. These relations carry through to each scalar coefficient $\widetilde{C}_1, \cdots, \widetilde{C}_4$, which has been checked in the calculations. Similar to the symmetric relation in eq. (**??**), we obtain an antisymmetric relation for $\widetilde{C}^{\mu\nu}$,

$$\widetilde{C}_A^{\mu\nu}(z_1, z_2) = -\widetilde{C}_A^{\mu\nu}(1-z_1, 1-z_2), \quad (4.104)$$

for Type-A diagrams, while for $\widetilde{C}_B$ this antisymmetry is broken by the difference of e_u^2 and e_d^2.

4.4.4 Cross section

Using eqs. (**??**), (4.101) and (4.98), we obtain the factorized scattering amplitude $\mathcal{M}^{\mu\nu}$ as

$$\begin{aligned}\mathcal{M}^{\mu\nu}_{N\pi\to N'\gamma\gamma} &= \frac{ie^2g^2f_\pi}{4\hat{s}^2}\frac{C_F}{N_c} \\ &\times\Bigg[i\left(\mathcal{M}_0\,\widetilde{g}_\perp^{\mu\nu}\,\hat{s}+\mathcal{M}_1\,\widetilde{\Delta}^\mu\bar{\Delta}^\nu+\mathcal{M}_2\,\widetilde{p}_2^\mu\bar{p}_2^\nu+\mathcal{M}_3\,\widetilde{\Delta}^\mu\bar{p}_2^\nu+\mathcal{M}_4\,\widetilde{p}_2^\mu\bar{\Delta}^\nu\right) \\ &\quad+\left(\widetilde{\mathcal{M}}_1\,\widetilde{\Delta}^\mu\varepsilon_\perp^{\nu\rho}q_{T\rho}+\widetilde{\mathcal{M}}_2\,\widetilde{p}_2^\mu\varepsilon_\perp^{\nu\rho}q_{T\rho}+\widetilde{\mathcal{M}}_3\,\bar{\Delta}^\nu\varepsilon_\perp^{\mu\rho}q_{T\rho}+\widetilde{\mathcal{M}}_4\,\bar{p}_2^\nu\varepsilon_\perp^{\mu\rho}q_{T\rho}\right)\Bigg],\end{aligned} \tag{4.105}$$

where

$$\begin{aligned}\mathcal{M}_i &= \int_{z_m}^{z_M}\mathrm{d}z_1\int_0^1\mathrm{d}z_2\,\widetilde{\mathcal{F}}^{ud}_{NN'}(z_1,\xi,t)\,\phi(z_2)\,C_i(z_1,z_2) \\ &= \mathcal{M}[C_i;\widetilde{\mathcal{F}}^{ud}_{NN'},(z_m,z_M);\phi,(0,1)], \\ \widetilde{\mathcal{M}}_i &= \int_{z_m}^{z_M}\mathrm{d}z_1\int_0^1\mathrm{d}z_2\,\mathcal{F}^{ud}_{NN'}(z_1,\xi,t)\,\phi(z_2)\,\widetilde{C}_i(z_1,z_2) \\ &= \mathcal{M}[\widetilde{C}_i;\mathcal{F}^{ud}_{NN'},(z_m,z_M);\phi,(0,1)]\,,\end{aligned} \tag{4.106}$$

with $i=0,\cdots,4$ for $\mathcal{M}_i$ or $1,\cdots,4$ for $\widetilde{\mathcal{M}}_i$. Like eq. (**??**), we have the full scattering amplitude squared, summing over the photon polarizations,

$$\begin{aligned}|\overline{\mathcal{M}}|^2 = \left(\frac{e^2g^2f_\pi}{4\hat{s}}\frac{C_F}{N_c}\right)^2\Bigg[&\left(|\mathcal{M}_0|^2+\left|\frac{\mathcal{M}_1+\mathcal{M}_2}{4}-\frac{(\Delta\cdot q_1)^2\mathcal{M}_3+(\Delta\cdot q_2)^2\mathcal{M}_4}{\hat{s}\,q_T^2}\right|^2\right) \\ &+\left|\frac{(\Delta\cdot q_1)\widetilde{\mathcal{M}}_1-(\Delta\cdot q_2)\widetilde{\mathcal{M}}_2}{\hat{s}}\right|^2+\left|\frac{(\Delta\cdot q_2)\widetilde{\mathcal{M}}_3-(\Delta\cdot q_1)\widetilde{\mathcal{M}}_4}{\hat{s}}\right|^2\Bigg],\end{aligned} \tag{4.107}$$

where the average (sum) over the spins of initial-state nucleon N (final-state N') is included in $|\mathcal{M}_i|^2$ and $|\widetilde{\mathcal{M}}_i|^2$.

Instead of summing (or averaging) over all nucleon spins, we can introduce GPDs sensitive to the hadron spin by expressing the matrix elements of nucleon states in eq. (4.95) in terms of independent combinations of nucleon spinors and corresponding "form factors" or spin dependent GPDs,

$$\begin{aligned}\mathcal{F}^{ud}_{NN'}(z_1,\xi,t) =&\frac{1}{2P^+}\Bigg[\mathcal{H}^{ud}_{NN'}(z_1,\xi,t)\,\bar{u}(p')\gamma^+u(p)\\ &-\mathcal{E}^{ud}_{NN'}(z_1,\xi,t)\,\bar{u}(p')\frac{i\sigma^{+\alpha}\Delta_\alpha}{2m_p}u(p)\Bigg], \qquad (4.108)\\ \widetilde{\mathcal{F}}^{ud}_{NN'}(z_1,\xi,t) =&\frac{1}{2P^+}\Bigg[\widetilde{\mathcal{H}}^{ud}_{NN'}(z_1,\xi,t)\,\bar{u}(p')\gamma^+\gamma_5u(p)\\ &-\widetilde{\mathcal{E}}^{ud}_{NN'}(z_1,\xi,t)\,\bar{u}(p')\frac{i\gamma_5\sigma^{+\alpha}\Delta_\alpha}{2m_p}u(p)\Bigg]. \qquad (4.109)\end{aligned}$$

Consequently, all scattering amplitudes corresponding to independent tensor structures, $\mathcal{M}_i$ and $\widetilde{\mathcal{M}}_i$ in eq. (4.107) can be expressed in terms of the spin dependent GPDs,

$$\begin{aligned}\mathcal{M}_i =&\frac{1}{2P^+}\left[\mathcal{M}_i^{[\widetilde{\mathcal{H}}]}\,\bar{u}(p')\gamma^+\gamma_5u(p)-\mathcal{M}_i^{[\widetilde{\mathcal{E}}]}\,\bar{u}(p')\frac{i\gamma_5\sigma^{+\alpha}\Delta_\alpha}{2m_p}u(p)\right],\\ \widetilde{\mathcal{M}}_i =&\frac{1}{2P^+}\left[\widetilde{\mathcal{M}}_i^{[\mathcal{H}]}\,\bar{u}(p')\gamma^+u(p)-\widetilde{\mathcal{M}}_i^{[\mathcal{E}]}\,\bar{u}(p')\frac{i\sigma^{+\alpha}\Delta_\alpha}{2m_p}u(p)\right], \qquad (4.110)\end{aligned}$$

where the superscript "$[\mathcal{H}]$" means to replace the corresponding $\mathcal{F}^{ud}_{NN'}$ in eq. (4.106) by $\mathcal{H}^{ud}_{NN'}$, etc. Multiplied by their complex conjugate with the spin of N (N') averaged (summed), we have

$$\begin{aligned}|\mathcal{M}_i|^2 =&(1-\xi^2)\left|\mathcal{M}_i^{[\widetilde{\mathcal{H}}]}\right|^2-2\xi^2\,\mathrm{Re}\left(\mathcal{M}_i^{[\widetilde{\mathcal{H}}]*}\mathcal{M}_i^{[\widetilde{\mathcal{E}}]}\right)-\frac{\xi^2t}{4m_p^2}\left|\mathcal{M}_i^{[\widetilde{\mathcal{E}}]}\right|^2, \qquad (4.111a)\\ \left|\widetilde{\mathcal{M}}_i\right|^2 =&(1-\xi^2)\left|\widetilde{\mathcal{M}}_i^{[\mathcal{H}]}\right|^2-2\xi^2\,\mathrm{Re}\left(\widetilde{\mathcal{M}}_i^{[\mathcal{H}]*}\widetilde{\mathcal{M}}_i^{[\mathcal{E}]}\right)-\left(\frac{t}{4m_p^2}+\xi^2\right)\left|\widetilde{\mathcal{M}}_i^{[\mathcal{E}]}\right|^2, \qquad (4.111b)\end{aligned}$$

where the factor 1/2 for the spin average has been included.

In our numerical analysis in the next section, we take $|t| \leq 0.2$ GeV^2, which constrains ξ to be $\xi \leq 0.23$ by eq. (4.88). Then the terms containing $\mathcal{M}_i^{[\widetilde{\mathcal{E}}]}$ or $\widetilde{\mathcal{M}}_i^{[\mathcal{E}]}$ are suppressed by a factor of about 0.1 or smaller, compared to the terms containing $|\mathcal{M}_i^{[\widetilde{\mathcal{H}}]}|^2$ or $|\widetilde{\mathcal{M}}_i^{[\mathcal{H}]}|^2$. We can thus neglect them for a rough estimate. Using eq. (4.111), we can rewrite eq. (4.107) as

$$\begin{aligned}
\left|\overline{\mathcal{M}}\right|^2 \approx{}& (1-\xi^2)\left(\frac{e^2 g^2 f_\pi}{4\hat{s}}\frac{C_F}{N_c}\right)^2 \\
&\times\left[\left(|\mathcal{M}_0^{[\widetilde{\mathcal{H}}]}|^2+\left|\frac{\mathcal{M}_1^{[\widetilde{\mathcal{H}}]}+\mathcal{M}_2^{[\widetilde{\mathcal{H}}]}}{4}-\frac{(\Delta\cdot q_1)^2\mathcal{M}_3^{[\widetilde{\mathcal{H}}]}+(\Delta\cdot q_2)^2\mathcal{M}_4^{[\widetilde{\mathcal{H}}]}}{\hat{s}\,q_T^2}\right|^2\right)\right. \\
&\left.+\left|\frac{(\Delta\cdot q_1)\widetilde{\mathcal{M}}_1^{[\mathcal{H}]}-(\Delta\cdot q_2)\widetilde{\mathcal{M}}_2^{[\mathcal{H}]}}{\hat{s}}\right|^2+\left|\frac{(\Delta\cdot q_2)\widetilde{\mathcal{M}}_3^{[\mathcal{H}]}-(\Delta\cdot q_1)\widetilde{\mathcal{M}}_4^{[\mathcal{H}]}}{\hat{s}}\right|^2\right]. \quad (4.112)
\end{aligned}$$

As discussed in Sec. 4.4.1, we can specify an event by $\boldsymbol{\Delta}_T, \xi$ and $\boldsymbol{q}_T$, with $\boldsymbol{q}_T$ being the transverse momentum of the photons in the photon frame S_γ. This gives

$$\mathrm{d}\sigma = \frac{1}{2s}\frac{\mathrm{d}\xi \mathrm{d}^2\boldsymbol{\Delta}_T}{(1-\xi^2)(2\pi)^3}\frac{\mathrm{d}^2\boldsymbol{q}_T}{8\pi^2\hat{s}}\frac{\left|\overline{\mathcal{M}}\right|^2}{\sqrt{1-\hat{\kappa}}}, \quad (4.113)$$

where $\left|\overline{\mathcal{M}}\right|^2$ is given in eq. (4.112) and $\hat{\kappa} = 4q_T^2/\hat{s} \leq 1$ is the analog of κ (defined below eq. (**??**)) for the photon system in the S_γ frame. The direction of $\boldsymbol{q}_T$ can be defined with respect to the $N - N'$ plane, or $\boldsymbol{p}$-$\boldsymbol{\Delta}_T$ plane. But since $\left|\overline{\mathcal{M}}\right|^2$ is for unpolarized scattering, it does not depend on the azimuthal angles of $\boldsymbol{q}_T$ and $\boldsymbol{\Delta}_T$, so we can integrate them out. That allows us to only use three scalars Δ_T, ξ and q_T to describe the events, which by eq. (4.87) can be transformed to the three scalar variables (t, ξ, q_T), and corresponding differential cross

section,

$$\frac{\mathrm{d}\sigma}{\mathrm{d}|t|\,\mathrm{d}\xi\,\mathrm{d}q_T^2} = \frac{\pi}{64}\left(\alpha_e\alpha_s\frac{f_\pi}{s^2}\frac{C_F}{N_c}\right)^2\frac{(1-\xi^2)}{\xi^2}\frac{(1+\xi)}{\xi}\frac{\mathcal{B}}{\sqrt{1-\hat{\kappa}}}\,, \tag{4.114}$$

where $\mathcal{B}$ stands for the big square bracket in eq. (4.112), which is dimensionless and can be evaluated numerically once we know the pion DAs and nucleon's GPDs. In eq. (4.114), we have separated the ξ dependent factor into two parts, in which the second part, $(1+\xi)/\xi$, is canceled when we integrate over q_T^2 from $q_{T\min}^2$ to $\hat{s}/4 = \xi/(1+\xi)(s/2)$.

4.4.5 Numerical results

In this section, we evaluate the cross sections for producing a pair of high transverse momentum photons in exclusive pion-pion and pion-nucleon scattering and test their sensitivity to the shape of DAs and GPDs in terms of active parton's momentum fraction.

4.4.5.1 End-point sensitivity and improvement from Sudakov suppression

Before we introduce our choices of DAs and GPDs to evaluate the factorized cross sections, we discuss the well-known "end-point" sensitivity associated with perturbative evaluation of factorized elastic scattering processes, and its impact on the new type of exclusive processes introduced in this paper.

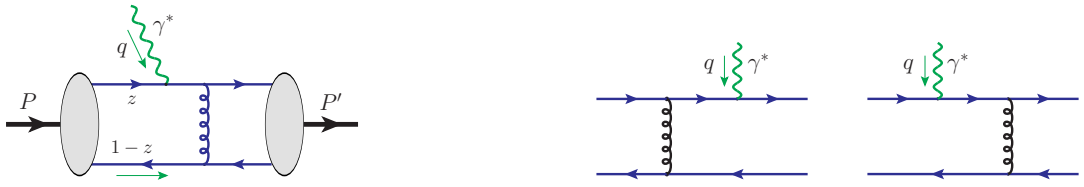

Fig. 4.9: (a) Sketch for pion Form Factor; (b) Leading order Feynman diagrams for the partonic hard part of the factorized pion Form Factor.

For the comparison, we consider the well-known perturbative calculation of pion Form Factor $F_\pi(Q^2)$, as sketched in figure 4.9(a), which can be extracted from elastic electron-pion scattering: $e(\ell)+\pi(p_\pi)\to e(\ell')+\pi(p'_\pi)$. When the momentum transfer $q=\ell-\ell'$ has a high virtuality, with $Q^2\equiv -q^2\gg\Lambda^2_{\rm QCD}$, the pion Form Factor takes the factorized form as [**?**],

$$F_\pi(Q^2)\approx\int_0^1 \mathrm{d}z_1\int_0^1 \mathrm{d}z_2\,\phi(z_1)T_B(z_1,z_2,Q^2)\,\phi(z_2)\,, \tag{4.115}$$

where ϕ is pion DA, $T_B(z_1,z_2,Q^2)$ represents the hard scattering, and the factorization scale dependence is suppressed. With the leading order diagrams in figure 4.9(b), the short-distance hard part is given by [**?**]

$$T_B(z_1,z_2,Q^2)\approx 16\pi C_F\,\frac{\alpha_s(Q^2)}{z_1z_2Q^2}\,, \tag{4.116}$$

with color factor $C_F=4/3$ for SU(3) color. By substituting this lowest order hard part in eq. (4.116) into eq. (4.115), it is clear that the pion Form Factor measurement is only sensitive to the "moment" of pion DA, $\int_0^1 dzz^{-1}\phi(z)$, not the detailed shape of $\phi(z)$, even when the probing scale Q^2 varies. Although the "moment" $\int_0^1 dzz^{-1}\phi(z)$ is expected to be finite since $\phi(z)\to 0$ as $z\to 0$, the short-distance hard part in eq. (4.116) is actually singular as z_1 (and/or z_2) $\to 0$, corresponding to the situation when the virtuality of the exchanged gluon in figure 4.9 goes to zero and the "hard" scattering is actually not taking place at a "short-distance". The reliability of this perturbative fixed-order calculation near the "end-point" region when z_1 (and/or z_2) $\to 0$ could be improved by taking into account the "Sudakov suppression" from resumming high order Sudakov logarithmic contributions. For example, the leading order perturbatively calculated hard part in eq. (4.116) could be

improved as [Li and Sterman(1992)]

$$T_B(z_1, z_2, Q^2) \approx 16\pi C_F \int_0^\infty \mathrm{d}b\, \alpha_s(t)\, b\, K_0(\sqrt{z_1 z_2} Q\, b)\, e^{-\mathcal{S}(z_1, z_2, b, Q)}\,, \tag{4.117}$$

where the running coupling constant α_s is evaluated at $t = \max(\sqrt{z_1 z_2} Q, 1/b)$, K_0 is the modified Bessel function of order zero and the Sudakov factor $\mathcal{S}(z_1, z_2, b, Q)$ is given in eq. (14) of Ref. [Li and Sterman(1992)]. In keeping the same factorized form in eq. (4.115) with the modified hard part in eq. (4.117), an evolution of pion $\phi(z)$'s factorization scale from $1/b$ to the hard scale Q was neglected. With the Sudakov suppression, the perturbative hard part $T_B(z_1, z_2, Q^2)$ in eq. (4.117) is no longer singular as z_1 (and/or z_2) goes to zero.

Like the pion Form Factor, the perturbative hard part calculated from the Type-B diagrams in figure **??** is also singular in the "end-point" region when z_1 (and/or z_2) $\to 0$ or 1, as clearly evident from the behavior of the three propagators in eq. (**??**). In addition, like the hard part of pion Form Factor in eq. (4.116), the dependence on active parton momentum fractions z_1 and z_2 in eq. (**??**) is completely decoupled from the external kinematic variables, and consequently, the contribution from the Type-B diagrams to the exclusive cross section is only sensitive to the "moment" of pion DA.

On the other hand, the three propagators for the Type-A diagrams in figure **??**, as shown in eqs. (**??**) and (**??**), have slightly different features. The contribution from the Type-A diagrams is less singular in the "end-point" region when z_1 or z_2 goes to zero. The dependence on active parton momentum fractions z_1 and z_2 cannot be completely decoupled from the external kinematic variables. As shown in eq. (**??**), z_1 and z_2 are entangled with externally measured photon transverse momentum q_T. It is this entanglement that makes the q_T-distribution of this exclusive cross section to be sensitive to the shape of the z-dependence

of pion DA, or GPDs in pion-baryon scattering.

4.4.5.2 Enhanced sensitivity to the shape of pion DAs

To demonstrate that the differential cross section $\mathrm{d}\sigma/\mathrm{d}q_T^2$ for exclusive $\pi^+\pi^- \to \gamma\gamma$ process is sensitive to both the "moment" as well as the detailed shape of pion DA, we introduce a power-form parametrization for the normalized pion DA,

$$\phi_\alpha(z) = \frac{z^\alpha(1-z)^\alpha}{\mathrm{B}(1+\alpha, 1+\alpha)}\,, \tag{4.118}$$

with $\alpha > 0$ so that the "moment" $\int_0^1 \mathrm{d}z z^{-1}\phi_\alpha(z)$ is finite. When $\alpha = 1$, this normalized pion DA is effectively the same as the so-called asymptotic form of pion DA when factorization scale $\mu \to \infty$ [Lepage and Brodsky(1980)]. In this subsection, we vary the power α to show how $\mathrm{d}\sigma/\mathrm{d}q_T^2$ changes. In the following numerical calculation, we use fixed electromagnetic coupling $\alpha_e = 1/137$ and the one-loop running strong coupling constant $\alpha_s(\mu)$ evaluated at the scale $\mu = q_T$. For exclusive $\pi^+\pi^- \to \gamma\gamma$, which could be a Sullivan-type process as a part of the $p\pi^- \to n\gamma\gamma$ diffractive scattering when the $|t|$ is small, we choose the collision energy $\sqrt{s} = 3 - 6$ GeV, and require q_T to be greater than 1 GeV.

In figure 4.10(a), we plot the "total" cross section defined in eq. (4.136) with $q_{T\mathrm{min}} = 1$ GeV as a function of the power α of the normalized pion DA for various collision energies. Corresponding shapes of the normalized pion DAs are shown in figure 4.10(b). To minimize its dependence on the collision energy, we multiplied a scaling factor s^2 to the cross section, which effectively puts all the curves with four different collision energies on top of each other. However, as shown in figure 4.10(a), the scaled cross section shows a very strong dependence on the value of α, which is not because the partonic hard part is a good probe of the shape

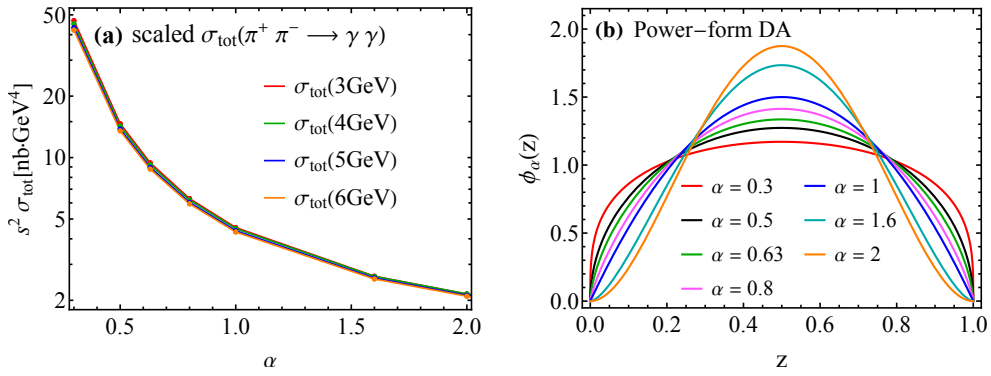

Fig. 4.10: The total cross section (in (a)) for different DAs (shown in (b)) and different CM energies, where a scaling factor s^2 has been multiplied. The total cross section is obtained by integrating over q_T from 1 GeV to $\sqrt{s}/2$. The dots on the curves are the points that were explicitly calculated.

of DAs. Instead, such a strong dependence on α is caused by the "end-point" sensitivity of the perturbatively calculated partonic hard part as discussed in the last subsection, and the fact, as shown in figure 4.10(b), that the value of pion DAs at different α have very different values near the "end-point".

Like the "Sudakov" suppression treatment for the "end-point" region of the pion Form Factor, an improvement of the "end-point" sensitivity is also needed to improve the reliability of perturbative calculation of the factorized hard parts for this new type of exclusive processes, which is beyond the scope of the current paper.

As pointed out in Sec. 4.4.5.1, the propagator of the gluon has a very different momentum structure for Type-A diagrams from those of the Type-B diagrams. The entanglement of momentum fraction z_1, z_2 and the observed q_T in the Type-A diagrams makes the q_T distribution sensitive to the z-dependence of the pion DAs.

In figure 4.11(a), we plot the normalized q_T distribution, defined as $\mathrm{d}\sigma/\mathrm{d}q_T$ divided by the total cross section $\sigma_{\rm tot} \equiv \sigma(q_{T\rm min} = 1\ \mathrm{GeV})$ as defined in eq. (4.136), with respect to the same normalized q_T distribution evaluated with asymptotic pion DA ($\alpha = 1$). Correspond-

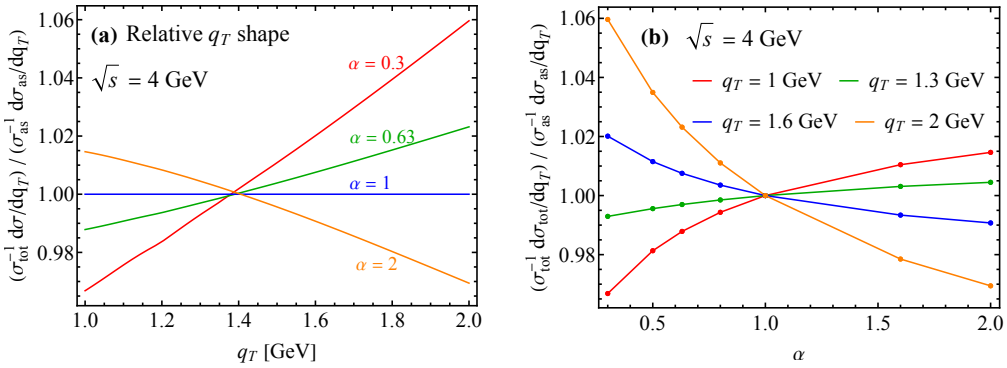

Fig. 4.11: (a) The relative q_T shape for a few choices of power-form DAs with different values of α. The relative q_T shape is obtained by dividing the normalized q_T distribution by the one with the asymptotic DA form. (b) The same normalized q_T distribution as a function of α of the power-form DAs.

ing normalized pion DAs are plotted in figure 4.10(b). In figure 4.11(b), we plot the same normalized q_T distribution as a function of the power α at different values of q_T. The normalized q_T distribution at different q_T values have very different dependence on the α. Naively, from figure 4.11, it seems that the q_T-dependence provides additional 10% sensitivity on the shape of the pion DA. Actually, the q_T-dependence should have provided a much stronger sensitivity to the shape of pion DAs, if the "end-point" sensitivity of the perturbatively calculated partonic hard parts are better controlled. As pointed out in Sec. 4.4.5.1, the Type-B diagrams have a much stronger singular behavior at the "end-point" than that of Type-A diagrams. Consequently, the Type-B diagrams give a much bigger fraction of $\mathrm{d}\sigma/\mathrm{d}q_T$ from the "end-point" region of the pion DAs than what the Type-A diagrams can give, while the Type-A diagrams are more sensitive to the shape of pion DAs. If we can improve the reliability of perturbatively calculated partonic hard cross section near the "end-point" for both Type-A and Type-B diagrams, the Type-A diagrams would contribute a much bigger fraction to the differential cross section $\mathrm{d}\sigma/\mathrm{d}q_T$, making the measurement of $\mathrm{d}\sigma/\mathrm{d}q_T$ more sensitive to the shape of the z-dependence of the pion DAs.

4.4.5.3 Enhanced sensitivity to the shape of GPDs

In this subsection, we try to demonstrate that the photon q_T distribution of exclusive meson-baryon scattering process is sensitive to the functional shapes of nucleon GPD and pion DA. The dependence on pion DA has been discussed in Sec. 4.4.5.2 along with the exclusive $\pi\pi$ annihilation process. We now focus on the sensitivity to the shape of nucleon GPD, and fix pion DA to the power-form in eq. (4.118) with $\alpha = 0.63$, which is the value compatible with the Lattice QCD calculation of the second moment of DA [**?**].

As discussed in Sec. **??**, the integration range of active momentum fraction z_1 of GPDs is extended from $(0, 1)$ to $((\xi - 1)/2\xi, (\xi + 1)/2\xi)$, as shown in eq. (4.97), and consequently, the propagators in partonic diagrams could be on-shell leading to poles along the integration contour of z_1. As discussed in Sec. **??**, the reduced diagram analysis ensures that the only perturbative pinch singularity at leading power is on the lines collinear to the external hadrons, which are systematically removed from the hard part of partonic scattering and absorbed into universal long-distance DAs or GPDs. The only possible singularities of the perturbatively calculated partonic hard part could appear at the "end-point" of the integration, and need to be suppressed by the behavior of non-perturbative DAs and/or GPDs, or by improving high order perturbative calculations as discussed in Sec. 4.4.5.1. When the non-pinched pole of z_1 locates along the contour, we use the distribution identity

$$\frac{1}{z_1 - a \pm i\varepsilon} = P\frac{1}{z_1 - a} \mp i\pi\delta(z_1 - a) \tag{4.119}$$

as a practical method to deform the contour [**?**], where P means the principal-value integration. Our numerical integration strategy is to individually separate each pole and use Eq. (4.119) to deal with the poles on the integration contour of z_1. In this approach, the non-

pinched poles lead to imaginary parts to the scalar coefficients $\mathcal{M}_i$ and $\widetilde{\mathcal{M}}_i$ of the factorized scattering amplitude, and both their real and imaginary parts contribute to the exclusive cross section through the absolute values in eq. (4.112).

For our numerical analysis below, we use the kinematics of J-PARC [**?**] with a charged pion beam of energy around 20 GeV, as well as that of AMBER [**?**] with a pion beam of energy 150 GeV hitting on fixed targets. For nucleon GPD, we choose the GK parametrization [**?**, **?**, **?**, **?**], which models the GPD using double distribution,

$$H_i(x,\xi,t) = \int_{-1}^{1} \mathrm{d}\beta \int_{-1+|\beta|}^{1-|\beta|} \mathrm{d}\alpha\, \delta(x-\beta-\xi\alpha)\, f_i(\beta,\alpha,t)\,, \tag{4.120}$$

where the subscript i refers to the choice of parton flavor and nucleon GPDs $H_i(x,\xi,t)$ are defined with the convention in Ref. [Diehl(2003)], as specified in eq. (4.95). The double distribution $f_i(\beta,\alpha,t)$ is parametrized as

$$f_i(\beta,\alpha,t) = e^{\left(b_i+\alpha_i' \ln|\beta|^{-1}\right)t} \cdot h_i(\beta) \cdot w_i(\beta,\alpha)\,, \tag{4.121}$$

where $h_i(\beta)$ is the forward PDF of flavor i, and w_i is a weight function

$$w_i(\beta,\alpha) = \frac{\Gamma(2n_i+2)}{2^{2n_i+1}\Gamma^2(n_i+1)} \frac{\left[(1-|\beta|)^2-\alpha^2\right]^{n_i}}{(1-|\beta|)^{2n_i+1}}\,, \tag{4.122}$$

which characterizes the ξ dependence of GPD $H_i(x,\xi,t)$ and is normalized as

$$\int_{-1+|\beta|}^{1-|\beta|} \mathrm{d}\alpha\, w_i(\beta,\alpha) = 1\,. \tag{4.123}$$

The larger the power n_i is, the less dependent $H_i(x,\xi,t)$ is on ξ. In the limit that $n_i \to \infty$,

$w_i \to \delta(\alpha)$, and we have

$$H_i(x,\xi,t) = e^{\left(b_i + \alpha_i' \ln|x|^{-1}\right)t} h_i(x)\,, \tag{4.124}$$

which has no dependence on ξ at all.

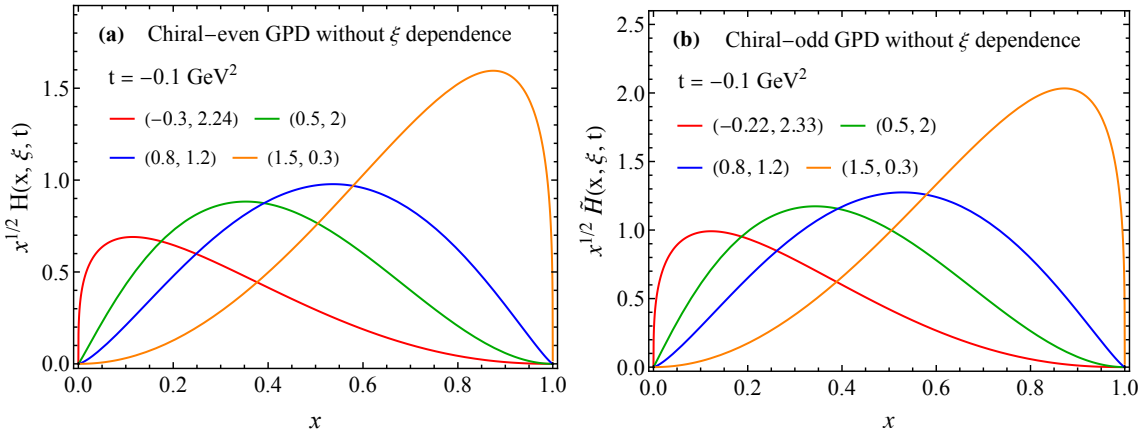

Fig. 4.12: Chiral-even GPD $H(x,\xi,t)$ (a) and chiral-odd GPD $\widetilde{H}(x,\xi,t)$ (b) for $t = -0.1$ GeV^2 and different power parameters (ρ,τ).

The quark double distribution is decomposed into valence and sea components, and sea quark components are taken to be the same for $u_{\rm sea}$ and $d_{\rm sea}$. Since our process is only sensitive to $H_u - H_d$ (or $\widetilde{H}_u - \widetilde{H}_d$) (see eq. (4.100)), the sea components cancel, and only valence components contribute,[3] for which we have

$$f^q_{\rm val}(\beta,\alpha,t) = \left[f^q(\beta,\alpha,t) + \varepsilon_f f^q(-\beta,\alpha,t)\right]\theta(\beta)\,, \tag{4.125}$$

where $\varepsilon = +1$ for H and -1 for $\widetilde{H}$. The condition $\theta(\beta)$ means that $H^q_{\rm val}(x,\xi,t) \neq 0$ only when $-\xi < x \leq 1$.

In the GK model, $b_{\rm val} = 0$ for both H and $\widetilde{H}$, and $\alpha'_{\rm val} = 0.9$ GeV^{-2} for H and

[3] This is also the reason that we neglected the so-called D-term in eq. (4.121) since it only appears for gluon and sea quarks.

0.45 GeV^{-2} for $\widetilde{H}$. The forward parton density $h_i(\beta)$ is parametrized as a "power series" of β, fitted to global-fit PDFs. It is not our purpose to use a realistic GPD, but instead we want to see how different forms of GPDs affect the q_T distribution, so it is convenient to use a simple functional form for $h(\beta)$, for which we choose

$$h_{ud}(\beta) = h_{u_\text{v}}(\beta) - h_{d_\text{v}}(\beta) = N \frac{\beta^\rho (1-\beta)^\tau}{B(1+\rho, 1+\tau)}\,, \tag{4.126}$$

which is similar to eq. (4.118) but with possibly different powers ρ and τ. The normalization factor is $N = 1$ for H and $N = \eta_u - \eta_d = 1.267$ for $\widetilde{H}$ [**?**]. The parameters ρ and τ are fitted to the GK model at $\mu = 2$ GeV, and we have the best fit

$$\begin{aligned}(\rho_0, \tau_0) &= (-0.30, 2.24) \text{ for } H\,,\\ (\rho_0, \tau_0) &= (-0.22, 2.33) \text{ for } \widetilde{H}\,.\end{aligned} \tag{4.127}$$

This gives a $h(\beta)$ peaked near $\beta = 0$. We will vary the powers (ρ, τ) around the best-fit values and compare the change of observables.

4.4.5.3.1 Sensitivity to GPD's x dependence First, we examine the sensitivity of measured photon q_T distribution to the x-dependence of nucleon GPDs. For simplicity we take $n_i \to \infty$ in eq. (4.122) to remove the ξ dependence for both H and $\widetilde{H}$, and have a simplified model for nucleon transition GPDs

$$\begin{aligned}H^{ud}_{pn}(x,\xi,t) &= \theta(x) x^{-0.9\, t/\text{GeV}^2} \frac{x^\rho (1-x)^\tau}{B(1+\rho, 1+\tau)}\,,\\ \widetilde{H}^{ud}_{pn}(x,\xi,t) &= \theta(x) x^{-0.45\, t/\text{GeV}^2} \frac{1.267\, x^\rho (1-x)^\tau}{B(1+\rho, 1+\tau)}\,.\end{aligned} \tag{4.128}$$

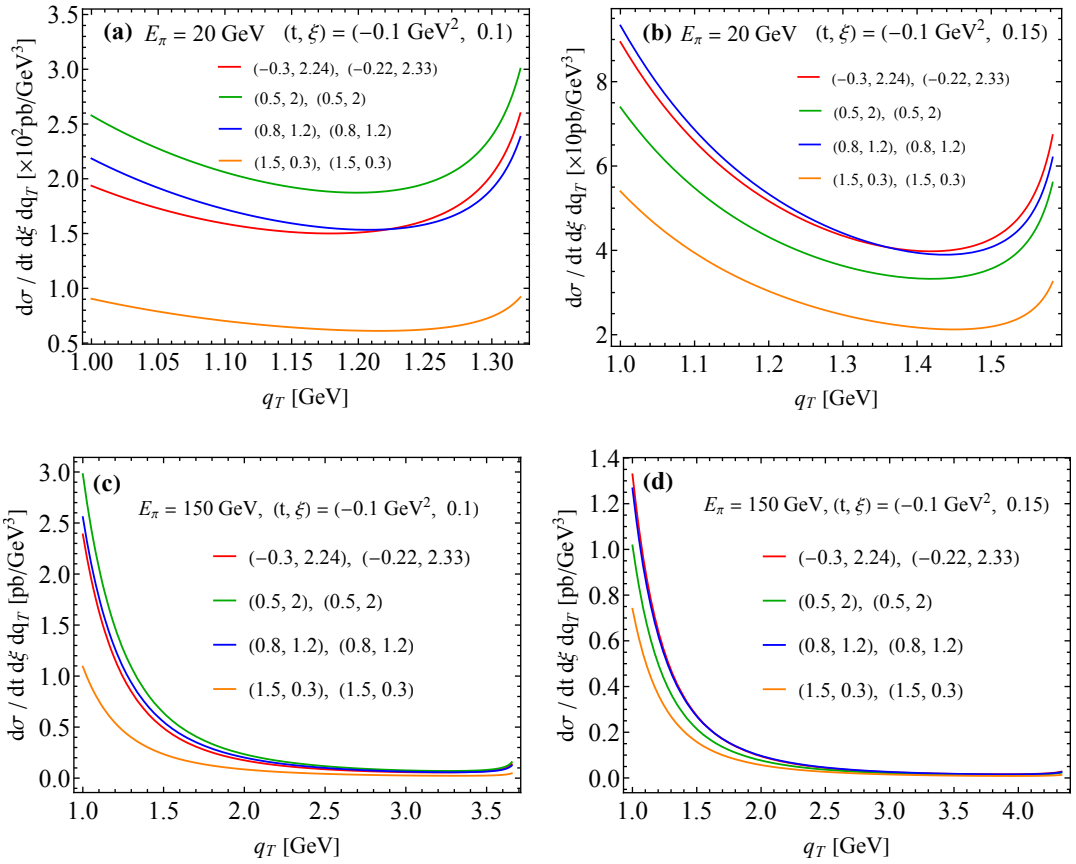

Fig. 4.13: Differential cross section in eq. (4.114) as a function of photon q_T for two choices of pion beam energies, along with two sets of $(t,\, \xi)$ values. Different curves correspond to different (ρ, τ) parameters for the GPD models of the chiral-even GPDs followed by that of the chiral-odd GPDs. The rise at large q_T is due to the Jacobian peak of the differential cross section.

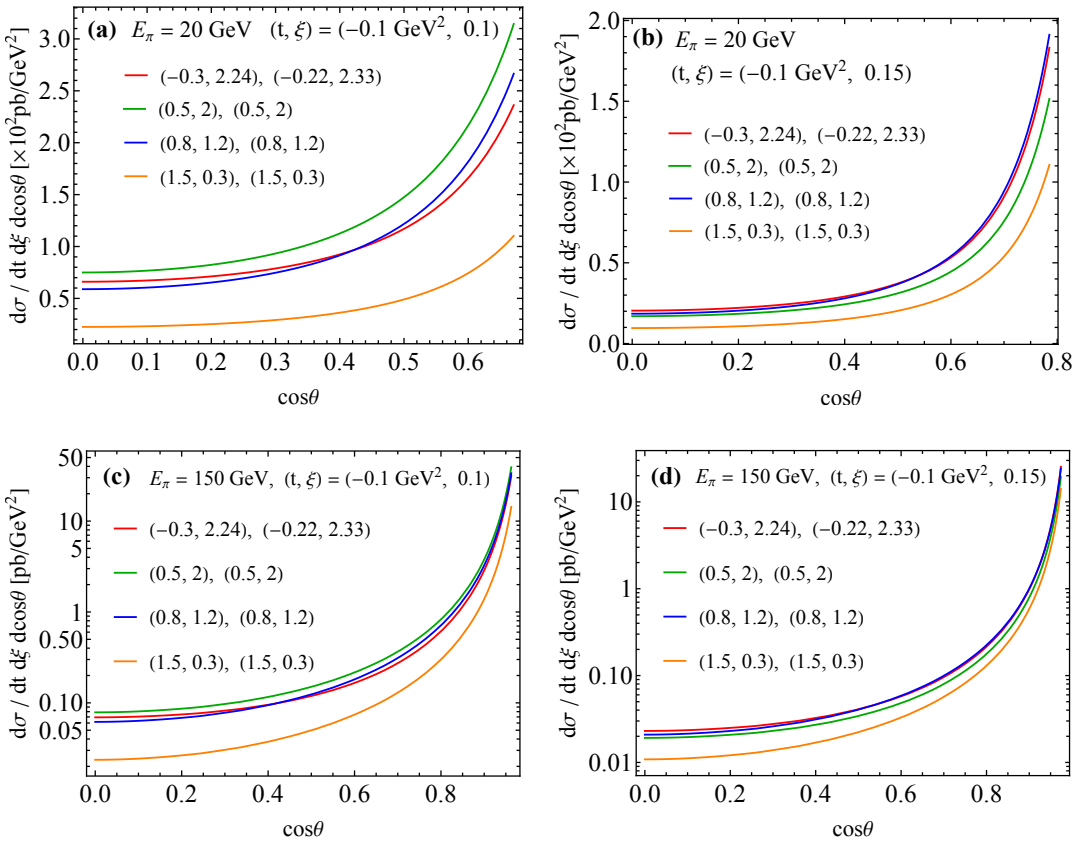

Fig. 4.14: Differential cross section in eq. (4.114) as a function of $\cos\theta$ of the observed photon with all parameters chosen to be the same as that in figure 4.13.

Apart from the best-fit parameters in eq. (4.127), we choose an additional set of parameters,

$$(\rho, \tau) = (0.5, 2),\ (0.8, 1.2),\ (1.5, 0.3), \tag{4.129}$$

for both $H^{ud}_{pn}(x, \xi, t)$ and $\widetilde{H}^{ud}_{pn}(x, \xi, t)$. This gives a set of GPDs with their x-dependence peaked between $x = 0$ and 1, as shown in Figs. 4.12 for $t = -0.1$ GeV^2. Although there is no explicit ξ dependence in eq. (4.128), the hard-part integration in (4.106) still knows about ξ since z_1 is a function of x and ξ as defined in eq. (4.96). Moreover, ξ characterizes the CM energy of the hard collision (eq. (4.86)) and thus the range of q_T. Therefore, the integration of q_T also differs for different ξ. As a result there will still be substantial ξ dependence of the cross section.

With the model nucleon GPDs in figure 4.12, we plot in figure 4.13 the absolute differential cross section in eq. (4.114) as a function of measured photon q_T at both J-PARC and AMBER pion beam energies, along with two choices of (t, ξ) values. We have restricted $q_T \geq 1$ GeV to ensure that power correction to the factorization formalism is sufficiently small. The upper bound of q_T depends on the collision energy and ξ. Different curves correspond to different choices of (ρ, τ) parameters for the GPD models, which are chosen to be the same for both chiral-even and chiral-odd GPDs. The rise at large q_T is due to the Jacobian peak of the differential cross section. We can avoid the Jacobian peak by plotting the differential cross sections with respect to $\cos\theta = \sqrt{1 - 4q_T^2/\hat{s}}$ with θ being the angle between the observed photon and collision $\hat{z}$-axis, instead of q_T, as shown in figure 4.14. By comparing plots on the left and right — with different ξ, and plots on the top and bottom — with increase of collision energy $\sqrt{s}$, the q_T distribution becomes more and more dominated by small q_T. As $\sqrt{s}$ and ξ (or $\sqrt{\hat{s}}$) increase, more phase space opens up for the production

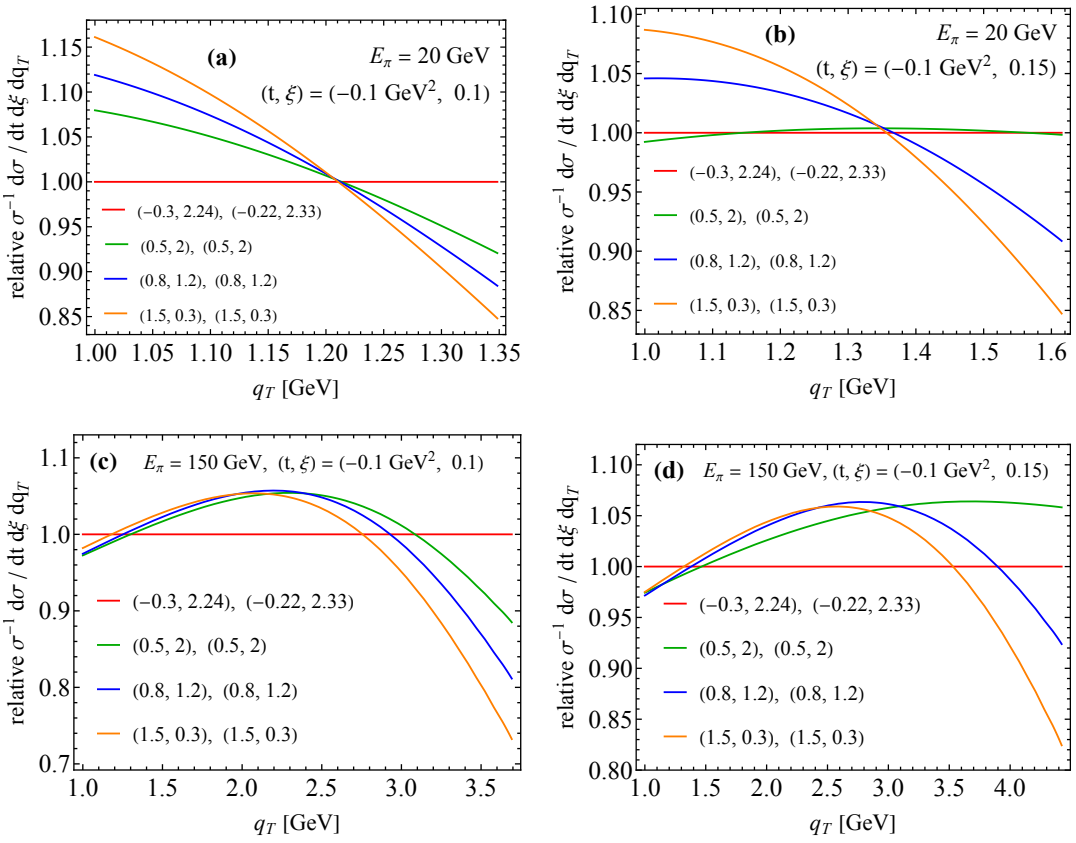

Fig. 4.15: Ratio of normalized differential cross sections $\sigma^{-1}\mathrm{d}\sigma/\mathrm{d}t\,\mathrm{d}\xi\,\mathrm{d}q_T$ as a function of observed photon q_T evaluated with the GPD model in eq. (4.128). Different curves correspond to different parameter sets of the GPD model in eq. (4.128).

of the two back-to-back photons. As q_T decreases, the virtualities of the quark propagators in the leading-order diagrams in figure **??** and **??** decrease, leading to the enhancement of differential cross sections.

To make the difference of q_T shapes more manifest to better visualize the sensitivity of measured q_T distribution to the x-dependence of nucleon GPDs, we plot in figure 4.15 the *ratio* of the normalized differential cross sections as a function of q_T for two different collision energies. The normalized cross sections are defined by dividing the differential cross sections by $\sigma(q_{T\text{min}} = 1 \text{ GeV})$ like what we plotted in figure 4.11. The *ratio* of the normalized differential cross sections is defined by dividing by the one evaluated with the best-fit GPD model parameters in eq. (4.127) — the red curve. Taking the ratio of normalized differential cross sections effectively removes the huge variation of the absolute values of the cross sections and enhances the dependence on the parameters of GPD models, as clearly shown in figure 4.15. It is evident that as the peak in x-distribution of GPD model in figure 4.12 shifts from 0 to 1, the q_T shape differs by around 10% to 20%, without even considering the possible improvement from better control of the "end-point" sensitivity as discussed in Sec. 4.4.5.1. And by comparing figure 4.11 and 4.15, we find more sensitivity to the shape of GPD than that of DA, which means the sensitivity comes more from the DGLAP region than the ERBL region. Hence, we can conclude that the *shape* of q_T distribution has significant sensitivity to the x-dependence (or equivalently, the z_1-dependence) of GPDs.

4.4.5.3.2 Sensitivity to GPD's ξ dependence In contrast to the x-dependence of GPDs, which is proportional to the relative momentum of the active quark-antiquark pair from the diffractive nucleon, the ξ and t are direct kinematic observables once we measure the momentum of the diffracted nucleon in an event. So, in principle, getting information

on ξ and t is much more direct than getting the x-dependence. However, since GPDs are collective functions of (x, ξ, t), extracting the (ξ, t) dependence of GPDs from measured (ξ, t) dependence of exclusive cross sections depends on how x-dependence is entangled with ξ- and t-dependence in GPDs, and also, in practice, how GPDs are parametrized in terms of their (x, ξ, t)-dependence.

The measured ξ-dependence of this new type of exclusive processes has three major sources: (1) ξ-dependence of GPDs, e.g., the parameter n_i-dependence of the GK model in eq. (4.122); (2) ξ-dependence from the factorized scattering amplitudes, i.e., the convolution in eq. (4.106)); and (3) kinematic effect from the fact that ξ characterizes the CM energy of the hard collision when cross section is expressed in terms of (t, ξ, q_T^2). The kinematic effect is reflected by the $(1 - \xi^2)/\xi^2$ factor in eq. (4.114) and is independent of (1) and (2). In principle, it is not possible to separate the x-dependence from the ξ-dependence of GPD because of (2), i.e., the convolution of GPD and hard coefficient depends on ξ. In this subsection, we try to explore to what extent the cross section depends on how ξ is parametrized in the GPD.

To focus on the x-dependence, we set $n_i \to \infty$ in our GPD model in eq. (4.122) in our discussion in last subsection, which led to a model of GPDs that has no dependence on ξ as shown in eq. (4.128). To test the sensitivity to ξ-dependence, we choose $n_i = 0$ and $n_i = 1$ as two additional model GPDs. We still keep the same parametrization of $h_i(\beta)$ in eq. (4.126). The advantage of using small integers for n_i is that we can analytically integrate out eq. (4.120) and express GPD in terms of special functions. Since our proposed process is only sensitive to the valence region, letting $n_i \to n_{\text{val}}$, and combining eq. (4.120) with

eqs. (4.121), (4.122), (4.125), and (4.126) gives us the GPD model,

$$(\mathrm{GPD})^{ud}_{pn}(x,\xi,t) = N \begin{cases} \dfrac{\mathrm{B}_{x_1}(1+\rho-\alpha'_v t,\tau) - \mathrm{B}_{x_2}(1+\rho-\alpha'_v t,\tau)}{2\,\xi\,B(1+\rho,\,1+\tau)} & x \geq \xi\,, \\ \dfrac{\mathrm{B}_{x_1}(1+\rho-\alpha'_v t,\tau)}{2\,\xi\,B(1+\rho,\,1+\tau)} & -\xi \leq x < \xi\,, \\ 0 & x < -\xi\,, \end{cases} \tag{4.130}$$

for $n_{\mathrm{val}} = 0$, and

$$\begin{aligned} &(\mathrm{GPD})^{ud}_{pn}(x,\xi,t) = N \\ &\times \begin{cases} \dfrac{3(1-\xi^2)}{4\xi^3 \mathrm{B}(1+\rho,\,1+\tau)} \times \Big[-\mathrm{B}_{x_1}(3+\rho-\alpha'_v t,\tau-2) + \mathrm{B}_{x_2}(3+\rho-\alpha'_v t,\tau-2) \\ \quad +(x_1+x_2)\Big(\mathrm{B}_{x_1}(2+\rho-\alpha'_v t,\tau-2) - \mathrm{B}_{x_2}(2+\rho-\alpha'_v t,\tau-2)\Big) \\ \quad -x_1 x_2\Big(\mathrm{B}_{x_1}(1+\rho-\alpha'_v t,\tau-2) - \mathrm{B}_{x_2}(1+\rho-\alpha'_v t,\tau-2)\Big)\Big] & x \geq \xi \\ \dfrac{3(1-\xi^2)}{4\xi^3 \mathrm{B}(1+\rho,\,1+\tau)} \times \Big[-\mathrm{B}_{x_1}(3+\rho-\alpha'_v t,\tau-2) \\ \quad +(x_1+x_2)\mathrm{B}_{x_1}(2+\rho-\alpha'_v t,\tau-2) - x_1 x_2 \mathrm{B}_{x_1}(1+\rho-\alpha'_v t,\tau-2)\Big] & -\xi \leq x < \xi \\ 0 & x < -\xi \end{cases} \end{aligned} \tag{4.131}$$

for $n_{\mathrm{val}} = 1$, where

$$x_1 = \frac{x+\xi}{1+\xi}, \quad x_2 = \frac{x-\xi}{1-\xi} \tag{4.132}$$

and

$$\mathrm{B}_x(a,\,b) = \int_0^x \mathrm{d}y\, y^{a-1}\,(1-y)^{b-1} \tag{4.133}$$

is the incomplete Beta function. The parameter b_v in eq. (4.121) has been set to 0. α'_v and

N are taken unchanged from $n_i = \infty$.

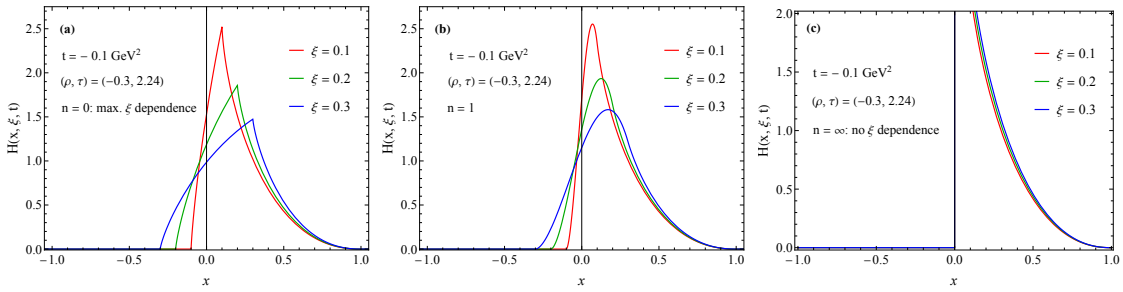

Fig. 4.16: Chiral-even GPD $H(x, \xi, t)$ as a distribution of x for three different ξ and three different values of $n_{\rm val}$, which controls the GPD ξ dependence in the GK model.

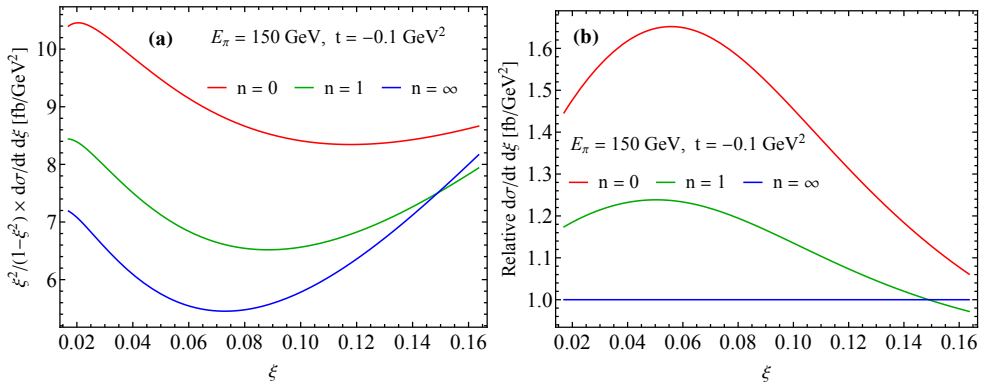

Fig. 4.17: (a) Absolute and (b) relative distributions of ξ at $t = -0.1$ GeV^2 for 150 GeV pion beam, for the three different GPD models shown in figure 4.16. The relative distribution in (b) is obtained by dividing each curve in (a) by the one with $n = \infty$.

In figure 4.16, we plot our models for chiral-even GPD $H(x, \xi, t)$ as functions of x for three values of $n_{\rm val} = 0, 1, \infty$. Our model GPDs for $n_{\rm val} = 0$ and 1 are given in eqs. (4.130) and (4.131), respectively. For $n_{\rm val} = \infty$, the GPDs are given in eq. (4.128). We fix (ρ, τ) to be the best-fit values (4.127), $t = -0.1$ GeV^2 and show GPDs for three values of $\xi (= 0.1, 0.2, 0.3)$. GPDs with $n_{\rm val} = 0$ have the maximum ξ dependence while those with $n_{\rm val} = \infty$ have no ξ dependence, which is clearly evident from the examples of chiral-even GPD $H(x, \xi, t)$ in figure 4.16.

By integrating out q_T, we plot the cross section as a distribution of ξ in figure 4.17 for the AMBER energy $E_\pi = 150$ GeV, where the kinematic factor $(1-\xi^2)/\xi^2$ has been divided

out. We see that different ξ parametrizations do reflect themselves in the ξ-distribution of differential cross sections. Their relative differences are better seen by taking ratios to the one with $n = \infty$, as seen in figure 4.17(b). Comparing $n = \infty$ with $n = 1$, we see that introducing some ξ dependence to GPDs through $n = 1$ leads to 20% change to the ξ distribution of the cross sections. Then increasing the ξ dependence from $n = 1$ to $n = 0$ leads to a further $20\% \sim 40\%$ change.

4.4.5.3.3 Sensitivity to GPD's t dependence Same as the ξ-dependence, the t-dependence of the diffractive cross section is experimentally determined. On the other hand, the t-dependence of theoretically factorized cross section comes from (1) the t dependence of GPD and (2) kinematic effect of hard process. As shown in eq. (4.88) the value of t actually constrains the available range of the ξ.

It is worth emphasizing that t does not enter the hard process directly as an immediate consequence of the leading-power factorization, which is accurate up to power corrections of $|t|/Q^2$. However, the information of t is not lost, but is captured by GPDs. The Fourier transform of GPDs with respect to the transverse component of t leads to transverse spatial density distributions of quarks and gluons inside a bound hadron, which could reveal very valuable information on how quarks and gluons are distributed in an environment of a confined hadron. Comparing with the x-dependence, t-dependence is more visible in a physical process and will not be explored in more details in this work.

4.5 Single diffractive hard exclusive photon-meson pair photoproduction

Generalized parton distributions (GPDs), $F(x, \xi, t)$, are important non-perturbative correlation functions to probe into the confined QCD dynamics (for reviews, see [**?**, Diehl(2003), **?**, **?**]). They entail tomographic parton images of hadrons, in the space of parton momentum fraction x and transverse position $\boldsymbol{b}_T$ [Burkardt(2000), Burkardt(2003)]. Their x moments can be related to the gravitational form factors which provide partonic contributions to a hadron's mass [**?**, **?**, **?**, **?**], spin [Ji(1997b)], internal pressure and shear force [Polyakov and Schweitzer(2018), **?**], etc.

Experimental measurement of GPDs relies on factorization theorems, which express the scattering *amplitudes* of diffractive exclusive processes as GPDs, convoluted in x with infrared-safe hard scattering coefficients. A number of processes have been proposed for this business [Ji(1997a), Radyushkin(1997), Brodsky et al.(1994)Brodsky, Frankfurt, Gunion, Mueller, and Stri Frankfurt et al.(1996)Frankfurt, Koepf, and Strikman, Berger et al.(2002b)Berger, Diehl, and Pire, Berger et al.(2001)Berger, Diehl, and Pire, Guidal and Vanderhaeghen(2003), **?**, **?**, Pedrak et al.(2017)Ped **?**, **?**, **?**], among which is the deeply virtual Compton scattering (DVCS) [Ji(1997a), Radyushkin(1997)], often referred to as the golden channel for probing GPDs. Nevertheless, most of the processes including DVCS do not give sensitive constraints on the x dependence of GPDs, a fact deeply rooted in their exclusive nature. In contrast to the inclusive deep inelastic scattering, where the condition for the struck parton to produce physical particles restricts its momentum fraction to be between the Bjorken x_{Bj} and 1, the amplitude nature of GPD factorization implies x as a loop momentum, which is thus always integrated from -1 to 1. The only sensitivity to the GPD's x dependence comes from the interplay between x and

some external observable Q.

However, in many cases like the DVCS, there is no such interplay. The hard coefficients are reduced to factors that only depend on x and ξ, so that the measured cross sections are probing GPDs only through their "moments" [Qiu and Yu(2023)]. This makes the full extraction of GPDs almost impossible [Bertone et al.(2021)Bertone, Dutrieux, Mezrag, Moutarde, and Sznaj
It is therefore necessary to have processes in which x is entangled with the external observables. We refer to such processes as having enhanced x-sensitivity [Qiu and Yu(2023)]. To fully map out the x distribution of GPDs, we should have as many observables as possible, especially those with enhanced sensitivity.

The way for this aim has been paved in Ref. [Qiu and Yu(2023)], where we proposed a general type of processes, the single diffractive hard exclusive processes (SDHEPs), which have the minimal kinematic configurations to be factorized into GPDs whereas are sufficiently general to cover almost all processes in the literature for studying GPDs. As a general condition for enhanced x sensitivity, the leading-order (LO) hard subdiagram should have at least one propagator that is not connected to two lightlike lines. This necessarily requires an "upgraded" topology beyond the simplest $2 \to 2$ configuration as in the DVCS. One example of such processes was studied in Ref. [Qiu and Yu(2022)] for the hard diphoton production in diffractive nucleon-pion scattering, $N(p) + \pi(p_2) \to N'(p') + \gamma(q_1) + \gamma(q_2)$, where the nontrivial topology comes from the large-momentum meson that attaches to the hard scattering by *two* collinear parton lines. It was demonstrated that the distribution of the hard transverse momenta of the photons provides a sensitive probe to the GPD x-dependence, especially in the DGLAP region [Qiu and Yu(2022)].

This Letter is devoted to the study of a related crossing process, the hard photon-meson

pair production in exclusive nucleon-photon scattering,

$$N(p) + \gamma(p_2) \to N'(p') + \pi(q_1) + \gamma(q_2). \tag{4.134}$$

Similarly, in this case, the transverse momentum, or equivalently, the polar angle θ, of the pion or final-state photon, provides an additional sensitive handle to the x dependence of GPDs. However, there are some major differences from the diphoton production process that highlight the photoproduction process: (1) the crossing kinematics provides an enhanced x-sensitivity mainly in the ERBL region, complementary to the diphoton production; (2) while only charged pion beams are accessible for the diphoton production, one can readily select neutral pion product in the photoproduction process; this makes it not restricted to the flavor transition GPDs, and, more importantly, will further enhance the x-sensitivity due to a cancellation of certain "moment" terms; and (3) the polarization of the initial-state photon beam can be easily controlled, as can be realized in the JLab Hall-D GlueX experiment [**?**]. This allows the study of various polarization asymmetries, which provide further independent constraints on GPDs. In the following, we provide a phenomenological study of the enhanced x sensitivity of the photoproduction process, focusing on the GlueX kinematics. In particular, we will show how GPDs can be constrained by use of multiple observables.

4.5.1 Single diffractive hard exclusive photoproduction of a photon-meson pair

Each event of the process in Eq. (4.134) is characterized in the following way. The lab frame is chosen as the center-of-mass (c.m.) system of the hadron N and photon γ beams, with the

$\hat{z}_{\rm lab}$ and $\hat{x}_{\rm lab}$ directions along the momentum p and transverse spin $\boldsymbol{s}_T$ of N, respectively. The photon carries a linear polarization ζ along the azimuth $\hat{\phi}_\gamma$. The diffraction $N \to N'$ is described by the momentum transfer $\Delta \equiv p - p'$, which defines three observables, its invariant mass $t \equiv \Delta^2$, skewness $\xi \equiv \Delta^+/(p+p')^+$, and azimuth $\hat{\phi}_\Delta$. The distribution of $\hat{\phi}_\Delta$ is determined by the $\boldsymbol{s}_T$, which we will not consider in this Letter. The kinematics of the final-state π-γ pair is described in the SDHEP frame, which is defined as their c.m. frame with the initial-state photon along the $-z$ direction and x lying on the diffractive plane along the direction of $\boldsymbol{\Delta}_T$ in the lab frame, as shown in Fig. 9.5, by the angles (θ, ϕ) of the pion.

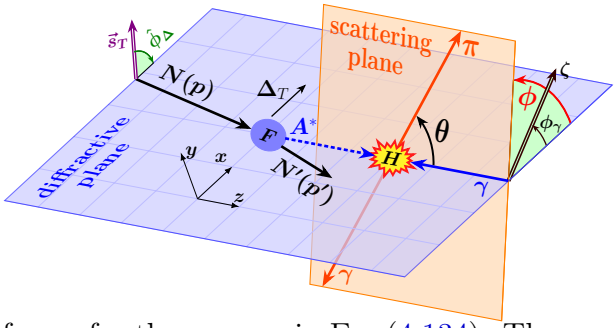

Fig. 4.18: The SDHEP frame for the process in Eq. (4.134). The x-y-z axes are with respect to the diffractive plane.The arrowed double lines on the left and right refer to the transverse spin and linear polarization of the initial-state nucleon N and photon γ, respectively.

Going from the lab frame to the SDHEP frame is achieved by a transverse boost [Diehl(2003)] followed by a rotation around the z direction, which only changes the direction of the linear photon polarization to $\phi_\gamma = \hat{\phi}_\gamma - \hat{\phi}_\Delta$. The use of the new SDHEP frame separates the diffractive production of the long-lived state A^*, $N \to N' + A^*$, and the following $2 \to 2$ hard scattering, $A^* + \gamma \to \pi + \gamma$, and makes it convenient to study the angular correlations due to initial-state polarizations.

The selection of pions forbids the channel when A^* is a virtual photon due to charge parity. The minimal configuration starts with A^* being a collinear parton pair. As elaborated in Ref. [Qiu and Yu(2023)], when the transverse momentum of the final-state pion (q_{1T}) or

photon (q_{2T}) is much greater than the invariant mass of the parton pair, i.e., $q_{1T} = q_{2T} = q_T \gg \sqrt{-t}$, the amplitude of the photoproduction process [Eq. (4.134)] can be factorized into GPDs for the nucleon transition $N \to N'$ and a distribution amplitude (DA) for the final-state pion creation, with hard perturbatively calculable coefficients,

$$\mathcal{M}_{N\gamma_\lambda \to N'\pi\gamma_{\lambda'}} = \sum_{q=u,d} \int_{-1}^{1} dx \int_0^1 dz\, \bar{D}_{q/\pi}(z) \times \left[F^q_{NN'}(x,\xi,t)\, \widetilde{C}_{\lambda\lambda'}(x,z) + \widetilde{F}^q_{NN'}(x,\xi,t)\, C_{\lambda\lambda'}(x,z) \right], \tag{4.135}$$

up to corrections suppressed by powers of t and $\Lambda_{\rm QCD}$. To the leading power, the spinless pion DA $\bar{D}_{q/\pi}$ only selects the unpolarized and polarized GPDs, $F^q_{NN'}$, and $\widetilde{F}^q_{NN'}$. We have neglected the contribution from the gluon GPD for simplicity. The hard coefficients $C_{\lambda\lambda'}$ and $\widetilde{C}_{\lambda\lambda'}$ are helicity amplitudes for the photon scattering off a collinear on-shell quark pair $[q\bar{q}']$, with λ and λ' denoting the photon helicities in the SDHEP frame. They can be reduced by parity symmetry to only four independent amplitudes, two helicity-conserving ones C_+ and $\widetilde{C}_+$ and two helicity-flipping ones C_- and $\widetilde{C}_-$. The explicit forms are collected in the Supplemental Material.

Including the dependence on the nucleon and photon polarizations, we have the differential cross section

$$\frac{d\sigma}{d|t|\, d\xi\, d\cos\theta\, d\phi} = \frac{1}{2\pi} \frac{d\sigma}{d|t|\, d\xi\, d\cos\theta} \cdot \big[1 + \lambda_N \lambda_\gamma\, A_{LL} + \zeta\, A_{UT} \cos 2(\phi - \phi_\gamma) + \lambda_N\, \zeta A_{LT} \sin 2(\phi - \phi_\gamma)\big], \tag{4.136}$$

where λ_N and λ_γ are the net helicities of the initial-state nucleon and photon, respectively.

In Eq. (4.136), we have used the unpolarized differential cross section,

$$\frac{d\sigma}{d|t|\,d\xi\,d\cos\theta} = \frac{\mathcal{N}^2\,(1-\xi)}{32\,s\,(2\pi)^3\,(1+\xi)}\Sigma_{UU}, \tag{4.137}$$

where $\mathcal{N}$ is a normalization factor defined below Eq. (**??**), and defined the Σ_{UU} and polarization asymmetries,

$$\begin{aligned}
\Sigma_{UU} &= |\mathcal{M}_+^{[\widetilde{H}]}|^2 + |\mathcal{M}_-^{[\widetilde{H}]}|^2 + |\widetilde{\mathcal{M}}_+^{[H]}|^2 + |\widetilde{\mathcal{M}}_-^{[H]}|^2, \\
A_{LL} &= 2\,\Sigma_{UU}^{-1}\,\mathrm{Re}\left[\mathcal{M}_+^{[\widetilde{H}]}\,\widetilde{\mathcal{M}}_+^{[H]*} + \mathcal{M}_-^{[\widetilde{H}]}\,\widetilde{\mathcal{M}}_-^{[H]*}\right], \\
A_{UT} &= 2\,\Sigma_{UU}^{-1}\,\mathrm{Re}\left[\widetilde{\mathcal{M}}_+^{[H]}\,\widetilde{\mathcal{M}}_-^{[H]*} - \mathcal{M}_+^{[\widetilde{H}]}\,\mathcal{M}_-^{[\widetilde{H}]*}\right], \\
A_{LT} &= 2\,\Sigma_{UU}^{-1}\,\mathrm{Im}\left[\mathcal{M}_+^{[\widetilde{H}]}\,\widetilde{\mathcal{M}}_-^{[H]*} + \mathcal{M}_-^{[\widetilde{H}]}\,\widetilde{\mathcal{M}}_+^{[H]*}\right],
\end{aligned} \tag{4.138}$$

where we have dropped terms suppressed by ξ or t, and used the notations $\mathcal{M}_\pm^{[\widetilde{H}]}$ and $\widetilde{\mathcal{M}}_\pm^{[H]}$ for the amplitudes,

$$\begin{aligned}
\mathcal{M}_\pm^{[\widetilde{H}]} &\equiv \int_{-1}^{1} dx \int_0^1 dz\, \widetilde{H}(x,\xi,t)\bar{D}(z)C_\pm(x,z;\theta), \\
\widetilde{\mathcal{M}}_\pm^{[H]} &\equiv \int_{-1}^{1} dx \int_0^1 dz\, H(x,\xi,t)\bar{D}(z)\widetilde{C}_\pm(x,z;\theta).
\end{aligned} \tag{4.139}$$

4.5.2 Enhanced x-sensitivity

One can see from Eq. (4.136) that while both the t and ξ dependence of GPDs can be directly measured, the x dependence (as well as the z dependence of DA) is only probed via the GPD convolutions [Eq. (4.139)] with hard coefficients, in which it is completely integrated out. All sensitivity to the GPD x dependence comes from the hard coefficients C. As explained in

Ref. [Qiu and Yu(2023)], however, in most cases, the LO hard coefficient C is composed of terms that factorize into x-dependent parts which are independent of external observables at all. This is because every internal propagator in the hard parts is connected to two external lightlike lines [Qiu and Yu(2023)].

In the case of the photoproduction process [Eq. (4.134)], it means

$$C(x,\xi;z;\cos\theta) = \sum_i G_i(x,\xi) J_i(z) T_i(\cos\theta), \tag{4.140}$$

so that the convolution [Eq. (4.139)] reduces to simple "moments" of GPD, $F_i(\xi,t) = \int dx\, G_i(x,\xi)\, F(x,\xi,t)$, and DA, $\bar{D}_i = \int dz\, J_i(z)\, \bar{D}(z)$, multiplied by predictable $\cos\theta$ distributions $T_i(\cos\theta)$. Such x-sensitivity through simple GPD moments that only depend on ξ and t is called moment sensitivity in Ref. [Qiu and Yu(2023)]. It applies to most known processes, including the DVCS [Ji(1997a), Radyushkin(1997)], deeply virtual meson production [Brodsky et al.(1994)Brodsky, Frankfurt, Gunion, Mueller, and Strikman, Frankfurt et al.(1996)Frank photoproduction of lepton [Berger et al.(2002b)Berger, Diehl, and Pire] or photon pair [Pedrak et al.(2017) Grocholski et al.(2021)Grocholski, Pire, Sznajder, Szymanowski, and Wagner, Grocholski et al.(2022)Groc and the exclusive Drell-Yan process [Berger et al.(2001)Berger, Diehl, and Pire]. The x poles in such processes are only at $\pm\xi$ [Qiu and Yu(2023)], and one may only constrain the moments,

$$F_0(\xi,t) = \mathcal{P}\int_{-1}^{1} dx \frac{F(x,\xi,t)}{x-\xi}, \tag{4.141}$$

with $\mathcal{P}$ indicating principle-value integration, and the diagonal values $F(\xi,\xi,t)$ through the imaginary parts picked around the poles, for some GPD component F, which for our purpose in this Letter can take the charge-conjugation-even or odd GPD combinations defined in Eq. (**??**).

As an example, the convolutions $\mathcal{M}_{-}^{[\widetilde{H}]}$ an $\widetilde{\mathcal{M}}_{-}^{[H]}$ in Eq. (4.138) of GPDs and helicity-flipping amplitues are only probing the moments, $\widetilde{H}_0^+(\xi,t)$ and $H_0^+(\xi,t)$, and the diagonal values, $\widetilde{H}^{\pm}(\xi,\xi,t)$ and $H^{\pm}(\xi,\xi,t)$, through the imaginary parts (see Eqs. (**??**) and (**??**)).

Having only moment sensitivity is far from enough to map out the x distribution of GPDs. One can easily construct null solutions to Eq. (4.141) that give zero to the moments, diagonal values and forward limits [Bertone et al.(2021)Bertone, Dutrieux, Mezrag, Moutarde, and Sznajder]. Such solutions are termed shadow GPDs, which are invisible to processes that only possess moment-type sensitivity. In other words, the hard coefficients are not invertible. By projecting the x distribution to a few moments, one loses the information in a whole degree of freedom, so that a complete deconvolution from those processes becomes impossible. Although it has been argued that taking evolution effects into account can help with this situation [**?**], the improvement suffers from high order suppression so is numerically not appreciable [Bertone et al.(2021)Bertone, Dutrieux, Mezrag, Moutarde, and Sznajder], unless one goes to a sufficiently high scale [**?**]. Such kinematic region, nevertheless, corresponds to a vanishingly low production rate, so will not give the required precision.

However, the helicity-conserving hard coefficients C_+ and $\widetilde{C}_+$ contain some e_1e_2-proportional terms that cannot be factorized as Eq. (4.140), so that the external observable θ is entangled with the partons' momentum fractions x and z. Their convolutions $\widetilde{\mathcal{M}}_{+}^{[H]}$ and $\mathcal{M}_{+}^{[\widetilde{H}]}$ with GPDs give the special integrals, in addition to terms that only depend on the moments,

$$(I[H], I[\widetilde{H}]) = \int_{-1}^{1} dx \frac{(H^+, \widetilde{H}^+)(x,\xi,t)}{x - x_p(\xi,z,\theta) + i\epsilon}. \tag{4.142}$$

Such special integrals arise from diagrams in which the two photon lines in Eq. (4.134) are attached to different fermion lines, so that the intermediate gluon is not connected to two

light-like lines. It contributes an x pole that is away from $\pm\xi$,

$$x_p(\xi, z, \theta) = \xi \cdot \left[\frac{\cos^2(\theta/2)(1-z) - z}{\cos^2(\theta/2)(1-z) + z}\right]. \tag{4.143}$$

This goes from ξ to $-\xi$ as z goes from 0 to 1, so it scans through the whole ERBL region. Even though Eq. (4.142) is further subject to the z integration with a profiling from the DA, the non-factoring feature necessarily causes the θ distribution to reflect *enhanced sensitivity* to the x dependence, especially in the ERBL region. This is in contrast to the diphoton production process [Qiu and Yu(2022)] which yields a special pole that scans through the whole DGLAP region.

This is similar to the double DVCS (DDVCS) process [Guidal and Vanderhaeghen(2003), **?**, **?**], for which the hard coefficient gives a pole at $x_p^{\text{DDVCS}} = \xi \cdot (Q^2 - Q'^2)/(Q^2 + Q'^2)$, which picks up the C-even GPD values at $x = x_p^{\text{DDVCS}} \in [0, \xi)$, where $Q > Q' > 0$ are the virtualities of the space-like and time-like photons, respectively. This is not under a further integration of z, so the imaginary part of the amplitude, which can be measured through single lepton beam helicity asymmetry, reflects a point-by-point sensitivity to the GPD x dependence. However, the amplitude is suppressed by the sixth power of the QED coupling and two hard photon propagators, so it suffers from a small production rate, which makes a practical measurement very challenging [**?**, **?**].

On the other hand, however, the four amplitudes $\mathcal{M}_{\pm}^{[\widetilde{H}]}$ and $\widetilde{\mathcal{M}}_{\pm}^{[H]}$ cannot be distinguished by only considering such one single observable as the unpolarized $\cos\theta$ distribution in Eq. (4.137); especially, the two amplitudes $\mathcal{M}_{+}^{[\widetilde{H}]}$ and $\widetilde{\mathcal{M}}_{+}^{[H]}$ with enhanced x-sensitivity cannot be distinguished. It is important to further consider the polarization asymmetry observables in Eq. (4.138). The single spin asymmetry, A_{UT}, mixes the helicity-conserving

and flipping amplitudes, and then depends more on the amplitudes with enhanced sensitivity, especially on their absolute signs. The double spin asymmetry observables, A_{LL} and A_{LT}, further mix the two GPDs H and $\widetilde{H}$, providing a better power to distinguish them. In particular, A_{LT} is given by the imaginary parts of the amplitudes, which probe the GPD values in the ERBL region due to the x poles at $\pm\xi$ from regular moment-type propagators and at $x_p(\xi, z, \theta)$ in Eq. (4.143) from the special propagators.

While these four observables still cannot fully disentangle the four helicity amplitudes, which have both real and imaginary parts, constructing the multiple observables makes the best power of the sensitivity information contained in the process [Eq. (4.134)]. It therefore provides most invaluable information to constrain the x dependence of GPDs. One may also consider the spin asymmetries with respect to the transverse spin of the initial-state nucleon. This further brings constraints on the GPD E and $\widetilde{E}$, which are beyond the scope of this paper.

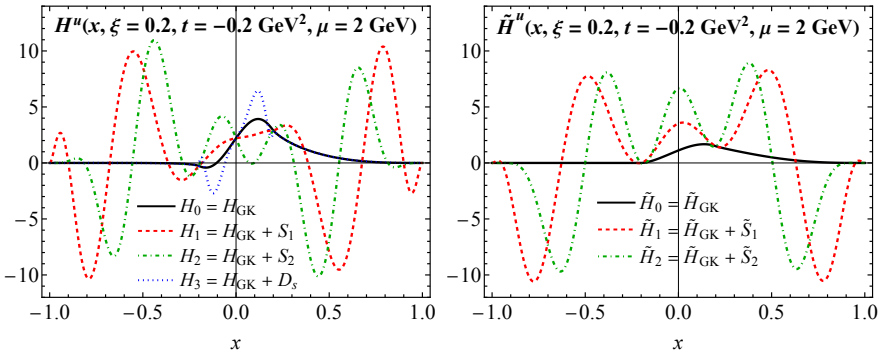

Fig. 4.19: Choices of the u-quark GPD models at $t = -0.2$ GeV^2 and $\xi = 0.2$, by adding shadow GPDs to the GK model.

4.5.3 Numerical effects of the x-sensitivity and production rates

We demonstrate the enhanced sensitivity by taking the GK model [**?**, **?**, **?**, **?**] as the standard GPD model, H_0 and $\widetilde{H}_0$, and varying the u-quark GPDs by some shadow GPDs, $S_i(x, \xi)$ or

$\widetilde{S}_i(x,\xi)$, or a shadow D-term $D_s(x/\xi)$, which are constructed (in the Supplemental Material) to give zero moments [Eq. (4.141)] and forward limit. The obtained GPD models $H_{0\sim3}$ and $\widetilde{H}_{0\sim2}$ are shown in Fig. 4.19, to be used in the following analysis. We fix the DA to be the asymptotic form. To unambiguously exhibit the enhanced sensitivity of the θ distributions to the GPD x dependence, we neglect evolution effects and fix both renormalization and factorization scales at 2 GeV.

The photon beam can be accessed at JLab Hall-D, with arbitrary polarization and energy $E_\gamma = 9$ GeV. The proton target can also be polarized in an arbitrary way. The unpolarized differential cross section [Eq. (4.137)] together with the polarization asymmetries [Eq. (4.138)] are shown in Fig. 4.20 for π^0 production. The differential rate exhibits a clear forward-backward asymmetry due to different collinear divergence structures between the forward and backward regions. The polarization asymmetries are significantly large so can also be used to probe GPDs.

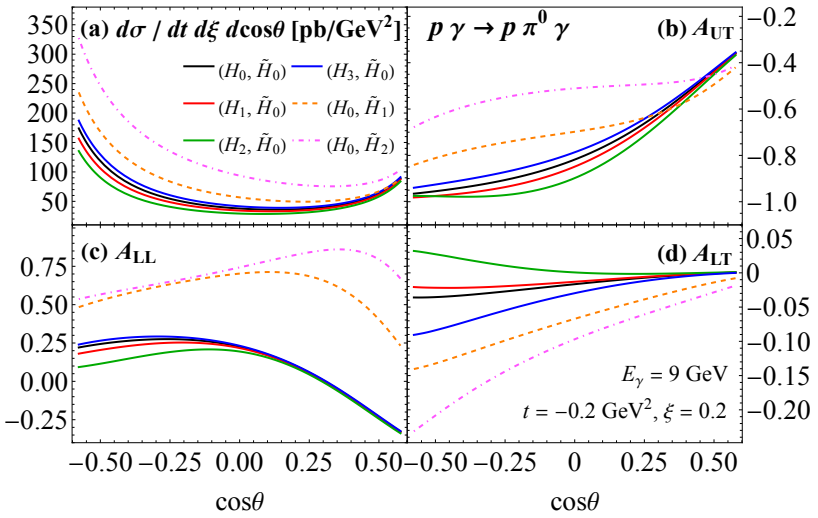

Fig. 4.20: Unpolarized rate (a) and polarization asymmetries (b)-(d) for the $p\gamma \to p\pi^0\gamma$ process as functions of $\cos\theta$, using different GPD sets as given in Fig. 4.19, at JLab GlueX energy with $(t,\xi) = (-0.2\ \text{GeV}^2, 0.2)$.

By construction, the shadow GPDs are not visible to the hard coefficients C_- and $\widetilde{C}_-$,

but now we see that they can be distinguished by C_+ and $\widetilde{C}_+$. By varying the GPDs one at a time, each GPD set in Fig. 4.20 only has one amplitude that is different. This leads to different rate and polarization asymmetry distributions, both in magnitude and shapes. While the rate only depends on the square of the amplitudes, the polarization asymmetries also have access to their phases. In particular, the A_{LT} is sensitive to the imaginary parts of the amplitudes, which are generated in the ERBL region, so it has better sensitivity to the shadow D-term than the other three observables. Overall, the degree of sensitivity has a positive correlation with the GPD magnitude in the ERBL region. The oscillation of shadow GPDs in the DGLAP region causes a big cancellation in their corresponding contribution to the amplitudes. The shadow GPDs $\widetilde{S}_i$ associated with the polarized GPD $\widetilde{H}$ gives bigger contribution to the amplitude $\mathcal{M}_+^{[\widetilde{S}]}$ than S_i to $\widetilde{\mathcal{M}}_+^{[S]}$ due to charge symmetry property, so they can be better probed.

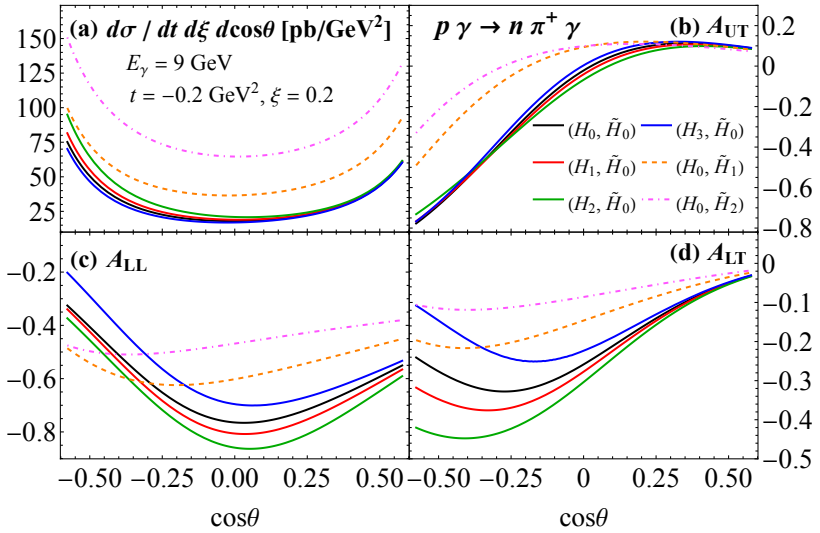

Fig. 4.21: Same as Fig. 4.20, but for the $p\gamma \to n\pi^+\gamma$ process.

For the neutral pion production, we have $e_1 = e_2$ in the hard coefficients in Eqs. (**??**)-(**??**), so that many of the unwanted moment-type terms are cancelled, making the maximum power of the enhanced sensitivity. The same study for the $p\gamma \to n\pi^+\gamma$ process is shown in

Fig. 4.21. It has a lower production rate and less significant forward-backward asymmetry, but the double-polarization asymmetries A_{LL} and A_{LT} become larger. Similar conclusions for sensitivity to the GPDs can be drawn. The $n\gamma \to p\pi^-\gamma$ process gives a similar result, but with an even smaller rate.

4.5.4 Summary and outlook

Pinning down the full x dependence of GPDs is important to probe the tomographic partonic images of hadrons. Such mission is practically impossible by only using exclusive processes with only moment-type sensitivity, as there can be an infinite number of shadow GPDs to which they hardly visible. In this Letter, we propose a new type of enhanced sensitivity for which the entanglement of the parton's x flow with the external observables makes the distribution of the latter a sensitive probe to the x dependence of GPDs.

Following our previous works on the SDHEPs [Qiu and Yu(2023), Qiu and Yu(2022)], we study the single diffractive hard exclusive photoproduction of photon-pion pair at JLab Hall-D experiment. By justifying its factorization into proton GPDs and a pion DA following Ref. [Qiu and Yu(2023)], we demonstrated that the differential event distribution in the polar angle θ of the final-state particles has sensitive dependence on the GPD x distribution. Especially, it can distinguish the GPD with its shadow variants. We also showed that there can be multiple significant polarization asymmetries, whose distributions in θ can provide important complementary constraints on the GPDs' x dependence.

Motivated from our study, we advocate a multiple-process *and* multiple-observable approach to studying GPDs. By a simultaneous analysis of all possible observables, especially with the ones possessing enhanced x-sensitivity, there will be little freedom in constructing "shadow GPDs" that escape all experimental detection. The x dependence of GPDs can

then be unambiguously determined.

Chapter 5

Summary and Outlook

One of the dominant features of QCD is that colors are fully entangled and confined within hadrons, which makes the internal structure of hadrons by no means like the atomic structure, where electrons are bound to nucleus in a sparsely distributed space. On the contrary, inside a hadron, quarks and gluons are densely distributed and strongly tied together. As a result, it is less useful to describe the hadronic structure using the concept of wavefunction in non-relativistic quantum mechanics. Instead, the study of hadrons' internal dynamics is to use parton correlation functions, which are the expectation values of a set of parton fields in a hadron state. A full understanding of partonic hadron structure can be obtained by knowing all possible parton correlation functions.

However, the correlation functions are by definition nonperturbative and require experimental measurement, given the lack of a full nonperturbative calculation method. The connection of the correlation functions to experimental observables is given by QCD factorization theorems. At a hard scattering process involving hadrons, one can show that the scattering cross section or amplitude can be factorized into certain parton correlation functions with perturbatively calculable hard coefficients, to the leading power of the hard scale. Depending on the specific type of processes, one end up with different type of parton correlation functions, which have operator definitions, can be studied on their own, and uncover different aspects of the hadronic structures.

For inclusive processes, the factorization of their cross sections leads to the forward parton distribution functions, which capture the one-dimensional longitudinal parton correlation on the light cone within a fast-moving hadron, and transverse-momentum-dependent parton distribution functions, which in addition capture the parton correlations in the transverse plane. Both distributions correspond to cut diagrams, and are expressed as the diagonal matrix elements of parton operators.

Exclusive processes, on the other hand, are factorized at amplitude level into new types of parton correlation functions, among which are the meson or baryon distribution amplitudes that play the role of hadron wavefunctions on the light cone, and the generalized parton distributions (GPDs), which form the main part of this paper. Among others, the GPDs entail three-dimensional parton pictures in the space of parton momentum fraction x and transverse position $\boldsymbol{b}_T$. We have shown a general class of $2 \to 3$ processes in Sec. 3.2, the single diffractive hard exclusive processes, whose amplitudes can be factorized into GPDs and which can provide useful experimental probes to GPDs.

While two of the three variables (x, ξ, t) of GPDs are directly related to the measured momenta of the diffractive hadron, $p - p'$, it is the relative momentum fraction x of the two exchanged partons, $[q\bar{q}']$ or $[gg]$, between the diffractive hadron and the hard probe that is the most difficult one to extract from the experimental measurement, while it is the most important one to define the slices of the hadron's spatial tomography. We have systematically examined the sensitivity of various SDHEPs for extracting the x-dependence of GPDs in Sec. 4.3, and divided the sensitivity into two types: moment type and enhanced type. We argued that the requirement for enhanced sensitivity on x is to have at least one internal propagator in the hard part that is not connected to two on-shell massless external lines on either of its ends, which usually requires observing more than one external particle

that comes out of the hard scattering. We gave two example processes, the hard diphoton production in single-diffractive pion-nucleon collision, and single-diffractive photoproduction of a hard photon-pion pair. These two processes give complementary enhanced sensitivity to the x dependence of GPDs, which were demonstrated by using the shadow GPDs. d Given both the theoretical and experimental difficulties to unambiguously extract the x-dependence of GPDs, one should not only study as many independent GPD-related processes as possible, but also identify more processes that yield enhanced sensitivity to the x dependence of GPDs. With a generic factorization proof, the SDHEP can serve as a framework to identify and categorize all specific processes for the study of GPDs. In this paper, we categorized these processes in terms of the type of the beam colliding with the diffractive hadron. With the two-stage paradigm of the SDHEP, we are well motivated for the search of new processes for extracting GPDs, and in particular, their x-dependence.

Part II

Single Transverse Polarization Phenomena at High-Energy Colliders

Chapter 6

Introduction

Spins are unique features of quantum mechanics, as a product of quantum Lorentz symmetry [Wigner(1939), Weinberg(2005)]. At high-energy colliders such as the Large Hadron Collider (LHC), however, spin phenomena are relatively rarely discussed, because (1) the LHC is an unpolarized proton-proton collider, so usually it does not produce polarized particles; and (2) the detectors of high-energy colliders only record the energy and momentum information, but do not measure the spins, so even if a particle is produced, the spin information will be lost. Both obstacles can be overcome. First, the Standard Model (SM) contains parity-violating weak interactions, so particles can be produced with net spin polarizations along their momentum directions, or net helicities. Furthermore, even without parity violations, there can be significant transverse polarizations produced even at unpolarized colliders. In both contexts, the polarization refers to a single particle, with all other particles' spins unobserved, so it belongs to the regime of single polarization production, similar to the discussion of single spin asymmetry at polarized colliders. Second, even though the high-energy detectors do not directly measure spins, if the polarized particle is unstable and decays into other particles, its polarization information will be imprinted on the kinematic distributions, especially angular distributions, of the decay products. This is because the polarization of the mother particle breaks the spatial rotational invariance, so it leads to certain angular distributions, which can be determined by rotation group properties.

The same story holds for high-energy quarks and gluons produced in the hard collisions. Due to the asymptotic freedom, such particles are produced as (quasi-)free particles, with well defined polarization properties. But as they travel away from the each other, the color interaction among them becomes stronger and stronger, and eventually turns each fast-moving quark or gluon into a jet of hadrons. It may be argued that such hadronization process will wash out all the original parton spin information, but it is more presumably motivated from the high-energy jetty event structures that only soft gluons are exchanged among the hard partons to neutralize colors [Collins(1993)]. Perturbatively, soft gluon exchanges do not change the spins of hard partons, so we can expect the polarization of the quark or gluon produced from the hard collision to be preserved when it fragments into a jet. As a result, the angular distribution of the jet constituents will reflect the polarization state of the parton that initiates the jet.

Therefore, it is equally feasible to study spin phenomena at high-energy colliders. This leads to much more observables than the pure production rates. Especially, as we will elaborate in this paper, the transverse polarization corresponds to the quantum interference between different helicity states. Such information would be lost had one not measured the decay distributions. The spin-sensitive observables hence provide new tests on the interaction structures of the SM.

This paper is devoted to the study of single transverse polarization phenomena at such high-energy colliders as the LHC. Historically, such study dates back to 1976 when it was discovered at Fermilab that the inclusively produced Λ^0 hyperon in hadron collisions had a substantial transverse polarization [Bunce et al.(1976), Heller et al.(1978)]. This triggered a number of both experimental and theoretical studies until today. Among the early theoretical works was done in [Kane et al.(1978)Kane, Pumplin, and Repko], where it was realized

that the single transverse spin of a quark is an infrared-safe observable in Quantum Chromodynamics (QCD), which can be calculated perturbatively by virtue of the asymptotic freedom. Following the observation that only the transverse spin component perpendicular to the scattering plane is allowed by parity conservation, the authors argued that this must be sourced by the imaginary part of the interference between a helicity-conserving amplitude and a helicity-flipping amplitude. Therefore, one necessarily requires a nonzero quark mass to flip the quark helicity *and* a threshold effect at loop level to generate a nonzero phase. So then in the scaling limit, the quark polarization is suppressed by $\alpha_s\, m_q/\sqrt{s}$, where α_s is the strong coupling due to the loop effect, m_q is the quark mass, and $\sqrt{s}$ is the scattering energy.

Although this means the single transverse spin of a strange quark produced at high-energy collisions would be too small to explain the observed large Λ^0 polarization [Dharmaratna and Goldstein(199 it does imply the possibility of having a largely polarized top quark [Kane et al.(1992)Kane, Ladinsky, and Y which is the heaviest quark in the SM and whose polarization could be a new probe for new physics. Any deviation from the SM prediction, especially a nonzero transverse spin within the production plane, could indicate the existence of a new interaction or even CP violation.

One advantage of the transverse spin is that it leads to a nontrivial azimuthal correlation of the decay products with the spin direction, as a result of breaking the rotational invariance. Since a transverse spin is the interference between different helicity states, λ_1 and λ_2, the specific correlation form can be easily obtained from rotational properties as $\cos(\lambda_1 - \lambda_2)\phi$ and/or $\sin(\lambda_1 - \lambda_2)\phi$, with ϕ characterizing the overall azimuthal direction of the decay products. Such correlations can be readily measured to determine the value of the transverse polarization. Unlike the helicity polarization that leads to a forward-backward asymmetry for the decay products with respect to the momentum direction of the mother particle, the

azimuthal correlations resulting from the transverse polarization stay invariant when the polarized particle is boosted. This makes them a source of new jet substructures for boosted objects. However, due to the spin-half nature, the azimuthal correlations associated with a transversely polarized quark are $\cos\phi$ and/or $\sin\phi$, the observation of which requires to identify the flavor of the decay products. For example, in a jet initialized by a transversely polarized u quark, one may be observing the correlation of a charged pion π^+ with the polarization direction.

On the other hand, a gluon can also be produced in high-energy collisions with a linear polarization, as was noticed around the same time as the transverse quark spin [Brodsky et al.(1978)Brodsky, I Contrary to the latter, though, the linear gluon polarization does not suffer from the mass and high-order suppression, and can in principle be produced at leading order with a large magnitude [Brodsky et al.(1978)Brodsky, DeGrand, and Schwitters, Olsen et al.(1980)Olsen, Osland, and Overb Devoto et al.(1980)Devoto, Pumplin, Repko, and Kane, Devoto et al.(1979)Devoto, Pumplin, Repko, and DeGrand and Petersson(1980), Petersson and Pire(1980), Olsen et al.(1981)Olsen, Osland, and Overbo, Devoto and Repko(1982), Korner and Schiller(1981), Olsen and Olsen(1984), Hara and Sakai(1989), Jacobsen and Olsen(1990), Groote et al.(1997)Groote, Korner, and Leyva, Groote et al.(1999)Groote, Kor Groote(2002), Yu et al.(2022)Yu, Mohan, and Yuan]. Since gluons are spin-one massless particles, their linear polarization is the interference between a $+1$ and -1 helicity states, with a helicity flip by two units. Hence, they will leave $\cos 2\phi$ and/or $\sin 2\phi$ azimuthal correlations in the fragmented jets. Such correlations are invariant under $\phi \to \phi + \pi$ so will not require distinguishing the particle flavors, but instead they will be reflected as an azimuthal anisotropy in the energy deposition. Observation of such polarized gluon jet substructure could be easier than for the polarized quark ones. As we will show, this can serve as a new tool to probe CP-violating interactions.

Similar effects also apply to massive vector bosons like the W and Z, which can also be produced with a linear polarization when they carry a nonzero transverse momentum. Such phenomena have actually been noticed all along when one studies the angular functions of the Drell-Yan pair in their rest frame [Lam and Tung(1978)]. However, one may still gain some insights when framing in terms of linear polarizations. Especially, as one goes to the boosted regime, a W or Z may be produced with a very high transverse momentum such that their decay products are highly collimated. In particular, when they decay hadronically, it may not be easily determined whether they are QCD jets or are indeed from the heavy boson decays, and one cannot simply reconstruct the rest frame for each event. Carefully designed jet substructure observables must be employed to tag the boosted objects. Then the angular function decomposition loses its advantage, but the azimuthal correlation substructures due to the linear polarization retain their simplicity and can be used to tag the observed jets.

Linearly polarized gluons can not only be produced from hard collisions, but also can exist ubiquitously elsewhere, such as from heavy meson decay [Brodsky et al.(1978)Brodsky, DeGrand, and Schw Koller et al.(1981)Koller, Streng, Walsh, and Zerwas, Robinett(1991)] and from parton showering [DeGrand and Petersson(1980)]. In particular, it has been noticed that a linearly polarized gluon can be emitted in the shower of an unpolarized parton and lead to nontrivial $\cos 2\phi$ correlations [Chen et al.(2021)Chen, Moult, and Zhu, Chen et al.(2022)Chen, Moult, and Zhu, Karlberg et al.(2021)Karlberg, Salam, Scyboz, and Verheyen, Hamilton et al.(2022)Hamilton, Karlberg, S The reason for this is that a $1 \to 2$ splitting in the boosted parton showering defines a plane and allows a linear polarization along or perpendicular to the plane. This resembles the gluon Boer-Mulders function in the transverse-momentum-dependent QCD factorization [Mulders and Rodrigues(2001), Nadolsky et al.(2007)Nadolsky, Balazs, Berger, and Yuan, Boer et al.(2011)Boer, Brodsky, Mulders, and Pisano, Catani and Grazzini(2012), Sun et al.(2011)Sun, Xi

Qiu et al.(2011)Qiu, Schlegel, and Vogelsang, Boer et al.(2012)Boer, den Dunnen, Pisano, Schlegel, and V for which a linearly polarized gluon distribution can exist in an unpolarized hadron target when the gluon carries a nonzero transverse momentum.

Again, similar effects can be extended to massive vector bosons, which can come from the decay of a boosted heavy object like a top quark or Higgs boson [Yu and Yuan(2022a)]. For the same reason, the intermediate vector boson can carry a linear polarization and then decays into light particles preferentially along the direction parallel or perpendicular to the polarization direction. This leads to a more complicated azimuthal correlation in the original boosted heavy particle. The minimal configuration is a $1 \to 3$ decay. When extended to the hadronic decay mode, the intermediate linearly polarized vector boson gives rise to an inhomogeneous azimuthal energy deposition pattern that makes the whole "fat" jet more circular or planar. Such phenomena could be measured as a precision test of the SM and probe for new physics.

The rest of this paper is organized as the following. First, to lay the foundation of the polarization study, I will review in Ch. 7 the definitions of the spin states and their Lorentz transformation behaviors which are governed by the corresponding little group, mainly following the discussion in [Weinberg(2005)]. Along the line will be derived the explicit little group forms for some important cases that will be used in later sections. Then in Ch. 8, I will discuss the transverse spins of quarks, using the top quark as a main example. The discussion is mainly as an introduction for the vector boson polarization in the following chapter, with most being known in the literature. A brief comparison between the single quark polarization and the quark spin-spin correlations is given at the end of this chapter. Next, Ch. 9 is devoted to the study of linear vector boson polarization at the LHC. This forms the main part of this paper. We will first discuss the linear polarization of a gluon as

produced directly from a hard collision. This discussion leads to the definition of a polarized gluon jet function, which provides a concrete procedure for measuring the gluon polarization at the LHC. As will be explained, such measurement will provide a sensitive probe for possible CP-violating effects. Then we will discuss the linear polarization of a vector boson that comes from the decay of a boosted heavy object. The focus will be on a boosted top quark that decays into a bottom quark and a W boson, which further decays into a lepton pair or quark pair. We will give a physical argument of why the W boson can be linearly polarized in the boosted regime. The derivation will clarify it as a general phenomenon that a boosted $1 \to 3$ decay system can exhibit such azimuthal correlation if it is mediated by a vector boson. Finally, in Ch. 10, we conclude our discussion and present the outlook.

Chapter 7

Poincare group representation and little group transformation

In this chapter, we review the Poincare group representation and the associated little group, following Ch. 2.5 of [Weinberg(2005)].

Setting the Poincare symmetry as the fundamental spacetime symmetry, we identify states that can transform among each other under a Poincare transformation as belonging to the same particle species. The Poincare symmetry transformation acts on the coordinate space as

$$x^\mu \to x'^\mu = \Lambda^\mu{}_\nu \, x^\nu + a^\mu, \tag{7.1}$$

which induces a unitary operator $U(\Lambda, a)$ on the Hilbert space, satisfying

$$U(\Lambda, a)\, U(\Lambda', a') = U(\Lambda\Lambda', a + \Lambda a'), \tag{7.2}$$

and

$$U(1,0) = 1, \quad U^\dagger(\Lambda, a) = U^{-1}(\Lambda, a) = U(\Lambda^{-1}, -\Lambda^{-1}a). \tag{7.3}$$

We also define the Lorentz transformation $U(\Lambda) \equiv U(\Lambda, 0)$, which forms a unitary subgroup. By the translation properties, we label each single-particle state by its momentum p^μ and

some internal quantum number collectively denoted as σ,

$$\hat{P}^\mu |p,\sigma\rangle = p^\mu |p,\sigma\rangle, \tag{7.4}$$

where $\hat{P}^\mu$ is the momentum operator, defined as the generator of the translation group,

$$U(1,a) = e^{i\hat{P}\cdot a}. \tag{7.5}$$

The momenta of two states can be related to each other under Lorentz transformation only if they have the same mass $m^2 = p^\mu p_\mu$ and, if $m^2 > 0$, sign of p^0. Since

$$\begin{aligned}\hat{P}^\mu\, U(\Lambda)|p,\sigma\rangle &= U(\Lambda)\left[U^{-1}(\Lambda)\hat{P}^\mu\, U(\Lambda)\right]|p,\sigma\rangle \\ &= U(\Lambda)\left[\Lambda^\mu{}_\nu\, \hat{P}^\mu\right]|p,\sigma\rangle = \left[\Lambda^\mu{}_\nu\, p^\mu\right] U(\Lambda)|p,\sigma\rangle,\end{aligned}$$

the state $U(\Lambda)|p,\sigma\rangle$ has a momentum Λp, and hence can be expanded as

$$U(\Lambda)|p,\sigma\rangle = \sum_{\sigma'} |\Lambda p,\sigma'\rangle\, D_{\sigma'\sigma}(\Lambda,p). \tag{7.6}$$

This forms the unitary representation of the Lorentz group, which is infinitely dimensional,

$$U(\Lambda)|p,\sigma\rangle = \sum_{\sigma'} \int \frac{d^3\boldsymbol{p'}}{(2\pi)^3 2E_{p'}} |p',\sigma\rangle \left[(2\pi)^3 2E_{p'}\delta^{(3)}(\boldsymbol{p'}-\boldsymbol{p})\, D_{\sigma'\sigma}(\Lambda,p)\right]. \tag{7.7}$$

By choosing the normalization

$$\langle p',\sigma'|p,\sigma\rangle = (2\pi)^3 2E_p \delta^{(3)}(\boldsymbol{p}-\boldsymbol{p'}), \tag{7.8}$$

we can write the representation matrix as

$$\langle p', \sigma' | U(\Lambda) | p, \sigma \rangle = (2\pi)^3 2E_{p'} \delta^{(3)}(\boldsymbol{p}' - \boldsymbol{p})\, D_{\sigma'\sigma}(\Lambda, p) \tag{7.9}$$

in the (p, σ) space. The matrix $D_{\sigma'\sigma}(\Lambda, p)$ is also unitary,

$$\sum_{\sigma'} D^{\dagger}_{\sigma''\sigma'}(\Lambda, p) D_{\sigma'\sigma}(\Lambda, p) = \delta_{\sigma''\sigma}, \tag{7.10}$$

and satisfies the multiplication rule,

$$D_{\sigma''\sigma}(\Lambda\Lambda', p) = \sum_{\sigma'} D_{\sigma''\sigma'}(\Lambda, \Lambda' p) D_{\sigma'\sigma}(\Lambda', p), \tag{7.11}$$

with

$$D(1, p) = 1, \quad D^{-1}(\Lambda, p) = D(\Lambda^{-1}, \Lambda p). \tag{7.12}$$

To find the representation matrix of the Lorentz group, it is necessary to first clearly define each particle state $|p, \sigma\rangle$, especially the quantum number σ. For a particular particle, we define all its states by choosing a reference momentum k, which has a defined quantum number σ for all values of σ. This can be chosen as

$$k = (m, 0, 0, 0) \tag{7.13}$$

for a massive particle with $m^2 = k^2 > 0$, or

$$k = (E_0, 0, 0, E_0) \quad (\text{with } E_0 = 1 \text{ GeV for example}) \tag{7.14}$$

for a massless particle. Any other possible momentum p is related to k by a standard Lorentz transformation $L(p) \equiv L(p;k)$,

$$p^\mu = L^\mu{}_\nu(p) k^\nu, \tag{7.15}$$

where we suppress the dependence on k since it is common for all the states of a particular particle. $L(p)$ can be standardly defined by first boosting along the $+\hat{z}$ direction by $U(\Lambda_z(\beta))$ such that $p_1 = \Lambda_z(\beta)k$ has the same energy as p, and then rotating p_1 to the same direction as p by first rotating around the y axis by θ and then around the z axis by ϕ,

$$L(p) = R(\theta,\phi)\Lambda_z(\beta) = R_z(\phi)R_y(\theta)\Lambda_z(\beta) = \Lambda_{\hat{p}}(\beta)R(\theta,\phi), \tag{7.16}$$

where θ and ϕ are the polar and azimuthal angles of p, and the last step gives an alternative definition of $L(p)$ that first rotates k to the direction of p by $R(\theta,\phi)$ and then boosting along the direction of p by $\Lambda_{\hat{p}}(\beta) = R(\theta,\phi)\Lambda_z(\beta)R^{-1}(\theta,\phi)$ to reach the same energy. The induced Lorentz transformation $U(L(p))$ in the Hilbert space is thus

$$U(L(p)) = U(R(\theta,\phi))U(\Lambda_z(\beta)) = U(\Lambda_{\hat{p}}(\beta))U(R(\theta,\phi)), \tag{7.17}$$

with

$$U(R(\theta,\phi)) = e^{-iJ_z\phi}e^{-iJ_y\theta}, \quad U(\Lambda_{\hat{n}}(\beta)) = e^{-i\boldsymbol{K}\cdot\hat{n}\beta}. \tag{7.18}$$

The state $|p,\sigma\rangle$ is defined as the Lorentz transformation of $|k,\sigma\rangle$ under $U(L(p))$,

$$|p,\sigma\rangle \equiv U(L(p))|k,\sigma\rangle. \tag{7.19}$$

Then under an arbitrary Lorentz transformation $U(\Lambda)$, the state $|p,\sigma\rangle$ becomes

$$\begin{aligned} U(\Lambda)|p,\sigma\rangle &= U(\Lambda)U(L(p))|k,\sigma\rangle = U(\Lambda L(p))|k,\sigma\rangle \\ &= U(L(\Lambda p))\, U(L^{-1}(\Lambda p)\Lambda L(p))|k,\sigma\rangle. \end{aligned} \tag{7.20}$$

Note that although the transformation $\Lambda L(p)$ brings the momentum k to Λp, it is not necessarily equal to $L(\Lambda p)$. But it does imply that the transformation

$$W(\Lambda,p) \equiv L^{-1}(\Lambda p)\Lambda L(p) \tag{7.21}$$

keeps k invariant,

$$W^{\mu}{}_{\nu}(\Lambda,p)k^{\nu} = k^{\mu}. \tag{7.22}$$

Now for a specific momentum k, all the Lorentz transformations that leave it invariant form a subgroup of the Lorentz group, which is called the *little group*. A little group transformation W thus only mixes the quantum number σ, so its representation can be easily obtained,

$$U(W)|k,\sigma\rangle = \sum_{\sigma'} |k,\sigma'\rangle D_{\sigma'\sigma}(W), \tag{7.23}$$

where $D(W)$ is a unitary matrix. Plugging Eq. (7.23) back to Eq. (7.20) then gives the Lorentz group representation,

$$\begin{aligned} U(\Lambda)|p,\sigma\rangle &= U(L(\Lambda p))U(W(\Lambda,p))|k,\sigma\rangle = U(L(\Lambda p))\sum_{\sigma'}|k,\sigma'\rangle D_{\sigma'\sigma}(W(\Lambda,p)) \\ &= \sum_{\sigma'}|\Lambda p,\sigma'\rangle D_{\sigma'\sigma}(W(\Lambda,p)). \end{aligned} \tag{7.24}$$

Compared with Eq. (7.6), we get

$$D_{\sigma'\sigma}(\Lambda, p) = D_{\sigma'\sigma}(W(\Lambda, p)), \tag{7.25}$$

which explains why the same symbol 'D' is used. In this way, the Lorentz group representation is induced from its little group representation.

We can now work out the Lorentz transformation behavior of a scattering amplitude. The helicity amplitude of a scattering $(p_1, \sigma_1; p_2, \sigma_2; \cdots) \to (q_1, r_1; q_2, r_2; \cdots)$ is obtained from the scattering S-operator by

$$\mathcal{M}_{\sigma_1,\ldots;r_1,\ldots}(p_1, \ldots; q_1, \ldots) \sim \langle q_1, r_1; \ldots | S | p_1, \sigma_1; \ldots \rangle. \tag{7.26}$$

If we transform the scattering system to another frame by Λ, the new helicity amplitude becomes

$$\mathcal{M}_{\sigma_1,\ldots;r_1,\ldots}(\Lambda p_1, \ldots; \Lambda q_1, \ldots) \sim \langle \Lambda q_1, r_1; \ldots | S | \Lambda p_1, \sigma_1; \ldots \rangle. \tag{7.27}$$

Their relations can be obtained by using $S = U(\Lambda) S U^{-1}(\Lambda)$ in the Eq. (7.27),

$$\langle \Lambda q_1, r_1; \ldots | S | \Lambda p_1, \sigma_1; \ldots \rangle = \langle \Lambda q_1, r_1; \ldots | U(\Lambda) S U^{-1}(\Lambda) | \Lambda p_1, \sigma_1; \ldots \rangle \tag{7.28}$$

Now Eq. (7.24) gives

$$U^{-1}(\Lambda)|\Lambda p, \sigma\rangle = \sum_{\sigma'} |p, \sigma'\rangle D_{\sigma'\sigma}(W(\Lambda^{-1}, \Lambda p)) = \sum_{\sigma'} |p, \sigma'\rangle D^{-1}_{\sigma'\sigma}(W(\Lambda, p)), \tag{7.29}$$

where we used $W(\Lambda^{-1}, \Lambda p) = W^{-1}(\Lambda, p)$ by the definition in Eq. (7.21). So then Eq. (7.28)

becomes

$$\langle \Lambda q_1, r_1; \ldots | S | \Lambda p_1, \sigma_1; \ldots \rangle$$
$$= \sum_{r_1', \ldots; \sigma_1', \ldots} \left[D_{r_1 r_1'}(W(\Lambda, q_1)) \cdots \right] \langle q_1, r_1'; \ldots | S | p_1, \sigma_1'; \ldots \rangle \left[D^{\dagger}_{\sigma_1' \sigma_1}(W(\Lambda, p_1)) \cdots \right]. \tag{7.30}$$

Therefore, helicity amplitudes in different frame differ by a unitary transformation,

$$\mathcal{M}_{\sigma_1, \ldots; r_1, \ldots}(\Lambda p_1, \ldots; \Lambda q_1, \ldots)$$
$$= \sum_{r_1', \ldots; \sigma_1', \ldots} \left[D_{r_1 r_1'}(W(\Lambda, q_1)) \cdots \right] \mathcal{M}_{\sigma_1', \ldots; r_1', \ldots}(p_1, \ldots; q_1, \ldots) \left[D^{\dagger}_{\sigma_1' \sigma_1}(W(\Lambda, p_1)) \cdots \right]. \tag{7.31}$$

Because of the unitarity of the representation matrices D's, multiplying the helicity amplitude by its complex conjugate and summing over all helicities leads to a Lorentz invariant unpolarized amplitude square.

The task of obtaining the transformation behavior of $|p, \sigma\rangle$ under $U(\Lambda)$ is reduced to finding the corresponding little group transformation $W(\Lambda, p)$ [Eq. (7.21)]. For this purpose, we need to clearly define k for each particle and the corresponding $L(p)$. We do this by categorizing the discussion into massive case and massless case.

7.1 Massive case: $m > 0$

The little group for a massive particle is the symmetry group in the three-dimensional rotation group, SO(3). For the reference momentum k, we define the quantum number σ to be

the angular momentum component along $\hat{z}$. Particles can be further decomposed into different species according to different irreducible representations D^j of SO(3). This introduces a total spin quantum number j, so we label the state as $|k, j, \sigma\rangle$,

$$J_z|k,j,\sigma\rangle = \sigma|k,j,\sigma\rangle, \quad U(W)|k,j,\sigma\rangle = \sum_{\sigma'=-j}^{j} |k,j,\sigma'\rangle D^j_{\sigma'\sigma}(W), \tag{7.32}$$

where $D^j(W)$ is the $(2j+1)$-dimensional irreducible representation matrix of the SO(3) group. The index σ for an arbitrary momentum p related to k by Eq. (7.16) is defined as the helicity,

$$\begin{aligned}(\boldsymbol{J}\cdot\hat{p})|p,j,\sigma\rangle &= U(R(\theta,\phi))J_z\,U^{-1}(R(\theta,\phi))|p,j,\sigma\rangle = U(R(\theta,\phi))J_z\,U(\Lambda_z(\beta))|k,j,\sigma\rangle \\ &= U(R(\theta,\phi))U(\Lambda_z(\beta))J_z|k,j,\sigma\rangle = \sigma|p,j,\sigma\rangle,\end{aligned} \tag{7.33}$$

where we have used Eq. (7.17) with $\beta = |\boldsymbol{p}|/\sqrt{\boldsymbol{p}^2+m^2}$, and that J_z commutes with $U(\Lambda_z(\beta))$. By Eq. (7.24), we can get the representation of a general Lorentz transformation $U(\Lambda)$, which mixes different helicity states of a given particle,

$$U(\Lambda)|p,j,\sigma\rangle = \sum_{\sigma'=-j}^{j} |p,j,\sigma\rangle D^j_{\sigma'\sigma}(W(\Lambda,p)). \tag{7.34}$$

The little group transformation $W(\Lambda, p)$ for a general Λ and p is not easily worked out. Here we only consider two special cases.

Pure Rotation: $\Lambda = \hat{R}$

The first is for a pure rotation $\Lambda = \hat{R}$. It only changes the direction $\hat{p}$ to $\hat{R}\hat{p}$, but does not change its energy. Following our notation of $R(\hat{n})$ as the standard rotation that takes $\hat{z}$ to

$\hat{n}$, we have

$$W(\hat{R},p)=\Lambda_z^{-1}(\beta)\left[R^{-1}(\hat{R}\hat{p})\hat{R}R(\hat{p})\right]\Lambda_z(\beta). \tag{7.35}$$

The rotation matrices in the square bracket first take $\hat{z}$ to $\hat{p}$, then to $\hat{R}\hat{p}$, and then back to $\hat{z}$, so it is at most a rotation around $\hat{z}$,

$$R^{-1}(\hat{R}\hat{p})\hat{R}R(\hat{p})=R_z(\delta(\hat{R},\hat{p})). \tag{7.36}$$

Inserting this back to Eq. (7.35) gives

$$W(\hat{R},p)=R_z(\delta(\hat{R},\hat{p})). \tag{7.37}$$

So the little group for a rotation $\hat{R}$ is merely a rotation around z. The corresponding Lorentz representation is thus a pure phase under,

$$U(\hat{R})|p,j,\sigma\rangle=e^{-i\sigma\delta(\hat{R},\hat{p})}|p,j,\sigma\rangle, \tag{7.38}$$

which keeps σ invariant. We consider three special examples of $\hat{R}$:

(1) $\hat{R}=R(\theta,\phi)R_z(\gamma)R^{-1}(\theta,\phi)$ is a rotation around $\hat{p}$ by γ, which gives $\delta(\hat{R},\hat{p})=\gamma$;

(2) $\hat{R}=R_z(\gamma)$ is a rotation around $\hat{z}$ by γ, which gives $\delta(\hat{R},\hat{p})=0$;

(3) $\hat{R}=R_z(\phi)R_y(\gamma)R_z^{-1}(\phi)$ is a rotation of the $\hat{z}$-$\hat{p}$ plane (usually defined as the inclusive scattering plane) by γ, which gives $\delta(\hat{R},\hat{p})=0$.

Boost along z: $\Lambda=\Lambda_z(\hat{\beta})$

The second case is for a pure Lorentz boost along the $\hat{z}$ direction. This is useful in two

circumstances. First, the spin state of a particle produced from a hard scattering can be usually calculated easily in the center-of-mass (CM) frame. But at a hadron collider such as the LHC, each hard scattering event in the lab frame differs from the CM frame event by a longitudinal boost along $\hat{z}$. Second, if the particle is produced from a heavy particle decay, its spin state is easily worked out in the rest frame of the mother particle. But the latter is likely to be boosted in the lab frame, so the connection between two frames requires the boost of the rest frame to the lab frame, along the momentum of the mother particle that we can define as $\hat{z}$.

Denote v, θ, and ϕ as the speed, polar angle, and azimuthal angle of p. The boost $\Lambda_z(\hat{\beta})$ transforms it to $\Lambda_z(\hat{\beta})p$, with speed v', polar angle θ', and azimuthal angle ϕ'. They are related by

$$\tan\theta' = \frac{v\sin\theta\sqrt{1-\hat{\beta}^2}}{\hat{\beta}+v\cos\theta}, \quad \phi' = \phi, \quad v' = \sqrt{1-\frac{(1-\hat{\beta}^2)(1-v^2)}{(1+\hat{\beta}v\cos\theta)^2}}. \tag{7.39}$$

By Eq. (7.21), the little group transformation is

$$\begin{aligned} W(\Lambda,p) &= \Lambda_z^{-1}(v')R_y^{-1}(\theta')R_z^{-1}(\phi)\Lambda_z(\hat{\beta})R_z(\phi)R_y(\theta)\Lambda_z(v) \\ &= \Lambda_z^{-1}(v')R_y^{-1}(\theta')\Lambda_z(\hat{\beta})R_y(\theta)\Lambda_z(v), \end{aligned} \tag{7.40}$$

where the ϕ dependence cancels since R_z commutes with Λ_z. Note that Eq. (7.40) only involves boosts along $\hat{z}$ and rotation around $\hat{y}$, which all keep the vector $(0,1,0,0)$ unchanged. So the resulting little group must be a rotation $R_y(\chi)$ around $\hat{y}$. This is verified by an explicit

calculation which gives

$$W(\Lambda,p)=R_y(\chi),\quad \cos\chi=\frac{v+\hat{\beta}\cos\theta}{\sqrt{(1+\hat{\beta}v\cos\theta)^2-(1-\hat{\beta}^2)(1-v^2)}},\quad \chi\in[0,\pi]. \tag{7.41}$$

Such a nontrivial little group transformation causes the boost $\Lambda_z(\hat{\beta})$ to mix the helicity states,

$$U(\Lambda_z(\hat{\beta}))\,|p,j,\sigma\rangle=\sum_{\sigma'=-j}^{j}|\Lambda_z(\hat{\beta})p,j,\sigma'\rangle\,d^j_{\sigma'\sigma}(\chi(\hat{\beta},p)), \tag{7.42}$$

where d^j is the Wigner-d function, being the representation matrix of $U(R_y(\chi))$.

7.2 Massless case: $m=0$

The little group that keeps invariant the standard reference momentum vector $k=(1,0,0,1)$ (suppressing the irrelevant E_0 factor in this section) is isomorphic to ISO(2), the two-dimensional translation and rotation group. I will first follow the treatment in [Weinberg(2005)], and then give another derivation in the next section.

First introduce an auxiliary vector $t^\mu=(1,0,0,0)$. The little group transformation W has the properties

$$W^\mu{}_\nu k^\nu=k^\mu,\quad (Wt)^\mu k_\mu=(Wt)\cdot(Wk)=t\cdot k=1,\quad (Wt)^\mu(Wt)_\mu=t^2=1. \tag{7.43}$$

The second equation implies that

$$W^\mu{}_\nu t^\nu=(1+\zeta,\alpha,\beta,\zeta) \tag{7.44}$$

and the third one constrains

$$\zeta = \frac{\alpha^2 + \beta^2}{2}. \tag{7.45}$$

This determines the first column of the W matrix, $W^{\mu}{}_0$. The first condition in Eq. (7.43) further constrains the last column, $W^{\mu}{}_3$. The remaining two columns can be determined by Lorentz group properties up to some degrees of freedom. One solution for W is

$$S = (S^{\mu}{}_{\nu}(\alpha, \beta)) = \begin{pmatrix} 1+\zeta & \alpha & \beta & -\zeta \\ \alpha & 1 & 0 & -\alpha \\ \beta & 0 & 1 & -\beta \\ \zeta & \alpha & \beta & 1-\zeta \end{pmatrix}. \tag{7.46}$$

To find the most general form of W, notice that by $Wt = St$, the transformation $S^{-1}W$ leaves t invariant, so $S^{-1}W \in$SO(3). On the other hand, $S^{-1}W$ also leaves k invariant, so it can only be a rotation $R_z(\theta)$ around $\hat{z}$. Hence, we have the general expression for the little group element,

$$W = W(\alpha, \beta, \theta) = S(\alpha, \beta) R_z(\theta), \tag{7.47}$$

which has three parameters α, β, and θ.

The little group multiplication properties can be worked out straightforward, and we get

1. the subgroup formed by S is Abelian and has a simple addition rule for the parameters (α, β): $S(\alpha, \beta)S(\alpha', \beta') = S(\alpha + \alpha', \beta + \beta')$;

2. the subgroup formed by R_z has the same property: $R_z(\theta)R_z(\theta') = R_z(\theta + \theta')$;

3. the parameters (α, β) have a simple rotation property under the action of $R_z(\theta)$: $R_z(\theta)S(\alpha, \beta)R_z^{-1}(\theta) = S(\alpha\cos\theta - \beta\sin\theta, \alpha\sin\theta + \beta\cos\theta)$.

The first and third properties together mean that the elements S form an invariant Abelian subgroup, so that the little group is not semi-simple. If we denote the $\boldsymbol{v} = (\alpha, \beta)$, the multiplication rules will become more transparent,

$$S(\boldsymbol{v})S(\boldsymbol{v}') = S(\boldsymbol{v} + \boldsymbol{v}'), \quad R_z(\theta)S(\boldsymbol{v})R_z^{-1}(\theta) = S(R_z(\theta)\boldsymbol{v}), \tag{7.48}$$

where in the expression $R_z(\theta)\boldsymbol{v}$, $R_z(\theta)$ is the rotation matrix adapted to the x-y plane in an obvious way. This clearly shows its isomorphism to ISO(2) on the x-y plane, which transforms a point (x, y) to $R_z(\theta)(x, y) + \boldsymbol{v}$. with $\boldsymbol{v}$ corresponding to the two-dimensional translation vector, and θ the rotation angle around $\hat{z}$.

In the neighborhood of the identity element, the little group element $W(\alpha, \beta, \theta)$ can be expanded around $\alpha = \beta = \theta = 0$, which gives

$$\begin{aligned} W &\simeq 1 + \begin{pmatrix} 0 & \alpha & \beta & 0 \\ \alpha & 0 & -\theta & -\alpha \\ \beta & \theta & 0 & -\beta \\ 0 & \alpha & \beta & 0 \end{pmatrix} \\ &= 1 - i(K_1\alpha + K_2\beta + J_1\beta - J_2\alpha + J_3\theta) \\ &\equiv 1 - i(A\,\alpha + B\,\beta + J_3\,\theta), \end{aligned} \tag{7.49}$$

such that the little group is spanned by three generators,

$$A = K_1 - J_2, \quad B = K_2 + J_1, \quad J_3. \tag{7.50}$$

Here K_i and J_i are the representation matrices of the Lorentz group in the vector space.

The corresponding Lie algebra is

$$[J_3, A] = iB, \quad [J_3, B] = -iA, \quad [A, B] = 0. \tag{7.51}$$

A finite little group element $W(\alpha, \beta, \theta)$ can then be generated from the exponential

$$W(\alpha, \beta, \theta) = e^{-i(A\alpha + B\beta)} e^{-iJ_3\theta}. \tag{7.52}$$

So far we have been working on the 4-dimensional Lorentz group representation in the Minkowski space. This can induce a unitary representation on the Hilbert space,

$$U(W(\alpha, \beta, \theta)) = e^{-i(\hat{A}\alpha + \hat{B}\beta)} e^{-i\hat{J}_3\theta}, \tag{7.53}$$

where $\hat{A}$, $\hat{B}$, and $\hat{J}_3$ are Hermitian operators and have the same properties as Eqs. (7.50) and (7.51).

The little group ISO(2) contains all Lorentz group elements that leave k invariant. The transformation property of the σ index in the state $|k, \sigma\rangle$ under the little group gives a physical definition of σ. Because only two of the Hermitian generators, A and B, commute, we may orient the reference state to be a simultaneous eigenstate, $|k, a, b\rangle$, of $\hat{P}^\mu$, A, and B,

$$A|k, a, b\rangle = a|k, a, b\rangle, \quad B|k, a, b\rangle = b|k, a, b\rangle, \tag{7.54}$$

with (a, b) the quantum numbers charactering the state, together with the momentum k. Now we define

$$(A_\theta, B_\theta) = e^{-iJ_3\theta}(A, B)e^{iJ_3\theta}. \tag{7.55}$$

Applying a derivative with respect to θ using Eq. (7.51) gives

$$\frac{d}{d\theta}(A_\theta, B_\theta) = (A_\theta, B_\theta) \begin{pmatrix} 0 & -1 \\ 1 & 0 \end{pmatrix} = -i(A_\theta, B_\theta)\sigma_2. \tag{7.56}$$

The solution is obtained by an exponentiation,

$$(A_\theta, B_\theta) = (A, B)\, e^{-i\sigma_2\theta} = (A, B)R_z(\theta) = (A\cos\theta + B\sin\theta, -A\sin\theta + B\cos\theta). \tag{7.57}$$

Then from Eq. (7.54), we have

$$\begin{aligned} Ae^{-iJ_3\theta}|k, a, b\rangle &= e^{-iJ_3\theta}A_{-\theta}|k, a, b\rangle = (a\cos\theta - b\sin\theta)e^{-iJ_3\theta}|k, a, b\rangle \\ Be^{-iJ_3\theta}|k, a, b\rangle &= e^{-iJ_3\theta}B_{-\theta}|k, a, b\rangle = (a\sin\theta + b\cos\theta)e^{-iJ_3\theta}|k, a, b\rangle, \end{aligned} \tag{7.58}$$

and so a rotation $R_z(\theta)$ mixes the two quantum numbers a and b,

$$e^{-iJ_3\theta}|k, a, b\rangle = |k, a\cos\theta - b\sin\theta, a\sin\theta + b\cos\theta\rangle. \tag{7.59}$$

Such a continuous spectrum is not observed in nature, and therefore we must have $a = b = 0$.

While J_3 does not commute with A or B, and so in general they cannot have simultaneous eigenstates, now A and B have zero eigenvalues, so the state can also be a simultaneous eigenstate of J_3,

$$|k, \sigma\rangle \equiv |k, (a, b) = (0, 0), \sigma\rangle, \tag{7.60}$$

with

$$A|k, \sigma\rangle = 0, \quad B|k, \sigma\rangle = 0, \quad J_3|k, \sigma\rangle = \sigma|k, \sigma\rangle, \tag{7.61}$$

without violating Eq. (7.51). The quantum number associated with A and B thus become redundant and σ has the physical meaning of helicity. The little group transformation is

$$U(W(\alpha,\beta,\theta))|k,\sigma\rangle = e^{-i\sigma\theta}|k,\sigma\rangle. \tag{7.62}$$

This then induces the Lorentz group representation,

$$U(\Lambda)|k,\sigma\rangle = e^{-i\sigma\theta(\Lambda,p)}|k,\sigma\rangle, \tag{7.63}$$

with $\theta(\Lambda,p)$ determined by

$$W(\Lambda,p) = L^{-1}(\Lambda p)\Lambda L(p) = S(\alpha,\beta)R_z(\theta), \tag{7.64}$$

where $S(\alpha,\beta)$ is the little group element *defined* to have the form in Eq. (7.46).

Similar to Sec. 7.1, now we give two special cases where the little group can be explicitly evaluated.

Pure Rotation: $\Lambda = \hat{R}$

A pure rotation $\Lambda = \hat{R}$ on massless states has the same effects as it applies on massive states, since it only involves the momentum directions. The little group transformation is the same as Eq. (7.37). Compared with Eq. (7.64), we have

$$\alpha = \beta = 0, \quad \theta = \delta(\hat{R},\hat{p}), \tag{7.65}$$

which gives the same Lorentz representation as Eq. (7.38),

$$U(\hat{R})|p,\sigma\rangle = e^{-i\sigma\delta(\hat{R},\hat{p})}|p,\sigma\rangle. \tag{7.66}$$

Boost along z: $\Lambda = \Lambda_z(\hat{\beta})$

A pure Lorentz boost along $\hat{z}$ results in a similar expression like Eq. (7.40), just with different values for θ', v, and v'. Before evaluating it, we make the observation that none of the transformations in Eq. (7.40) changes $\hat{y} = (0,0,1,0)$. On the other hand, however, the little group element in Eq. (7.64) takes it to

$$\hat{y}' = (\beta\cos\theta - \alpha\sin\theta, -\sin\theta, \cos\theta, \beta\cos\theta - \alpha\sin\theta). \tag{7.67}$$

Therefore, we must have

$$\beta = \theta = 0. \tag{7.68}$$

This is easily verified by an explicit evaluation of Eq. (7.40), which gives

$$\alpha = -\frac{E_0}{E}\frac{\hat{\beta}\sin\theta_p}{1+\hat{\beta}\cos\theta_p}, \tag{7.69}$$

where E_0 and E are the energies of k and p, respectively, and θ_p is the polar angle of p. As a result, even if the corresponding little group transformation is not identity, the Lorentz boost along $\hat{z}$ does leave the helicity invariant,

$$U(\Lambda_z)|p,\sigma\rangle = |\Lambda_z p,\sigma\rangle, \tag{7.70}$$

which is in contrast to the massive case in Eq. (7.42).

Chapter 8

Polarization of fermions at high-energy colliders

8.1 Fermion spin density matrix

At high-energy colliders, fermion spins are usually described in the helicity basis $\{|p,\pm\rangle\}$. A general fermion spin state is described by the density matrix, defined as

$$\rho^{1/2}_{\alpha\alpha'}(p) = \langle p,\alpha|\hat{\rho}^{1/2}|p,\alpha'\rangle, \quad \alpha,\alpha' = \pm 1/2, \tag{8.1}$$

with $\hat{\rho}^{1/2}$ being the spin density operator. It is a 2×2 Hermitian matrix with a unity trace, so can be decomposed in terms of the Pauli matrices $\boldsymbol{\sigma} = (\sigma_1,\sigma_2,\sigma_3)$,

$$\rho^{1/2}_{\alpha\alpha'}(p) = \frac{1}{2}\left(1+\boldsymbol{s}(p)\cdot\boldsymbol{\sigma}\right)_{\alpha\alpha'} = \frac{1}{2}\begin{pmatrix} 1+\lambda(p) & b_1(p)-ib_2(p) \\ b_1(p)+ib_2(p) & 1-\lambda(p)\end{pmatrix}_{\alpha\alpha'}, \tag{8.2}$$

which defines the spin vector $\boldsymbol{s}(p) = (b_1(p), b_2(p), \lambda(p))$ for the fermion. From now on, we will suppress the momentum dependence of the density matrix and spin vector, unless necessary.

The positivity condition requires

$$\det\left[\rho^{1/2}\right] = 1 - \boldsymbol{s}^2 \geq 0, \tag{8.3}$$

which means

$$\boldsymbol{s}^2 = b_1^2 + b_2^2 + \lambda^2 \leq 1, \tag{8.4}$$

where $\boldsymbol{s}^2 = 1$ refers to a pure state and $\boldsymbol{s}^2 < 1$ to a mixed state.

Under a general Lorentz transformation Λ, the density matrix becomes

$$\rho_{\alpha\alpha'}(p) \to \langle \Lambda p, \alpha | \left[U(\Lambda)\, \hat{\rho}\, U^{-1}(\Lambda) \right] | \Lambda p, \alpha' \rangle, \tag{8.5}$$

where we have temporarily suppressed the superscript '1/2' because it applies to all cases. Then using Eq. (7.29), we have

$$\rho_{\alpha\alpha'}(p) \to \sum_{\bar{\alpha},\bar{\alpha}'} D_{\alpha\bar{\alpha}}(W(\Lambda,p)) \rho_{\bar{\alpha}\bar{\alpha}'}(p) D^{\dagger}_{\bar{\alpha}'\alpha'}(W(\Lambda,p)), \tag{8.6}$$

which transforms in a similar way to the helicitiy amplitude [Eq. (7.30)]. As a result, a general Lorentz transformation mixes different components of the density matrix.

The physical meaning of (b_1, b_2, λ) can be examined through their properties under a rotation $\hat{R}(\phi)$ around the momentum direction. That gives the little group $W(\hat{R}(\phi), p) = R_z(\phi)$, by Eq. (7.37), and thus

$$\rho^{1/2}_{\alpha\alpha'}(\boldsymbol{s}') = e^{-i\,\alpha\,\phi}\, \rho^{1/2}_{\alpha\alpha'}(\boldsymbol{s})\, e^{+i\,\alpha'\,\phi}, \tag{8.7}$$

which gives

$$\lambda' = \lambda, \quad b_1' = b_1 \cos\phi - b_2 \sin\phi, \quad b_2' = b_1 \sin\phi + b_2 \cos\phi. \tag{8.8}$$

Hence $\lambda = \rho_{++}^{1/2} - \rho_{--}^{1/2}$ is the "net" helicity of the fermion, which is unchanged under the rotation $\hat{R}(\phi)$, and $\boldsymbol{b}_T \equiv (b_1, b_2)$ is the *transverse spin* of the fermion, which rotates as a two-dimensional vector.

Let us choose the particle momentum direction as the z direction, and the two perpendicular directions as x and y directions. Since each Pauli matrix σ^i can be decomposed into the spin eigenstates along the i-th direction,

$$\sigma^i = |i\rangle\langle i| - |-i\rangle\langle -i|, \quad (i = x, y, z) \tag{8.9}$$

where the bra and ket notations are abused to refer to two-component spinors, then Eq. (8.2) implies

$$\begin{aligned}\rho^{1/2} = \frac{1}{2}\,[1 &+ b_1\,(|x\rangle\langle x| - |-x\rangle\langle -x|) \\ &+ b_2\,(|y\rangle\langle y| - |-y\rangle\langle -y|) + \lambda\,(|z\rangle\langle z| - |-z\rangle\langle -z|)]\,,\end{aligned} \tag{8.10}$$

where the z direction is along the particle momentum. This gives a clear physical meaning for each component of the spin vector,

$$b_1 = \rho_x^{1/2} - \rho_{-x}^{1/2}, \quad b_2 = \rho_y^{1/2} - \rho_{-y}^{1/2}, \quad \lambda = \rho_z^{1/2} - \rho_{-z}^{1/2}, \tag{8.11}$$

where $\rho_i^{1/2} \equiv \langle i|\rho^{1/2}|i\rangle$. That is, $(1 \pm s_i)/2$ is the probability for the particle spin to to be along the i or $-i$ direction.

8.2 Singly polarized fermion production: general discussion

In this section, we focus on the production of a singly polarized fermion, that is, we only observe the polarization of a certain fermion in the final state, and inclusively sum over all the other particles' spins. Intuitively, such an unpolarized scattering should not produce a singly polarized particle. However, there is an interesting correlation between spins and momenta, which can yield singly polarized particle.

We consider a $2 \to 2$ scattering

$$a(p_1, \alpha_1) + b(p_2, \alpha_2) \to c(p_3, \alpha_3) + f(p, \alpha), \tag{8.12}$$

in which f is the fermion whose spin α we observe. In the CM frame, we choose a to be along the $\hat{z}_{\text{lab}}$ direction, which together with the fermion momentum direction $\hat{p}(\theta_f, \phi_f)$ defines a scattering plane, whose normal is $\hat{z}_{\text{lab}} \times \hat{p}$. The spin density matrix of f can be obtained form the helicity amplitude $\mathcal{M}_{\alpha_1\alpha_2\alpha_3\alpha}(p_1, p_2, p_3, p)$ by

$$\rho_{\alpha\alpha'}(p) = \frac{\sum_{\alpha_1,\alpha_2,\alpha_3} \mathcal{M}_{\alpha_1\alpha_2\alpha_3\alpha}\, \mathcal{M}^*_{\alpha_1\alpha_2\alpha_3\alpha'}}{\sum_{\alpha_1,\alpha_2,\alpha_3,\alpha_4} \left|\mathcal{M}_{\alpha_1\alpha_2\alpha_3\alpha_4}\right|^2}, \tag{8.13}$$

which in turn defines the spin vector $\boldsymbol{s} = (\boldsymbol{b}_T, \lambda)$ through Eq. (8.2). Then a nonzero λ implies the asymmetry between productions of a right-handed f and a left-handed f. The transverse spin $\boldsymbol{b}_T$ is provided by the off-diagonal elements of ρ, which is given by the interference of two amplitudes, $\mathcal{M}_{\alpha_1\alpha_2\alpha_3+}$ and $\mathcal{M}_{\alpha_1\alpha_2\alpha_3-}$, which differ by only flipping the helicity of f. Before going further, let us first clarify with respect to which axes the transverse spin is

defined.

Note that the state vector $|p,\alpha\rangle$ used in the calculation of the helicity amplitude is constructed from a reference state $|k,\alpha\rangle$ in the standard way as specified in Eq. (7.16). Similarly, the transverse spin eigenstates $|p,\perp,\varphi\rangle$, defined as linear superpositions of the helicity eigenstates,

$$|p,\perp,\varphi\rangle = \frac{1}{\sqrt{2}}\left(e^{-i\varphi/2}|p,+\rangle + e^{i\varphi/2}|p,-\rangle\right), \tag{8.14}$$

are obtained from $|k,\perp,\varphi\rangle$ by the same set of transformations in Eq. (7.16). Since the same definitions of $\boldsymbol{b}_T$ in Eq. (8.11) hold for the density matrix in Eq. (8.13), using the transverse spin basis $|p,\perp,\varphi\rangle$, the reference directions $\hat{x}$ and $\hat{y}$ of $\boldsymbol{b}_T$ are obtained from the lab frame $x_{\rm lab}$ and $y_{\rm lab}$ by first rotating around $y_{\rm lab}$ by angle θ_f and then around $z_{\rm lab}$ by angle ϕ_f. And the $\hat{z}$ direction referred by λ in Eq. (8.13) is the direction $\hat{p}$. Therefore, we have

$$\hat{z} = \hat{p}, \quad \hat{y} = \frac{\hat{z}_{\rm lab}\times\hat{z}}{|\hat{z}_{\rm lab}\times\hat{z}|}, \quad \hat{x} = \hat{y}\times\hat{z}, \tag{8.15}$$

such that $\hat{x}$ and $\hat{y}$ are perpendicular to the particle momentum, with $\hat{x}$ lying on the scattering plane, and $\hat{y}$ perpendicular.

8.2.1 Constraints from parity conservation

Assuming parity conservation, the helicity amplitude has the property

$$\mathcal{M}_{\alpha_1,\alpha_2,\alpha_3,\alpha}(p_1,p_2,p_3,p) = (\text{phase})\times\mathcal{M}_{-\alpha_1,-\alpha_2,-\alpha_3,-\alpha}(\bar{p}_1,\bar{p}_2,\bar{p}_3,\bar{p}), \tag{8.16}$$

where the overall phase is independent of α's. We note that the parity inversion flips not only all helicities, but also all the momenta. To relate it back to the original scattering, we perform a rotation on the scattering plane by π. This rotation will restore all the flipped momenta but retain the helicities being flipped. So overall we are examining the symmetry transformation

$$U_P = U(R_3(\phi_f))U(R_2(\pi))U^{-1}(R_3(\phi_f))P, \tag{8.17}$$

where P is the parity operator. The rotation operation in Eq. (8.17) is similar to the third rotation case below Eq. (7.38), which gives an identity little group transformation. However, one key difference is that the rotation $R_2(\pi)$ will change the polar angle θ_i particle to $\theta_i + \pi$, which will cross the boundary the θ domain: $\theta \in [0, \pi]$. The discontinuity of the SO(3) topology will thus play a nontrivial role. It introduces an extra phase that depends on the helicity,

$$\mathcal{M}_{\alpha_1,\alpha_2,\alpha_3,\alpha}(p_1, p_2, p_3, p) = (\text{phase}) \cdot e^{i\delta_{123}} \, (-1)^{\alpha - 1/2} \mathcal{M}_{-\alpha_1,-\alpha_2,-\alpha_3,-\alpha}(p_1, p_2, p_3, p), \tag{8.18}$$

where δ_{123} is the phase associated with the particles a, b, c, which may depend on $\alpha_{1,2,3}$, but will eventually cancel when we multiply $\mathcal{M}$ by its complex conjugate in Eq. (8.13). The phase $(-1)^{\alpha-1/2}$ for the particle f gives an extra minus sign when $\alpha = -1/2$. Such phase will also cancel in the diagonal elements of ρ, but not in the off-diagonal elements, and therefore will set a special constraint on the transverse spin.

Using Eq. (8.18), we can get the parity relation for the density matrix,

$$\rho_{\alpha\alpha'}(p) = \frac{\sum_{\alpha_1,\alpha_2,\alpha_3}(-1)^{\alpha+\alpha'-1}\mathcal{M}_{-\alpha_1,-\alpha_2,-\alpha_3,-\alpha}\,\mathcal{M}^*_{-\alpha_1,-\alpha_2,-\alpha_3,-\alpha'}}{\sum_{\alpha_1,\alpha_2,\alpha_3,\alpha_4}\left|\mathcal{M}_{\alpha_1\alpha_2\alpha_3\alpha_4}\right|^2}$$
$$= (-1)^{\alpha+\alpha'-1}\rho_{-\alpha,-\alpha'}(p), \tag{8.19}$$

which means

$$\rho_{++} = \rho_{--}, \quad \rho_{+-} = -\rho_{-+}, \tag{8.20}$$

and thus

$$\lambda = b_1 = 0. \tag{8.21}$$

Therefore, b_2 is the only allowed spin degree of freedom if parity is conserved. In the case with parity violation, all three components are not forbidden.

8.2.2 Constraints from the amplitude structure

In the general case, the scattering amplitude has both real and imaginary parts,

$$\mathcal{M}_{\alpha_1\alpha_2\alpha_3\alpha} = \mathrm{Re}\,\mathcal{M}_{\alpha_1\alpha_2\alpha_3\alpha} + i\,\mathrm{Im}\,\mathcal{M}_{\alpha_1\alpha_2\alpha_3\alpha}. \tag{8.22}$$

Introducing the shorthand notation

$$A_\alpha * B_{\alpha'} \equiv \sum_{\alpha_1\alpha_2\alpha_3} A_{\alpha_1\alpha_2\alpha_3\alpha}B_{\alpha_1\alpha_2\alpha_3\alpha'}, \quad |A_\alpha|^2 = \sum_{\alpha_1\alpha_2\alpha_3\alpha}|A_{\alpha_1\alpha_2\alpha_3\alpha}|^2, \tag{8.23}$$

we have

$$\rho_{\alpha\alpha'} = \frac{(\mathrm{Re}\,\mathcal{M}_\alpha + i\,\mathrm{Im}\,\mathcal{M}_\alpha) * (\mathrm{Re}\,\mathcal{M}_{\alpha'} - i\,\mathrm{Im}\,\mathcal{M}_{\alpha'})}{|\,\mathrm{Re}\,\mathcal{M}_\alpha|^2 + |\,\mathrm{Im}\,\mathcal{M}_\alpha|^2}, \tag{8.24}$$

which gives the spin vector

$$\begin{aligned}
\lambda &= \frac{M_+ * M_+^* - M_- * M_-^*}{M_+ * M_+^* + M_- * M_-^*}, \\
b_1 &= 2\frac{\mathrm{Re}\,\mathcal{M}_+ * \mathrm{Re}\,\mathcal{M}_- + \mathrm{Im}\,\mathcal{M}_+ * \mathrm{Im}\,\mathcal{M}_-}{|\,\mathrm{Re}\,\mathcal{M}_\alpha|^2 + |\,\mathrm{Im}\,\mathcal{M}_\alpha|^2}, \\
b_2 &= 2\frac{\mathrm{Re}\,\mathcal{M}_+ * \mathrm{Im}\,\mathcal{M}_- - \mathrm{Im}\,\mathcal{M}_+ * \mathrm{Re}\,\mathcal{M}_-}{|\,\mathrm{Re}\,\mathcal{M}_\alpha|^2 + |\,\mathrm{Im}\,\mathcal{M}_\alpha|^2}.
\end{aligned} \tag{8.25}$$

Therefore, b_2 can only exist if the amplitude has an imaginary part. In a parity-conserving perturbation theory, such a phase can only occur through loops, which necessarily suppresses b_2 by the coupling constant. In contrast, there is no such constraint for λ and b_1, which can be produced at tree level as long as there is parity violation.

8.2.3 Constraints from chiral symmetry

It is crucial that transverse spin arises from the interference between two amplitudes which only differ in the observed fermion helicity. In terms of the cut diagram notation, a fermion line always forms a closed loop. A nonzero interference thus requires that the fermion helicity is flipped at some point of the fermion loop. This can only happen if (1) the fermion is massive, or (2) there is a Yukawa or tensor interaction vertex. In the SM, there is no tensor interaction, and the only Yukawa interaction is the source for the fermion mass, so the necessary condition to generate a single transverse spin is to have the fermion being massive. This in turn means that the magnitude of the transverse spin will be proportional to the fermion mass m_f, which is compensated by the scattering energy $\sqrt{s}$. That means,

$$b_T \propto \frac{m_f}{\sqrt{s}}, \tag{8.26}$$

which will be highly suppressed at high energies.

On the other hand, in a new physics or effective field theory scenario with tensor interactions, one may have a single transverse spin that does not suffer from such suppression.

8.2.4 Summary

Summarizing this section, we note that the transverse spin b_2 is the only spin degree of freedom allowed by parity, but it must require an imaginary part of the amplitude, which only occurs beyond tree level. In contrast, the other two spin degrees of freedom, λ and b_1, can occur at tree level as long as parity is violated. Furthermore, a single transverse spin can only happen to massive fermions, not to massive ones, and the magnitude is suppressed by the fermion mass.

We note that the derivation for the parity relation in Eq. (8.19) only applies to $2 \to 2$ scattering and inclusive one-particle production. It cannot be trivially extended to more complicated final states. But it is generally true that a single transverse spin is allowed by symmetries.

8.3 Example: s-channel single top production

In this section, we illustrate the single spin production with the example of s-channel single top quark production at the LHC. This is well suited for illustrating all the points discussed in Sec. 8.2 because (1) the top quark is a massive fermion whose mass m_t is not negligible at the LHC energy, which makes production of transverse spin possible; (2) the top quark is produced via an s-channel W boson, whose interaction violates parity, such that a nonzero λ and b_1 can be produced at tree level; (3) beyond tree level, the one-loop QCD correction

can trigger a threshold effect to generate an imaginary part in the amplitude, so that a b_2 can be produced.

At LO, we consider the partonic process $u(p_1,\alpha_1)+\bar{d}(p_2,\alpha_2)\to t(q_1,\sigma_1)+\bar{b}(q_2,\sigma_2)$, which happens through an s-channel W^+ boson, in its CM frame, with u along $\hat{z}$, and t along $\hat{n}(\theta,\phi)$. The kinematics can be easily worked out by momentum conservation,

$$p_{1,2}=\frac{\sqrt{s}}{2}(1,0,0,\pm 1),\quad q_{1,2}=\frac{\sqrt{s}}{2}\left(\frac{s\pm m_t^2}{s},\pm\frac{s-m_t^2}{s}\hat{n}\right), \tag{8.27}$$

with $s=(p_1+p_2)^2$ being the partonic CM energy squared. The scattering amplitude $i\mathcal{M}$ is

$$\begin{aligned} i\mathcal{M}_{\alpha_1\alpha_2\sigma_1\sigma_2} &= \bar{u}(q_1,\sigma_1)\left(\frac{-ig}{\sqrt{2}}\gamma^\mu P_L\right)v(q_2,\sigma_2)\frac{-ig^{\mu\nu}}{s-m_w^2}\bar{v}(p_2,\alpha_2)\left(\frac{-ig}{\sqrt{2}}\gamma^\nu P_L\right)u(p_1,\alpha_1)\\ &= \frac{ig^2}{2(s-m_w^2)}\left[\bar{u}(q_1,\sigma_1)\gamma^\mu P_L v(q_2,\sigma_2)\right]\left[\bar{v}(p_2,\alpha_2)\gamma_\mu P_L u(p_1,\alpha_1)\right], \end{aligned} \tag{8.28}$$

where g is the SU(2) gauge coupling. The helicity structure is greatly simplified by the left-handed vector current interaction and that u, $\bar{d}$, and $\bar{b}$ are taken massless. This constrains $\alpha_1=-1/2$ and $\alpha_2=\sigma_2=+1/2$. So we are only reduced to two helicity amplitudes, with $\sigma_1=\pm 1/2$, wherein only the $-1/2$ helicity can exist if we take $m_t\to 0$, and thus the amplitude with $\sigma_1=+1/2$ is proportional to m_t. By explicit calculation, we obtain

$$\mathcal{M}_{-+-+}=N\,(1+\cos\theta),\quad \mathcal{M}_{-+++}=N\,\frac{m_t}{\sqrt{s}}\sin\theta,\quad N=-\frac{g^2}{2}\frac{s\,e^{-i\phi}}{s-m_w^2}\sqrt{1-\frac{m_t^2}{s}}. \tag{8.29}$$

A few remarks are in order.

- The overall phase $e^{-i\phi}$ arises from the initial $(u\bar{d})$ state having a nonzero spin, $\alpha_1-\alpha_2=-1$, along $\hat{z}$, which gives a phase factor $e^{i(\alpha_1-\alpha_2)\phi}=e^{-i\phi}$. This phase applies to both

amplitudes, $\mathcal{M}_{-+-+}$ and $\mathcal{M}_{-+++}$, and will cancel when we take a product between an amplitude and a complex conjugate amplitude. And so it will not contribute to b_2.

- The factor N contains a threshold factor $\sqrt{1-m_t^2/s}$ to suppress the amplitude as $s \gtrsim m_t^2$. As $s \gg m_t^2$, N approaches a constant $-(g^2/2)e^{-i\phi}$.

- $\mathcal{M}_{-+-+}$ is the only amplitude that survives as $s \gg m_t^2$, and it favors production of the top quark in the forward region, controlled by the angular function $d^1_{-1,-1}(\theta) \propto (1+\cos\theta)$, as a result of the left-handed coupling. In contrast, the amplitude $\mathcal{M}_{-+++}$ flips the top quark helicity by a mass insertion, and so is only significant when s is not much greater than m_t^2. The angular distribution is controlled by $d^1_{1,0}(\theta) \propto \sin\theta$, which is symmetric between forward and backward regions.

The density matrix of the top quark can be easily calculated by Eq. (8.13),

$$\rho^t_{\alpha\alpha'} = \frac{\mathcal{M}_{-,+,\alpha,+}\mathcal{M}^*_{-,+,\alpha',+}}{|\mathcal{M}_{-+-+}|^2 + |\mathcal{M}_{-+++}|^2}, \tag{8.30}$$

which gives

$$\rho^t = \left(\frac{m_t^2}{s}\sin^2\theta + (1+\cos\theta)^2\right)^{-1} \begin{pmatrix} \frac{m_t^2}{s}\sin^2\theta & \frac{m_t}{\sqrt{s}}\sin\theta(1+\cos\theta) \\ \frac{m_t}{\sqrt{s}}\sin\theta(1+\cos\theta) & (1+\cos\theta)^2 \end{pmatrix}, \tag{8.31}$$

where the factor in front plays the role of normalizing ρ^t. Clearly, due to the fact that there are only two non-zero helicity amplitudes, the density matrix has the structure

$$\rho^t \sim \begin{pmatrix} a^2 & ab \\ ab & b^2 \end{pmatrix}, \tag{8.32}$$

up to a normalization. This immediately leads to $\det \rho^t = 0$ such that the polarization vector $|\boldsymbol{s}_t| = 1$, recalling Eq. (8.3). As a result, the top quark must be at a pure spin state at LO; in other words, it is 100% polarized. From Eq. (8.31), one can obtain the polarization vector,

$$\lambda = -\frac{s - m_t^2 + (s + m_t^2)\cos\theta}{s + m_t^2 + (s - m_t^2)\cos\theta}, \quad b_1 = \frac{m_t}{\sqrt{s}} \frac{2s \cdot \sin\theta}{s + m_t^2 + (s - m_t^2)\cos\theta}, \quad b_2 = 0, \tag{8.33}$$

from which we can easily verify $\lambda^2 + b_1^2 = 1$.

We note that the polarization vector expression in Eq. (8.33) holds only in the partonic CM frame. When the whole system is boosted along $\hat{z}$ by $\Lambda_z(\beta)$, the density matrix transforms according to Eq. (8.6). The little group corresponding to such boost has been obtained in Eq. (7.41), which is a rotation around $\hat{y}$ by χ, with

$$\cos\chi = \frac{v + \beta\cos\theta}{\sqrt{(1 + \beta v\cos\theta)^2 - (1 - \beta^2)(1 - v^2)}}, \quad v = \frac{s - m_t^2}{s + m_t^2}. \tag{8.34}$$

Therefore, Eq. (8.6) becomes

$$\rho^t(\boldsymbol{s}_t) \to d^{1/2}(\chi) \cdot \rho^t(\boldsymbol{s}_t) \cdot \left[d^{1/2}(\chi)\right]^\dagger, \tag{8.35}$$

which keeps b_2 invariant but mixes b_1 with λ,

$$\lambda \to \lambda\cos\chi - b_1\sin\chi, \quad b_1 \to b_1\cos\chi + \lambda\sin\chi. \tag{8.36}$$

Because of this mixing, it is necessary to analyze the top polarization in the partonic rest frame event by event.

The mixing [Eq. (8.36)] does not alter the fact $\lambda^2 + b_1^2 = 1$, but also provides a physical

understanding for the full polarization. If we take an infinite boost with $\beta = 1$, which gives

$$\cos\chi = \frac{v + \cos\theta}{1 + v\cos\theta}, \quad \sin\chi = \frac{\sqrt{1-v^2}\sin\theta}{1 + v\cos\theta}, \tag{8.37}$$

then Eq. (8.36) gives

$$\lambda \to -1, \quad b_1 \to 0, \tag{8.38}$$

so that the top quark becomes completely left-handed. This agrees with the physical picture that the infinite boost takes t and $\bar{b}$ to be collinear along $\hat{z}$. Their spins sum up to -1 along $\hat{z}$, equal to the spin of the initial state. Such "infinite momentum frame" explains why the top quark is 100% polarized, and the nonzero b_1 in the "finite momentum frame" is a result of polarization mixing when going from the "infinite momentum frame" to the "finite momentum frame".

8.4 Observing the fermion spin

The high energy colliders do not directly measure the spins, so that information is usually lost in merely constructing the production rates. However, if the polarized particle decays, the kinematic distributions of the decay products are likely to retain the spin information of the mother particle. This is the case for the heavy fermions in the SM, especially for the top quark.

This is best illustrated in the rest frame of top quark, constructed by choosing the $\hat{z}$ axis as the top quark momentum $\boldsymbol{p}_t$ direction in the lab frame, and $\hat{y}$ as the the normal vector of the top production plane in the lab frame, $\hat{y} = \hat{z}_{\rm lab} \times \hat{z}/|\hat{z}_{\rm lab} \times \hat{z}|$, and $\hat{x} = \hat{y} \times \hat{z}$. The helicity

amplitude of the decay $t(\alpha_t) \to W^+(\alpha_w) b(\alpha_b)$ can be written generally as [Tung(1985)]

$$\mathcal{M}_{\alpha_t \alpha_w \alpha_b}(\theta^\star, \phi^\star) = A_{\alpha_w, \alpha_b} D^{1/2*}_{\alpha_t, \alpha_w - \alpha_b}(\phi^\star, \theta^\star, 0) = A_{\alpha_w, \alpha_b}\, e^{i\alpha_t \phi^\star}\, d^{1/2}_{\alpha_t, \alpha_w - \alpha_b}(\theta^\star). \quad (8.39)$$

where α's denote the helicities, α_t being with respect to the $\hat{z}$ axis, and $d^{1/2}$ is the Wigner d-function. The angles $\theta^\star$ and $\phi^\star$ characterize the W boson direction in the top rest frame. The coefficient A_{α_w, α_b} does not depend on top helicity or the angles. The angular distribution of the W is given by

$$\frac{d\Gamma_t}{d\cos\theta^\star d\phi^\star} \propto \rho^t_{\alpha_t \alpha'_t}(\boldsymbol{s}_t) \mathcal{M}_{\alpha_t \alpha_w \alpha_b}(\theta^\star, \phi^\star) \mathcal{M}^*_{\alpha'_t \alpha_w \alpha_b}(\theta^\star, \phi^\star), \quad (8.40)$$

where the summation over repeated indices is implied, and $\boldsymbol{s}_t = (b_1, b_2, \lambda)$ is the top spin vector. Inserting Eq. (8.39) into Eq. (8.45) gives

$$\frac{1}{\Gamma_t} \frac{d\Gamma_t}{d\cos\theta^\star d\phi^\star} = \frac{1}{4\pi} \left[1 + \kappa_w\, \boldsymbol{s}_t \cdot \boldsymbol{\Omega}^\star\right], \quad (8.41)$$

where $\boldsymbol{s}_t \cdot \boldsymbol{\Omega} = b_1 \sin\theta^\star \cos\phi^\star + b_2 \sin\theta^\star \sin\phi^\star + \lambda \cos\theta^\star$ and

$$\kappa_w = \frac{|A_{1,1/2}|^2 - |A_{0,1/2}|^2 + |A_{0,-1/2}|^2 - |A_{-1,-1/2}|^2}{|A_{1,1/2}|^2 + |A_{0,1/2}|^2 + |A_{-1,-1/2}|^2 + |A_{0,-1/2}|^2} \quad (8.42)$$

is the spin analyzing power for the W. As a result, the nonzero polarization $\boldsymbol{s}_t$ of the mother particle leads to a forward-backward asymmetry with respect to the polarization direction. In the $\hat{x}$-$\hat{y}$-$\hat{z}$ frame of choice, the longitudinal polarization λ leads to a forward-backward asymmetry while the transverse spin $\boldsymbol{b}_T$ introduces an azimuthal asymmetry.

It is worth noting that using such single-particle distribution as a spin observable belongs

to the single-spin phenomenon. It relies on parity violation in the tbW interaction. As can be obviously noticed, if the top decay process preserves parity, one would have $\kappa_w = 0$, which gives no power to probe the top polarization. In the SM with a purely left-handed tbW current and neglecting the b mass, the leading-order coefficients A_{λ_w,λ_b} are

$$A_{-1,-1/2} = -g\sqrt{m_t^2 - m_w^2}, \quad A_{0,-1/2} = -g\sqrt{m_t^2 - m_w^2}\frac{m_t}{\sqrt{2}m_w}, \tag{8.43}$$

with all the others being 0. This gives the spin-analyzing power for W as

$$\kappa_w = \frac{m_t^2 - 2m_w^2}{m_t^2 + 2m_w^2} \simeq 0.4. \tag{8.44}$$

It is positive, so the W prefers to be along the spin direction of t, as a result of being dominantly produced with a longitudinal polarization.

In the real situation, the W boson from top decay rapidly decays to another fermion-anti-fermion pair $f\bar{f}'$, so that the top quark decays into a three particles, $t \to bf\bar{f}'$. The single-particle distribution in Eq. (8.45) simply generalizes to the three-body case,

$$\frac{1}{\Gamma_t}\frac{d\Gamma_t}{d\cos\theta_f^\star d\phi_f^\star} = \frac{1}{4\pi}\left[1 + \kappa_f\, \boldsymbol{s}_t \cdot \boldsymbol{\Omega}_f^\star\right], \tag{8.45}$$

where f can be b, f, or $\bar{f}'$, $\boldsymbol{\Omega}_f^\star = (\sin\theta_f^\star\cos\phi_f^\star, \sin\theta_f^\star\sin\phi_f^\star, \cos\theta_f^\star)$ is its direction in the top rest frame, and κ_f is the corresponding spin-analyzing power. This general form [Eq. (8.45)] holds because of rotational invariance and the fact that spin vectors $\boldsymbol{s}_t$ appears at most in a linear form.

Eq. (8.45) can be marginalized to give a $\cos\theta^\star$ distribution that exclusively probes the

helicity λ,

$$\frac{1}{\Gamma_t}\frac{d\Gamma_t}{d\cos\theta_f^\star} = \frac{1}{2}(1+\kappa_f\,\lambda\cos\theta_f^\star), \tag{8.46}$$

or a $\phi^\star$ distribution that only probes the transverse spin $\boldsymbol{b}_T$,

$$\frac{1}{\Gamma_t}\frac{d\Gamma_t}{d\phi_f^\star} = \frac{1}{2\pi}\left[1+\frac{\pi}{4}\kappa_f\,(b_1\sin\theta_f^\star\cos\phi_f^\star + b_2\sin\theta_f^\star\sin\phi_f^\star)\right]. \tag{8.47}$$

While the $\theta_f^\star$ and $\phi_f^\star$ distributions play similar roles in the rest frame, they do not when the top quark is boosted. In the boosted frame, the θ_f distribution becomes highly distorted such that f prefers to be collinear with t regardless of the value of λ. Thus Eq. (8.46) loses its power as a spin polarimeter in the boosted frame. The azimuthal angle ϕ_f, on the other hand, remains unchanged by the boost, so Eq. (8.47) still gives a good method for measuring the transverse spin. Since at the LHC, the top quark can be produced with a large boost, the transverse spin stands out against the longitudinal polarization, which is one of the reasons why we study the transverse spin in this paper. While one can convert the polar angle distribution [Eq. (8.46)] into the energy fraction distribution of the daughter particle and produces a new polarimeter for λ, it is not the focus of our discussion in this paper. We will instead give another method for measuring λ for a highly boosted top quark, based on the azimuthal correlation among the three daughter particles of the top decay, in Sec. 9.4.

Chapter 9

Linear polarization of vector bosons at high-energy colliders

The transverse spin of fermions is an interesting phenomenon that is readily overlooked by only examining the total production rate. It encodes the quantum interference information at high energy scattering experiments, and reveals itself as an azimuthal distribution, $\cos\phi$ or $\sin\phi$, which can be easily measured at high-energy colliders. The natural question, then, is whether a similar phenomenon holds for vector bosons.

Unlike the fermions, the spin of a vector boson cannot be pictured as an arrow pointing to a certain direction in the space, but we have the same understandings that (1) a transverse spin is an interference of different helicity states, and (2) it sets a special direction in the transverse plane, which breaks the rotational invariance around the particle momentum. For a massless vector bosons, superposition of the two helicity states $|\pm\rangle$ can make up the familiar *linear polarization* states,

$$|x\rangle = \frac{-1}{\sqrt{2}}\left(|+\rangle - |-\rangle\right), \quad |y\rangle = \frac{i}{\sqrt{2}}\left(|+\rangle + |-\rangle\right), \tag{9.1}$$

which transform as a transverse vector under a rotation $R_z(\phi)$ around the momentum direc-

tion,

$$|x\rangle \to \cos\phi\,|x\rangle + \sin\phi\,|y\rangle, \quad |y\rangle \to \cos\phi\,|y\rangle - \sin\phi\,|x\rangle. \tag{9.2}$$

They, therefore, play the counterpart roles of the fermion transverse spins for the vector bosons. A massive vector boson, on the other hand, has one additional helicity state $|0\rangle$, which can make up more "transverse spin" states by superposing with $|x\rangle$ and $|y\rangle$.

The mass suppression for single fermion transverse spin is due to the chiral symmetry for a massless fermion. For a vector boson, however, there is no chiral symmetry to protect the helicity from being flipped. As a result, the linear polarization of a vector boson is more readily produced. Since now the helicity is flipped by up to two units, we can have $\cos 2\phi$ and $\sin 2\phi$ azimuthal patterns in the decay products of the vector boson. Thus, the linear polarization phenomenon is richer than the fermion transverse spin. In this section, we will lay down the formalism for describing the linear polarization phenomena, and give two physical examples where it can be produced and lead to interesting observation signals.

9.1 Vector boson spin density matrix

Massless vector boson, such as gluons and photons, have only two helicity states, so their spin density matrix is also a 2×2 Hermitian matrix with a unity trace, like the fermion case. So we can also decompose it into Pauli matrices, and thereby define three polarization parameters $\boldsymbol{\xi} = (\xi_1, \xi_2, \xi_3)$ in the helicity basis,

$$\left(\rho^1_{\lambda\lambda'}(p)\right) = \frac{1}{2}(1 + \boldsymbol{\xi}(p)\cdot\boldsymbol{\sigma}) = \frac{1}{2}\begin{pmatrix} 1+\xi_3(p) & \xi_1(p) - i\xi_2(p) \\ \xi_1(p) + i\xi_2(p) & 1-\xi_3(p) \end{pmatrix}. \tag{9.3}$$

As for the fermion case, $\xi_3 = \rho^1_{++} - \rho^1_{--}$ is the net helicity, while the off-diagonal elements (ξ_1, ξ_2), being interference of different helicity states, are the linear polarization. In terms of the linear polarization state

$$|\phi\rangle = \frac{-1}{\sqrt{2}}\left[e^{-i\phi}|+\rangle - e^{i\phi}|-\rangle\right] \tag{9.4}$$

along the ϕ direction (in the transverse plane), (ξ_1, ξ_2) can be represented as

$$\xi_1 = \rho^1_{+-} + \rho^1_{-+} = \langle \pi/2|\hat{\rho}^1|\pi/2\rangle - \langle 0|\hat{\rho}^1|0\rangle = \rho^1_{yy} - \rho^1_{xx}, \tag{9.5a}$$

$$\xi_2 = i(\rho^1_{+-} - \rho^1_{-+}) = \langle 3\pi/4|\hat{\rho}^1|3\pi/4\rangle - \langle \pi/4|\hat{\rho}^1|\pi/4\rangle. \tag{9.5b}$$

They are differences of the linear polarization degrees along two orthogonal directions, as shown in Fig. 9.1. Under a rotation around the gluon momentum by ϕ, the density matrix changes as

$$\rho^1_{\lambda\lambda'}(\boldsymbol{\xi}) \to \rho^1_{\lambda\lambda'}(\boldsymbol{\xi}') = e^{-i(\lambda-\lambda')\phi}\rho^1_{\lambda\lambda'}(\boldsymbol{\xi}), \tag{9.6}$$

so that $\boldsymbol{\xi}$ transforms as

$$\xi_3' = \xi_3, \quad \xi_1' = \cos 2\phi\, \xi_1 - \sin 2\phi\, \xi_2, \quad \xi_2' = \cos 2\phi\, \xi_2 + \sin 2\phi\, \xi_1. \tag{9.7}$$

This shows the difference of the linear polarization $\boldsymbol{\xi}_\perp = (\xi_1, \xi_2)$ from the fermion transverse spin $\boldsymbol{b}_T$: the former transforms like a spin-2 tensor, whereas the latter like a spin-1 vector.

Massive vector bosons, on the other hand, have one extra longitudinal polarization $|0\rangle$,

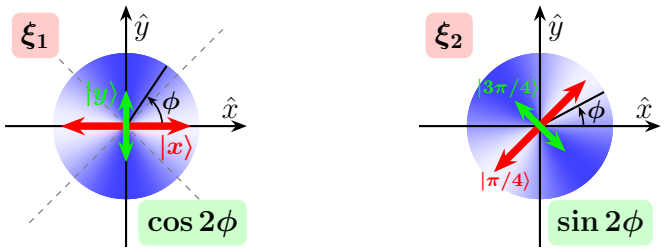

Fig. 9.1: Interpretations of the polarization ξ_1 and ξ_2 in the linear polarization basis, and the associated azimuthal angular distributions.

which extends the density matrix to 3×3. We parametrize it as

$$\left(\rho^M_{\lambda\lambda'}\right) = \begin{pmatrix} \frac{1}{3} + \frac{\delta_L}{6} + \frac{J_3}{2} & \frac{J_1+Q_{xz}-i(J_2+Q_{yz})}{2\sqrt{2}} & \frac{\xi-iQ_{xy}}{2} \\ \frac{J_1+Q_{xz}+i(J_2+Q_{yz})}{2\sqrt{2}} & \frac{1-\delta_L}{3} & \frac{J_1-Q_{xz}-i(J_2-Q_{yz})}{2\sqrt{2}} \\ \frac{\xi+iQ_{xy}}{2} & \frac{J_1-Q_{xz}+i(J_2-Q_{yz})}{2\sqrt{2}} & \frac{1}{3} + \frac{\delta_L}{6} - \frac{J_3}{2} \end{pmatrix}, \tag{9.8}$$

on the helicity basis, in terms of the eight real polarization parameters (J_1, J_2, J_3, Q_{xy}, Q_{yz}, Q_{xz}, δ_L, ξ). We have suppressed their dependence on the vector boson momentum p. Under the rotation by ϕ around $\hat{p}$, the same transformation in Eq. (9.6) holds for ρ^M, which gives the transformation behaviors of the polarization parameters,

$$\begin{pmatrix} J_1' & Q_{xz}' \\ J_2' & Q_{yz}' \end{pmatrix} = \begin{pmatrix} \cos\phi & -\sin\phi \\ \sin\phi & \cos\phi \end{pmatrix} \begin{pmatrix} J_1 & Q_{xz} \\ J_2 & Q_{yz} \end{pmatrix}, \quad \begin{pmatrix} \xi' \\ Q_{xy}' \end{pmatrix} = \begin{pmatrix} \cos 2\phi & -\sin 2\phi \\ \sin 2\phi & \cos 2\phi \end{pmatrix} \begin{pmatrix} \xi \\ Q_{xy} \end{pmatrix}, \tag{9.9}$$

with J_3 and δ_L unchanged. In this way, all the parameters in off-diagonal elements behave like transverse spins. As interference between $|\pm$ and $|0\rangle$, the parameters (J_1, J_2, Q_{xz}, Q_{yz}) behave like transverse vectors with spin 1. Similarly, as interference between $|+\rangle$ and $|-\rangle$, (ξ, Q_{xy}) like transverse vectors with spin 2. The density matrix for a massive vector boson reduces to the massless case by taking (J_1, J_2, Q_{xz}, Q_{yz}) $\to 0$, and equating (ξ, Q_{xy}, J_3)

with (ξ_1, ξ_2, ξ_3).

The physical meaning of (ξ_1, ξ_2, ξ_3) carry through to (ξ, Q_{xy}, J_3) for the massive case, as the linear polarization states and helicity. The parameter δ_L characterizes the longitudinal polarization state. In the rest frame of the massive vector boson, J_1, J_2, and J_3 are the angular momentum (spin) components along the x, y, and z directions, which can be obtained by tracing ρ^M with the spin operators,

$$\hat{J}_1 = \frac{1}{\sqrt{2}} \begin{pmatrix} 0 & 1 & 0 \\ 1 & 0 & 1 \\ 0 & 1 & 0 \end{pmatrix}, \quad \hat{J}_2 = \frac{1}{\sqrt{2}} \begin{pmatrix} 0 & -i & 0 \\ i & 0 & -i \\ 0 & i & 0 \end{pmatrix}, \quad \hat{J}_3 = \begin{pmatrix} 1 & 0 & 0 \\ 0 & 0 & 0 \\ 0 & 0 & -1 \end{pmatrix}. \tag{9.10}$$

The other five parameters can be made analogous to the electric quadrupole moments. By transforming Eq. (9.8) into the linear polarization basis, constituted by Eq. (9.1) and $|z\rangle = |0\rangle$, we have

$$\left(\rho_{ij}^M\right) = \frac{1}{2} \begin{pmatrix} \frac{2}{3} + \frac{\delta_L}{3} - \xi & -Q_{xy} - iJ_3 & -Q_{xz} + iJ_2 \\ -Q_{xy} + iJ_3 & \frac{2}{3} + \frac{\delta_L}{3} + \xi & -Q_{yz} - iJ_1 \\ -Q_{xz} - iJ_2 & -Q_{yz} + iJ_1 & \frac{2}{3}(1 - \delta_L) \end{pmatrix}. \tag{9.11}$$

This immediately gives the quadrupole moments,

$$Q_{xy} = -(\rho_{xy}^M + \rho_{yx}^M), \quad Q_{yz} = -(\rho_{yz}^M + \rho_{zy}^M), \quad Q_{xz} = -(\rho_{xz}^M + \rho_{zx}^M), \tag{9.12}$$

for the off-diagonal elements, and

$$\xi = \rho_{yy}^M - \rho_{xx}^M, \quad \delta_L = \rho_{xx}^M + \rho_{yy}^M - 2\rho_{zz}^M, \tag{9.13}$$

for the diagonal elements. This representation also gives a physical picture for the transformation in Eq. (9.9).

Under a general Lorentz transformation Λ, the spin-1 density matrices also transform as Eq. (8.6), with the transformation matrix D determined by the little group $W(\Lambda, p)$ in the same way. For massless vector bosons, this matrix D is only a phase $e^{-i\lambda\theta(\Lambda,p)}$ [Eq. (7.63)], which only mixes between ξ_1 and ξ_2, but does not change ξ_3. Also, for the special Lorentz boost along $\hat{z}$, D is an identity matrix [Eq. (7.70)], which does not change $\boldsymbol{\xi}$ at all. For massive vector bosons, however, D can be an arbitrary rotation that mixes among various components of the polarization, especially it can mix the linear polarization (ξ, Q_{xy}) with other components. As a result, even if the linear polarization is 0 in one frame, it is likely to be nonzero in some other frame. We will further study this in detail below.

9.2 Parity constraint on the vector boson polarization

We showed in Sec. 8.2 that the single transverse spin of a fermion can be produced only if it is massive. A parity-conserving case further constrains b_2 to be the only possible polarization degree of freedom, which can only appear through threshold effects at a loop level so is destined to be small. The linear polarization of a vector boson, on the other hand, does not suffer from these constraints, because there is no counterpart of the chiral symmetry to protect the helicity of a vector boson from being flipped. So, in general, we should expect a nonzero linear polarization to be produced for a vector boson.

Similar to Eq. (8.19), if the vector boson is produced in a $2 \to 2$ process via a parity

conserving interaction, its polarization density matrix would satisfy

$$\rho^1_{-\lambda,-\lambda'}(p) = (-1)^{\lambda+\lambda'}\rho^1_{\lambda\lambda'}(p), \tag{9.14}$$

which is obtained by performing the same U_P transformation in Eq. (8.17) and use the transformation behavior of a vector boson state.

$$U_P|p,\lambda\rangle = (-1)^{\lambda}|p,-\lambda\rangle. \tag{9.15}$$

Eq. (9.14) applies to both massless and massive vector bosons. For a massless vector boson, it implies $\rho^1_{++} = \rho^1_{--}$ and $\rho^1_{+-} = \rho^1_{-+}$, such that only the linear polarization ξ_1 is allowed to be nonzero, while ξ_2 and the helicity ξ_3 are forbidden. This reduces Eq. (9.3) to

$$\left(\rho^1_{\lambda\lambda'}\right) = \frac{1}{2}\begin{pmatrix} 1 & \xi_1 \\ \xi_1 & 1 \end{pmatrix}, \quad \text{(if parity conserves.)} \tag{9.16}$$

Since $\xi_1 = 2\,\mathrm{Re}(\rho^1_{+-})$, it does not require an imaginary part from the amplitude, so it can appear at tree level. The same conclusion also holds for a massive vector boson, for which Eq. (9.14) means $J_1 = J_3 = Q_{yz} = Q_{xy} = 0$, and we are only allowed to have nonzero δ_L, Q_{xz}, J_2, or ξ. Then Eq. (9.8) is reduced to

$$\left(\rho^M_{\lambda\lambda'}\right) = \frac{1}{2}\begin{pmatrix} \frac{2+\delta_L}{3} & \frac{Q_{xz}-iJ_2}{\sqrt{2}} & \xi \\ \frac{Q_{xz}+iJ_2}{\sqrt{2}} & \frac{2(1-\delta_L)}{3} & \frac{-Q_{xz}-iJ_2}{\sqrt{2}} \\ \xi & \frac{-Q_{xz}+iJ_2}{\sqrt{2}} & \frac{2+\delta_L}{3} \end{pmatrix}, \quad \text{(if parity conserves.)} \tag{9.17}$$

There are no other general symmetries to constrain the density matrix. For a particular

situation, one only needs to examine whether a single helicity flip is allowed for the vector boson under study.

The parity-conserving cases include pure QED and/or QCD production, but not the processes involving EW or other parity-violating new physics interactions. In the latter case, all the polarization parameters are in principle not forbidden, and they are mixed under transformations between different frames. But then the parity-violating polarization parameters would be sensitively dependent on the parity-violating interactions, so they can serve as useful probes for the latter. This will be illustrated in Sec. 9.3 for the gluon polarization.

9.3 Linearly polarized gluon and CP violation

Pinning down the CP nature of the Higgs-top interaction ($ht\bar{t}$) is an important program being pursued at the Large Hadron Collider (LHC) [Sirunyan et al.(2021), Sirunyan et al.(2020), Aad et al.(2020), arX(2022a), Aad et al.(2020), ATL(2022a)]. Any deviation from a Standard-Model-like $ht\bar{t}$ coupling could indicate new physics as well as provide a potential source for the CP violation as required by the baryogenesis [Sakharov(1967)]. Unlike CP-violating Higgs interactions with vector bosons, which arise from dimension-six operators, CP-violating effects in the $ht\bar{t}$ coupling could occur via a dimension-four operator,

$$\mathcal{L} \supset -\frac{y_t}{\sqrt{2}}\, h\, \bar{t}\, (\kappa + i\,\widetilde{\kappa}\,\gamma_5)\, t\,, \tag{9.18}$$

and can be potentially larger. In Eq. (9.18), $y_t = \sqrt{2}m_t/v$ is the Yukuwa coupling of Higgs and top quark in the Standard Model (SM), and $(\kappa, \widetilde{\kappa})$ parametrize the CP-even and CP-odd $ht\bar{t}$ interactions, respectively, which can be reparametrized as $(\kappa, \widetilde{\kappa}) = \kappa_t(\cos\alpha, \sin\alpha)$,

with α being the CP phase. The SM corresponds to $(\kappa, \widetilde{\kappa}) = (1, 0)$ or $(\kappa_t, \alpha) = (1, 0)$.

Numerous approaches have been proposed for determining the CP phase, either directly via associated Higgs and top production [Ellis et al.(2014)Ellis, Hwang, Sakurai, and Takeuchi, Boudjema et al.(2015)Boudjema, Godbole, Guadagnoli, and Mohan, Buckley and Goncalves(2016), Gritsan et al.(2016)Gritsan, Röntsch, Schulze, and Xiao, Mileo et al.(2016)Mileo, Kiers, Szynkman, Crane Amor Dos Santos et al.(2017), Azevedo et al.(2018)Azevedo, Onofre, Filthaut, and Gonçalo, Li et al.(2018)Li, Si, Wu, and Yue, Gonçalves et al.(2018)Gonçalves, Kong, and Kim, Faroughy et al.(202 Bortolato et al.(2021)Bortolato, Kamenik, Košnik, and Smolkovič, Cao et al.(2021)Cao, Xie, Zhang, and Gonçalves et al.(2022)Gonçalves, Kim, Kong, and Wu, Patrick et al.(2020)Patrick, Scaffidi, and Sharma], or indirectly via Higgs or top induced loop effects [Brod et al.(2013)Brod, Haisch, and Zupan, Dolan et al.(2014)Dolan, Harris, Jankowiak, and Spannowsky, Englert et al.(2013)Englert, Goncalves-Net Bernlochner et al.(2019)Bernlochner, Englert, Hays, Lohwasser, Mildner, Pilkington, Price, and Spannows Englert et al.(2019)Englert, Galler, Pilkington, and Spannowsky, Gritsan et al.(2020)Gritsan, Roskes, Sar Bahl et al.(2020)Bahl, Bechtle, Heinemeyer, Katzy, Klingl, Peters, Saimpert, Stefaniak, and Weiglein, Martini et al.(2021)Martini, Pan, Schulze, and Xiao]. The sensitivity to α can be enhanced by using observables that are odd under CP transformation [Mileo et al.(2016)Mileo, Kiers, Szynkman, Cra Gonçalves et al.(2018)Gonçalves, Kong, and Kim]. Machine learning techniques have also been considered [Patrick et al.(2020)Patrick, Scaffidi, and Sharma, Ren et al.(2020)Ren, Wu, and Yang, Bortolato et al.(2021)Bortolato, Kamenik, Košnik, and Smolkovič, Bahl and Brass(2022), Barman et al.(2 to optimize the sensitivity. The current experimental bound from direct measurements is $|\alpha| \leq 22^\circ \sim 66^\circ$ [Sirunyan et al.(2020), arX(2022a), Aad et al.(2020), ATL(2022a)], which needs to be further constrained by the upcoming High-Luminosity LHC (HL-LHC) [Apollinari et al.(2017)A and a possible future pp collider at 100 TeV (FCC-hh) [Mangano and Mangano(2017)].

Here, we propose a new CP-odd observable, for probing the $ht\bar{t}$ interaction, which orig-

inates from a linearly polarized gluon in the associated production of a Higgs boson and gluon jet (hg). The essential observation is that a singly polarized gluon can be produced from the hard scattering of unpolarized partons. After its production, the gluon fragments into a jet with some linear polarization that breaks the rotational invariance around the jet direction and orients the jet constituents according to the hippopedal distribution,

$$\text{const.} + \xi_1 \cos 2\phi + \xi_2 \sin 2\phi \,. \tag{9.19}$$

Here, as will be defined below, ξ_1 and ξ_2 parameterize the two degrees of freedom of the linear polarization and depend on both the kinematics of the hard process and the $ht\bar{t}$ couplings, κ and $\tilde{\kappa}$. The azimuthal angle ϕ is defined in the $\hat{x}$-$\hat{y}$ plane of the coordinate system,

$$\hat{z} = \frac{\boldsymbol{k}}{|\boldsymbol{k}|}\,, \quad \hat{y} = \frac{\hat{z}_{\rm lab} \times \hat{z}}{|\hat{z}_{\rm lab} \times \hat{z}|}\,, \quad \hat{x} = \hat{y} \times \hat{z}\,, \tag{9.20}$$

shown in Fig. 9.2 (right), where $\hat{z}_{\rm lab}$ is the beam direction, and $\boldsymbol{k}$ is three-momentum of the gluon jet in the partonic center-of-mass (CM) frame.

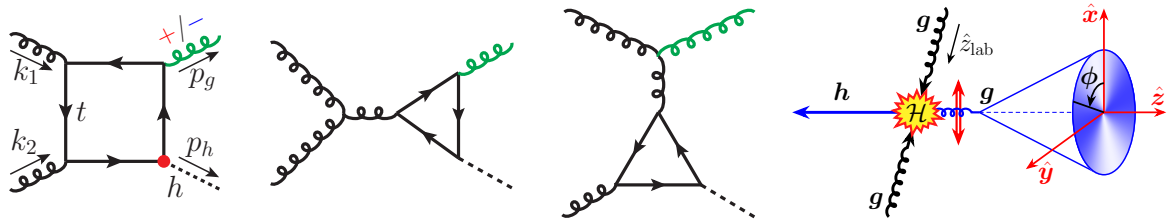

Fig. 9.2: Left three: Representative diagrams for $gg \to hg$ via a top loop. Rightmost one: the gluon $\hat{x}$-$\hat{y}$-$\hat{z}$ frame defined in Eq. (9.20).

The azimuthally anisotropic jet image in Eq. (9.19) can be measured as a new jet substructure observable and provide sensitivity to the CP phase of the $ht\bar{t}$ interaction. We will show that ξ_1 is a CP-even quantity and is sensitive to $(\kappa^2 - \widetilde{\kappa}^2) \propto \cos 2\alpha$, while $\xi_2 \propto \kappa\,\widetilde{\kappa} \propto \sin 2\alpha$

is CP-odd, arising from the interference between the CP-even and CP-odd couplings. Being linear to $\widetilde{\kappa}$, ξ_2 is more sensitive to a small CP phase α, including its sign.

We emphasize that ξ_2 is a genuine CP-odd observable that is constructed purely out of the kinematic information in the gluon jet, and not via a neutral state of charged particles and antiparticles [**?**]. Such CP sensitivity would not be possible without the gluon jet substructure, which has not been considered previously. Also note that associated Higgs-top production and indirect measurements via hV or VV production also depend on the hVV couplings and require assumptions on the latter, whereas hg production only depends on the $ht\bar{t}$ coupling.

In the following, we first show the linear polarization of the final-state gluon in the hg production process, and then lay out the factorization formalism for the polarized gluon jet, which specifies an infrared (IR) safe method for constructing the azimuthal anisotropy in Eq. (9.19). A brief phenomenological discussion follows before concluding this section.

9.3.1 Linearly polarized gluon in hg production

The polarization state of the produced gluon is described by a density matrix, which can be represented in the helicity basis as

$$\rho_{\lambda\lambda'} = \frac{1}{2}\left(1 + \boldsymbol{\xi}\cdot\boldsymbol{\sigma}\right)_{\lambda\lambda'} = \frac{1}{2}\begin{pmatrix} 1+\xi_3 & \xi_1 - i\,\xi_2 \\ \xi_1 + i\,\xi_2 & 1-\xi_3 \end{pmatrix}, \tag{9.21}$$

with three polarization degrees of freedom, $\boldsymbol{\xi} \equiv (\xi_1, \xi_2, \xi_3)$. $\xi_3 = \rho_{++} - \rho_{--}$ is the net helicity of the gluon, whereas $\xi_1 = 2\,\mathrm{Re}\,\rho_{+-}$ and $\xi_2 = -2\,\mathrm{Im}\,\rho_{+-}$ are associated with the interference between the gluon $+$ and $-$ helicity states. In terms of the linear polarization state $|\phi\rangle$ in the

$\hat{x}$-$\hat{y}$-$\hat{z}$ frame, which is related to the helicity eigenstates $|\pm\rangle$ by $|\phi\rangle = [\, e^{i\phi}|-\rangle - e^{-i\phi}|+\rangle\,]/\sqrt{2}$, we can express ξ_1 and ξ_2 as

$$\begin{aligned}\xi_1 &= \langle \pi/2\,|\rho|\,\pi/2\rangle - \langle 0\,|\rho|\,0\rangle = \rho_{yy} - \rho_{xx}\,,\\ \xi_2 &= \langle 3\pi/4\,|\rho|\,3\pi/4\rangle - \langle \pi/4\,|\rho|\,\pi/4\rangle\ .\end{aligned} \tag{9.22}$$

Thus, ξ_1 and ξ_2 are differences between the linear polarization degrees along two orthogonal directions. One can immediately see that under CP transformation, $(\xi_1, \xi_2) \to (\xi_1, -\xi_2)$ and are thus CP-even and CP-odd, respectively. The ambiguity in defining $\hat{z}_{\rm lab}$ in Eq. (9.20) at a pp collider merely implies the change $(\hat{x}, \hat{y}) \to (-\hat{x}, -\hat{y})$, which does not affect linear polarization states, contrary to the transverse spin of the top quark [Kane et al.(1992)Kane, Ladinsky, and Yuan].

The gluon produced in the hg process is predicted to have large linear polarization. At leading order (LO), both gg fusion and $q\bar{q}$ annihilation contribute via a top loop, as exemplified in Fig. 9.2 (left) for the gg channel. Even though the $q\bar{q}$ channel can also produce a substantially polarized gluon, its contribution to the total cross section is much smaller and will be neglected. Parametrizing the helicity amplitudes $g(\lambda_1)\, g(\lambda_2) \to h\, g(\lambda_3)$ in the partonic CM frame in terms of the gluon's transverse momentum p_T, rapidity y_g, and azimuthal angle ϕ_g, we have

$$\begin{aligned}\mathcal{M}_{\lambda_1\lambda_2\lambda_3}(p_T, y_g, \phi_g) &= f^{abc}\, e^{i(\lambda_1-\lambda_2)\phi_g}\\ &\times \Big[\kappa\, \mathcal{A}_{\lambda_1\lambda_2\lambda_3}(p_T, y_g) + i\,\widetilde{\kappa}\, \widetilde{\mathcal{A}}_{\lambda_1\lambda_2\lambda_3}(p_T, y_g)\Big]\,,\end{aligned} \tag{9.23}$$

with f^{abc} the color factor, and λ_i the gluon helicities. The p_T and y_g sufficiently determine the Higgs energy, $E_h^2 = m_H^2 + p_T^2 \cosh^2 y_g$, and the partonic CM energy $\sqrt{\hat{s}} = p_T \cosh y_g + E_h$,

with m_H being the Higgs mass. $\mathcal{A}$ and $\widetilde{\mathcal{A}}$ are the CP-even and CP-odd helicity amplitudes, respectively, constrained by their CP properties as

$$(\mathcal{A},\, \widetilde{\mathcal{A}})_{-\lambda_1,-\lambda_2,-\lambda_3}(p_T, y_g) = (-\mathcal{A}, +\widetilde{\mathcal{A}})_{\lambda_1\lambda_2\lambda_3}(p_T, y_g). \tag{9.24}$$

The gluon density matrix is determined through

$$\frac{1}{4\,N_{c,g}^2}\mathcal{M}_{\lambda_1\lambda_2\lambda}\mathcal{M}^*_{\lambda_1\lambda_2\lambda'} \equiv \rho_{\lambda\lambda'}(\boldsymbol{\xi})\,|\mathcal{M}|^2, \tag{9.25}$$

where the convention of summing over repeated indices is taken, and $|\mathcal{M}|^2$ is the unpolarized squared amplitude, averaged/summed over the spins and colors, with $N_{c,g} = 8$. Due to their CP properties in Eq. (9.24), $\mathcal{A}$ and $\widetilde{\mathcal{A}}$ individually only contribute to ξ_1, while it is their interference that contributes to ξ_2. In terms of the CP phase α, ξ_1 and ξ_2 can be expressed as

$$\xi_1 = \frac{\omega + \beta_1 \cos 2\alpha}{1 + \Delta \cos 2\alpha}, \quad \xi_2 = \frac{\beta_2 \sin 2\alpha}{1 + \Delta \cos 2\alpha}\,, \tag{9.26}$$

where we have defined the polarization parameters

$$\begin{aligned}
\Delta &= \frac{|\mathcal{A}|^2 - |\widetilde{\mathcal{A}}|^2}{|\mathcal{A}|^2 + |\widetilde{\mathcal{A}}|^2}\,, \quad \omega = \frac{2(\mathcal{A}_+ \cdot \mathcal{A}^*_- + \widetilde{\mathcal{A}}_+ \cdot \widetilde{\mathcal{A}}^*_-)}{|\mathcal{A}|^2 + |\widetilde{\mathcal{A}}|^2}\,, \\
\beta_1 &= \frac{2(\mathcal{A}_+ \cdot \mathcal{A}^*_- - \widetilde{\mathcal{A}}_+ \cdot \widetilde{\mathcal{A}}^*_-)}{|\mathcal{A}|^2 + |\widetilde{\mathcal{A}}|^2}\,, \quad \beta_2 = \frac{4\,\mathrm{Re}(\mathcal{A}_+ \cdot \widetilde{\mathcal{A}}^*_-)}{|\mathcal{A}|^2 + |\widetilde{\mathcal{A}}|^2}\,,
\end{aligned}$$

with the notations

$$A_+ \cdot B_- \equiv A_{\lambda_1\lambda_2+}B_{\lambda_1\lambda_2-}, \quad |A|^2 \equiv A_{\lambda_1\lambda_2\lambda_3}\,A^*_{\lambda_1\lambda_2\lambda_3}.$$

Parametrizing $\xi_{1,2}$ as in Eq. (9.26) clearly shows that the polarization only depends on the CP phase α, but not on the coupling strength κ_t, which only controls the event rate. The helicity polarization ξ_3 is also nonzero as $\sqrt{\hat{s}} > 2m_t$, but its value is generally small compared to ξ_1 and ξ_2, and will not be discussed in this work.

The parameters $(\Delta, \omega, \beta_1, \beta_2)$ are functions of p_T and y_g, as shown in Fig. 9.3(a) for some benchmark phase-space points. While the parameter Δ, which describes the relative difference between the CP-even and CP-odd amplitudes squared, stays relatively flat around -0.4 in the range $p_T < 10$ TeV, the parameters ω, β_1, and β_2, which control the sizes of the polarizations ξ_1 and ξ_2, vary sizably with p_T. Based on their p_T dependence, we divide the phase space into three p_T regions and discuss them in turn.

1. Low-p_T region, with $p_T \lesssim 100$ GeV. In this region, both $|\omega|$ and β_1 have large values, whereas $\beta_2 \simeq 0$. The linear polarization is thus dominated by ξ_1, with $\xi_2 \simeq 0$. The dominance of ω over β_1 further implies that ξ_1 does not depend sensitively on α. Being well below the $\sqrt{\hat{s}} = 2m_t$ threshold, this region can be well approximated by the infinite-top-mass effective field theory (EFT) [Dawson(1991), Djouadi et al.(1991)Djouadi, Spira, and Zerwas]. In Fig. 9.3(b), the SM predictions for ξ_1 are shown for both the full one-loop calculation and the EFT approximation, where one can see that ξ_1 generally has a large negative value, which means that the produced gluon is dominantly polarized along the $\hat{x}$ direction in the production plane, cf. Eq. (9.22). Furthermore, it is not dramatically dependent on the gluon rapidity y_g.

Since the low-p_T region contains most of the hg events, it is suitable for testing the gluon linear polarization phenomenon. Here we expect a significant $\cos 2\phi$ jet anisotropy due to the dominant ξ_1. Its insensitivity to α also means that this region can serve as a calibration region for experimentally measuring the linear polarization, which is important to ensure

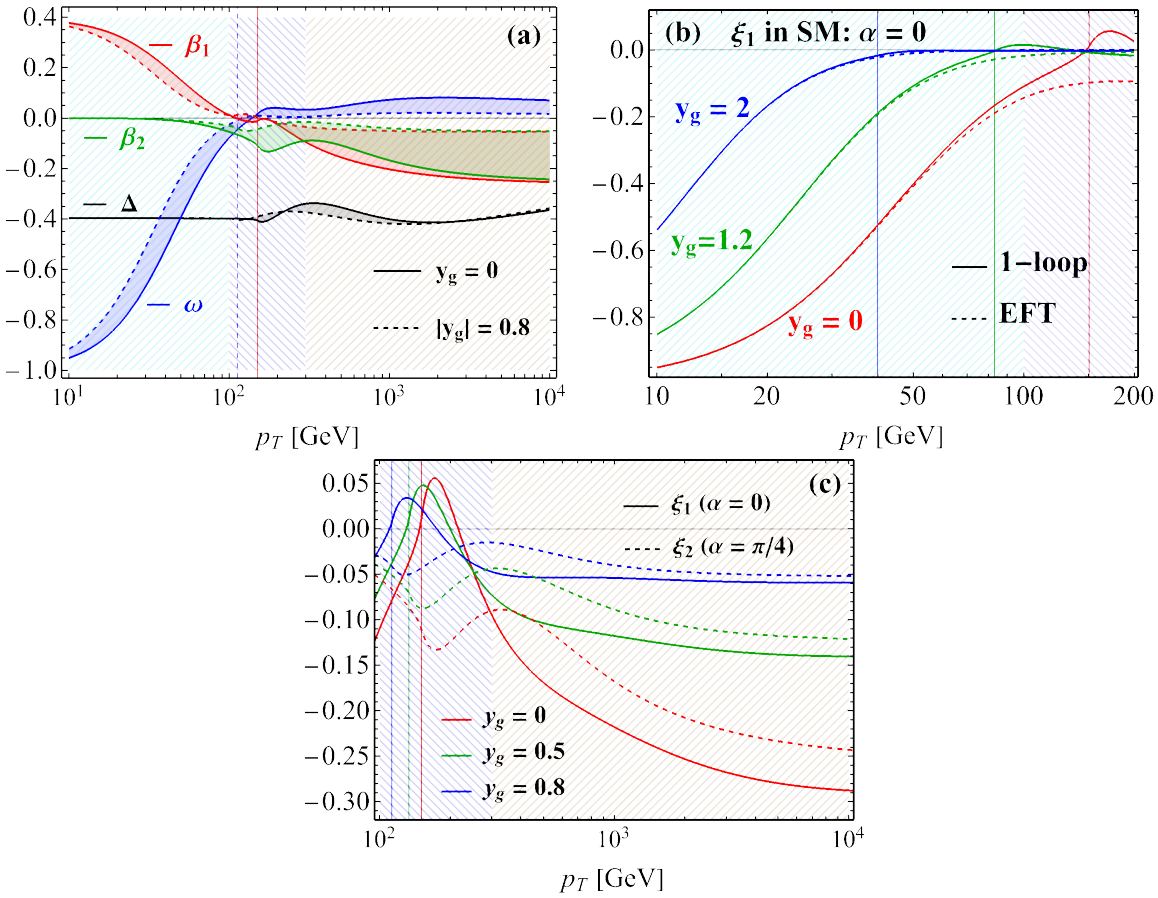

Fig. 9.3: (a) Polarization parameters Δ, ω, β_1, and β_2, as functions of the gluon p_T in the partonic CM frame. Each parameter is shown as a shaded region constrained by $|y_g| \leq 0.8$, bounded by a solid curve and a dashed curve, corresponding to $y_g = 0$ and $|y_g| = 0.8$, respectively. The two vertical lines stand for the $\sqrt{\hat{s}} = 2m_t$ threshold for $y_g = 0$ (red, solid) and $|y_g| = 0.8$ (blue, dashed), respectively. The three hatching-shaded regions are the low-p_T region (cyan) for $p_T < 100$ GeV, transition region (blue) for $p_T \in (100, 300)$ GeV, and high-p_T region (brown) for $p_T > 300$ GeV. (b) ξ_1 in the low-p_T region with the SM Lagrangian ($\alpha = 0$) for three values of y_g, where the full one-loop calculation (solid) is compared with the EFT result (dashed). The three vertical lines are the $\sqrt{\hat{s}} = 2m_t$ threshold for $y_g = 0$ (red), $y_g = 1.2$ (green) and $y_g = 2$ (blue). (c) ξ_1 and ξ_2 in the transition and high-p_T regions, for CP phase $\alpha = 0$ and $\pi/4$, respectively, at which ξ_1 and ξ_2 peak respectively.

its viability and to understand the systematic uncertainties of the measurement since such phenomenon has not been observed before.

2. Transition region, with 100 GeV $\lesssim p_T \lesssim$ 300 GeV. In this region, β_1 and ω rapidly go to 0 and flip their signs, while $|\beta_2|$ starts growing to an appreciable value. Hence, the linear polarization is dominated by ξ_2 if α is not too small, as illustrated in Fig. 9.3(c) for ξ_1 at $\alpha = 0$, and ξ_2 at $\alpha = \pi/4$, which corresponds to a maximal CP mixing. A nonzero α would then lead to a linearly polarized gluon jet that features a $\sin 2\phi$ anisotropy, whose measurement provides a good opportunity for constraining the CP-odd coupling. Furthermore, this region covers the $\sqrt{\hat{s}} = 2m_t$ threshold, so the EFT is no longer a good approximation, as indicated in the right half of Fig. 9.3(b). In this region, both ξ_1 and ξ_2 are sensitive to y_g, and their magnitudes are larger for gluon jets at more central rapidity region.

3. High-p_T region, with $p_T \gtrsim$ 300 GeV. Here, both β_1 and β_2 have appreciable negative magnitude. Their values grow and approach each other as p_T increases. Moreover, ω, being smaller than $|\beta_1|$, becomes less important in ξ_1. Qualitatively, we can interpret this region by taking ω, $\Delta \to 0$ and β_1, $\beta_2 \to \beta$, which gives $(\xi_1, \xi_2) \sim \beta(\cos 2\alpha, \sin 2\alpha)$. Then the jet anisotropy in Eq. (9.19) can be recast as

$$\text{const.} + \beta \cos 2(\phi - \alpha)\,, \tag{9.27}$$

so that the main axis direction of the jet image gives a direct measure of the CP phase. It can be shown that as $\hat{s} \to \infty$, this qualitative simplification becomes exact in the one-loop calculation. The quantitative behavior of ξ_1 and ξ_2 in the high-p_T region is shown in the right half of Fig. 9.3(c), where we see that they drop rapidly to 0 as $|y_g|$ increases, and a

simple kinematic cut $|y_g| < 0.8$ yields the polarization $|\beta_{1,2}| \gtrsim 0.05$.

9.3.2 Polarized gluon jet function.

Around the same time as QCD was developed, it was noted that a linearly polarized gluon with a nonzero ξ_1 can be produced in the hard collision process [Brodsky et al.(1978)Brodsky, DeGrand, and Olsen et al.(1980)Olsen, Osland, and Overbo, Devoto et al.(1980)Devoto, Pumplin, Repko, and Kane, Devoto et al.(1979)Devoto, Pumplin, Repko, and Kane, DeGrand and Petersson(1980), Petersson and Pir Koller et al.(1981)Koller, Streng, Walsh, and Zerwas, Olsen et al.(1981)Olsen, Osland, and Overbo, Devoto and Repko(1982), Korner and Schiller(1981), Olsen and Olsen(1984), Hara and Sakai(1989), Robinett(1991), Jacobsen and Olsen(1990), Groote et al.(1997)Groote, Korner, and Leyva, Groote et al.(1999)Groote, Korner, and Leyva, Groote(2002)], and some non-perturbative arguments were used in favor of an oblate gluon jet characterized by a $\cos 2\phi$ distribution. In the presence of a CP-violating interaction as considered in this work, a nonzero ξ_2 polarization is also produced leading to an additional $\sin 2\phi$ structure, which serves as a handle to probe the CP structure.

Here, we introduce the polarized gluon jet in terms of the modern factorization formalism, for the first time. The polarized gluon turns into a jet that imprints its polarization information in the azimuthal distribution of its constituents, which can be projected out by weighting each event by some azimuth-sensitive observable. The azimuthally weighted cross section σ_w of the inclusive hg production at a pp collider can be factorized into the hard scattering coefficient, as given in Eq. (9.25), multiplied by a polarized gluon jet function, in much the same way as the factorization for an unpolarized jet function [Berger et al.(2003)Berger, Kucs, and Sterman, Almeida et al.(2009a)Almeida, Lee, Perez, Sung, and Almeida et al.(2009b)Almeida, Lee, Perez, Sterman, Sung, and Virzi] or fragmentation func-

tion [Nayak et al.(2005)Nayak, Qiu, and Sterman, Collins(2013)]. It reads as

$$\frac{d\sigma_w}{dy_g\, dp_T^2\, dm_J^2\, d\phi} = \frac{d\hat{\sigma}}{dy_g\, dp_T^2} \frac{dJ(\boldsymbol{\xi}(p_T, y_g), m_J^2, \phi)}{d\phi}\,, \tag{9.28}$$

up to corrections of powers of m_J/p_T and the jet size R. Here,

$$d\hat{\sigma}/dy_g\, dp_T^2 = \mathcal{L}(s, \hat{s})\, |\mathcal{M}|^2/16\pi E_h \sqrt{\hat{s}} \tag{9.29}$$

is the differential cross section for the on-shell gluon production, where

$$\mathcal{L}(s, \hat{s}) = \int_{\hat{s}/s}^1 dx/(xs)\, f_{g/\mathrm{p}}(x,\, \mu_F) f_{g/\mathrm{p}}(\hat{s}/xs,\, \mu_F) \tag{9.30}$$

is the gluon-gluon parton luminosity, with the factorization scale chosen at $\mu_F = p_T$ in the parton distribution function (PDF) $f_{g/\mathrm{p}}(x,\, \mu_F)$ of the proton, and we have used the LO kinematics to integrate over the Higgs phase space.

In the partonic CM frame, the gluon momentum k defines the jet mass $m_J^2 = k^2$ and direction $\hat{z}$ as in Eq. (9.20). By defining two lightlike vectors $n^\mu = (1, -\hat{z})/\sqrt{2}$ and $\bar{n}^\mu = (1, \hat{z})/\sqrt{2}$, we can approximate the gluon momentum in the hard part to be on shell by only retaining the large component, $p_g^\mu = (k \cdot n)\bar{n}^\mu$, which then defines the rapidity y_g and $p_T = k \cdot n/(\sqrt{2} \cosh y_g)$. To the leading power of m_J/p_T, the on-shell gluon carries the polarization

$\boldsymbol{\xi}$ and fragments into a jet, described by the polarized jet function $dJ(\boldsymbol{\xi}, m_J^2, \phi)/d\phi$,

$$\begin{aligned}\frac{dJ}{d\phi} = \frac{1}{2\pi N_{c,g}(k\cdot n)^2}\sum_X \int d^4x\, e^{ik\cdot x}\left[\rho_{\lambda\lambda'}(\boldsymbol{\xi})O(\phi, X)\right] \\ \times \varepsilon^*_{\lambda'\nu}(p_g)\,\langle 0|W_{ac}(\infty, x; n)\, n_\sigma G_c^{\sigma\nu}(x)|X\rangle \\ \times \varepsilon_{\lambda\mu}(p_g)\,\langle X|W_{ab}(\infty, 0; n)\, n_\rho G_b^{\rho\mu}(0)|0\rangle\,,\end{aligned} \tag{9.31}$$

where X denotes the state of the particles within the jet, in accordance with the jet algorithm [Almeida et al.(2009a)Almeida, Lee, Perez, Sung, and Virzi, Ellis et al.(2010)Ellis, Vermilion, Walsh] whose momenta are dominantly along $\bar{n}$. $G_c^{\mu\nu}$ is the gluon field strength tensor, and $W_{ab}(\infty, x; n)$ is the Wilson line in the adjoint representation from x to ∞ along n, with the color indices a, b, and c summed over. In Eq. (9.31), the gluon polarization states are projected using the on-shell polarization vectors $\varepsilon^\mu_\lambda(p_g)$ with helicity $\lambda = \pm 1$, which are then averaged with the density matrix $\rho_{\lambda\lambda'}(\boldsymbol{\xi})$. The resultant azimuthal distribution is extracted by inserting the observable

$$O(\phi, X) = \frac{1}{\sum_{i\in X} p_{i,T}}\sum_{i\in X} p_{i,T}\,\delta(\phi - \phi_i), \tag{9.32}$$

where $p_{i,T}$ and ϕ_i are, respectively, the transverse momentum and azimuthal angle of the jet constituent i with respect to the $\hat{x}$-$\hat{y}$ plane defined in Eq. (9.20). The ϕ distribution is a new jet substructure observable introduced by the linear polarization. The dependence on ξ_3 would vanish due to parity invariance of $O(\phi, X)$.

As a result of the $p_{i,T}$ weight, the observable $O(\phi, X)$ is IR safe, and hence the polarized gluon jet function is insensitive to hadronization effects and becomes perturbatively calculable, with a predictable ϕ dependence. However, it was noted long before [DeGrand and Petersson(1980),

Hara and Sakai(1989)] that the gluon polarization information will be greatly washed out by the cancellation between the $g \to gg$ and $g \to q\bar{q}$ channels, which was also found recently in a similar situation [Chen et al.(2021)Chen, Moult, and Zhu, Chen et al.(2022)Chen, Moult, and Zhu, Larkoski(2022)]. It is possible to mitigate these effects by using jet flavor tagging techniques [Gallicchio and Schwartz(2011), Gallicchio and Schwartz(2013), Ferreira de Lima et al.(2017)Ferrei Frye et al.(2017)Frye, Larkoski, Thaler, and Zhou, Banfi et al.(2006)Banfi, Salam, and Zanderighi, Gras et al.(2017)Gras, Höche, Kar, Larkoski, Lönnblad, Plätzer, Siódmok, Skands, Soyez, and Thaler, Metodiev and Thaler(2018), Larkoski et al.(2014)Larkoski, Thaler, and Waalewijn, Bhattacherjee et al.(20 Kasieczka et al.(2019a)Kasieczka, Kiefer, Plehn, and Thompson, Larkoski and Metodiev(2019), Bright-Thonney et al.(2022)Bright-Thonney, Moult, Nachman, and Prestel]. For example, one may recluster the identified gluon jet into two subjets, and only keep those gluon jets with their two subjets tagged as quarks. At $\mathcal{O}(\alpha_s)$, requiring a tagged quark in the gluon jet leaves $g \to q\bar{q}$ as the only diagram, giving the polarized gluon jet function,

$$\frac{dJ^{(q)}}{d\phi} = \frac{\alpha_s T_F}{6\pi^2 m_J^2} \left[1 + \frac{1}{2}\left(\xi_1 \cos 2\phi + \xi_2 \sin 2\phi\right)\right], \tag{9.33}$$

where the jet algorithm dependence does not come in at this order to the leading power of m_J. Eq. (9.33) needs to be multiplied by the tagging efficiency when used in Eq. (9.28). Although flavor tagging reduces the statistics significantly, it enhances the gluon spin analyzing power from $\mathcal{O}(1\%)$ to about 50% [Hara and Sakai(1989)] and will improve the statistical precision.

Before closing this section, we note the difference of the gluon polarization from a quark. While a transversely polarized light (massless) quark can also be produced from hard scattering processes, its transverse spin cannot be conveyed via the *perturbative* quark jet function due to the chiral symmetry of a massless quark. It is hence related to chiral symmetry break-

ing and must require the presence of some non-perturbative functions [Collins et al.(1994)Collins, Heppelma Collins(2013), Kang et al.(2020)Kang, Lee, and Zhao].

9.3.3 Phenomenology

The gluon jet azimuthal anisotropy in Eq. (9.33) can be experimentally measured by simply constructing the asymmetry observables [Yu and Yuan(2022b)]

$$A_i = \frac{\int_0^{2\pi} d\phi \, (d\sigma_w/d\phi) \cdot \mathrm{sgn}\left[F_i(\phi)\right]}{\int_0^{2\pi} d\phi \, (d\sigma_w/d\phi)} = \frac{\xi_i}{\pi}, \tag{9.34}$$

where $i \in \{1, 2\}$, $F_1(\phi) = \cos 2\phi$ and $F_2(\phi) = \sin 2\phi$. The uncertainties of the asymmetries $A_{1,2}$ are dominated by statistical ones, given by $1/\sqrt{N}$ with N being the number of the observed events. Now we provide a simple demonstration of the constraining power of the gluon linear polarization on the CP phase, by confining ourselves to the transition region for both the HL-LHC at 14 TeV and FCC-hh at 100 TeV, with integrated luminosities 3 ab^{-1} and 20 ab^{-1}, respectively.

The hg cross section in the transition region is estimated for the Lagrangian [Eq. (9.18)] using CT18NNLO PDFs [Hou et al.(2021)] with `MG5_aMC@NLO 2.6.7` [Alwall et al.(2014)Alwall, Frederix, I by first generating the hg events with $p_T \in [100, 300]$ GeV and $\left|\eta_g\right| \leq 2.5$ in the lab frame, and then boosting to the partonic CM frame with the further cut $\left|y_g\right| \leq 0.8$, which gives $\kappa_t^2(0.57\cos^2\alpha + 1.3\sin^2\alpha)$ pb for the HL-LHC and $\kappa_t^2(13.7\cos^2\alpha + 30.7\sin^2\alpha)$ pb for the FCC-hh. While both κ_t and α affect the total production rate and can be constrained by the measurement of the latter, only α determines the polarization. In the following, we take $\kappa_t = 1$ and consider the constraint on α from the polarization data.

We are interested in final states where the (fat) gluon jet is composed of a pair of quark

subjets. While it is possible to also discriminate light quark subjets from gluon subjets, here we only provide a conservative estimate by restricting to the bottom (b) and charm (c) quark tagging as used in experiments [CMS(2016), ATL(2016), Sirunyan et al.(2018), Aaboud et al.(2018a), Aaboud et al.(2018b), Aad et al.(2019a), Aad et al.(2019b), Tumasyan et al.(2022), Aad et al.(2022), ATL(2022b), ATL(2022c)]. We estimate the branching fraction $f_{g_{b\bar{b}}}$ ($f_{g_{c\bar{c}}}$) of $g \to b\bar{b}$ ($g \to c\bar{c}$) through parton shower simulation using `Pythia 8.307` [Sjöstrand et al.(2015)Sjöstrand, which gives $f_{g_{b\bar{b}}} = 0.013$ and $f_{g_{c\bar{c}}} = 0.019$ in the selected kinematic region. Following Refs. [Aad et al.(2019a), Aaboud et al.(2018b)], we take b-tagging efficiency $\epsilon_b = 0.7$ and c-tagging efficiency $\epsilon_c = 0.3$. We consider the diphoton decay channel of the SM Higgs boson and assume a Higgs tagging efficiency $\epsilon_h = 0.002$. This then gives about $(51\cos^2\alpha + 115\sin^2\alpha)$ reconstructed events at the HL-LHC and $(8100\cos^2\alpha + 18200\sin^2\alpha)$ events at the FCC-hh.

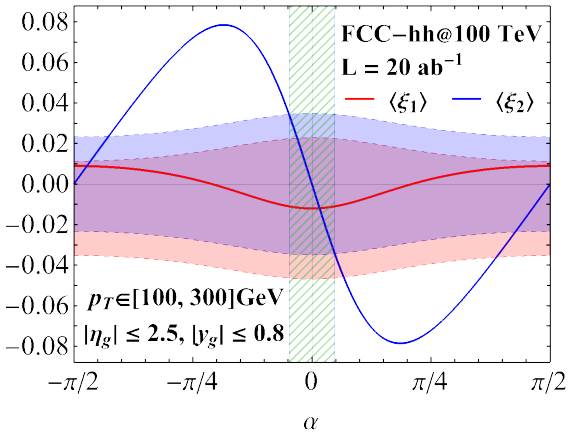

Fig. 9.4: Constraining power of the FCC-hh gluon polarization data, in the transition region, on the CP phase α. $\langle\xi_{1,2}\rangle$ are the average values of $\xi_{1,2}$ in the specified kinematic region. Their statistical uncertainties are indicated by the red and blue bands, respectively, around the SM prediction (with $\alpha = 0$). The green-hatched region is the α range allowed by the ξ_2 measurement.

In Fig. 9.4, we display the predicted average values of $\xi_{1,2}$ in the transition region at the FCC-hh as functions of the CP phase α, together with their uncertainty bands around

the SM central values. As expected, it is ξ_2 that constrains small values of α, whereas ξ_1 is too small to have an impact in this region. Assuming the SM scenario with $\xi_2 = 0$, we can project the constraint $|\alpha| \leq 8.6^\circ$. In this estimate, we have only used the gluon polarization information with Higgs decaying to diphotons. In order to make a significant impact with data from the HL-LHC, one will have to include other Higgs decay channels and light quark flavor tagging in the gluon jets, as well as data from the low-p_T and high-p_T regions, which will significantly improve the constraints. A more careful phenomenological study is left for future.

9.3.4 Summary

A precise understanding of the CP property of the Higgs boson is important both to test the SM and to probe new physics. In this section, we proposed a novel way of probing the CP structure of the Higgs-top interaction, by measuring the azimuthal anisotropy substructure of the gluon jet produced in association with a Higgs boson, which originates from the linear polarization of the final-state gluon. We have introduced a factorization formalism and defined a perturbative polarized gluon jet function with insertion of an IR-safe azimuthal observable. Experimental measurement of the linearly polarized gluon jet will be an important test of the SM and can also serve as a new tool to search for new physics.

9.4 Linearly polarized W boson and boosted top quark jet substructure

Boosted top quarks, with their energies much greater than their mass, provide a unique opportunity for testing the Standard Model (SM) and searching for new physics [Schätzel(2015)]. In this kinematic region, the top quark decay products are collimated, resembling a light QCD jet in appearance. Such a cone signature enhances the selection efficiency of boosted top quark events with respect to the background, which compensates for the small production rate [Abdesselam et al.(2011)]. In addition, the semileptonic decay mode no longer possesses special advantage over the hadronic mode, and one ought to take the latter into account to enhance the statistics. Then, the boosted top can be readily identified as a single "fat" jet by some jet algorithm and becomes difficult to distinguish from a QCD jet. Hence, for the experimental study of boosted tops, one needs first to be able to distinguish a boosted top quark jet from a QCD jet.

There have been many tagging algorithms proposed and applied to discriminate boosted top quark events from QCD jets [CMS(2014), Plehn et al.(2010)Plehn, Spannowsky, Takeuchi, and Zerwas, Aaboud et al.(2019)]. Also, machine learning methods have been applied and found to improve the tagging efficiency substantially, especially when multiple taggers are included [Kasieczka et al.(201 Bhattacharya et al.(2022)Bhattacharya, Guchait, and Vijay, arX(2022b)]. Those techniques mainly make use of the top and W mass conditions and the three-subjet structure. In this Letter, we propose a new substructure observable of the boosted top quark jet that exploits the azimuthal angular correlation among the decay products without the need to identify the two-pronged decay signature of the W boson. When used together with other top taggers, this observable shall further improve the tagging efficiency.

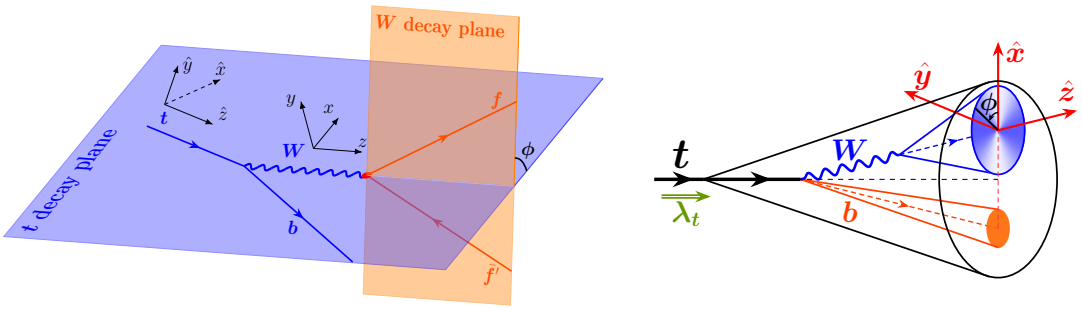

(a) (b)

Fig. 9.5: (a) The two successive decay planes in $t \to bW(\to f\bar{f}')$ decay process. The coordinate systems of top frame and W frame are shown separately. The x axis of W frame lies on the t decay plane, while the $\hat{x}$ axis of the top frame may not. (b) The azimuthal correlation in the boosted top quark jet is reflected as energy deposition.

The azimuthal correlation of interest to us is the angle between the decay planes of $t \to bW$ and $W \to f\bar{f}'$, shown as the ϕ angle in Fig. 9.5. We point out an interesting $\cos 2\phi$ distribution that arises from the linear polarization of W, which is a superposition of its $+1$ and -1 helicity eigenstates. Such polarization does not exist in the top rest frame but emerges as a result of W helicity mixing when going to the boosted top frame, which makes it a unique observable for the boosted top jet. We will show that this phenomenon is generic to many boosted $1 \to 3$ decay systems, especially for QCD jets [Chen et al.(2021)Chen, Moult, and Zhu]. Nevertheless, the correlation in QCD jets is much less significant than that in the boosted top jet, so the azimuthal correlation can be used as a top tagger against QCD jets.

The measurement of top quark polarization is important for testing the SM and exploring new physics models [Kane et al.(1992)Kane, Ladinsky, and Yuan, Berger et al.(2011)Berger, Cao, Chen, a which is commonly done in the top rest frame for the semileptonic decay mode [ATL(2021), Aad et al.(2013a), Jezabek(1994), Brandenburg et al.(2002)Brandenburg, Si, and Uwer, Sirunyan et al.(20 Mahlon and Parke(2010), Schwienhorst et al.(2011)Schwienhorst, Yuan, Mueller, and Cao, Aguilar-Saaved

In the boosted regime, however, it is no longer a good choice to go to the top rest frame because the finite granular size of the detector leads to large uncertainties of the angular separations (especially in polar angles) among the subjets inside the top jet, inhibiting the full reconstruction of its rest frame. As a result, we study the boosted top polarization within the boosted regime. For this purpose, some methods have been designed [Shelton(2009), Krohn et al.(2010)Krohn, Shelton, and Wang, Kitadono and Li(2016), Godbole et al.(2019)Godbole, Guch by making use of the energy or polar angular distribution of the decay products. Below, we will show how the $\cos 2\phi$ azimuthal correlation can serve as an additional top polarimeter in the boosted regime, and we will propose an experimental observable for extracting this correlation.

9.4.1 W density matrix.

In a top quark production process, we choose the $\hat{z}$ axis as the top moving direction, while the $\hat{x}$ axis lies on its production plane and $\hat{y} = \hat{z} \times \hat{x}$. For instance, for a top production event at the LHC, the production plane is formed by the initial-state proton beams and the top momentum, and $\hat{y}$ is perpendicular to this plane. In this frame, called the "boosted top frame", the top is boosted with energy E_t. Its decay into $bf\bar{f}'$ can be described as two successive steps: first, t decays to b and W, whose polarization is described by the unnormalized density matrix

$$W_{\lambda_w \lambda'_w} = \rho^t_{\lambda_t \lambda'_t} \mathcal{M}_{\lambda_t \lambda_w \lambda_b} \mathcal{M}^*_{\lambda'_t \lambda'_w \lambda_b}, \tag{9.35}$$

where a sum over repeated indices is implied; and then W decays into a fermion pair $f\bar{f}'$. $\mathcal{M}_{\lambda_t \lambda_w \lambda_b}$ is the helicity amplitude of $t \to bW$, and $\rho^t = (1 + \boldsymbol{s}_t \cdot \boldsymbol{\sigma})/2$ is the top quark's

spin density matrix, with $\boldsymbol{s}_t = (b_1, b_2, h_t)$ being its polarization vector and $\boldsymbol{\sigma} = (\sigma_1, \sigma_2, \sigma_3)$ the Pauli matrices.

Before proceeding with our discussion, we first define some frames. Apart from the boosted top frame already defined, we define the "top rest frame" as having the *same* $\hat{x}$-$\hat{y}$-$\hat{z}$ coordinate system as the boosted top frame but with the top at rest, and we also define the "W frame" by having the z axis along $\boldsymbol{p}_W$, and y axis along $\boldsymbol{p}_b \times \boldsymbol{p}_W$, where $\boldsymbol{p}_b$ and $\boldsymbol{p}_W$ are the three-momenta of b and W, respectively, in the boosted top frame. The "W rest frame" is obtained by boosting the W frame back along z. See Fig. 9.5 for a graphic illustration.

As a massive spin-1 particle, the W's density matrix [Eq. (9.35)] is a 3×3 Hermitian matrix and so can be described by eight real parameters in addition to its trace. In the helicity basis (W_+, W_L, W_-), for $\lambda_w = 1, 0, -1$, it can be written as

$$\left(W_{\lambda_w \lambda_w'}\right) = \begin{pmatrix} \frac{\mathrm{tr}W}{3} - \frac{\delta_L}{3} + \frac{J_z}{2} & \frac{Jx+2Qxz-i(Jy+2Qyz)}{2\sqrt{2}} & \xi - iQ_{xy} \\ \frac{Jx+2Qxz+i(Jy+2Qyz)}{2\sqrt{2}} & \frac{\mathrm{tr}W}{3} + \frac{2\delta_L}{3} & \frac{Jx-2Qxz-i(Jy-2Qyz)}{2\sqrt{2}} \\ \xi + iQ_{xy} & \frac{Jx-2Qxz+i(Jy-2Qyz)}{2\sqrt{2}} & \frac{\mathrm{tr}W}{3} - \frac{\delta_L}{3} - \frac{J_z}{2} \end{pmatrix}, \tag{9.36}$$

where tr$W$ is the production rate of W boson, J_i is its spin angular momentum along the ith direction ($i = x, y, z$), and the others its quadrupole moments. They will be referred to as (unnormalized) W polarization parameters. The diagonal elements describe the rates of each W helicity state, and the off-diagonal ones arise from the interference between different helicity states.

How does the azimuthal distribution depend on the W polarization parameters? If the W boson is at helicity eigenstate $|\lambda_w\rangle$, the ϕ dependence of its decay products is fully captured

by a phase factor $e^{i\lambda_w\phi}$, which ends up being a constant in the amplitude square. To get a nontrivial azimuthal dependence requires the *interference* between different helicity states. Among the polarization parameters in Eq. (9.36), (J_x, Q_{xz}) and $\left(J_y, Q_{yz}\right)$ are associated with $\cos\phi$ and $\sin\phi$ distributions, respectively, as they are the interference between $W_\pm$ and W_L states, and ξ and Q_{xy} are associated with $\cos 2\phi$ and $\sin 2\phi$ modulations, respectively, for being the interference between W_+ and W_- states.

The angular correlation between the two decay planes in the boosted top system manifests itself as a $\cos 2\phi$ modulation in the SM. We interpret this modulation in the W's linear polarization basis, which consists of the states $\{|x\rangle, |y\rangle, |z\rangle\}$, related to the helicity eigenstates by $|\pm\rangle = (\mp|x\rangle - i|y\rangle)/\sqrt{2}$ and $|0\rangle = |z\rangle$. In this basis, $\xi = \left(W_{yy} - W_{xx}\right)/2$, which means that ξ denotes the difference between the fraction of linearly polarized W events along y and along x. The linear polarization sets a special azimuthal direction, which breaks the azimuthal rotational invariance in W's decay so that the $f\bar{f}'$ plane tends to be perpendicular to the linear polarization of the W boson. For example, if the W were purely linearly polarized along y, the $f\bar{f}'$ plane would tend to be aligned with the x-z plane; cf. Fig. 9.5.

9.4.2 Origin of ξ

The specific values of W density matrix $W_{\lambda_w\lambda'_w}$, and hence the polarization parameters, depend on the reference frame. In the top rest frame, the $t \to bW$ helicity amplitudes are constrained by angular momentum conservation. Because t has spin $1/2$, a certain b helicity state cannot be produced together with both the W_+ and W_- states. This conclusion holds even when the b quark mass is not neglected. For example, if $\lambda_b = -1/2$, W can only have $\lambda_w = -1$ or 0 because $\lambda_w = +1$ would lead to a total spin momentum $3/2$ along the W momentum direction, which cannot be produced from a spin-$1/2$ t. So there cannot be any

interference between the W_+ and W_- states. Consequently, in the top rest frame, ξ must vanish, and hence there is no $\cos 2\phi$ angular correlation.

Now, we go from the top rest frame to the boosted top frame by boosting the tbW system along the $\hat{z}$ direction by the Lorentz boost transformation $\Lambda_t = \Lambda_z(\beta_t)$, where $\beta_t = p_t/E_t$ is determined by the top momentum in the boosted top frame. Under this boost, the W helicity state transforms according to its little group [Weinberg(2005)], which is a rotation around the $\hat{y}$ axis by angle $\chi \in [0, \pi]$, with

$$\cos\chi = \frac{v_w + \beta_t \cos\theta_w}{\sqrt{(1+\beta_t v_w \cos\theta_w)^2 - (1-\beta_t^2)(1-v_w^2)}}, \tag{9.37}$$

where v_w and θ_w are, respectively, the speed and polar angle of W in the top rest frame. The W density matrix [Eq. (9.35)] transforms as a rank-2 tensor by the Wigner-d^1 function, $\left(W_{\lambda\lambda'}\right) \to d^1(\chi)\cdot\left(W_{\lambda\lambda'}\right)\cdot[d^1(\chi)]^T$. This leads to a mixing among ξ, δ_L, and Q_{xz}, particularly with

$$\xi' = \frac{3\xi - \delta_L}{4} + \frac{1}{2}\left(Q_{xz}\sin 2\chi + \frac{\xi + \delta_L}{2}\cos 2\chi\right), \tag{9.38}$$

where the primed (unprimed) polarization parameters refer to the ones in the boosted top frame (top rest frame). Though we have shown that $\xi = 0$ in the top rest frame, a nonzero value (*i.e.*, $\xi' \neq 0$) can be generated in the boosted top frame due to the mixing. The mixing originates from the massiveness of the W boson and is the source of such *new* kind of polarization in the boosted top system that is absent in the top rest frame.

It should be noted that the presence of $\cos 2\phi$ modulation in the boosted top frame arises as a mixing with other nonzero parameters (Q_{xz} and δ_L) present in the top rest frame. As a

whole, the physical information is conserved in both reference frames; it merely appears in a different form as a new $\cos 2\phi$ distribution in the boosted top frame. Nevertheless, the $\cos 2\phi$ distribution does have some advantages over the angular functions associated with Q_{xz} and δ_L, which are $\sin 2\theta_f^\star \cos\phi_f$ and $(1 - 3\cos^2\theta_f^\star)/3$, respectively. To measure the latter two angular distributions, it is necessary to both distinguish f from $\bar{f}'$ and measure the polar angle ($\theta_f^\star$) of f (or $\bar{f}'$) in the W rest frame. Because of the finite angular resolution of the detector, it may become difficult to measure the polar angle precisely in the boosted case in order to reconstruct the W rest frame. In contrast, the azimuthal angle is relatively easier to measure, since it only concerns the relative orientation of the energy deposits, and, due to the invariance of $\cos 2\phi$ under $\phi \to \phi + \pi$, it only cares about the *plane* of $Wf\bar{f}'$ and does not require one to distinguish f from $\bar{f}'$; the latter feature is important for detecting the boosted top quark in its hadronic decay mode.

9.4.3 Azimuthal angular correlation

Assuming the SM W-t-b coupling, the azimuthal angular correlation between the fermion pair plane and the bW plane in the boosted top quark jet takes the form

$$P_t(\phi) \equiv \frac{\pi}{\Gamma_t}\frac{\mathrm{d}\Gamma_t}{\mathrm{d}\phi} = 1 + \langle \xi' \rangle \cos 2\phi, \quad \phi \in [0, \pi), \tag{9.39}$$

where $\langle \xi' \rangle \equiv \left(m_t^2/2m_w^2 + 1\right)^{-1} \left(\int \mathrm{d}\Omega_w^\star\, \xi'/4\pi\right)$ is the average of ξ' over the W angles. Since the angle between the two decay planes does not require one to distinguish f from $\bar{f}'$, the above correlation can be measured in the hadronic decay mode of the top quark with $\phi \in [0, \pi)$. To measure the above correlation in the semileptonic decay mode of the top quark, one needs to first reconstruct the missing neutrino three-momentum by imposing kinematic

constraints of the event [Aad et al.(2013b), Chatrchyan et al.(2012b)]. In that case, one can use the full information of $\phi_f \in [0, 2\pi)$ to include an additional $\cos\phi_f$ angular dependence associated with the polarization parameter J'_x. Here, by focusing on the angle ϕ between the two decay planes, instead of the azimuthal angle ϕ_f of one particular particle from the W decay, we only have to consider the $\cos 2\phi$ angular correlation.

The coefficient $\langle \xi' \rangle$ depends on the top quark's energy E_t and longitudinal polarization h_t and takes the analytic form

$$\langle \xi' \rangle = \kappa(\beta_t, r) \cdot (h_t - \beta_t)\,, \tag{9.40}$$

where $r = m_w/m_t$ and the spin analyzing power is

$$\begin{aligned}\kappa(\beta_t, r) \;=\; & \frac{r}{2\beta_t^2\sqrt{1-\beta_t^2}\,\left(1-r^2\right)^2\left(1+2r^2\right)} \\ & \times \left\{ 4r\sqrt{1-\beta_t^2}\left[\left(1+r^2\right)\log\left|\frac{\beta_t\left(1+r^2\right)+\left(1-r^2\right)}{\beta_t\left(1+r^2\right)-\left(1-r^2\right)}\right| - \beta_t\left(1-r^2\right)\right] \right. \\ & \left. - \left[4r^2 + \left(1-\beta_t^2\right)\left(1+r^2\right)^2\right]\tanh^{-1}\left[\frac{4\beta_t\sqrt{1-\beta_t^2}\,r\left(1-r^2\right)}{\left(1-\beta_t^2\right)\left(1-r^2\right)^2 + 4\beta_t^2 r^2}\right] \right\}. \end{aligned} \tag{9.41}$$

The dependence on E_t converges very quickly to the infinitely boosted limit, such that a top quark with $E_t \gtrsim 500$ GeV can already be considered as highly boosted. Therefore, for phenomenological study of boosted tops, we can well approximate $\langle \xi' \rangle$ by its limit with $E_t = \infty$, which takes the numerical form $\langle \xi' \rangle \simeq 0.145\,(h_t - 1)$, with a spin-analyzing power 0.145.

In the case for antitop quark, we have the same $\cos 2\phi$ correlation as in Eq. (9.39), but the coefficient $\langle \bar{\xi}' \rangle$ differs from Eq. (9.40) by $h_t \to -h_t$ due to CP invariance.

9.4.4 Comparison to QCD jet.

The derivation of Eqs. (9.38) and (9.39) makes it clear that the $\cos 2\phi$ azimuthal correlation is not only relevant to boosted top quarks, but also to any boosted $1 \to 3$ decay systems as long as they are mediated by virtual vector bosons, such as boosted QCD jets with a virtual gluon, boosted $b \to sl^+l^-$ decay through a virtual photon or Z boson, or $b \to c\bar{\nu}_l l^-$ decay via a virtual W. In more general cases with CP violation, there will also be an additional $\sin 2\phi$ correlation.

A particular example is the three-pronged QCD jets, for which the azimuthal angular correlation $P_j(\phi) = 1 + \langle \xi_j \rangle \cos 2\phi$ has been pointed out for the three-point energy correlator [Chen et al.(2021)Chen, Moult, and Zhu]. This is relevant to boosted top quarks because QCD jets can be a source of background of the latter and needs to be distinguished when studying the hadronically decayed boosted top quarks. However, there are more diagrams contributing to the three-point energy correlator of QCD jet that are not mediated by a virtual gluon. Furthermore, for the diagrams that *are* mediated by a virtual gluon, the splittings of $g^* \to gg$ and $g^* \to q\bar{q}$ are not distinguishable if no flavor tagging criterion is imposed, and their contributions to the $\cos 2\phi$ correlation have opposite signs to each other [Chen et al.(2021)Chen, Moult, and Zhu, Hara and Sakai(1989)]. As a result, the $\langle \xi_j \rangle$ is rather small. The analytic formula in the collinear limit is given by Eq. (3) of [Chen et al.(2021)Chen, Moult, and Zhu]. For an active fermion number $n_f = 5$, $\langle \xi_j \rangle$ is -0.01 for quark jets and -0.006 for gluon jets.

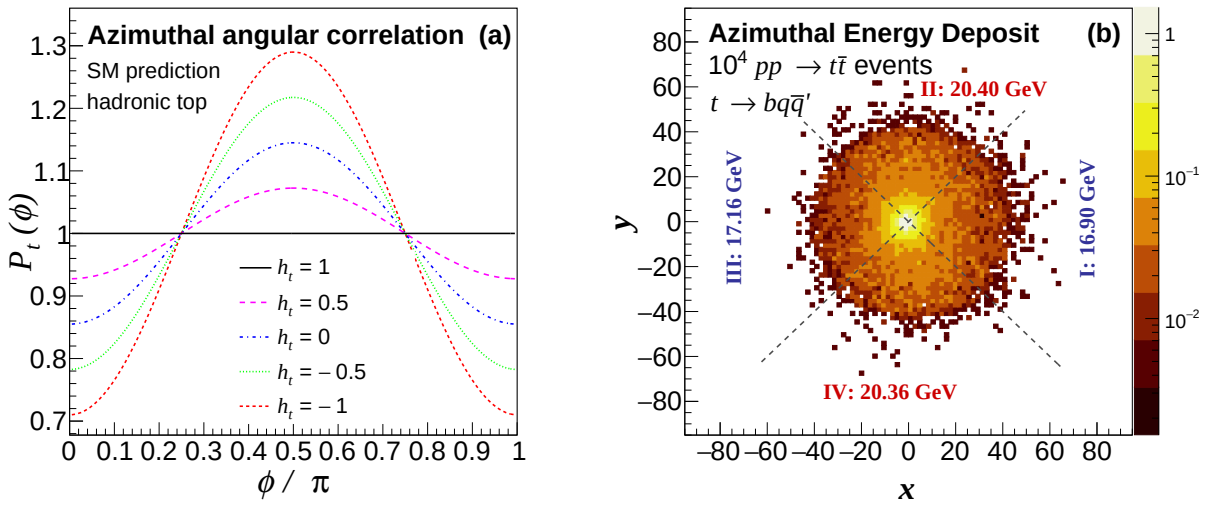

Fig. 9.6: (a) Azimuthal angular correlation in the decay of boosted top quark for different values of top longitudinal polarization h_t. (b) The transverse momentum distribution of W decay products in the azimuthal plane of W frame, viewed from the z direction in Fig. 9.5. The accumulated transverse momentum, averaged over 10^4 events, has been indicated in each quadrant.

9.4.5 Phenomenological implication.

Here, we discuss a few applications of the proposed azimuthal correlation for exploring some aspects of top quark phenomenology at the LHC.

On the one hand, the h_t dependence of $\langle \xi' \rangle$ in Eq. (9.39) enables the measurement of the longitudinal polarization of the top quark, without the need to reconstruct the top rest frame. For example, in Fig. 9.6(a), we show the azimuthal correlation for a few different values of h_t in the boosted limit. The top quark polarization can give clues about its production mechanism, which is useful in testing the SM and searching for new physics. For example, in the QCD production of $t\bar{t}$ pairs, the inclusive top (anti)quark should be unpolarized because QCD preserves parity symmetry, while in the single top production through electroweak interaction, *i.e.*, the s- or t-channel single top and Wt productions, the top quark should be predominantly left-handed because the charged current interaction is purely left-handed in

the SM. In various new physics models, top quarks can be produced with various degrees of polarization [Berger et al.(2011)Berger, Cao, Chen, and Zhang]. Hence, the measured value of $\langle \xi' \rangle$ can help discriminate new physics models. Below, we show how to construct such an experimental observable in hadronically decayed tops.

Even though we only performed a leading order calculation in the analysis, the $\cos 2\phi$ correlation arises from the W boson polarization, which is robust against perturbative QCD correction [Do et al.(2003)Do, Groote, Korner, and Mauser] and parton showering. In reality, we need to take the latter into account by defining an infrared (IR) safe observable. Note that the energies of W decay products are not correlated with the azimuthal angle ϕ, and therefore Eq. (9.39) can directly translate into energy distribution in the transverse plane of the W frame,

$$\frac{\mathrm{d}E}{\mathrm{d}\phi} = \frac{E_{\mathrm{tot}}}{2\pi} \left(1 + \langle \xi' \rangle \cos 2\phi\right), \quad \phi \in [0, 2\pi), \tag{9.42}$$

where E can also be taken as the transverse momentum in the W frame, which is equally IR safe, and we have extended ϕ to $[0, 2\pi)$.

The $\cos 2\phi$ distribution leads to an asymmetry of azimuthal energy deposition between the regions with $\cos 2\phi > 0$ and $\cos 2\phi < 0$, which divides the transverse plane into four quadrants, as shown by the two dashed diagonal lines in Fig. 9.6(b). This consideration motivates the following method to extract the coefficient $\langle \xi' \rangle$ that is suitable in experimental analysis:

(1) construct the top jet and its four-momentum p_t^μ;

(2) use jet substructure technique with b tagging to reconstruct the b subjet with its four-momentum p_b^μ;

(3) determine the W's four-momentum $p_W^\mu = p_t^\mu - p_b^\mu$;

(4) construct the W frame coordinate system (x-y-z) as in Fig. 9.5, *i.e.*, z along $\boldsymbol{p}_W$ and y along $\boldsymbol{p}_b \times \boldsymbol{p}_W$; and

(5) remove the particles in the b subjet and determine the energy distribution of the rest of top quark jet in the transverse plane (x-y).

This method does not require identifying the quarks or subjets from W decay. As a demonstration, in Fig. 9.6(b) we show the transverse energy deposit distributed in the azimuthal plane of W frame, which is the average of 10^4 hadronically decayed top quarks with $p_T \in (500, 600)$ GeV from the $t\bar{t}$ pair production in proton-proton collision at $\sqrt{s} = 13$ TeV. The decayed events are generated with `MG5_aMC@NLO 2.6.7` [Alwall et al.(2014)Alwall, Frederix, Frixione, Hirsc at leading order and passed to `Pythia 8.307` [Bierlich et al.(2022)] for parton showering, with full initial and final state radiations. Since hadronization is not correlated with the azimuthal distribution, it will not change the IR-safely defined azimuthal asymmetry. A similar argument also holds for the effect of underlying events that cancel in the asymmetry observable. The anti-k_T algorithm [Cacciari et al.(2008)Cacciari, Salam, and Soyez] implemented in `FastJet 3.4.0` [Cacciari et al.(2012)Cacciari, Salam, and Soyez, Cacciari and Salam(2006)] is used for the jet analysis, with a radius parameter $R = 1.0$ for finding the top jets and $R = 0.2$ for reclustering the top jets and identifying the b-tagged subjets. The energy deposits in the four quadrants are denoted as $E_1, \cdots, E_4$, sequentially, which have been indicated in Fig. 9.6(b). Evidently, there are more energy deposits in the y direction, perpendicular to the tbW plane, than the x direction, which is parallel to the tbW plane. Then we have

$$\langle \xi' \rangle = \frac{\pi}{2} \cdot \frac{(E_1 + E_3) - (E_2 + E_4)}{(E_1 + E_3) + (E_2 + E_4)}. \tag{9.43}$$

This gives $\langle\xi'\rangle = -0.141 \pm 0.016$ in the simulated $t\bar{t}$ events, which agrees well with analytic calculation in Eq. (9.40) for top helicity $h_t = 0$. The quoted uncertainty is only of statistical origin, which is the dominant uncertainty in asymmetry observables [Aad et al.(2019c), CMS(2021)]. When using the same event selection criteria as in Ref. [arX(2022b)], which yields 17 261 boosted $t\bar{t}$ events at the LHC Run-2 with 139 fb^{-1} integrated luminosity, we obtain an uncertainty $\delta\langle\xi'\rangle = 0.012$. Hence, the azimuthal correlation can already be observed with the Run-2 data. Since $\delta\langle\xi'\rangle \propto 1/\sqrt{N_{\text{events}}}$, we can project an uncertainty of 0.008 for 300 fb^{-1} at the LHC Run-3 and 0.0026 for 3000 fb^{-1} at the High-Luminosity LHC [Apollinari et al.(2017)Apollinari, Brüning, Nakamoto, and Rossi]. It is evident that the LHC data allow the precision measurement of such azimuthal correlation.

On the other hand, the hadronically decayed boosted top quark may well be clustered into a single jet by some jet algorithm, which may be contaminated by some QCD jet background events. To have a precision measurement of the top event rate, it is necessary to distinguish top jets from QCD jets. Here, instead of constructing an event-by-event top tagger against QCD jets, we propose a simpler "tagger" that acts on the whole ensemble of boosted top candidates to determine the fraction of top quark events. In this ensemble, one can first measure the azimuthal asymmetry coefficient ξ_0 following the same strategy discussed above. This ξ_0 is not the same as the one for pure top quark events, as given in Eq. (9.40), but is for a mixture of top and QCD jet events. Then, if the top quark events account for a fraction δ_t of the whole ensemble, we should have $\xi_0 = \delta_t\,\langle\xi'\rangle + (1-\delta_t)\,\langle\xi_j\rangle$, from which we can determine $\delta_t = \big(\xi_0 - \langle\xi_j\rangle\big) \,/\, \big(\langle\xi'\rangle - \langle\xi_j\rangle\big)$, where $\langle\xi_j\rangle$ is obtained by averaging over the light quark and gluon jet contributions and only depends on their relative fraction in the boosted QCD jet events. As an example, for single top quarks produced via s-channel SM-like heavy resonance W' with a mass > 1 TeV, $\langle\xi'\rangle \sim -0.29$, while the magnitude of

$\langle \xi_j \rangle \lesssim 0.01$. As long as the top quark yield is not more than an order of magnitude smaller than the QCD jet background rate, δ_t can be precisely determined from the measurement of ξ_0 to constrain the parameter space of this new physics model, such as the W'-t-b coupling strength. We leave a more detailed phenomenological study for future publication.

9.4.6 Conclusion

In this Letter, we proposed a novel substructure observable in the boosted top quark jet based on the azimuthal correlation between the $t \to bW$ and $W \to f\bar{f}'$ decay planes. The boosted top quark decays into a W boson with a linear polarization, which results in a $\cos 2\phi$ azimuthal correlation and translates into an energy deposition asymmetry in the azimuthal plane. Such linear polarization is not present in the top rest frame but only emerges under the boost as a result of mixing with other polarization parameters. We have also demonstrated that such correlation can be used to either measure the longitudinal polarization of a boosted top quark for testing the SM and probing new physics or distinguish a boosted top quark from the QCD jet background.

Chapter 10

Summary and Outlook

Spin property is a long-studied subject throughout the history of particle physics but remains relatively poorly explored in the context of high-energy unpolarized colliders such as the LHC. Following the early works, we re-emphasized the importance of transverse polarization phenomena at the LHC, which correspond to the quantum interference effects between different helicity states, entail information about the hard scattering that is not probed by the unpolarized production rate, and can bring out a wealth of new physical observables. In particular, in the boosted regime, a heavy unstable particle produced with a transverse polarization can lead to a jet of decay products with a new substructure characterized by certain azimuthal correlations.

We have discussed two kinds of single transverse polarization productions. The first kind is to have the polarized particle directly produced from the hard scattering with a hard transverse momentum. This applies to both spin-half quarks and spin-one massless gluons and massive W and Z bosons. For the quark case, chiral symmetry requires a nonzero quark mass, which strongly suppresses the degree of the transverse spin, except for heavy quarks like the top quark. No such suppression exists for the linear polarization of vector bosons, and one generally expects a large degree of linear polarization. At the hadron colliders, however, the lab frame generally differs from the c.m. frame of the hard scattering by a longitudinal boost, under which transverse polarizations of massive particles mix with other

polarization components but those of massless particles remain invariant. As a result, it is better to measure the polarization in the partonic c.m. frame. The second kind is for linearly polarized vector bosons that are not directly produced from the hard scattering, but appear from the decay of a boosted heavy object. One example is the linear gluon polarization in a parton showering. The other example, as we discussed in detail, is for the boosted top quark that decays into a collimated pair of bottom quark and W boson. The linearly polarized W leads to a nontrivial azimuthal correlation, which is in turn reflected as a new boosted top quark jet substructure.

The main idea of linear polarization is the resultant azimuthal correlation caused by helicity interference effects. Therefore, the subject of this paper can be readily extended to more broad physical contexts. A direct application is to use azimuthal correlations to determine the spin of the mother particle. Further, in the context with new physics extensions of the SM, possible fermionic tensor interaction can lead to different fermion helicity structures from the SM interactions, which can interfere and generate nonzero fermion transverse spin. Similarly, new physics operators can also generate linearly polarized vector bosons. In particular, with possible CP-violating new physics interactions, new correlation functions can appear due to CP-violating transverse polarization components, such as the $\sin 2\phi$ components in the polarized gluon jet. The measurements of transverse polarizations thus provide new opportunities to probe possible new physics.

BIBLIOGRAPHY

BIBLIOGRAPHY

[Gross and Wilczek(1973)] D. J. Gross and F. Wilczek, Phys. Rev. Lett. **30**, 1343 (1973).

[Politzer(1973)] H. D. Politzer, Phys. Rev. Lett. **30**, 1346 (1973).

[Workman et al.(2022)] R. L. Workman et al. (Particle Data Group), PTEP **2022**, 083C01 (2022).

[Collins et al.(1989)Collins, Soper, and Sterman] J. C. Collins, D. E. Soper, and G. F. Sterman, Adv. Ser. Direct. High Energy Phys. **5**, 1 (1989), hep-ph/0409313.

[Collins(2013)] J. Collins, *Foundations of perturbative QCD*, vol. 32 (Cambridge University Press, 2013), ISBN 978-1-107-64525-7, 978-1-107-64525-7, 978-0-521-85533-4, 978-1-139-09782-6.

[Constantinou et al.(2021)] M. Constantinou et al., Prog. Part. Nucl. Phys. **121**, 103908 (2021), 2006.08636.

[Feynman(1969)] R. P. Feynman, Phys. Rev. Lett. **23**, 1415 (1969).

[Dokshitzer(1977)] Y. L. Dokshitzer, Sov. Phys. JETP **46**, 641 (1977).

[Gribov and Lipatov(1972)] V. N. Gribov and L. N. Lipatov, Sov. J. Nucl. Phys. **15**, 438 (1972).

[Lipatov(1974)] L. N. Lipatov, Yad. Fiz. **20**, 181 (1974).

[Altarelli and Parisi(1977)] G. Altarelli and G. Parisi, Nucl. Phys. B **126**, 298 (1977).

[Chatrchyan et al.(2012a)] S. Chatrchyan et al. (CMS), Phys. Lett. B **716**, 30 (2012a), 1207.7235.

[Aad et al.(2012)] G. Aad et al. (ATLAS), Phys. Lett. B **716**, 1 (2012), 1207.7214.

[Cid Vidal et al.(2019)] X. Cid Vidal et al., CERN Yellow Rep. Monogr. **7**, 585 (2019), 1812.07831.

[Collins et al.(1985)Collins, Soper, and Sterman] J. C. Collins, D. E. Soper, and G. F. Sterman, Nucl. Phys. B **250**, 199 (1985).

[Bacchetta et al.(2007)Bacchetta, Diehl, Goeke, Metz, Mulders, and Schlegel] A. Bacchetta, M. Diehl, K. Goeke, A. Metz, P. J. Mulders, and M. Schlegel, JHEP **02**, 093 (2007), hep-ph/0611265.

[Diehl(2016)] M. Diehl, Eur. Phys. J. A **52**, 149 (2016), 1512.01328.

[Qiu et al.(2020)Qiu, Rogers, and Wang] J.-W. Qiu, T. C. Rogers, and B. Wang, Phys. Rev. D **101**, 116017 (2020), 2004.13193.

[Accardi et al.(2016)] A. Accardi et al., Eur. Phys. J. A **52**, 268 (2016), 1212.1701.

[Abdul Khalek et al.(2021)] R. Abdul Khalek et al. (2021), 2103.05419.

[Liu et al.(2021a)Liu, Melnitchouk, Qiu, and Sato] T. Liu, W. Melnitchouk, J.-W. Qiu, and N. Sato, Phys. Rev. D **104**, 094033 (2021a), 2008.02895.

[Liu et al.(2021b)Liu, Melnitchouk, Qiu, and Sato] T. Liu, W. Melnitchouk, J.-W. Qiu, and N. Sato, JHEP **11**, 157 (2021b), 2108.13371.

[Lepage and Brodsky(1980)] G. P. Lepage and S. J. Brodsky, Phys. Rev. D **22**, 2157 (1980).

[Brodsky and Lepage(1989)] S. J. Brodsky and G. P. Lepage, Adv. Ser. Direct. High Energy Phys. **5**, 93 (1989).

[Burkardt(2000)] M. Burkardt, Phys. Rev. D **62**, 071503 (2000), [Erratum: Phys.Rev.D 66, 119903 (2002)], hep-ph/0005108.

[Burkardt(2003)] M. Burkardt, Int. J. Mod. Phys. A **18**, 173 (2003), hep-ph/0207047.

[Hofstadter and McAllister(1955)] R. Hofstadter and R. W. McAllister, Phys. Rev. **98**, 217 (1955).

[Hofstadter(1956)] R. Hofstadter, Rev. Mod. Phys. **28**, 214 (1956).

[Simon et al.(1980)Simon, Schmitt, Borkowski, and Walther] G. G. Simon, C. Schmitt, F. Borkowski, and V. H. Walther, Nucl. Phys. A **333**, 381 (1980).

[Bernauer et al.(2010)] J. C. Bernauer et al. (A1), Phys. Rev. Lett. **105**, 242001 (2010), 1007.5076.

[Bernauer et al.(2014)] J. C. Bernauer et al. (A1), Phys. Rev. C **90**, 015206 (2014), 1307.6227.

[Zhan et al.(2011)] X. Zhan et al., Phys. Lett. B **705**, 59 (2011), 1102.0318.

[Mihovilovič et al.(2017)] M. Mihovilovič et al., Phys. Lett. B **771**, 194 (2017), 1612.06707.

[Mihovilovič et al.(2021)] M. Mihovilovič et al., Eur. Phys. J. A **57**, 107 (2021), 1905.11182.

[Xiong et al.(2019)] W. Xiong et al., Nature **575**, 147 (2019).

[Feynman(1972)] R. P. Feynman, *Photon-hadron interactions* (Addison-Wesley, 1972), reading 1972, 282p, URL http://www-library.desy.de/cgi-bin/spiface/find/hep/www?key=6634834&FORMAT=WWWBRIEFBIBTEX.

[Landau(1959)] L. D. Landau, Nucl. Phys. **13**, 181 (1959).

[Collins(2020)] J. Collins (2020), 2007.04085.

[Coleman and Norton(1965)] S. Coleman and R. E. Norton, Nuovo Cim. **38**, 438 (1965).

[Diehl and Gousset(1998)] M. Diehl and T. Gousset, Phys. Lett. B **428**, 359 (1998), hep-ph/9801233.

[Li and Sterman(1992)] H.-n. Li and G. F. Sterman, Nucl. Phys. B **381**, 129 (1992).

[Nayak et al.(2005)Nayak, Qiu, and Sterman] G. C. Nayak, J.-W. Qiu, and G. F. Sterman, Phys. Rev. D **72**, 114012 (2005), hep-ph/0509021.

[Collins and Metz(2004)] J. C. Collins and A. Metz, Phys. Rev. Lett. **93**, 252001 (2004), hep-ph/0408249.

[Qiu and Yu(2022)] J.-W. Qiu and Z. Yu, JHEP **08**, 103 (2022), 2205.07846.

[Landshoff(1974)] P. V. Landshoff, Phys. Rev. D **10**, 1024 (1974).

[Botts and Sterman(1989)] J. Botts and G. F. Sterman, Nucl. Phys. B **325**, 62 (1989).

[Ji(1997a)] X.-D. Ji, Phys. Rev. D **55**, 7114 (1997a), hep-ph/9609381.

[Kang et al.(2014)Kang, Ma, Qiu, and Sterman] Z.-B. Kang, Y.-Q. Ma, J.-W. Qiu, and G. Sterman, Phys. Rev. D **90**, 034006 (2014), 1401.0923.

[Berger et al.(2001)Berger, Diehl, and Pire] E. R. Berger, M. Diehl, and B. Pire, Phys. Lett. B **523**, 265 (2001), hep-ph/0110080.

[Pedrak et al.(2017)Pedrak, Pire, Szymanowski, and Wagner] A. Pedrak, B. Pire, L. Szymanowski, and J. Wagner, Phys. Rev. D **96**, 074008 (2017), [Erratum: Phys.Rev.D 100, 039901 (2019)], 1708.01043.

[Radyushkin(1997)] A. V. Radyushkin, Phys. Rev. D **56**, 5524 (1997), hep-ph/9704207.

[Brodsky et al.(1994)Brodsky, Frankfurt, Gunion, Mueller, and Strikman] S. J. Brodsky, L. Frankfurt, J. F. Gunion, A. H. Mueller, and M. Strikman, Phys. Rev. D **50**, 3134 (1994), hep-ph/9402283.

[Frankfurt et al.(1996)Frankfurt, Koepf, and Strikman] L. Frankfurt, W. Koepf, and M. Strikman, Phys. Rev. D **54**, 3194 (1996), hep-ph/9509311.

[Collins and Freund(1999)] J. C. Collins and A. Freund, Phys. Rev. D **59**, 074009 (1999), hep-ph/9801262.

[Collins et al.(1997)Collins, Frankfurt, and Strikman] J. C. Collins, L. Frankfurt, and M. Strikman, Phys. Rev. D **56**, 2982 (1997), hep-ph/9611433.

[Qiu and Yu(2023)] J.-W. Qiu and Z. Yu, Phys. Rev. D **107**, 014007 (2023), 2210.07995.

[Collins and Rogers(2008)] J. C. Collins and T. C. Rogers, Phys. Rev. D **78**, 054012 (2008), 0805.1752.

[Berger et al.(2002a)Berger, Qiu, and Zhang] E. L. Berger, J.-W. Qiu, and X.-f. Zhang, Phys. Rev. D **65**, 034006 (2002a), hep-ph/0107309.

[Guidal and Vanderhaeghen(2003)] M. Guidal and M. Vanderhaeghen, Phys. Rev. Lett. **90**, 012001 (2003), hep-ph/0208275.

[Einhorn and Ellis(1975)] M. B. Einhorn and S. D. Ellis, Phys. Rev. D **12**, 2007 (1975).

[Chang(1980)] C.-H. Chang, Nucl. Phys. B **172**, 425 (1980).

[Berger and Jones(1981)] E. L. Berger and D. L. Jones, Phys. Rev. D **23**, 1521 (1981).

[Bodwin et al.(1995)Bodwin, Braaten, and Lepage] G. T. Bodwin, E. Braaten, and G. P. Lepage, Phys. Rev. D **51**, 1125 (1995), [Erratum: Phys.Rev.D 55, 5853 (1997)], hep-ph/9407339.

[Berger et al.(2002b)Berger, Diehl, and Pire] E. R. Berger, M. Diehl, and B. Pire, Eur. Phys. J. C **23**, 675 (2002b), hep-ph/0110062.

[Grocholski et al.(2021)Grocholski, Pire, Sznajder, Szymanowski, and Wagner] O. Grocholski, B. Pire, P. Sznajder, L. Szymanowski, and J. Wagner, Phys. Rev. D **104**, 114006 (2021), 2110.00048.

[Grocholski et al.(2022)Grocholski, Pire, Sznajder, Szymanowski, and Wagner] O. Grocholski, B. Pire, P. Sznajder, L. Szymanowski, and J. Wagner, Phys. Rev. D **105**, 094025 (2022), 2204.00396.

[Boussarie et al.(2017)Boussarie, Pire, Szymanowski, and Wallon] R. Boussarie, B. Pire, L. Szymanowski, and S. Wallon, JHEP **02**, 054 (2017), [Erratum: JHEP 10, 029 (2018)], 1609.03830.

[Duplančić et al.(2018)Duplančić, Passek-Kumerički, Pire, Szymanowski, and Wallon] G. Duplančić, K. Passek-Kumerički, B. Pire, L. Szymanowski, and S. Wallon, JHEP **11**, 179 (2018), 1809.08104.

[Soper(1997)] D. E. Soper, AIP Conf. Proc. **407**, 147 (1997), hep-ph/9707384.

[Collins(1998)] J. C. Collins, Phys. Rev. D **57**, 3051 (1998), [Erratum: Phys.Rev.D 61, 019902 (2000)], hep-ph/9709499.

[Landshoff and Polkinghorne(1971)] P. V. Landshoff and J. C. Polkinghorne, Nucl. Phys. B **33**, 221 (1971), [Erratum: Nucl.Phys.B 36, 642 (1972)].

[Henyey and Savit(1974)] F. Henyey and R. Savit, Phys. Lett. B **52**, 71 (1974).

[Cardy and Winbow(1974)] J. L. Cardy and G. A. Winbow, Phys. Lett. B **52**, 95 (1974).

[DeTar et al.(1975)DeTar, Ellis, and Landshoff] C. E. DeTar, S. D. Ellis, and P. V. Landshoff, Nucl. Phys. B **87**, 176 (1975).

[Collins et al.(1993)Collins, Frankfurt, and Strikman] J. C. Collins, L. Frankfurt, and M. Strikman, Phys. Lett. B **307**, 161 (1993), hep-ph/9212212.

[Qiu and Sterman(1991a)] J.-W. Qiu and G. F. Sterman, Nucl. Phys. B **353**, 105 (1991a).

[Qiu and Sterman(1991b)] J.-W. Qiu and G. F. Sterman, Nucl. Phys. B **353**, 137 (1991b).

[Diehl(2003)] M. Diehl, Phys. Rept. **388**, 41 (2003), hep-ph/0307382.

[Polyakov and Schweitzer(2018)] M. V. Polyakov and P. Schweitzer, Int. J. Mod. Phys. A **33**, 1830025 (2018), 1805.06596.

[Ji(1997b)] X.-D. Ji, Phys. Rev. Lett. **78**, 610 (1997b), hep-ph/9603249.

[Lam and Tung(1978)] C. S. Lam and W.-K. Tung, Phys. Rev. D **18**, 2447 (1978).

[Bertone et al.(2021)Bertone, Dutrieux, Mezrag, Moutarde, and Sznajder] V. Bertone, H. Dutrieux, C. Mezrag, H. Moutarde, and P. Sznajder, Phys. Rev. D **103**, 114019 (2021), 2104.03836.

[Diehl et al.(2005)Diehl, Feldmann, Jakob, and Kroll] M. Diehl, T. Feldmann, R. Jakob, and P. Kroll, Eur. Phys. J. C **39**, 1 (2005), hep-ph/0408173.

[Hashamipour et al.(2020)Hashamipour, Goharipour, and Gousheh] H. Hashamipour, M. Goharipour, and S. S. Gousheh, Phys. Rev. D **102**, 096014 (2020), 2006.05760.

[Hashamipour et al.(2022)Hashamipour, Goharipour, Azizi, and Goloskokov] H. Hashamipour, M. Goharipour, K. Azizi, and S. V. Goloskokov, Phys. Rev. D **105**, 054002 (2022), 2111.02030.

[Guo et al.(2022)Guo, Ji, and Shiells] Y. Guo, X. Ji, and K. Shiells, JHEP **09**, 215 (2022), 2207.05768.

[Wigner(1939)] E. P. Wigner, Annals Math. **40**, 149 (1939).

[Weinberg(2005)] S. Weinberg, *The Quantum theory of fields. Vol. 1: Foundations* (Cambridge University Press, 2005), ISBN 978-0-521-67053-1, 978-0-511-25204-4.

[Collins(1993)] J. C. Collins, Nucl. Phys. B **396**, 161 (1993), hep-ph/9208213.

[Bunce et al.(1976)] G. Bunce et al., Phys. Rev. Lett. **36**, 1113 (1976).

[Heller et al.(1978)] K. J. Heller et al., Phys. Rev. Lett. **41**, 607 (1978), [Erratum: Phys.Rev.Lett. 45, 1043 (1980)].

[Kane et al.(1978)Kane, Pumplin, and Repko] G. L. Kane, J. Pumplin, and W. Repko, Phys. Rev. Lett. **41**, 1689 (1978).

[Dharmaratna and Goldstein(1990)] W. G. D. Dharmaratna and G. R. Goldstein, Phys. Rev. D **41**, 1731 (1990).

[Kane et al.(1992)Kane, Ladinsky, and Yuan] G. L. Kane, G. A. Ladinsky, and C. P. Yuan, Phys. Rev. D **45**, 124 (1992).

[Brodsky et al.(1978)Brodsky, DeGrand, and Schwitters] S. J. Brodsky, T. A. DeGrand, and R. Schwitters, Phys. Lett. B **79**, 255 (1978).

[Olsen et al.(1980)Olsen, Osland, and Overbo] H. A. Olsen, P. Osland, and I. Overbo, Phys. Lett. B **89**, 221 (1980).

[Devoto et al.(1980)Devoto, Pumplin, Repko, and Kane] A. Devoto, J. Pumplin, W. W. Repko, and G. L. Kane, Phys. Lett. B **90**, 436 (1980).

[Devoto et al.(1979)Devoto, Pumplin, Repko, and Kane] A. Devoto, J. Pumplin, W. Repko, and G. L. Kane, Phys. Rev. Lett. **43**, 1062 (1979), [Erratum: Phys.Rev.Lett. 43, 1540 (1979)].

[DeGrand and Petersson(1980)] T. A. DeGrand and B. Petersson, Phys. Rev. D **21**, 3129 (1980).

[Petersson and Pire(1980)] B. Petersson and B. Pire, Phys. Lett. B **95**, 119 (1980).

[Olsen et al.(1981)Olsen, Osland, and Overbo] H. A. Olsen, P. Osland, and I. Overbo, Nucl. Phys. B **192**, 33 (1981).

[Devoto and Repko(1982)] A. Devoto and W. W. Repko, Phys. Rev. D **25**, 904 (1982).

[Korner and Schiller(1981)] J. G. Korner and D. H. Schiller (1981).

[Olsen and Olsen(1984)] O. E. Olsen and H. A. Olsen, Phys. Scripta **29**, 12 (1984).

[Hara and Sakai(1989)] Y. Hara and S. Sakai, Phys. Lett. B **221**, 67 (1989).

[Jacobsen and Olsen(1990)] T. Jacobsen and H. A. Olsen, Phys. Scripta **42**, 513 (1990).

[Groote et al.(1997)Groote, Korner, and Leyva] S. Groote, J. G. Korner, and J. A. Leyva, Phys. Rev. D **56**, 6031 (1997), hep-ph/9703416.

[Groote et al.(1999)Groote, Korner, and Leyva] S. Groote, J. G. Korner, and J. A. Leyva, Eur. Phys. J. C **7**, 49 (1999), hep-ph/9806464.

[Groote(2002)] S. Groote (2002), hep-ph/0212039.

[Yu et al.(2022)Yu, Mohan, and Yuan] Z. Yu, K. A. Mohan, and C. P. Yuan (2022), 2211.00845.

[Koller et al.(1981)Koller, Streng, Walsh, and Zerwas] K. Koller, K. H. Streng, T. F. Walsh, and P. M. Zerwas, Nucl. Phys. B **193**, 61 (1981).

[Robinett(1991)] R. W. Robinett, Z. Phys. C **51**, 89 (1991).

[Chen et al.(2021)Chen, Moult, and Zhu] H. Chen, I. Moult, and H. X. Zhu, Phys. Rev. Lett. **126**, 112003 (2021), 2011.02492.

[Chen et al.(2022)Chen, Moult, and Zhu] H. Chen, I. Moult, and H. X. Zhu, JHEP **08**, 233 (2022), 2104.00009.

[Karlberg et al.(2021)Karlberg, Salam, Scyboz, and Verheyen] A. Karlberg, G. P. Salam, L. Scyboz, and R. Verheyen, Eur. Phys. J. C **81**, 681 (2021), 2103.16526.

[Hamilton et al.(2022)Hamilton, Karlberg, Salam, Scyboz, and Verheyen] K. Hamilton, A. Karlberg, G. P. Salam, L. Scyboz, and R. Verheyen, JHEP **03**, 193 (2022), 2111.01161.

[Mulders and Rodrigues(2001)] P. J. Mulders and J. Rodrigues, Phys. Rev. D **63**, 094021 (2001), hep-ph/0009343.

[Nadolsky et al.(2007)Nadolsky, Balazs, Berger, and Yuan] P. M. Nadolsky, C. Balazs, E. L. Berger, and C. P. Yuan, Phys. Rev. D **76**, 013008 (2007), hep-ph/0702003.

[Boer et al.(2011)Boer, Brodsky, Mulders, and Pisano] D. Boer, S. J. Brodsky, P. J. Mulders, and C. Pisano, Phys. Rev. Lett. **106**, 132001 (2011), 1011.4225.

[Catani and Grazzini(2012)] S. Catani and M. Grazzini, Eur. Phys. J. C **72**, 2013 (2012), [Erratum: Eur.Phys.J.C 72, 2132 (2012)], 1106.4652.

[Sun et al.(2011)Sun, Xiao, and Yuan] P. Sun, B.-W. Xiao, and F. Yuan, Phys. Rev. D **84**, 094005 (2011), 1109.1354.

[Qiu et al.(2011)Qiu, Schlegel, and Vogelsang] J.-W. Qiu, M. Schlegel, and W. Vogelsang, Phys. Rev. Lett. **107**, 062001 (2011), 1103.3861.

[Boer et al.(2012)Boer, den Dunnen, Pisano, Schlegel, and Vogelsang] D. Boer, W. J. den Dunnen, C. Pisano, M. Schlegel, and W. Vogelsang, Phys. Rev. Lett. **108**, 032002 (2012), 1109.1444.

[Yu and Yuan(2022a)] Z. Yu and C. P. Yuan, Phys. Rev. Lett. **129**, 112001 (2022a), 2110.11539.

[Tung(1985)] W. K. Tung, *GROUP THEORY IN PHYSICS* (1985).

[Sirunyan et al.(2021)] A. M. Sirunyan et al. (CMS), Phys. Rev. D **104**, 052004 (2021), 2104.12152.

[Sirunyan et al.(2020)] A. M. Sirunyan et al. (CMS), Phys. Rev. Lett. **125**, 061801 (2020), 2003.10866.

[Aad et al.(2020)] G. Aad et al. (ATLAS), Phys. Rev. Lett. **125**, 061802 (2020), 2004.04545.

[arX(2022a)] Tech. Rep., CERN, Geneva (2022a), 2208.02686, URL https://cds.cern.ch/record/2824073.

[ATL(2022a)] Tech. Rep., CERN, Geneva (2022a), URL https://cds.cern.ch/record/2805772.

[Sakharov(1967)] A. D. Sakharov, Pisma Zh. Eksp. Teor. Fiz. **5**, 32 (1967).

[Ellis et al.(2014)Ellis, Hwang, Sakurai, and Takeuchi] J. Ellis, D. S. Hwang, K. Sakurai, and M. Takeuchi, JHEP **04**, 004 (2014), 1312.5736.

[Boudjema et al.(2015)Boudjema, Godbole, Guadagnoli, and Mohan] F. Boudjema, R. M. Godbole, D. Guadagnoli, and K. A. Mohan, Phys. Rev. D **92**, 015019 (2015), 1501.03157.

[Buckley and Goncalves(2016)] M. R. Buckley and D. Goncalves, Phys. Rev. Lett. **116**, 091801 (2016), 1507.07926.

[Gritsan et al.(2016)Gritsan, Röntsch, Schulze, and Xiao] A. V. Gritsan, R. Röntsch, M. Schulze, and M. Xiao, Phys. Rev. D **94**, 055023 (2016), 1606.03107.

[Mileo et al.(2016)Mileo, Kiers, Szynkman, Crane, and Gegner] N. Mileo, K. Kiers, A. Szynkman, D. Crane, and E. Gegner, JHEP **07**, 056 (2016), 1603.03632.

[Amor Dos Santos et al.(2017)] S. Amor Dos Santos et al., Phys. Rev. D **96**, 013004 (2017), 1704.03565.

[Azevedo et al.(2018)Azevedo, Onofre, Filthaut, and Gonçalo] D. Azevedo, A. Onofre, F. Filthaut, and R. Gonçalo, Phys. Rev. D **98**, 033004 (2018), 1711.05292.

[Li et al.(2018)Li, Si, Wu, and Yue] J. Li, Z.-g. Si, L. Wu, and J. Yue, Phys. Lett. B **779**, 72 (2018), 1701.00224.

[Gonçalves et al.(2018)Gonçalves, Kong, and Kim] D. Gonçalves, K. Kong, and J. H. Kim, JHEP **06**, 079 (2018), 1804.05874.

[Faroughy et al.(2020)Faroughy, Kamenik, Košnik, and Smolkovič] D. A. Faroughy, J. F. Kamenik, N. Košnik, and A. Smolkovič, JHEP **02**, 085 (2020), 1909.00007.

[Bortolato et al.(2021)Bortolato, Kamenik, Košnik, and Smolkovič] B. Bortolato, J. F. Kamenik, N. Košnik, and A. Smolkovič, Nucl. Phys. B **964**, 115328 (2021), 2006.13110.

[Cao et al.(2021)Cao, Xie, Zhang, and Zhang] Q.-H. Cao, K.-P. Xie, H. Zhang, and R. Zhang, Chin. Phys. C **45**, 023117 (2021), 2008.13442.

[Gonçalves et al.(2022)Gonçalves, Kim, Kong, and Wu] D. Gonçalves, J. H. Kim, K. Kong, and Y. Wu, JHEP **01**, 158 (2022), 2108.01083.

[Patrick et al.(2020)Patrick, Scaffidi, and Sharma] R. Patrick, A. Scaffidi, and P. Sharma, Phys. Rev. D **101**, 093005 (2020), 1909.12772.

[Brod et al.(2013)Brod, Haisch, and Zupan] J. Brod, U. Haisch, and J. Zupan, JHEP **11**, 180 (2013), 1310.1385.

[Dolan et al.(2014)Dolan, Harris, Jankowiak, and Spannowsky] M. J. Dolan, P. Harris, M. Jankowiak, and M. Spannowsky, Phys. Rev. D **90**, 073008 (2014), 1406.3322.

[Englert et al.(2013)Englert, Goncalves-Netto, Mawatari, and Plehn] C. Englert, D. Goncalves-Netto, K. Mawatari, and T. Plehn, JHEP **01**, 148 (2013), 1212.0843.

[Bernlochner et al.(2019)Bernlochner, Englert, Hays, Lohwasser, Mildner, Pilkington, Price, and Spannow F. U. Bernlochner, C. Englert, C. Hays, K. Lohwasser, H. Mildner, A. Pilkington, D. D. Price, and M. Spannowsky, Phys. Lett. B **790**, 372 (2019), 1808.06577.

[Englert et al.(2019)Englert, Galler, Pilkington, and Spannowsky] C. Englert, P. Galler, A. Pilkington, and M. Spannowsky, Phys. Rev. D **99**, 095007 (2019), 1901.05982.

[Gritsan et al.(2020)Gritsan, Roskes, Sarica, Schulze, Xiao, and Zhou] A. V. Gritsan, J. Roskes, U. Sarica, M. Schulze, M. Xiao, and Y. Zhou, Phys. Rev. D **102**, 056022 (2020), 2002.09888.

[Bahl et al.(2020)Bahl, Bechtle, Heinemeyer, Katzy, Klingl, Peters, Saimpert, Stefaniak, and Weiglein] H. Bahl, P. Bechtle, S. Heinemeyer, J. Katzy, T. Klingl, K. Peters, M. Saimpert, T. Stefaniak, and G. Weiglein, JHEP **11**, 127 (2020), 2007.08542.

[Martini et al.(2021)Martini, Pan, Schulze, and Xiao] T. Martini, R.-Q. Pan, M. Schulze, and M. Xiao, Phys. Rev. D **104**, 055045 (2021), 2104.04277.

[Ren et al.(2020)Ren, Wu, and Yang] J. Ren, L. Wu, and J. M. Yang, Phys. Lett. B **802**, 135198 (2020), 1901.05627.

[Bahl and Brass(2022)] H. Bahl and S. Brass, JHEP **03**, 017 (2022), 2110.10177.

[Barman et al.(2022)Barman, Gonçalves, and Kling] R. K. Barman, D. Gonçalves, and F. Kling, Phys. Rev. D **105**, 035023 (2022), 2110.07635.

[Apollinari et al.(2017)Apollinari, Brüning, Nakamoto, and Rossi] G. Apollinari, O. Brüning, T. Nakamoto, and L. Rossi, CERN Yellow Report pp. 1–19. 21 p (2017), 21 pages, chapter in High-Luminosity Large Hadron Collider (HL-LHC) : Preliminary Design Report, 1705.08830, URL https://cds.cern.ch/record/2120673.

[Mangano and Mangano(2017)] M. Mangano and M. Mangano, *Physics at the FCC-hh, a 100 TeV pp collider*, CERN Yellow Reports: Monographs (CERN, Geneva, 2017), URL http://cds.cern.ch/record/2270978.

[Dawson(1991)] S. Dawson, Nucl. Phys. B **359**, 283 (1991).

[Djouadi et al.(1991)Djouadi, Spira, and Zerwas] A. Djouadi, M. Spira, and P. M. Zerwas, Phys. Lett. B **264**, 440 (1991).

[Berger et al.(2003)Berger, Kucs, and Sterman] C. F. Berger, T. Kucs, and G. F. Sterman, Phys. Rev. D **68**, 014012 (2003), hep-ph/0303051.

[Almeida et al.(2009a)Almeida, Lee, Perez, Sung, and Virzi] L. G. Almeida, S. J. Lee, G. Perez, I. Sung, and J. Virzi, Phys. Rev. D **79**, 074012 (2009a), 0810.0934.

[Almeida et al.(2009b)Almeida, Lee, Perez, Sterman, Sung, and Virzi] L. G. Almeida, S. J. Lee, G. Perez, G. F. Sterman, I. Sung, and J. Virzi, Phys. Rev. D **79**, 074017 (2009b), 0807.0234.

[Ellis et al.(2010)Ellis, Vermilion, Walsh, Hornig, and Lee] S. D. Ellis, C. K. Vermilion, J. R. Walsh, A. Hornig, and C. Lee, JHEP **11**, 101 (2010), 1001.0014.

[Larkoski(2022)] A. J. Larkoski, Phys. Rev. D **105**, 096012 (2022), 2201.03159.

[Gallicchio and Schwartz(2011)] J. Gallicchio and M. D. Schwartz, Phys. Rev. Lett. **107**, 172001 (2011), 1106.3076.

[Gallicchio and Schwartz(2013)] J. Gallicchio and M. D. Schwartz, JHEP **04**, 090 (2013), 1211.7038.

[Ferreira de Lima et al.(2017)Ferreira de Lima, Petrov, Soper, and Spannowsky] D. Ferreira de Lima, P. Petrov, D. Soper, and M. Spannowsky, Phys. Rev. D **95**, 034001 (2017), 1607.06031.

[Frye et al.(2017)Frye, Larkoski, Thaler, and Zhou] C. Frye, A. J. Larkoski, J. Thaler, and K. Zhou, JHEP **09**, 083 (2017), 1704.06266.

[Banfi et al.(2006)Banfi, Salam, and Zanderighi] A. Banfi, G. P. Salam, and G. Zanderighi, Eur. Phys. J. C **47**, 113 (2006), hep-ph/0601139.

[Gras et al.(2017)Gras, Höche, Kar, Larkoski, Lönnblad, Plätzer, Siódmok, Skands, Soyez, and Thaler] P. Gras, S. Höche, D. Kar, A. Larkoski, L. Lönnblad, S. Plätzer, A. Siódmok, P. Skands, G. Soyez, and J. Thaler, JHEP **07**, 091 (2017), 1704.03878.

[Metodiev and Thaler(2018)] E. M. Metodiev and J. Thaler, Phys. Rev. Lett. **120**, 241602 (2018), 1802.00008.

[Larkoski et al.(2014)Larkoski, Thaler, and Waalewijn] A. J. Larkoski, J. Thaler, and W. J. Waalewijn, JHEP **11**, 129 (2014), 1408.3122.

[Bhattacherjee et al.(2015)Bhattacherjee, Mukhopadhyay, Nojiri, Sakaki, and Webber] B. Bhattacherjee, S. Mukhopadhyay, M. M. Nojiri, Y. Sakaki, and B. R. Webber, JHEP **04**, 131 (2015), 1501.04794.

[Kasieczka et al.(2019a)Kasieczka, Kiefer, Plehn, and Thompson] G. Kasieczka, N. Kiefer, T. Plehn, and J. M. Thompson, SciPost Phys. **6**, 069 (2019a), 1812.09223.

[Larkoski and Metodiev(2019)] A. J. Larkoski and E. M. Metodiev, JHEP **10**, 014 (2019), 1906.01639.

[Bright-Thonney et al.(2022)Bright-Thonney, Moult, Nachman, and Prestel] S. Bright-Thonney, I. Moult, B. Nachman, and S. Prestel (2022), 2207.12411.

[Collins et al.(1994)Collins, Heppelmann, and Ladinsky] J. C. Collins, S. F. Heppelmann, and G. A. Ladinsky, Nucl. Phys. B **420**, 565 (1994), hep-ph/9305309.

[Kang et al.(2020)Kang, Lee, and Zhao] Z.-B. Kang, K. Lee, and F. Zhao, Phys. Lett. B **809**, 135756 (2020), 2005.02398.

[Yu and Yuan(2022b)] Z. Yu and C. P. Yuan, Phys. Rev. Lett. **129**, 112001 (2022b), 2110.11539.

[Hou et al.(2021)] T.-J. Hou et al., Phys. Rev. D **103**, 014013 (2021), 1912.10053.

[Alwall et al.(2014)Alwall, Frederix, Frixione, Hirschi, Maltoni, Mattelaer, Shao, Stelzer, Torrielli, and Za
J. Alwall, R. Frederix, S. Frixione, V. Hirschi, F. Maltoni, O. Mattelaer, H. S. Shao, T. Stelzer, P. Torrielli, and M. Zaro, JHEP **07**, 079 (2014), 1405.0301.

[CMS(2016)] Tech. Rep., CERN, Geneva (2016), URL http://cds.cern.ch/record/2195743.

[ATL(2016)] Tech. Rep., CERN, Geneva (2016).

[Sirunyan et al.(2018)] A. M. Sirunyan et al. (CMS), JINST **13**, P05011 (2018), 1712.07158.

[Aaboud et al.(2018a)] M. Aaboud et al. (ATLAS), JHEP **08**, 089 (2018a), 1805.01845.

[Aaboud et al.(2018b)] M. Aaboud et al. (ATLAS), Phys. Rev. Lett. **120**, 211802 (2018b), 1802.04329.

[Aad et al.(2019a)] G. Aad et al. (ATLAS), Eur. Phys. J. C **79**, 970 (2019a), 1907.05120.

[Aad et al.(2019b)] G. Aad et al. (ATLAS), Eur. Phys. J. C **79**, 836 (2019b), 1906.11005.

[Tumasyan et al.(2022)] A. Tumasyan et al. (CMS), JINST **17**, P03014 (2022), 2111.03027.

[Aad et al.(2022)] G. Aad et al. (ATLAS), Eur. Phys. J. C **82**, 95 (2022), 2109.10627.

[ATL(2022b)] Tech. Rep., CERN, Geneva (2022b), URL https://cds.cern.ch/record/2811135.

[ATL(2022c)] Tech. Rep., CERN, Geneva (2022c), URL https://cds.cern.ch/record/2804062.

[Sjöstrand et al.(2015)Sjöstrand, Ask, Christiansen, Corke, Desai, Ilten, Mrenna, Prestel, Rasmussen, and T. Sjöstrand, S. Ask, J. R. Christiansen, R. Corke, N. Desai, P. Ilten, S. Mrenna, S. Prestel, C. O. Rasmussen, and P. Z. Skands, Comput. Phys. Commun. **191**, 159 (2015), 1410.3012.

[Schätzel(2015)] S. Schätzel, Eur. Phys. J. C **75**, 415 (2015), 1403.5176.

[Abdesselam et al.(2011)] A. Abdesselam et al., Eur. Phys. J. C **71**, 1661 (2011), 1012.5412.

[CMS(2014)] Tech. Rep., CERN, Geneva (2014), URL http://cds.cern.ch/record/1647419.

[Plehn et al.(2010)Plehn, Spannowsky, Takeuchi, and Zerwas] T. Plehn, M. Spannowsky, M. Takeuchi, and D. Zerwas, JHEP **10**, 078 (2010), 1006.2833.

[Aaboud et al.(2019)] M. Aaboud et al. (ATLAS), Eur. Phys. J. C **79**, 375 (2019), 1808.07858.

[Kasieczka et al.(2019b)Kasieczka, Plehn, Butter, Cranmer, Debnath, Dillon, Fairbairn, Faroughy, Fedork G. Kasieczka, T. Plehn, A. Butter, K. Cranmer, D. Debnath, B. M. Dillon, M. Fairbairn, D. A. Faroughy, W. Fedorko, C. Gay, et al., SciPost Phys. **7**, 014 (2019b), URL https://scipost.org/10.21468/SciPostPhys.7.1.014.

[Bhattacharya et al.(2022)Bhattacharya, Guchait, and Vijay] S. Bhattacharya, M. Guchait, and A. H. Vijay, Phys. Rev. D **105**, 042005 (2022), 2010.11778.

[arX(2022b)] Tech. Rep., CERN, Geneva (2022b), 2205.02817, URL https://cds.cern.ch/record/2808775.

[Berger et al.(2011)Berger, Cao, Chen, and Zhang] E. L. Berger, Q.-H. Cao, C.-R. Chen, and H. Zhang, Phys. Rev. D **83**, 114026 (2011), 1103.3274.

[ATL(2021)] Tech. Rep., CERN, Geneva (2021), URL http://cds.cern.ch/record/2773738.

[Aad et al.(2013a)] G. Aad et al. (ATLAS), Phys. Rev. Lett. **111**, 232002 (2013a), 1307.6511.

[Jezabek(1994)] M. Jezabek, Nucl. Phys. B Proc. Suppl. **37**, 197 (1994), hep-ph/9406411.

[Brandenburg et al.(2002)Brandenburg, Si, and Uwer] A. Brandenburg, Z. G. Si, and P. Uwer, Phys. Lett. B **539**, 235 (2002), hep-ph/0205023.

[Sirunyan et al.(2019)] A. M. Sirunyan et al. (CMS), Phys. Rev. D **100**, 072002 (2019), 1907.03729.

[Mahlon and Parke(2010)] G. Mahlon and S. J. Parke, Phys. Rev. D **81**, 074024 (2010), 1001.3422.

[Schwienhorst et al.(2011)Schwienhorst, Yuan, Mueller, and Cao] R. Schwienhorst, C. P. Yuan, C. Mueller, and Q.-H. Cao, Phys. Rev. D **83**, 034019 (2011), 1012.5132.

[Aguilar-Saavedra et al.(2017)Aguilar-Saavedra, Boudreau, Escobar, and Mueller] J. A. Aguilar-Saavedra, J. Boudreau, C. Escobar, and J. Mueller, Eur. Phys. J. C **77**, 200 (2017), 1702.03297.

[Shelton(2009)] J. Shelton, Phys. Rev. D **79**, 014032 (2009), 0811.0569.

[Krohn et al.(2010)Krohn, Shelton, and Wang] D. Krohn, J. Shelton, and L.-T. Wang, JHEP **07**, 041 (2010), 0909.3855.

[Kitadono and Li(2016)] Y. Kitadono and H.-n. Li, Phys. Rev. D **93**, 054043 (2016), 1511.08675.

[Godbole et al.(2019)Godbole, Guchait, Khosa, Lahiri, Sharma, and Vijay] R. Godbole, M. Guchait, C. K. Khosa, J. Lahiri, S. Sharma, and A. H. Vijay, Phys. Rev. D **100**, 056010 (2019), 1902.08096.

[Aad et al.(2013b)] G. Aad et al. (ATLAS), Phys. Rev. D **88**, 012004 (2013b), 1305.2756.

[Chatrchyan et al.(2012b)] S. Chatrchyan et al. (CMS), JHEP **12**, 015 (2012b), 1209.4397.

[Do et al.(2003)Do, Groote, Korner, and Mauser] H. S. Do, S. Groote, J. G. Korner, and M. C. Mauser, Phys. Rev. D **67**, 091501 (2003), hep-ph/0209185.

[Bierlich et al.(2022)] C. Bierlich et al. (2022), 2203.11601.

[Cacciari et al.(2008)Cacciari, Salam, and Soyez] M. Cacciari, G. P. Salam, and G. Soyez, JHEP **04**, 063 (2008), 0802.1189.

[Cacciari et al.(2012)Cacciari, Salam, and Soyez] M. Cacciari, G. P. Salam, and G. Soyez, Eur. Phys. J. C **72**, 1896 (2012), 1111.6097.

[Cacciari and Salam(2006)] M. Cacciari and G. P. Salam, Phys. Lett. B **641**, 57 (2006), hep-ph/0512210.

[Aad et al.(2019c)] G. Aad et al. (ATLAS), Eur. Phys. J. C **79**, 760 (2019c), 1904.05631.

[CMS(2021)] Tech. Rep., CERN, Geneva (2021), URL http://cds.cern.ch/record/2783928.